High Frequency Electron Dynamics in Thin Film Superconductors and Applications to Fast, Sensitive THz Detectors

A Dissertation

Presented to the Faculty of the Graduate School

of

Yale University

in Candidacy for the Degree of

Doctor of Philosophy

By

Peter John Burke

Dissertation Director: Professor Daniel E. Prober

December, 1997

Abstract

High Frequency Electron Dynamics in Thin Film Superconductors and Applications to Fast, Sensitive THz Detectors

Peter John Burke

December, 1997

This thesis is an experimental study of the dynamics and noise processes in diffusion and phonon-cooled superconducting hot-electron bolometer mixers which will serve as ultra-low noise detectors in THz heterodyne receivers. The conversion efficiency and output noise of devices of varying lengths were measured with rf frequencies between 8 and 40 GHz. The devices studied consist of 100 Å thin film Nb bridges connected to thick (1000 Å), high conductivity normal metal (Au) leads. The lengths of the devices studied range from 0.08 μm to 3 μm. For devices longer than the electron-phonon interaction length $L_{e-ph} \equiv \sqrt{D\tau_{e-ph}}$, with D the diffusion constant and τ_{e-ph}^{-1} the electron-phonon interaction rate, the hot-electrons are cooled dominantly by the electron-phonon interaction, which in Nb is too slow for practical applications. If the device length is less than $\pi\ L_{e-ph}$ ($\approx$ 1 μm at 4.2 K), then out-diffusion of heat into the high conductivity leads dominates the cooling process. In this limit, the intermediate frequency (IF) bandwidth is found to vary as L^{-2}, with L the bridge length, as expected for diffusion cooling. The shortest device has an IF bandwidth greater than 6 GHz, the largest reported for a low-T_c superconducting bolometric mixer. The component of the output noise not due to Johnson noise decreases with frequency in the same manner as the conversion efficiency, consistent with a model based on thermal fluctuations. The noise bandwidth is 1.4-9.4 times larger than the gain bandwidth, and the mixer noise is *low*, ranging from 120-530 K (double side-band).

The crossover from phonon dominated to diffusion dominated behavior is also demonstrated using noise thermometry measurements in the normal state. Scalar measurements of the device differential impedance in the intermediate state agree with a theoretical model which takes into account the thermal and electrical dynamics.

Acknowledgments

This thesis work is the result of many individual efforts combined. I must first thank my collaborators at JPL, namely Rob McGrath, Anders Skalare, Boris Karasik, Bruce Bumble, and Rick LeDuc. My collaboration with them was very productive and enjoyable. During my visits to JPL, many conference calls, and meetings, they were always willing to help support my thesis research in any way they could, and they did.

Additionally, I have enjoyed the company and support of the entire cast of characters in Becton Center over the years. I was very impressed by the willingness of everyone I worked with at Yale to take time out from their busy schedules to help fix this or that piece of equipment or understand this or that theoretical concept. I have tried to emulate that behavior myself, and reciprocate some of the assistance I have been given. I must also provide special thanks to Jean Belfonti for guiding me through the Yale bureaucracy.

I have also enjoyed immensely the people I worked closely with in ProberLab, namely Lianne Verheijen, Alex Kozhevnikov, and especially Rob Schoelkopf. The first thing Rob taught me was how to make SMA connectors, but that was just the beginning. I have continued learning from him about topics mundane and profound alike. I hope that will continue.

The relationship between advisor and student is in many ways like the relationship between parent and child. A child receives more support and care from the parent than it can repay, and when mature it leaves the parent with only memories. My relationship with Dan Prober was no exception. He selflessly provided me with more support and training than I can ever hope to repay, to which I can only say: Thanks.

I am also happy to acknowledge the State of Connecticut and NASA for financial support.

Finally, my parents have provided me with an enormous amount of support, both moral and financial, and have always merrily put up with my complaints about graduate school, providing advice and reminiscing about their own experiences as graduate students when necessary. I can only imagine how difficult it was for them to go through graduate school with me screaming in the back seat. They instilled in me the work ethic required to complete this thesis, and so in many ways it is not only my work, but theirs also. I hope they are proud.

Contents

List of Figures

List of Tables

List of symbols and abbreviations

HEB Hot-electron bolometer

SIS Superconducting-insulating-superconducting (tunnel junction)

LO Local oscillator

rf radio frequency

IF Intermediate frequency

T_{rec} Receiver noise temperature

T_{IFamp} IF amplifier (input) noise temperature

T_{out} Output noise

T_{mix} Mixer noise temperature

T_e Electron temperature

T_b Bath temperature

$T_{T.F.}$ Output noise due to thermal fluctuations

$T_{John.}$ Output noise due to Johnson noise

DSB Double side band

SSB Single side band

η_{rf} rf coupling

η_{mixer} Mixer conversion efficiency

η_{IF} IF mismatch factor

Γ Voltage reflection coefficient

Z_L Load impedance

Z_0 Characteristic impedance (377 Ω in free space)

R_L Load resistance

ϵ_{avg} Average dielectric constant of vacuum and substrate

D Diffusion constant

L_{e-ph} Electron-phonon length $\equiv \sqrt{D\tau_{e-ph}}$

L_{e-e} Electron-electron length $\equiv \sqrt{D\tau_{e-e}}$

l Elastic mean free path

τ_{th} Thermal time constant

τ_m Momentum relaxation time

τ_{e-ph} Electron-phonon interaction time

τ_{e-e} Electron-electron interaction time

τ_{eff} Effective thermal time constant

$\tau_{effNOISE}$ Effective thermal time constant fit to output noise

R Resistance

R_N Normal state resistance

I_{dc} dc current

V_{dc} dc voltage

T' normalized temperature

p' normalized power

$\mathcal{L}$ Lorenz number

K Thermal conductivity

G Thermal conductance

c Specific heat

C Heat capacity

G_{eff} Effective thermal conductance

α_0 Electro-thermal feedback factor, no load

α Electro-thermal feedback factor, with load

$f_{noise3dB}$ 3 dB noise bandwidth, i.e. frequency at which mixer noise doubles

$f_{gain3dB}$ 3 dB gain bandwidth, i.e. frequency at which conversion efficiency falls by 3 dB

β Parameter which quantifies relative amount of diffusion and phonon cooling based on device length: $0.25\ (L/L_{e-ph})^2$

γ Electronic specific heat per Kelvin; also magnitude of random force in Langevin equation

Chapter 1

Introduction

One of the most fundamental methods of studying physical systems is to observe electromagnetic emissions which result from changes in the system's physical state. Therefore, the development of sensitive detectors is of paramount importance, especially for astronomical and remote sensing experiments where signal levels are generally weak. This is especially true in regions of the spectrum where the earth's atmosphere is opaque, and observation time is limited to high altitude, airborne, and satellite-based telescopes. The submillimeter range of the spectrum (defined loosely as $f =$ 100 GHz to $f = 3$ THz) is one these regions, which is the motivation for the work described in this thesis.

In the past ten years, remarkable progress has been made in the development of ultra-low noise receivers for the millimeter and sub-millimeter band. These receivers use as detectors superconducting-insulating-superconducting (SIS) tunnel junctions. For reasons described below, these receivers do not perform well above approximately 1 THz, and therefore there is still a need for sensitive detectors above 1 THz.

As research described in this thesis will show, superconducting hot-electron bolometers are excellent candidates as ultra-low noise detectors in THz receivers. The goal of the work described in this thesis is to develop and test experimentally a model for the physical processes governing the performance of hot-electron bolometers (HEB). In this chapter, we first motivate further the development of such a detector. Next, existing technologies already in use are described. Finally,

the hot-electron bolometer is described and its advantages and disadvantages are discussed. The remainder of the thesis describes measurements to determine the sensitivity and speed of diffusion-cooled Nb HEB's under various operating conditions and device geometries and compares them with theoretical predictions.

1.1 Motivations and Applications

1.1.1 Emission in the Sub-mm

Emissions in the sub-mm region of the spectrum from naturally occurring objects can be divided into broadband continuum emission and emission at discrete frequencies. Broadband emission includes black-body radiation at temperatures such that $k_B T \sim \hbar\omega$. For the frequency range of interest here, this corresponds to temperatures of order 10-100 K. While broadband radiation (such as the cosmic microwave background) is very interesting topic to study at millimeter wavelengths, there is also much to be learned by looking in more detail at the spectral intensity. Since the hot-electron bolometer is being considered primarily for use in precision THz spectroscopy applications, emissions at discrete frequencies will be considered in more detail. Sources of discrete frequencies in the sub-mm arise from transitions between molecular vibration and rotational energy levels. Two important examples of systems which can be studied by THz spectroscopy are interstellar molecular dust clouds and the earth's atmosphere.

Figure 1.1 indicates schematically the emission in the submillimeter band from a typical interstellar cloud. A fundamental outstanding problem in physics and astronomy is the birth of stars and planetary systems. Stars are born by gravitational collapse of interstellar dust in clouds, and heat must be radiated away for this collapse to continue. Much of this heat is radiated by molecular transitions in the sub-millimeter band. Information on the composition, density, and temperature of such clouds is clearly vital to the study of star and planetary formation, and can be provided by THz astronomy.

THz spectroscopy has also been applied to studies of atmospheric chemistry with great success (Manney et al. 1996). Many important molecules in atmospheric chemistry such as ClO, O_3, OH, and H_20 have emission lines in the mm and sub-mm band. The first global measurements of ClO, an

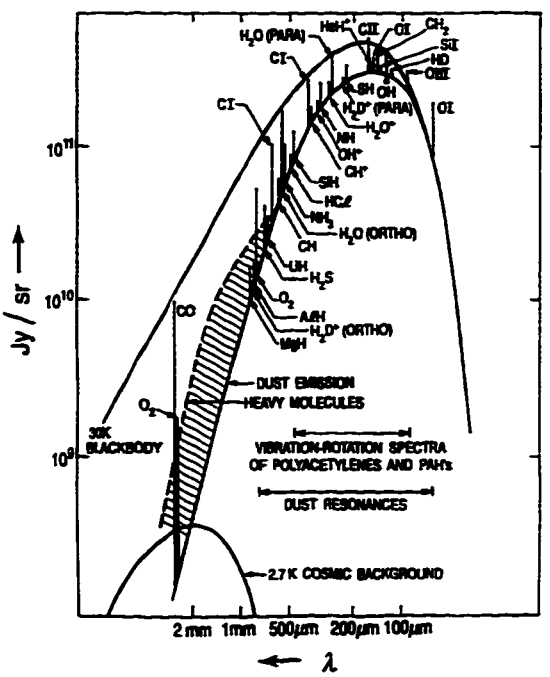

Figure 1.1: Schematic emission in the sub-mm band from a molecular cloud, birth place of stars and planets. Typical temperatures inside molecular clouds are 10-30 K. (From Phillips et al, 1992, with permission.)

important molecule in the destruction of O_3, were done using mm-wave spectroscopy. Details of the line shape provide important information about the density, pressure, and temperature of molecules of interest. Future satellite, airborne, and balloon missions will continue these measurements on the global scale.

Sub-mm emission can also be produced in artificial quantum wells. Bloch-oscillations and Rabi-oscillations in semiconductor quantum-well systems have emission in the sub-mm, since the energy levels of electrons in quantum wells are typically split by a few meV.

1.1.2 Detection in the Sub-mm

At radio and microwave frequencies below about 100 GHz, low noise semiconductor based amplifiers are available to pre-amplify incoming signals before detection and further signal-processing (Maas 1993). At higher frequencies, incoming signals are coupled directly to a detector. Therefore, the noise performance of the detector dominates the system noise and is thus deserving of the most

attention.

Generally, there are two modes of detection to consider: *incoherent* or *direct* detection, and *coherent* or *heterodyne* detection. In direct detection mode, a dc signal is generated across the detector which is proportional to the rf power coupled to the device over a very wide frequency range. (The phase of the incoming signal is not preserved, hence the term incoherent.) Therefore, a device operating in direct detection mode offers essentially no spectral resolution. To get spectral resolution, the rf radiation must be filtered before it is detected. Fourier transform spectrometers in the sub-mm band can be built for this purpose, but the spectral resolution is at best $\Delta\nu/\nu \sim 10^{-5}$ (Harris 1990). For identification of single molecular species, a spectral resolution of at least $\Delta\nu/\nu \sim 10^{-6}$ is required. Therefore, heterodyne detection is required for spectral line studies. Additionally, the hot-electron bolometers developed in this thesis are intended for use in heterodyne systems, so more attention will be devoted to such systems.

Heterodyne detection requires a non-linearity in the detector which "mixes" the signal with a local oscillator. For this reason, the detector is also referred to as a *mixer*. Figure 1.2 indicates a schematic of heterodyne detection. The (weak) signal to be detected and a locally produced coherent signal (the local oscillator, LO) are applied to the detector. Non-linearity in the detector produces an output signal at the difference or *intermediate* frequency (IF), which is then amplified, typically by a cooled, low-noise GaAs based HEMT transistor and then detected by a spectrum analyzer. The phase of the IF signal is equal to the phase of the incoming signal (plus a constant), hence the term coherent detection.

The parameter used to quantify the noise of a given heterodyne system is the power per frequency at the rf input required to give a signal to noise of one at the output intermediate frequency. Therefore, the units are W/Hz. Since a (matched) resistor at physical temperature T radiates $k_B T$ power per frequency in the Rayleigh-Jeans limit, a common unit for noise power is *noise temperature*. This is the temperature a matched resistor would be at to radiate $k_B T$ power per frequency into the receiver. (This does not necessarily correspond to the temperature of any physical system.) The receiver noise temperature is related to the various components of figure 1.2 as follows:

$$T_{rec.} = \frac{T_{out}}{\eta_{rf}\eta_{mixer}} + \frac{T_{IFamp.}}{\eta_{rf}\eta_{mixer}\eta_{IF}}. \tag{1.1}$$

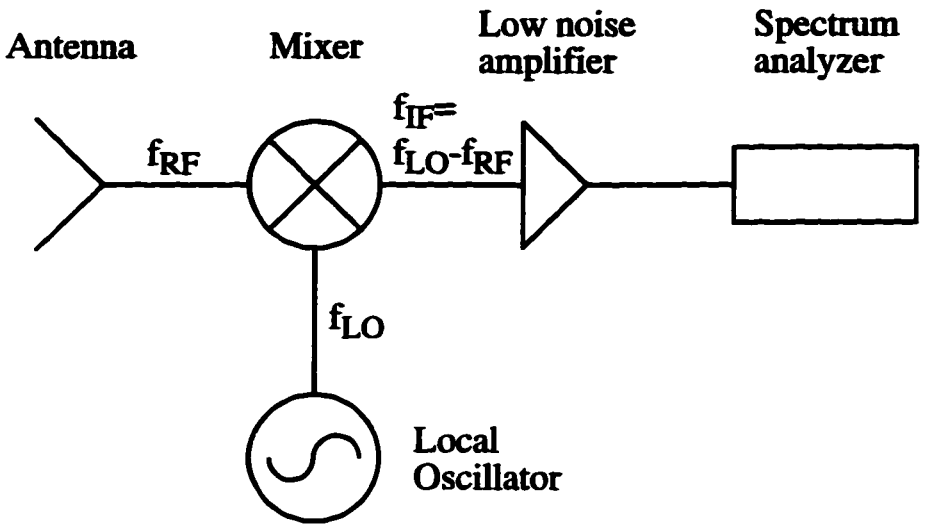

Figure 1.2: Schematic of a heterodyne detection system. For frequencies below 100 GHz, a low-noise pre-amplifier would be used between the antenna and the mixer.

Here T_{out} is the output noise generated by the mixer itself, $T_{IFamp.}$ is the *input* noise of the IF amplifier, η_{rf} is the input (rf) power coupling to the mixer, η_{IF} is the coupling between the mixer and the IF amplifier, and η_{mixer} is the conversion efficiency of the mixer, defined as the ratio of the available power at the mixer IF output to the available signal power at the mixer rf input. IF amplifiers with noise temperatures in the range of $2-3\ K$ are readily available. It should be clear the the mixer output noise and conversion efficiency are crucial parameters in the system. The rf and IF coupling can be made unity at select frequencies by careful circuit design, if the input and output impedance of the mixer are known. In order to quantify the contribution of the mixer itself to the system's overall noise, independent of the coupling circuit, the *mixer noise* is defined as

$$T_{mix} \equiv \frac{T_{out}}{\eta_{mixer}} \tag{1.2}$$

For a given device, this is the minimum *receiver* noise temperature, if the coupling circuits are perfect and the IF amplifier generates little noise in comparison with T_{out}. Clearly the mixer noise is the most important device property, but there are other practical considerations that define desired mixer properties. In addition to having a low noise, it should *1) require low LO power, 2) be fast*

3) be easy to couple to at both rf and IF frequencies.

Local oscillators at THz frequencies are usually fixed in frequency, and have limited power, typically not more than a few mW at best. Therefore, a mixer which requires low local oscillator power is desirable. During observation, the local oscillator frequency is fixed, and the IF output of the device is sent into a spectrum analyzer, with many GHz of bandwidth. The spectrum analyzer (usually an acousto-optic spectrometer) is designed to measure all frequencies within its band simultaneously. The signal-to-noise in each frequency bin depends on the integration time at each bin, and therefore the most efficient use of the available observation time is to measure as many different frequencies as possible simultaneously. For this to be possible, the detector should be fast enough to allow detection of signals within several (10-20) GHz of the local oscillator. If the local oscillator could be swept, and the intermediate frequency were kept at some low value, say 1 MHz, then the system would be "viewing" only a 1 MHz bin of the signal at a time. A broader band IF system allows the device to view a larger slice of the signal spectrum for a given LO frequency, and results in a larger observation/integration time per rf frequency bin.

At THz frequencies, the rf coupling is usually achieved quasi-optically. A Si or quartz lens focuses an incoming THz (Gaussian) beam onto a micro-fabricated antenna, which can be a dipole, slot, bow-tie, spiral, or log-periodic antenna, for example. The antenna is a coupling circuit and transformer in one. Since the coupled device is much less than a wavelength in size, it can be treated as a lumped circuit element. The effect of the antenna is described as a voltage source with a particular source impedance. The source impedance is usually of order $Z_0/\sqrt{\epsilon_{avg}}$ ($=$ 105 Ω for Si), where ϵ_{avg} is the average dielectric constant of vacuum and the dielectric lens (Rebeiz 1992; Rutledge et al. 1983; Elliott 1981), and $Z_0 = 377\ \Omega$ is the characteristic impedance of free space. For example, the source impedance of self-complimentary antennas (which have broadband frequency response) is 114 Ω on quartz (Rebeiz 1992). In order to achieve maximum coupling between the device and the incoming beam, the device impedance should be equal to the complex conjugate of the source impedance. ***Broadband matching to the device is easiest if the device impedance is real and of order*** 100 Ω.

The device output impedance should be well-matched to the IF amplifier. The input impedance of most "off the shelf" IF amplifiers is 50 Ω, by convention. From this point of view, an output

impedance of 50 Ω is most desirable for a mixer. In principle, IF amplifiers can be designed with an input impedance that is different from 50 Ω. The ideal system would have a mixer output impedance equal to the input impedance of the HEMT (the first stage of the IF amplifier), since this would require no matching network between the device output and the HEMT gate input. However, since low-noise amplifiers with 50 Ω input impedance are readily available, a mixer output impedance near 50 Ω is the best compromise.

So far, we have considered an input at only one signal frequency (i.e. single-side-band operation). However, it should be clear that two different signal frequencies, if symmetrically placed above and below the local oscillator frequency, will cause an IF output at one frequency, given by the absolute value of the difference between the LO and rf frequency. More sophisticated circuits can be constructed which are sensitive to only one "side" of the local oscillator, the "upper side band", or "lower side band." Engineers must decide whether to build the more complicated circuit, or to keep the circuit simple and use other methods to determine whether a particular feature in the intermediate frequency spectrum arose from the upper-side-band, or lower-side-band, such as adjusting the LO frequency and tracking which way the peaks move.

If the system is being used to detect signals in both the upper-side-band and the lower-side-band at the same time, then the important noise parameter is the ***double side band*** noise temperature. This is defined as the signal power per frequency at the rf input in the upper-side-band ***plus*** the signal power per frequency at the rf input in the lower-side-band required to give a signal to noise of one at the output intermediate frequency. The ***single-side-band*** noise temperature is simply that power per frequency at the rf input in *one* of the side-bands required to give a signal-to-noise of one at the output intermediate frequency. In most systems, the sensitivity to the upper-side-band is equal to the sensitivity of the lower-side-band, and therefore the noise temperatures are related by:

$$T_{rec}(DSB) = T_{rec}(SSB)/2. \tag{1.3}$$

Classically, there is no lower-limit to the noise temperature of a receiver. However, quantum mechanically this is not the case. The mixers considered in this thesis can be classified as phase-insensitive linear amplifiers, since the system gain is independent of the phase of the rf input signal, and the output power at the IF is proportional to (and larger than) the input power at the rf.

Regardless of the details of the system, it can be shown on very general grounds (Caves 1981) that the minimum noise temperature of such an amplifier is given by

$$T_{min} = \hbar\omega/k_B\kappa, \tag{1.4}$$

where κ is a number of order unity. The noise temperature must be very clearly defined when operating near this noise floor, and for the various possible definitions, $\kappa = 1$, 2, ln2, or ln3 (Tucker and Feldman 1985). Since the experiments described in this thesis do not approach this noise floor, we will not discuss the issue further and take $\kappa = 1$. This noise can be considered a combination of quantum fluctuations in the input signal as well as quantum fluctuations in the internal degrees of freedom of the measurement system (i.e., the mixer). As long as the amplifier is linear and phase-insensitive, the details of the internal degrees of freedom always conspire to enforce equation 1.4. This limit is referred to as the "quantum limit". The goal of any research on THz mixers is to construct a device which achieves this limit of sensitivity and fulfills the three practical requirements mentioned above. As we will see, HEB's promise to achieve these goals.

1.2 Existing technologies

There are two types of mixers in broad use at THz frequencies: Schottky diodes and SIS tunnel junctions. Both are briefly discussed here.

1.2.1 SIS tunnel junctions

SIS tunnel junctions are widely used as ultra-sensitive mixers for frequencies between 100 GHz and 1 THz. The material of choice is Nb, which has a critical temperature of 9.25 K. The energy gap in this material, 3 meV, corresponds to 740 GHz. Experiments performed during the 1980's demonstrated that the quantum limit of sensitivity, eq. 1.4, could be achieved using SIS detectors (McGrath et al. 1981; Face et al. 1986; Mears et al. 1990). Today, practical systems utilizing SIS mixers are in wide use, and typically achieve a noise temperature a few times the quantum limit. SIS detectors have a geometric capacitance which necessitates careful design of rf coupling circuits. Thus, SIS tunnel junctions are *low noise, fast, and require low LO power.* However, they are *not*

easy to match at IF and RF frequencies. Additionally, SIS detectors have degraded performance above the gap frequency, and are expected to degrade sharply at twice this frequency. Higher-gap superconductors such as NbN or even high-T_c superconductors may achieve quantum-limited performance at frequencies above 1 THz, but none have been demonstrated so far. Finally, the geometric capacitance requires the construction of low-loss tuning circuits which are difficult to construct at frequencies above the gap frequency of Nb.

1.2.2 Schottky diodes

Schottky diodes are used as mixers for frequencies above 1 THz. The noise performance of Schottky diodes is typically no better than 150 times the quantum limit (Crowe, Mattauch, Roser, Bishop, Peatman, and Liu 1992). Additionally, Schottky diodes require large LO power, mW, necessitating the use of bulky molecular gas lasers as local oscillators. Schottky diodes are *fast*, but they are *not low noise, and require large LO power.*

1.3 Hot-electron bolometers

A bolometer is a detector that functions on the following simple principle: rf signal power heats a device, and this temperature shift is measured via an appropriate thermometer. In a *hot-electron* bolometer, the electrons are heated by dc and rf power above the temperature of the lattice. If the resistance of the electronic system depends on the electron temperature, then the resistance can be used as a thermometer. A bolometer can operate as a mixer since the temperature shift is proportional to the power absorbed:

$$\begin{aligned} \delta T \propto V(t)^2/R &\sim \left(V_{LO}cos(\omega_{LO}t) + V_{sig}cos(\omega_{sig}t)\right)^2 \\ &\sim V_{LO}V_{sig}cos\left((\omega_{LO} - \omega_{sig})t\right) + \textit{dc and high frequency terms.} \end{aligned} \tag{1.5}$$

Since the temperature changes at the intermediate frequency $(\omega_{LO} - \omega_{sig})$, the resistance changes at the intermediate frequency. Under a current bias, this leads to an oscillating voltage at the intermediate frequency. Thus, the device performs as a mixer. This process will be analyzed in detail in later chapters. Here it is important to note the intermediate frequency must be less than

the energy-relaxation rate for the electron system, otherwise the electron temperature will be unable to follow the difference frequency. Quantitatively, the mixer conversion efficiency drops by 3 dB at an intermediate frequency given by

$$f_{3dB} = 1/(2\pi\tau_{th}), \tag{1.6}$$

where τ_{th} is the thermal (cooling) time constant. For the purposes of this thesis, this frequency will be defined as the *gain bandwidth*. It is this issue that has limited the use of hot-electron-bolometer mixers, and which research in this thesis addresses in a very direct way.

1.3.1 Semiconductor based HEBs: InSb, AlGaAs

The first hot-electron-bolometer mixers used electrons in lightly doped n-type bulk InSb. When the InSb is cooled to 4 K or below, the electrons become decoupled from the lattice and hence can be heated above the lattice temperature. The mobility and hence the resistance depends on the temperature ($\mu \propto T_e^{3/2}$), so the semiconductor can be used as a mixer. The results of the first mixing experiments in InSb were published in Arams et al. (1966). The first practical receiver was described in Phillips and Jefferts (1973). Since then, receivers have achieved noise temperatures of 20 to 25 times the quantum limit at rf frequencies of 500, 600 and 800 GHz (Brown et al. 1985; Padman et al. 1992). Higher rf frequency operation is more difficult since the bulk InSb sample would have to be integrated into an antenna. (The above results utilized waveguide coupling.) Additionally, higher frequency operation based on resonant absorption at the cyclotron frequency (as in Brown et al. (1985)) requires a magnetic field up to 1 Tesla.

The main reason that InSb receivers are not in widespread use is the limitation on the maximum intermediate frequency, given by the electron-phonon inelastic interaction rate. In InSb, this rate is $\approx (0.1\mu s)^{-1}$, which limits the intermediate frequency bandwidth to about 1 MHz. This is usually unacceptably low. A multi-GHz intermediate frequency bandwidth is desired. InSb mixers are *low noise*, but *slow*.

The two dimensional electron gas (2-DEG) in modulation-doped AlGaAs/GaAs heterostructures has also been investigated as a potential medium for use as hot-electron mixers (Yang et al. 1995; Yang et al. 1993). By applying enough LO and dc power to heat the electrons in a quantum well to approximately 90 K from a lattice temperature of 4.2 K or 19 K, it was possible to observe

mixing and measure the thermal time-constant. A gain bandwidth of 1.7 GHz was measured. Low-noise receivers based on the 2-DEG medium have not yet been demonstrated, and would have to overcome some obstacles. The operating temperature of the electrons must be above approximately 80 K, because the mobility is only weakly temperature dependent below this temperature. This will increase the noise compared to lower temperature devices. Additionally, due to the high mobility the momentum-relaxation time τ_m is long enough to cause $\omega\tau_m > 1$ at THz frequencies. This will cause the rf (THz) impedance of the 2-DEG to develop an inductive component, decreasing the absorption of THz power and hence decreasing the device efficiency, or bandwidth if a tuning circuit is designed to compensate the kinetic inductance.

1.3.2 Superconductor based HEBs: Nb, NbN

A superconductor near T_c can be used as a very sensitive bolometer, since the resistance depends sharply on temperature. In dirty metal thin films below about 10 K, the electron-electron interaction rate is much faster than the electron-phonon interaction rate, so that dc and rf power can heat the electrons above the temperature of the lattice. Additionally, in dirty metals, the electron momentum relaxation time is very short (< 1 fs), so that power should be absorbed up to very high frequencies, $\sim$ 100 THz. Gershenzon et al. (1982) showed that dirty Nb superconducting thin films absorb radiation uniformly from 10^{10} to 10^{15} Hz, with approximately the same efficiency. There, a magnetic field as well as a current bias was applied to bring the films into the "resistive" state near T_c. High frequency radiation was applied, and the change in the resistance was measured.

Nb superconducting HEB's were first used in mixing experiments in 1983. In these experiments (Gershenzon et al. 1983; Gershenzon et al. 1988; Gershenzon et al. 1989; Gershenzon et al. 1990; Gershenzon et al. 1990), the electron-energy relaxation rate in Nb (the electron-phonon interaction rate) was measured for a variety of samples at temperatures from 1.6-10 K. It was found that the electron-phonon interaction time was $\approx$ 1 ns at 4.2 K for dirty films, with a diffusion constant of $D = 1\ cm^2/s$. This would allow for an intermediate frequency bandwidth of $\approx$ 150 MHz, which is still too small for practical applications. Additional theoretical modeling (Gershenzon et al. 1990) suggested that the mixer noise temperature could approach 50 K, which is the quantum limit at 1 THz. This prediction was independent of the rf frequency, as long as the rf radiation

was absorbed by the electron system. This is true up to the electron-momentum relaxation rate, $\sim$ 100 THz (Prober 1993). Thus, the noise was predicted to be low up to very high rf frequencies, but the IF bandwidth was not sufficient.

Two approaches have been proposed to increase the intermediate frequency bandwidth of the superconducting bolometer, while keeping the noise low and the rf frequency range broad. The first approach is to use a material with a shorter electron-phonon interaction time. NbN has a somewhat higher T_c than Nb, and therefore also a stronger electron-phonon interaction. The predicted noise is still low, and the rf frequency range should also be broad. Initial experiments indicated an IF bandwidth of 5.3 GHz (Gol'tsman et al. 1991; Gousev et al. 1994). There, results between 1.6 K and 5.3 K were presented. By extrapolating the data to 10 K, the authors claim a bandwidth of 10 GHz could be achieved. Subsequent experiments have been unable to reproduce these results. The results have varied for the intermediate frequency bandwidth (0.6 GHz (Dzardanov et al. 1994), 1.1 GHz (Gol'tsman et al. 1995), 0.8 GHz (Karasik et al. 1995; Ekström et al. 1995), $3-4$ GHz (Yagoubov et al. 1996), 1.6 GHz (Kawamura et al. 1996), 2.2 GHz (Kawamura et al. 1997).) For some films apparently comparable to those of Gousev et al. (1994), the mixing bandwidth was less than 1 GHz. Recent experiments (Yagoubov et al. 1996) indicate that control of the film thickness may allow more control over the achieved bandwidth for NbN. Very thin films (3.5 nm) achieve the largest bandwidths. Promising sensitivities have also been achieved, between 410 K (DSB) at an rf frequency of 410 GHz, and 9000 K (DSB) at 1.2 THz. Thus NbN is worthy of further investigation.

A different approach was proposed by Prober (1993), and is the approach investigated in this thesis. The approach consists of using a very short strip of Nb as a hot-electron bolometer, less than the electron-phonon interaction length, $L_{e-ph} \equiv \sqrt{D\tau_{e-ph}}$, where τ_{e-ph}^{-1} is the electron-phonon interaction rate and D the diffusion constant. The electron-phonon interaction length is essentially the length which an electron diffuses before emitting a phonon. For short bridges, cooling of the electrons can occur by out-diffusion of heat into high-conductivity, normal metal leads. In this case, the thermal time constant is the diffusion time, given by

$$\tau_{diff} = \frac{L^2}{\pi^2 D}. \tag{1.7}$$

(The numerical factor will be derived in chapter 2.) Thus, for a 0.1 μm bridge with a diffusion constant of 1 cm^2/s, a time constant of order 10 ps is predicted, allowing an intermediate frequency bandwidth of order 10 GHz to be achieved.

1.4 Thesis overview

The research in this thesis was designed to determine the limits on the speed and sensitivity of "diffusion-cooled" hot-electron bolometers. In chapter 2, an overview of the expected theoretical performance is presented, and the expected validity of the theories is discussed, with suggestions for future modifications of the theory. In chapter 3, the experimental designs and techniques are further discussed. The device geometries, dc properties, and fabrication techniques are discussed in chapter 4. Due to the relative ease of experiments below 100 GHz, mixing experiments were performed on devices of different lengths with rf and LO frequencies of 10-40 GHz. The results will be presented in chapter 5. The thermal time-constant is found to obey the scaling law predicted by equation 1.7. Additionally, the noise and conversion efficiency were measured, as a function of LO and dc power and intermediate frequency, for devices of different lengths at a bath temperature of 2 K. The output noise is found to be dominated by thermal fluctuation noise, whose frequency dependence is similar to the frequency dependence of the conversion gain. This result increases the available intermediate frequency bandwidth by a factor of 1.4-9.4. In chapter 6, the results are put into a broader context by comparing with other results on diffusion-cooled bolometers. Then, in chapter 7, conclusions are drawn. The hot-electron bolometer can be fast, with a bandwidth of at least 6 GHz, and is very sensitive. The measured mixer noise is between 120 K and 530 K (DSB). Thus, diffusion-cooled hot-electron mixers can simultaneously achieve very low noise and very large bandwidth, and promise to dramatically improve the noise performance of THz receivers.

Chapter 2

Theory

We begin this chapter with a generic description of bolometers as mixers, and then the particular realization for Nb hot-electron bolometers is discussed, first as a lumped element and then using a distributed element approach. The important quantities of interest are the conversion efficiency and noise as a function of intermediate frequency, dc power, LO power, and temperature. The device geometry will also be discussed, as it is important for diffusion-cooled bolometers.

2.1 Mixing in bolometers: generic description

In this section, the conversion efficiency and noise for hot-electron bolometers is derived using a pedagogical approach. More rigorous derivations can be found in the cited literature. Although we are only considering the case of hot-electron bolometers, the expressions are valid for any generic bolometric mixer. There are two intrinsic noise sources that are important for hot-electron bolometers: Johnson noise and thermal fluctuation noise. *Quantum* noise will be an important noise source in the future if the other noise sources are made small. This will be discussed at the appropriate times in the following sub-sections. In the mixers described in this thesis, thermal fluctuation noise dominates. In the first sub-section, the conversion efficiency will be calculated. Next, the thermal fluctuation noise will be calculated, in the absence of electro-thermal feedback. Then, the total noise at the output in the presence of electro-thermal feedback is calculated. The final subsection

discusses the *mixer noise.*

2.1.1 Calculation of conversion efficiency

In bolometric mixers, the non-linearity which causes mixing between the LO and signal (rf) frequencies is the fact that the resistance change is proportional to the power, which is proportional to the voltage *squared.* This concept is indicated schematically in figure 2.1. The LO voltage and signal voltage are shown before they are combined. The signal voltage is usually much smaller than the LO voltage. The voltages are added and then applied to the device. (This can be achieved optically, for example, in a 50/50 beam splitter before the gaussian beam is focused onto the device.) The instantaneous power dissipated is given by $V(t)^2/R$. The electron temperature cannot follow the rf and LO frequencies. However, if the difference frequency is small enough, then the electron temperature is modulated at the difference frequency. This causes a resistance change at the difference frequency, and hence a voltage drop across the device at the difference frequency.

In order to describe this process quantitatively, we write down a differential equation to describe the electron temperature as a function of time in the case of a pure current bias at the dc and IF frequencies. This will allow the development of an intuitive way to describe the mixing, as well as introduce the concept of electro-thermal feedback. In a later section, the assumption of current bias at the IF will be relaxed. We assume the dissipated power oscillates at the difference frequency, and write:

$$P_{input}(t) = I_{dc}^2 R(T_e(t)) + P_{ac} e^{i\omega_{IF} t}, \tag{2.1}$$

where $\omega_{IF} \equiv \omega_{LO} - \omega_{rf}$, $P_{ac} = 2\sqrt{P_{LO} P_{rf}}$ (from equation 1.5), and P_{LO}, P_{rf} are the LO and rf powers, respectively. (There will also be rf oscillations in the input power which the electron temperature will not be able to follow.) The LO and rf power will cause a dc component of the input power, which is not included because the response at the IF is of interest here. $R(T_e(t))$ is the resistance, which depends on temperature, which in turn depends on time.[1] The power flowing out is (in the linear response regime) proportional to the temperature difference between the bolometer

[1] At this point, no non-linearities in the underlying I-V curve are being postulated. The mechanism for the R(T) curve is not described at all; it is simply a phenomenological input parameter of the theory.

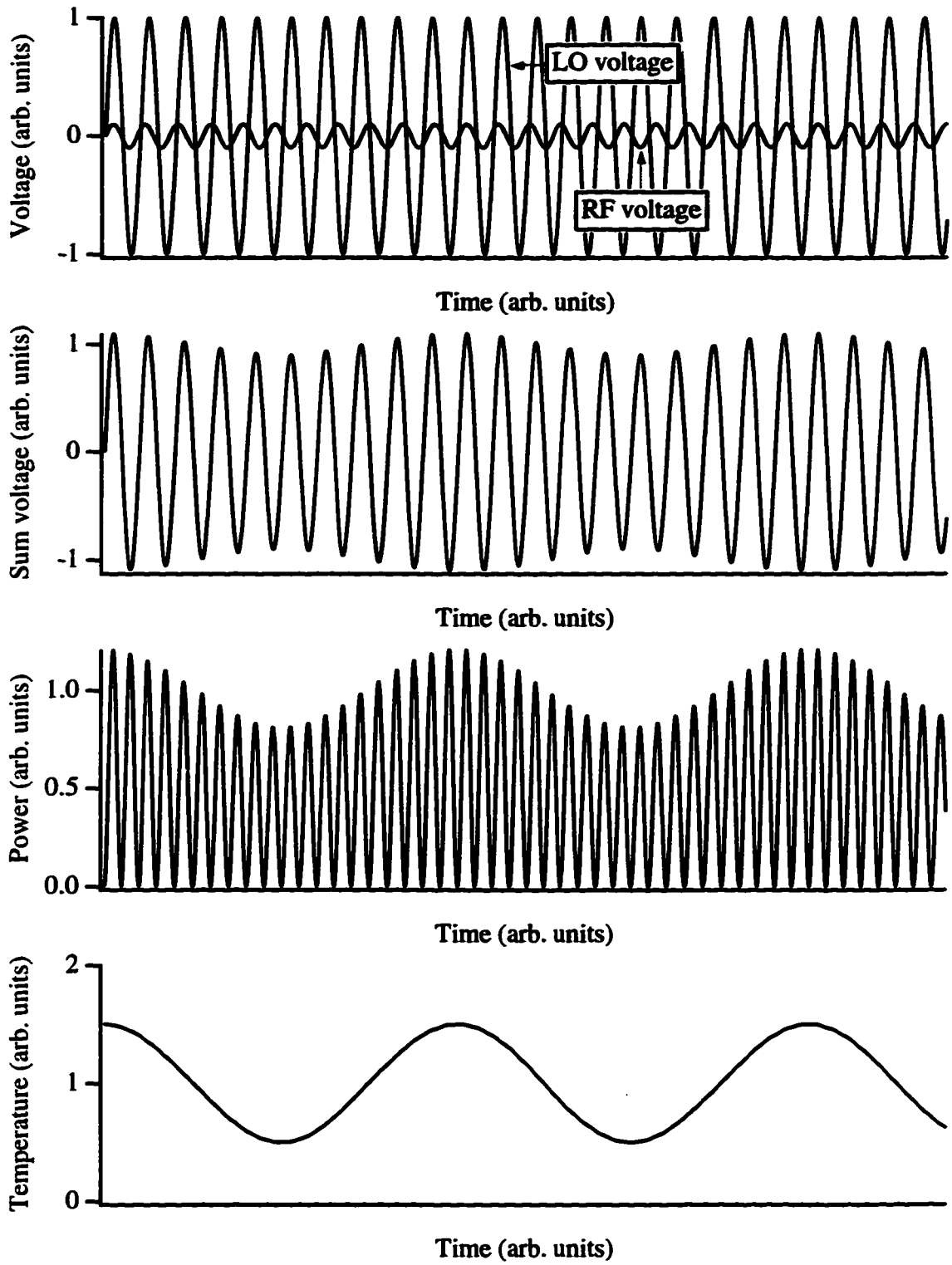

Figure 2.1: Schematic of the mixing process in bolometers. The electron temperature cannot follow the high-frequency signal, but it can follow the intermediate frequency. The parameters used to generate this plot are: $\omega_{IF} = 0.1\,\omega_{LO}$, $V_{RF} = 0.1\,V_{LO}$.

and a thermal reservoir or "bath":

$$P_{out}(t) = G(T_e(t) - T_b). \tag{2.2}$$

Here T_e is the bolometer temperature, which will be the electron temperature when we consider the special case of hot-electron bolometers below. T_b is the bath temperature. The electron temperature is time dependent, but the bath temperature is held fixed. (In the more general case, the expressions derived below based on equation 2.2 are still valid if G is replaced by dP_{out}/dT_e (Keizer 1987).) The inflowing power can either heat up the electrons or flow out to the bath. The conservation of energy then takes the form:

$$P_{input}(t) = dE(t)/dt + P_{out}(t) = CdT_e(t)/dt + P_{out}(t). \tag{2.3}$$

Here, $C = dE/dT_e$, with E the (thermal) energy stored in the electron system. (C is assumed to be independent of temperature in this calculation.) The electron temperature will have a dc shift above the bath temperature, as well as an oscillating component. Therefore, we make the ansatz:

$$\delta T_e(t) \equiv T_e(t) - T_b = \delta T_{dc} + \delta T_{ac} e^{i\omega_{IF}t}. \tag{2.4}$$

We can now solve for the temperature by Taylor expanding $R(T)$ as

$$R(T_e(t)) \approx R(T_b) + dR/dT_e * (T_e(t) - T_b) = R(T_b) + dR/dT_e * \delta T_e(t), \tag{2.5}$$

and substituting into equation 2.3 expression 2.4 for the temperature of the system. This results in[2]

$$\delta T_{dc} = \frac{P_{dc}}{G_{eff}} \tag{2.6}$$

$$\delta T_{ac} = \frac{P_{ac}}{G_{eff}} \frac{1}{1 + i\omega_{IF}\tau_{eff}} \tag{2.7}$$

[2]To include the effect of the rf and LO power on the dc shift in the electron temperature, P_{dc} should be replaced by $P_{dc} + P_{LO} + P_{rf}$.

where

$$\tau_{eff} \equiv \tau_{th}/(1-\alpha_0), \tag{2.8}$$

$$\tau_{th} \equiv C/G, \tag{2.9}$$

$$G_{eff} \equiv G\,(1-\alpha_0), \tag{2.10}$$

$$\alpha_0 \equiv \frac{I_{dc}^2 dR/dT}{G}. \tag{2.11}$$

The electron temperature will be modulated by P_{ac}/G if the intermediate frequency is small. As the intermediate frequency increases, the ac component of the electron temperature decreases.

The effect of the electro-thermal feedback between the electron temperature and the dc bias supply is described quantitatively by the parameter α_0. If α_0 is small (due to small current or small dR/dT), then the effect of electro-thermal feedback is small. In particular, the effective time constant τ_{eff} is equal to the "bare" thermal time constant τ_{th}, and the effective thermal conductance G_{eff} is equal to the bare thermal conductance G. If the parameter α_0 is large, then "electro-thermal feedback" is strong. There is a simple explanation for this: under a current bias, a small increase in the resistance causes the dc power dissipated to increase, since $P_{dc} = I^2R$. An increase in the input power causes the system temperature to rise. If dR/dT is positive, as is the case for superconducting bolometers, increasing the temperature serves to further increase the resistance, and there is positive feedback. Thus, α_0 is a quantitative measure of this feedback: when $\alpha_0 \simeq 1$, there is thermal runaway. In practice, the temperature will increase until the normal state is reached, and then dR/dT and α_0 will be zero, stopping the process. On the other hand, if the dc power supply is a ***voltage bias***, then it will serve to stabilize the system temperature: an increase in the resistance will cause a ***decrease*** in the power, since $P_{dc} = V^2/R$, which will cause a decrease in the system temperature, which will cause a decrease in the resistance, opposing the postulated resistance increase. Note that this will have the same effect on fluctuations: thus, electro-thermal feedback affects the system's response to an external stimulus as well as internal fluctuations of the temperature, enhancing both in the case of a current bias, and suppressing both in the case of a voltage bias[3].

[3]If dR/dT is negative (as in InSb), then the conclusions are reversed: A current bias will tend to stabilize, while a voltage bias will destabilize.

The ac voltage at the intermediate frequency is given by:

$$V_{ac} = I_{dc} dR/dT \; \delta T_{ac} = I_{dc} dR/dT_e \frac{P_{ac}}{G_{eff}} \frac{1}{1 + i\omega_{IF}\tau_{eff}}. \tag{2.12}$$

The conversion efficiency is defined as the ratio of the available output power at the IF to the available input power at the RF. The output power at the IF is proportional to V_{ac}^2. The above calculation was done assuming no load at the IF. If the IF load is equal to the bolometer resistance, then the AC voltage calculated above will be divided in half. The power coupled into the amplifier will be $(1/2)|V_{ac}|^2/R$, where V_{ac} is given by one half the value of equation 2.12. Thus, the conversion efficiency is given by

$$\eta(\omega_{IF}) = \frac{P_{LO}}{2\,R} \left(\frac{I_{dc}(dR/dT)}{G_{eff}} \right)^2 \frac{1}{1 + (\omega_{IF}\tau_{eff})^2}. \tag{2.13}$$

From this equation, it is clear that the conversion efficiency drops by 3 dB at an intermediate frequency given by equation 1.6, with τ_{th} replaced by the more general τ_{eff}:

$$f_{3dB} = 1/(2\pi\tau_{eff}) \tag{2.14}$$

In a later section, the physical processes which govern τ_{th} will be discussed in more detail.

The above calculation assumes that the current bias applies at both dc and at the intermediate frequency. However, at the intermediate frequency there is an additional load resistance, given by the input impedance of the intermediate frequency amplifier. If the intermediate frequency is in the GHz range, the amplifier input impedance is usually on the order of 50 Ω. A more careful analysis of the electro-thermal feedback taking into account the different environmental impedance at the dc and IF frequencies shows that the effect of the load resistance is to modify α_0 as follows (Arams et al. 1966; Mather 1984; Karasik and Elantiev 1996):

$$\alpha \equiv \frac{I_{dc}^2 dR/dT}{G} \left(\frac{R_L - R}{R_L + R} \right) = \alpha_0 \left(\frac{R_L - R}{R_L + R} \right), \tag{2.15}$$

where R_L is the load resistance at the IF, i.e. the input resistance of the IF amplifier. This definition of α reduces to the previous definition when $R_L \to \infty$. Since the load resistance is typically 50 Ω, if the device impedance is comparable to this, the electro-thermal feedback will be significantly

suppressed, according to 2.15. Physically, this is because the device is no longer "seeing" a current source at the intermediate frequency, but a 50 Ω "shunt". This is more like a voltage source than a current source, which tends to suppress electro-thermal feedback, as discussed above.

In addition to modifying the electro-thermal feedback, there will also be an impedance mismatch factor between the device output impedance and the input impedance of the IF amplifier, which should multiply equation 2.13 to predict the *coupled* conversion efficiency (Arams, Allen, Peyton, and Sard 1966). It is given by:

$$\eta_{IF} = \frac{4RR_L}{(R+R_L)^2}. \tag{2.16}$$

This factor is not actually a standard mismatch factor in the usual sense, since the device impedance is not independent of frequency whereas equation 2.16 is. The factor results from a more rigorous calculation of the effect of a finite load impedance at the intermediate frequency on the electron dynamics (Karasik and Elantev 1995). The parameter varies between zero and one, and is one when the device output impedance is equal to the input impedance of the IF amplifier.

Finally, it should be noted that the resistance in the above calculations was assumed to depend only on the electron temperature, and not on the current. This is not necessarily true *a priori* for any bolometer, including those studied in this thesis. However, the deviations from linearity are generally difficult to predict theoretically, so the standard approach is to neglect the dependence of the resistance on the current, assume it is not important, and see how well this assumption is validated by experiments. This will be discussed further in later sections.

2.1.2 Thermodynamic temperature fluctuations: Langevin approach

In this subsection, we will calculate the fluctuations in the electron temperature using a Langevin equation approach, where a stochastic forcing function is applied to the system[4]. Any thermal system in equilibrium with a bath exchanges energy with that bath on a very rapid time-scale. Thus, the mean energy of the system will be constant, but it will fluctuate in time about the mean value. The energy fluctuations will give rise to temperature fluctuations, which cause resistance fluctuations if dR/dT is non-zero and hence voltage fluctuations if there is a current bias.

[4]This discussion is not rigorous but illustrates the important physical concepts. A rigorous presentation would require discussion of the Wiener-Khintchine theorem.

Consider the flow of energy, when no external power is applied. Then:

$$P_{input}(t)/C = dT_e/dt + \frac{G}{C}(T_e - T_b) \quad (2.17)$$

$$= d\delta T_e/dt + (\tau_{th})^{-1}\delta T_e = f(t). \quad (2.18)$$

If no external power is applied, there is still a random exchange of energy with the bath. This is modeled by postulating a forcing function f(t) which is random, whose auto-correlation function is given by:

$$< f(0)f(t) >= \gamma\delta(t). \quad (2.19)$$

Here the brackets $< \ldots >$ denote an ensemble average, which is equivalent to a time average if the system is stationary. The strength of the forcing function is given by γ. According to equation 2.18, the time evolution of the electron temperature is no longer a deterministic process. However, there is a mean and variance of the electron temperature, and these can be calculated from the theory of Langevin and Fokker-Planck equations (Gardiner 1983). The result, for equation 2.18, is

$$< \delta T_e > \quad = 0 \quad (2.20)$$

$$< (\delta T_e)^2 > \quad = \tfrac{1}{2}\gamma\tau_{th} \quad (2.21)$$

Result 2.21 is sometimes referred to as the fluctuation-dissipation theorem (Keizer 1987). It relates the magnitude of the forcing function (γ), the variance of the system ($< (\delta T_e)^2 >$), and the "dissipative" term, $(\tau_{th})^{-1}$. Usually, the dissipative term describes real dissipation. For example, in Brownian motion, the equation of motion for a particle's position is given by an analog of equation 2.18, namely

$$dv/dt + \beta v = f(t). \quad (2.22)$$

Here, it is clear that β describes real friction. (The fluctuation-dissipation theorem for equation 2.22 would relate a random force to the friction β and $< (\delta v)^2 >$). This does not allow the determination of the variance of the electron temperature. For this, we need to insert a result from thermodynamics. We can calculate $< (\delta T_e)^2 >$ using the Boltzmann distribution, namely that the probability for the

system to be in a state with energy E is proportional to e^{-E/k_BT}. Thus (Kittel 1980):

$$< (\delta T_e)^2 >= \frac{k_B T_e^2}{C} \tag{2.23}$$

From this expression, and 2.21, the magnitude of the forcing function can be calculated, and then the spectrum of the thermal fluctuations can be calculated. One finds

$$\gamma = \frac{2}{\tau_{th}} \frac{k_B T_e^2}{C} \tag{2.24}$$

Now consider the spectrum of the fluctuations of the electron temperature (Van der Ziel 1976). We make the ansatz:

$$\delta T_e(t) = \sum_\omega \delta T_e(\omega) e^{i\omega t} \ , \ f(t) = \sum_\omega f(\omega) e^{i\omega t}. \tag{2.25}$$

Now $\delta T_e(\omega)$ and $f(\omega)$ are random variables. Upon substituting this into equation 2.18, one finds a relationship between $f(\omega)$ and $\delta T_e(\omega)$. Since the spectral density of $\delta T_e(\omega)$ is given by $2\delta T_e(\omega)\delta T_e^*(\omega)$, and since the spectral density of $f(\omega)$ is white, one finds

$$\left(\delta T_e(\omega)\right)^2 = \frac{4k_B T_e^2}{G} \frac{1}{1+(\omega\tau_{th})^2}. \tag{2.26}$$

This is the central result of this sub-section. If the temperature fluctuates, then so does the resistance. If there is a current bias, there will be a voltage fluctuation, hence the term "thermal fluctuation noise." The fluctuating voltage can be calculated, and is found to be

$$\left(\delta V(\omega)\right)^2 = \left(I_{dc} dR/dT_e\right)^2 \frac{4k_B T_e^2}{G} \frac{1}{1+(\omega\tau_{th})^2}. \tag{2.27}$$

The assumption of a white noise source is equivalent to the assumption of random energy exchanges with a reservoir. Since, for most hot-electron bolometers, the energy exchange is via phonons, thermal fluctuation noise is sometimes referred as "phonon noise". It is assumed that the phonons are uncorrelated and are emitted and absorbed on a very fast time-scale by the electron system, much faster than τ_{th}^{-1}. If this is not the case, then the above theory would need to be modified.

If the output impedance of the device is equal to the input impedance of the IF amplifier, then the ac noise voltage is also halved. In that case, by calculating the power coupled into the device, we can determine the output noise temperature of the device due to temperature fluctuations. This method yields:

$$P_{out} \equiv k_B T_{out}\ \Delta B = \left(I_{dc} T_e (dR/dT_e)\right)^2 \frac{k_B}{RG} \frac{1}{1+(\omega\tau_{th})^2}\ \Delta B, \tag{2.28}$$

where ΔB is the bandwidth.

In the case of Brownian motion, there is a quantum analog of equation 2.22 (Callen and Welton 1951; Gardiner 1991). In that case, the position and momentum of the particle are interpreted as quantum mechanical operators. Thus, there is also a quantum fluctuation-dissipation theorem. The quantum fluctuation-dissipation theorem is usually referred to as "the" fluctuation-dissipation theorem. The quantum result is equivalent to the classical result so long as $k_B T > \hbar\omega$. If this is not the case, quantum noise must be considered in the motion of the particle. This can be done, and in that case the forcing function on the R.H.S. of equation 2.22 is replaced by a more complicated operator expression (Gardiner 1991). The fact that a quantum treatment can give results that are equivalent in certain limits to the classical case can be viewed as profound and interesting, or as just another example of the Bohr correspondence principle.

Later it will be important to discuss the ultimate limits of the bolometer. Classical predictions, based on the *classical* Langevin equation 2.18 can predict a mixer noise temperature less than the "quantum limit", equation 1.4. This is because the classical calculation outlined above does not take into account quantum fluctuations in the resistance or temperature of the electrons. In order to quantify these quantum fluctuations, a *quantum* Langevin approach will be necessary. Unfortunately, the temperature is not an operator in quantum mechanics. However, it should be possible to define an *energy* operator, and calculate the energy fluctuations in a fully quantum mechanical way. The formalism for this approach has been developed (Gardiner 1991), but is not usually applied to the energy of a system. This is because in most experiments demonstrating quantum effects, the energy is not an observable. However, to the extent that the electron resistance is dependent on the energy of the electrons, the energy *is* an observable in hot-electron bolometer experiments, and so further theoretical work is merited.

The above approach has taken a top down view of the problem. However, a more microscopic theory can be investigated, and has been to a certain extent (Kogan 1996). In a more microscopic theory, a Boltzman equation approach is taken, where the occupation probability is calculated for a position in phase space at a given time. A fluctuation term can be added to the scattering term in the Boltzman equation, as in equation 2.18 for the electron temperature. Again, that treatment is semi-classical, and does not allow for quantum fluctuations to be accounted for within the theory. Recently, Kogan (1991) developed a *quantum Langevin-Boltzman* equation, generalizing the Keldysh non-equilibrium approach to include, in a quantum mechanical manner, fluctuations in the occupation probability. However, this approach has not been applied to the problem of thermal fluctuation noise in electron bolometers. To do so would require calculating how quantum fluctuations in the occupation probabilities of regions in phase space translate into fluctuations in macroscopic observables, such as energy, temperature, or resistance. There is hope for a quantum treatment of thermal fluctuation noise, but none has yet been given. Thus, in this thesis, the thermal fluctuation noise will be treated classically. In the midst of theoretical confusion, this much is clear: *A full quantum treatment of hot-electron bolometers will not predict a mixer noise below the quantum limit of equation 1.4.* Therefore, as far as the development of detectors goes, the easiest way to build a quantum-noise limited detector will be to find a detector whose classical prediction for the noise is below the quantum limit. This is because quantum mechanics usually predicts more noise than a classical calculation. Let the reader beware, however, that, this is not a theorem. There are (at least) two counter-examples: sub-shot noise in mesoscopic microbridges (de Jong 1995; Steinbach et al. 1996) and sub-shot noise in quantum optics (Mandel and Wolf 1995).

2.1.3 Effects of electro-thermal feedback on output noise

Above, the fluctuating ac voltage generated by a current bias was calculated with no load at the intermediate frequency, and in the absence of electro-thermal feedback. In the presence of electro-thermal feedback, and an amplifier load R_L, an educated guess as to the form of the thermal fluctuation noise would be a modification analogous to the modification of the conversion efficiency. This is because, as discussed above, electro-thermal feedback serves to enhance or suppress both fluctuation and the response to an external stimulus in the same way. The prediction for the

(coupled) output power in the presence of electro-thermal feedback is (Mather 1982; Karasik and Elantev 1995; Keizer 1987):

$$T_{T.F.} = \left(I_{dc}T_e(dR/dT_e)\right)^2 \frac{1}{RG_{eff}(1-\alpha)} \frac{1}{1+(\omega\tau_{eff})^2}\,\eta_{IF}, \tag{2.29}$$

where η_{IF} is the IF mismatch factor in equation 2.16.

In addition to affecting the thermal fluctuation noise, electro-thermal feedback also affects the Johnson noise. In the absence of electro-thermal feedback, the Johnson output noise temperature would be equal to the average temperature of the electrons. However, the result is modified in the presence of electro-thermal feedback. The physical reason for this is as follows (Kogan 1996): Consider the case of a voltage bias at all frequencies. If the current fluctuates, then the power dissipated in the system fluctuates. Thus, the temperature fluctuates. But this causes a change in the resistance, which further changes the current under a voltage bias condition. Thus, temperature fluctuations and Johnson noise are coupled. The resultant expression for the Johnson output noise is given by (Mather 1982; Karasik and Elantev 1995):

$$T_{out} = T_e\,\frac{1}{(1-\alpha)^2}\left(\frac{1+(\omega\tau_{th})^2}{1+(\omega\tau_{eff})^2}\right)\eta_{IF}. \tag{2.30}$$

This should be added to equation 2.29 to get the total output noise. Above it was argued that α would usually be much less than one when the load resistance of the amplifier was 50 Ω, as is typical for high frequency amplifiers. This fact will also cause the Johnson noise to tend toward the Johnson noise in the absence of electro-thermal feedback, since $\tau_{eff} \to \tau_{th}$ when $\alpha \to 0$. For the remainder of this thesis, we will treat the Johnson noise as that in the absence of electro-thermal feedback because of this effect.

2.1.4 Mixer noise

The *mixer noise*, defined in equation 1.2, can now be calculated on the basis of the above calculations. The result is:

$$T_{mix}(\omega_{IF}) = \frac{2T_e^2G}{P_{LO}} + \frac{2RT_eG^2}{P_{LO}I_{dc}^2(dR/dT_e)^2}\left(1+(\omega_{IF}\tau_{eff})^2\right). \tag{2.31}$$

The first term is due to the thermal fluctuation noise, while the second term is due to the Johnson noise. There are a few important observations to make. First, the term due to thermal fluctuation noise is independent of the intermediate frequency, and it contains no effects of electro-thermal feedback. Both of these are the result of the "fluctuation-dissipation" result: The fluctuations are related to the response to an external stimulus. Therefore, the spectrum of the fluctuations is the same as the frequency response to applied power. Additionally, the enhancement or suppression of the fluctuations at a given frequency due to electro-thermal feedback is the same as the enhancement or suppression of the response of the system to an external signal.

The second term, due to Johnson noise, is dependent on the intermediate frequency. This is simply due to that fact that Johnson noise is white, whereas the conversion efficiency decreases as the intermediate frequency is increased[5]. As a result of this, the *gain bandwidth* (i.e., the intermediate frequency at which the conversion gain drops by 3 dB) is not necessarily equal to the *noise bandwidth*, which we define as the frequency at which the *mixer noise* increases by a factor of two. In fact, using equation 2.31, it is simple to show that:

$$\frac{f_{noise3dB}}{f_{gain3dB}} = \sqrt{\frac{T_{John.} + T_{T.F.}(0)}{T_{John.}}}. \tag{2.32}$$

Typically, the thermal fluctuation noise if 50 K, and the Johnson output noise is 5 K, so that the noise bandwidth is predicted to be larger than the gain bandwidth by a factor of three.

2.2 Mixing in superconducting hot-electron bolometers: electron and phonon dynamics

In all of the above calculations, the thermal time constant was specified as C/G, and not investigated further. However, as was mentioned in the introductory chapter, this time constant is usually much too long to allow reasonable (i.e. multi-GHz) intermediate frequency operation. In this section, the dynamics which determine this time-constant in superconducting hot-electron bolometers will be discussed in more detail. In order to discuss these dynamics, we must also discuss the important

[5]The Johnson noise is only white up to $k_B T_e/\hbar \approx 100$ GHz for $T_e = 5\ K$, which is much higher than the frequencies used in this thesis.

length scales of the problem. In the following, we will limit the discussion to the length and time scales in normal metals. Only later will the superconducting properties be discussed.

2.2.1 Electron-electron interaction rate

In dirty thin films at cryogenic temperatures, the electron-electron interaction is enhanced compared to the electron-phonon interaction. If the rf power is being absorbed by electrons, the electron-electron interactions will be strong enough to force a steady-state electron energy distribution close to a Fermi-Dirac distribution. Therefore, an effective electron temperature can be defined. The electron-phonon interaction is weaker, yet will allow energy to flow from the hot-electron system to the (cooler) phonon system. The Nb films studied in this thesis have an elastic mean free path of $5 - 10$ Å (Gershenzon, Gubandov, and Zhuravlev 1983). The inelastic electron-electron interaction rate can be related to the resistivity, and for dirty films is approximately given by

$$\tau_{ee}^{-1}(s^{-1}) \approx 10^8 R_{sq} T, \tag{2.33}$$

where T is the temperature in K and R_{sq} is the sheet resistance in ohms (Santhanam et al. 1987; Altshuler and Aronov 1985). Thus, for a temperature of 5.5 K and a sheet resistance of 30 Ω (typical of the thin films studied in this thesis), $\tau_{ee} \approx 60\ ps$.

2.2.2 Electron-phonon interaction rate

The electron-phonon interaction rate in dirty metallic thin films is difficult to calculate theoretically from first principles. (For a review, the reader is referred to Mittal (1996).) Numerous experiments have measured the rate at various temperatures, and the experiments for different metals disagree. In clean, bulk 3d metals, it is well established that the electron-phonon energy relaxation rate, τ_{e-ph}^{-1}, varies as T^3 at temperatures well below the Debye temperature. However, two separate effects are important in dirty thin films which are expected to modify this behavior. First, disorder is expected to modify the electron-phonon interaction. Various theoretical calculations disagree about how this modifies the interaction rate. Second, in thin films, the effective dimensionality of the film may be reduced from 3d to 2d. This can also change the power law. For the devices studied in this thesis,

then, a phenomenological approach must be taken to estimate the electron-phonon interaction rate. In this thesis, two separate methods are used to determine this: noise thermometry in the normal state and mixing measurements in the resistive state. The results obtained here agree quantitatively with the measurements of Gershenzon et al. (1990), who measured the electron-phonon interaction rate using mixing measurements and weak-localization measurements on a variety of Nb films of different thickness and resistivity. In both Gershenzon et al. (1990) and here, the electron-phonon interaction rate is found to vary as T^2 below 10 K. For the 100 Å films measured in this thesis with $R_{sq} = 30\ \Omega$, both groups have found that the electron-phonon interaction rate at 4.2 K is $\tau_{e-ph}^{-1} \approx (1\ ns)^{-1}$.

2.2.3 Electron-phonon and electron-electron interaction lengths

In this subsection, we consider the transition from a macroscopic resistor to a microscopic resistor. Other than the length of the resistor itself, there are three other important length scales: the elastic mean free path, the electron-phonon length, and the electron-electron length. The electron-phonon length, $L_{e-ph} \equiv \sqrt{D\tau_{e-ph}}$, is the length a hot-electron will diffuse before emitting a phonon, on average. For the films studied in this thesis, $D \approx 1\ cm^2/s$, so the electron-phonon length is approximately 0.3 μm at 4.2 K. The electron-electron length, $L_{e-e} \equiv \sqrt{D\tau_{e-e}}$, is the length a hot-electron will diffuse, on average, before undergoing an inelastic scattering event with another electron. For the films studied in this thesis, at 4.2 K, $L_{ee} \approx 0.09\ \mu m$. The minimum length scale over which is it meaningful to define an electron temperature is L_{ee}. For length scales smaller than this, the electrons are not able to come to a steady-state local Fermi-Dirac distribution before diffusing away from the region of interest.

2.2.4 Thermal time constant: diffusion and phonon cooling

In the previous section, the bolometer was treated as one lumped element, with a heat capacity C and a thermal conductance to the thermal "bath" G. However there are two mechanisms for the transfer of heat away from the electronic system: the electron-phonon interaction, and out-diffusion of heat into the leads. The thermal circuit which indicates this is shown in figure 2.2. For the purposes of this thesis, the two thermal conductances are assumed to add. Thus, the thermal conductance to

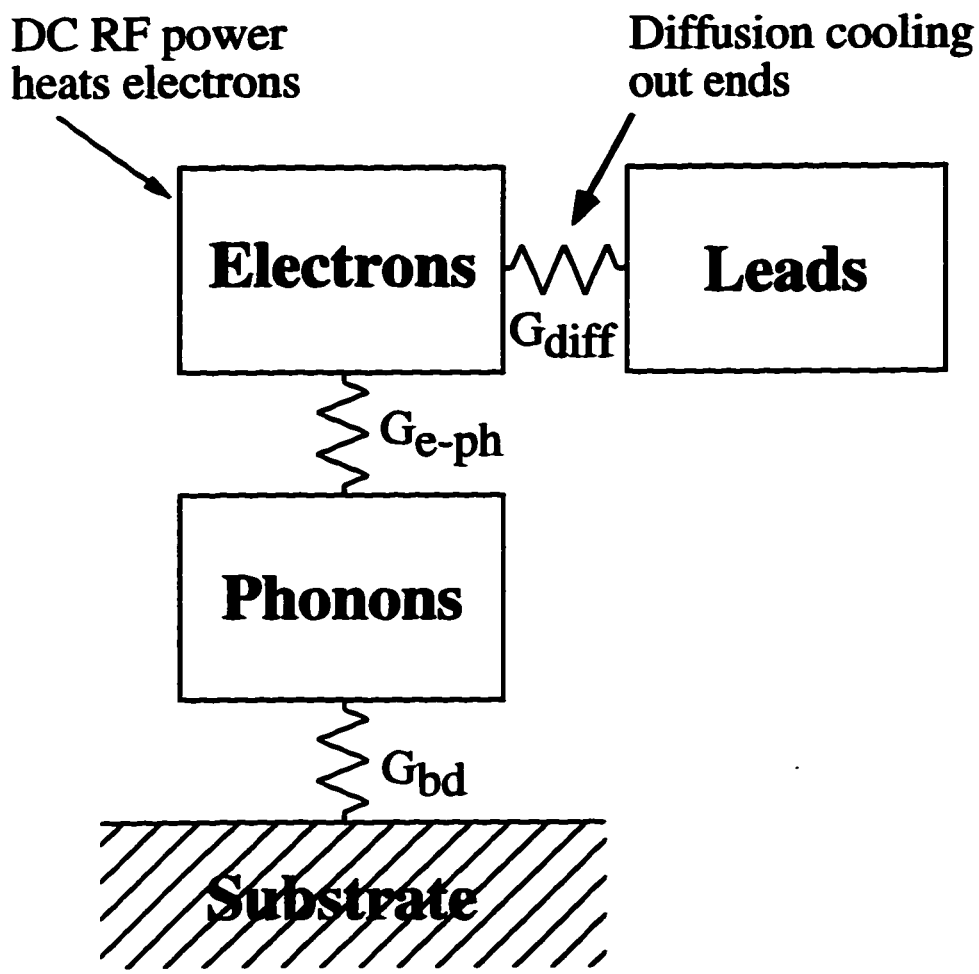

Figure 2.2: Thermal circuit diagram.

the bath G is modeled as two separate thermal conductances in parallel: $G = G_{e-ph} + G_{diff}$. The boundary thermal conductance, G_{bd}, can be assumed to be much larger than the electron-phonon conductance G_{e-ph} if the film thickness is less than 10 nm (Gershenzon et al. 1990). Therefore, in this approximation, the thermal time constant is the result of two separate, independent cooling mechanisms:

$$\tau_{th}^{-1} = G/C = (G_{e-ph} + G_{diff})/C = G_{e-ph}/C + G_{diff}/C = \tau_{e-ph}^{-1} + \tau_{diff}^{-1}. \qquad (2.34)$$

We now discuss the scaling of the thermal time constant with the bridge geometry, if we neglect

end effects and if the thermal conductance of the substrate is high. The (electronic) heat capacity C is proportional to the volume of the electronic system. The electron-phonon thermal conductance G_{e-ph} is proportional to the electronic volume also, since this is a bulk-effect. Therefore, τ_{e-ph} will be independent of the bridge geometry.

The cooling via out-diffusion can be related to the bridge resistance via the Wiedemann-Franz law, and hence to its length. The Wiedemann-Franz law relates the electrical conductivity to the thermal conductivity in a metal[6], and is given by:

$$K \equiv \sigma_{thermal} = \mathcal{L}T\sigma_{electrical}. \tag{2.35}$$

The prefactor will be worked out below, but it is clear that G_{diff} should be proportional to $G_{electrical} = 1/R$. Thus, $G_{diff} \sim L^{-1}$. Additionally, the heat capacity also scales linearly with the length, so that $\tau_{diff} \sim L^2$. The net result is the sum of two terms, one of which is independent of the length, and the other depends on the length squared. Schematically,

$$\tau_{th}^{-1} = A + BL^{-2}. \tag{2.36}$$

If the length is very long compared to L_{e-ph}, then the second term is negligible and the first term (the electron-phonon time) dominates. In this case, the diffusion cooling is only useful for electrons that are within approximately L_{e-ph} of the end, while the rest of the electrons are cooled by the electron-phonon interaction, hence the electron-phonon interaction time is the relevant time for τ_{th}. On the other hand, if the bridge is short compared to L_{e-ph}, then the second term dominates. In this case, a dramatic increase in the cooling rate is expected, which is desired in order to increase the intermediate frequency bandwidth. This is the central result of this section. In order to derive the crossover length quantitatively, it will be necessary to determine the constant of proportionally between the total electrical resistance and the total thermal conductance. To do this, it will be necessary to calculate the temperature profile, which will be done in the following section.

If the length of the bridge is less than L_{e-e}, then the concept of a local temperature within the bridge cannot be meaningfully applied. The bridge is then in the "mesoscopic" regime, and a

[6]At the temperatures used in this thesis (<10 K), the dominant source of scattering is elastic impurity scattering, so that the Wiedemann-Franz law is valid.

qualitatively new theory may be required for that case.

2.3 Temperature Profile

Although the theory presented in the previous section predicts the conversion efficiency and output noise of a lumped thermal element, the devices studied in this thesis should be treated as a distributed thermal system. For a distributed system, the output noise due to Johnson noise is predicted to be the average temperature along the length of the bridge. However, a quantitative theory for the conversion efficiency and thermal fluctuation noise which treats the device as a distributed system has not yet been developed[7]. Therefore, in this section we will calculate the temperature profile under conditions of uniform dissipation of dc and ac power and attempt to relate the distributed system approach to the lumped element approach by deriving an effective time constant and thermal conductance between the electrons and the bath. These quantities can then be used in the theory of section 2.1 as an approximation to expected device performance.

The outline of this section is as follows: In the first subsection, the temperature profile for weak and strong dc heating will be discussed in the absence of any electron-phonon interactions. In the second and third subsections, the temperature profile for weak ac heating will be derived, again in the absence of any electron-phonon interaction. In the fourth subsection, the results of numerical simulations in the presence of electron-phonon interactions will be presented. The most general case of dc and ac heating in the presence of electron-phonon interactions is discussed in the final subsection.

2.3.1 Strong and weak dc heating

In the steady state, the flow of heat and the electron temperature are governed by the time-independent heat-diffusion equation, namely

$$p_{in}(x) - p_{out}(x) = -\frac{d}{dx}\left(K\frac{dT_e}{dx}\right). \tag{2.37}$$

[7]The case of a lumped element connected to a bath *through* a distributed system was considered in Mather (1982) and Karasik and Elantev (1995).

Here, $p_{in}(x)$ is the input power density delivered to the electrons, and $p_{out}(x)$ is the outflow power density. The input power density is $P_{total}/Volume = I^2R/Volume$, if the power dissipation is uniform along the length of the bridge. The outflow power density is zero if the electron-phonon coupling is neglected. As the coordinate system, take the bridge to lie between x=0 and x=L. The boundary condition is $T(x = 0, L) = T_b$, the bath temperature. This approximation assumes that the conductivity of the metal leads is very large compared to the conductivity of the microbridge. It is useful to rewrite equation 2.37 in dimensionless variables, namely

$$T' \equiv T_e/T_b \tag{2.38}$$

$$x' \equiv x/L \tag{2.39}$$

$$p' \equiv \frac{P_{total}R}{\mathcal{L}T_b^2} = \frac{I^2R^2}{\mathcal{L}T_b^2} = \frac{V^2}{\mathcal{L}T_b^2}. \tag{2.40}$$

In this case, equation 2.37 becomes

$$\left(\frac{dT'}{dx'}\right)^2 + T'\left(\frac{d^2T'}{dx'^2}\right) = -p'. \tag{2.41}$$

The solution to this equation for the electron temperature can be shown to be (Mittal 1995; de Jong 1995)

$$T' = \sqrt{1 + x'(1-x')p'}, \text{ or} \tag{2.42}$$

$$T_e(x) = T_b\sqrt{1 + \frac{x}{L}\left(1 - \frac{x}{L}\right)\frac{PR}{T^2\mathcal{L}}}. \tag{2.43}$$

This result contains in principle all the information about the temperature profile in the case of dc heating. For concreteness' sake, the profile is illustrated in figure 2.3 for three different values of p'.

The temperature profile is not directly measured in this thesis. To relate the above calculation more directly to measurements, we need to calculate the average temperature rise as a function of input power. The result is (Skalare 1994):

$$< T_e > = \frac{T_b}{2} + \left[T_b^2\sqrt{\frac{\mathcal{L}}{PR}} + \frac{1}{4}\sqrt{\frac{PR}{\mathcal{L}}}\right]\arcsin\left(\sqrt{\frac{PR}{4T_b^2\mathcal{L} + RP}}\right) \tag{2.44}$$

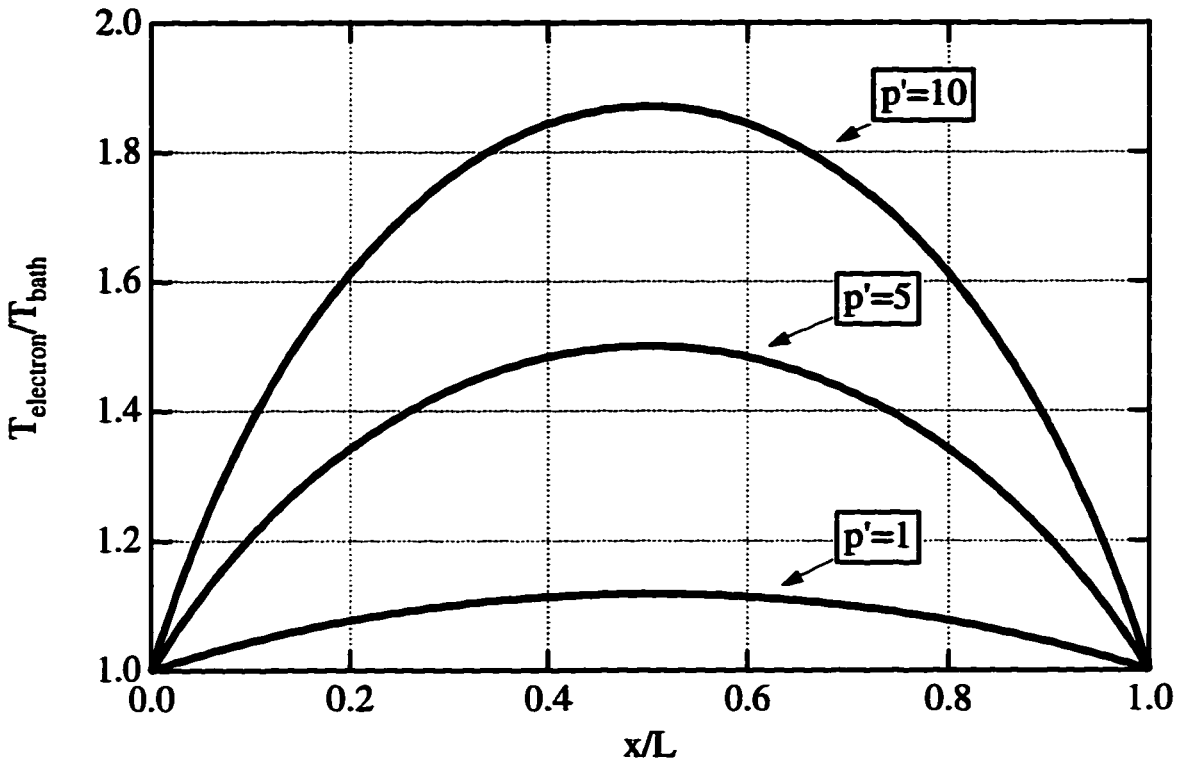

Figure 2.3: Temperature profile in the absence of electron-phonon interaction, for various values of the input power, $p' \equiv PR/T_b^2\mathcal{L}$.

Case:	$\frac{T_e(x)}{T_b}$	$\frac{<T_e>}{T_b}$	$\frac{\partial P}{\partial <T_e>}$	$\frac{T_{max}}{T_b}$	$\frac{\partial P}{\partial T_{max}}$	$\frac{\Delta T_{max}}{<\Delta T_e>}$
weak heating	$1+x'(1-x')p'/2$	$1+p'/12$	$\frac{\mathcal{L}T_b}{R/12}$	$1+p'/8$	$\frac{\mathcal{L}T_b}{R/8}$	1.5
strong heating	$\sqrt{x'(1-x')p'}$	$(\pi/8)\sqrt{p'}$	$\frac{\mathcal{L}T_b}{R/(\frac{2^7}{\pi^2})}$	$(1/2)\sqrt{p'}$	$\frac{\mathcal{L}T_b}{R/8}$	$4/\pi \approx 1.27$

Table 2.1: Limits of thermal profile calculations in weak ($P < \mathcal{L}T_b^2/R$) and strong ($P > \mathcal{L}T_b^2/R$) heating limits.

$$= \frac{T_b}{2}\left[1+\left[\frac{2}{\sqrt{p'}}+\frac{\sqrt{p'}}{2}\right]\arcsin\left(\sqrt{\frac{p'}{4+p'}}\right)\right] \tag{2.45}$$

An additional result of interest is how hot the center gets, compared to the rest of the bridge. The maximum temperature of the bridge is given by

$$T_{max} = T_b\sqrt{1+\frac{PR}{4\mathcal{L}T_b^2}} = T_b\sqrt{1+\frac{p'}{4}}. \tag{2.46}$$

Although the bolometer is really a distributed system, one can attempt to define an effective lumped-element thermal conduction to the bath due to diffusion, in analogy with equation 2.35. There are two possible ways to define this, as (1) the average change in temperature with power, or as (2) the change in the temperature at the center with power. Both results can be related to the electrical resistance in the case of weak heating ($p' < 1$) through:

$$G_{eff} = \mathcal{L}T_b/R_{eff}; R_{eff} = R/12, def.(1)(Prober1993) \tag{2.47}$$

$$= R/8, def.(2) \tag{2.48}$$

For strong heating, the 12 is replaced by ≈ 13, while the 8 remains unchanged. Table 2.1 summarizes the results for limits of the above calculations for the weak and strong heating cases. A final note is that the maximum temperature rise is only about 30-50% higher than the average temperature rise, in both the weak and strong heating cases.

2.3.2 Weak ac heating

When the source of heating is time-dependent, as in most of the experiments in this thesis, the equation that governs the temperature profile is the time-dependent generalization of equation 2.37, namely:

$$p_{in}(x,t) - p_{out}(x,t) = -\frac{\partial}{\partial x}\left(K\frac{\partial T_e(x,t)}{\partial x}\right) + \frac{\partial(c\,T_e(x,t))}{\partial t}. \tag{2.49}$$

Here c is the specific heat. In the case of weak heating, we neglect the dependence of the thermal conductivity and specific heat on the (local) temperature. For this sub-section, we let the total bridge length be $L = 2l$, and the bridge lie between $x = \pm l$. If the power dissipated in the device is

written in terms of its Fourrier components as

$$P(t) = \sum_{\omega} P_{\omega} e^{i\omega t}, \tag{2.50}$$

and if the initial conditions are that the device is initially at T_b and the ends (at $x = \pm l$) are always at T_b, then the full solution to the time-dependent diffusion equation can be calculated using Duhamel's theorem (Carslaw and Jaeger 1959). The author finds:

$$T_e(x,t) = T_b + \frac{16l^2}{\pi^2 K} \sum_{\omega} \sum_{n=0}^{+\infty} \frac{(-1)^n}{(2n+1)^3} cos\left[\frac{(2n+1)\pi x}{2l}\right] \frac{P_{\omega}}{1+i\omega\tau_n} \left(e^{i\omega t} + e^{-t/\tau_n}\right), \tag{2.51}$$

where K is the thermal conductivity, and

$$\tau_n \equiv \frac{L^2}{\pi^2 D(2n+1)^2}. \tag{2.52}$$

Here the diffusion constant D is equal to the thermal conductivity K divided by the specific heat c. In the case where the heating is dc only, this reduces to the results of section 2.3.1.

The time-dependent temperature profile is not measured in this thesis. However, an approximation to the average electron temperature over the length as a function of time is measured, so that is a quantity of interest. This can be calculated from equation 2.51 to be

$$< T_e(x,t) >_x = T_b + \frac{8}{\pi^2} \frac{\tau_0}{C} \sum_{\omega} \sum_{n=0}^{+\infty} \frac{1}{(2n+1)^4} \frac{P_{\omega}}{1+i\omega\tau_n} \left(e^{i\omega t} + e^{-t/\tau_n}\right). \tag{2.53}$$

In the case being considered here, the power is never negative. so that there are always at least two terms in equation 2.50, one with $\omega = 0$, and one with $\omega \neq 0$, i.e.

$$P(t) = P_0 + P_{\omega} e^{i\omega t}. \tag{2.54}$$

In that simple case, we have

$$< T_e(x,t) >_x = T_b + P_0 \frac{\frac{L^2}{12D}}{C} + e^{i\omega t} P_{\omega} \frac{8}{\pi^2} \frac{\tau_0}{C} \sum_{n=0}^{+\infty} \frac{1}{(2n+1)^4} \frac{1}{1+i\omega\tau_n}, \tag{2.55}$$

where the heat capacity C is the specific heat c times the volume. The second term simply gives the dc rise in the average temperature, and is equivalent to equation 2.47, if the Drude model expressions for c, D, and $\mathcal{L}$ are used. In other words,

$$< T_e >_x = \frac{P_0}{C/\frac{L^2}{12D}} = \frac{P_0}{\mathcal{L}T_b/\frac{R}{12}}. \tag{2.56}$$

The third term in equation 2.55 is the ac component of the average temperature rise. Note that there is not one single time constant that characterizes this quantity. This is due to the distributed nature of the time-dependent heat flow. Equation 2.55 is therefore not equivalent to equation 2.7, with a suitable redefinition of τ. However, it turns out that the first term in the series in equation 2.55 dominates, and therefore, to a good approximation, equation 2.7 can still be used, provided an effective time constant of

$$\tau_{eff} = \frac{L^2}{\pi^2 D} \tag{2.57}$$

is used. This time constant is *not* equal to the heat capacity divided by the dc thermal conductance G, defined in equation 2.47. In figure 2.4, the ac component of the average temperature vs. frequency is plotted for the exact result, equation 2.55, the approximation suggested in equation 2.57, and the (incorrect) result obtained by using the heat capacity divided by dc thermal conductance (eq. 2.47) as the effective time constant. The conclusion of this subsection is then this: The distributed nature of the time-dependent heat flow gives rise (approximately) to an effective time-constant given by equation 2.57, which is *not* obtained by using the dc thermal conductance to calculate the time-constant. An additional conclusion is that the diffusion time constant is equal to τ_{e-ph} when the bridge length is equal to πL_{e-ph}. Therefore, the crossover from phonon-cooled to diffusion-cooled behavior occurs at $L = \pi L_{e-ph}$.

2.3.3 Spatially distributed temperature fluctuations

In section 2.1.2, the fluctuations in the temperature of a single thermal element connected through a thermal conductance to the thermal bath was considered. A more appropriate model for the diffusion-cooled bolometer is a distributed element approach. Each element is considered to be linked to its nearest neighbor through a thermal conductance. Fluctuations in the flow between

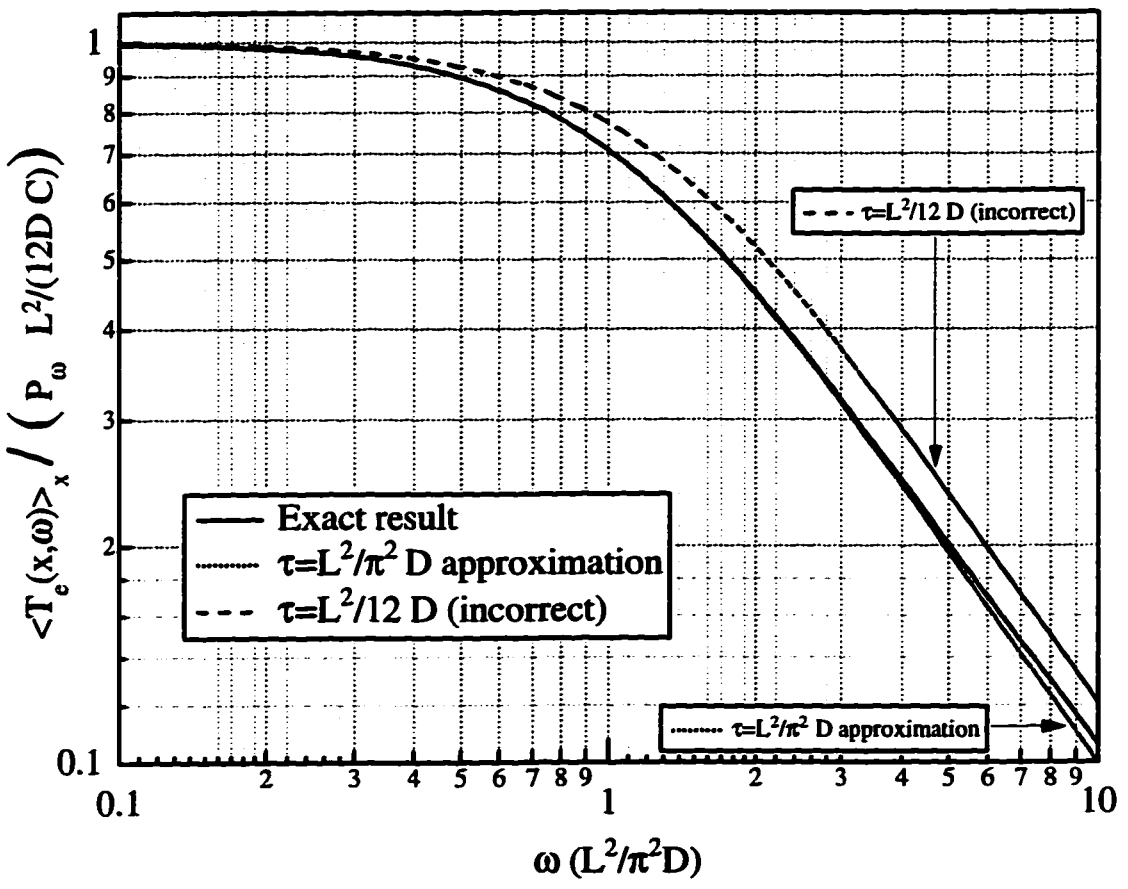

Figure 2.4: Distributed vs. lumped element temperature rise. The lumped element approximation 2.57 is close to the exact solution 2.55, but different from the dc lumped element approximation.

nearest neighbors are then postulated, and the magnitude of forcing function must be calculated. A generalization of the lumped element Langevin equation 2.18 can be derived (Landau and Lifshitz 1980), and is stated here:

$$-\frac{\partial}{\partial x}\left(K\frac{\partial T_e(x,t)}{\partial x}\right)+\frac{\partial(c\,T_e(x,t))}{\partial t}=\frac{\partial f(x,t)}{\partial x}. \tag{2.58}$$

Here the forcing function is random in both space and time, i.e.

$$< f(0,0)f(x,t) > \;\sim\; \delta(t)\delta(x). \tag{2.59}$$

The solution to this equation is considered in van Vliet and Fassett (1965) and Voss and Clarke (1976). There, the case of an infinite one dimensional system is considered. For the devices studied in this thesis, the appropriate system to consider is a finite one dimensional system. The boundary conditions are that the temperature at the ends are fixed. In equation 3.12 of Voss and Clarke (1976), the spectral density of the temperature fluctuations averaged along the length of a one dimensional system is expressed as an integral over a continuum of allowed k-vectors. If the ends of the system are kept at a fixed temperature, then only discrete k-vectors are allowed. The integral can be converted to a sum, and the author finds the following for the resultant spectral density of the temperature fluctuations:

$$\left(< \delta T_e(x,\omega) >_x\right)^2=\frac{4k_BT_e^2}{\frac{\tau_0}{C}\frac{\pi^2}{8}}\sum_{n=0}^{+\infty}\frac{1}{(2n+1)^4}\frac{1}{1+(\omega\tau_n)^2}. \tag{2.60}$$

This equation was derived when no external power is applied, so that T_e is well defined, and equal to the bath temperature. The conclusion of this section is that the spectral density of the temperature fluctuations is not equivalent to the lumped element case with a suitable redefinition of τ. The first term in equation 2.60 again is the dominant term, and so the lumped element approximation can still be used to a very good approximation, provided an effective time constant given by 2.57 is used. Finally, the low-frequency limit of equation 2.60 can be shown to be:

$$\lim_{\omega\to 0}\left(< \delta T_e(x,\omega) >_x\right)^2=\frac{4k_BT_e^2}{C/\frac{L^2}{12D}}=\frac{4k_BT_e^2}{CT_b/\frac{R}{12}}. \tag{2.61}$$

2.3.4 DC heating with electron-phonon interaction

So far, we have been neglecting the electron-phonon interaction. However, in the presence of electron-phonon interaction, the diffusion-equation 2.37 contains a "sink" term for the heat flow: power can flow from the electron system directly to the phonon system. The power flow density depends on the electron temperature and the phonon temperature, as well as the electron mean-free-path. As discussed in section 2.2.2, there is no theoretical prediction that accounts for the strength or dependence of the electron-phonon coupling in Nb, so empirical results must be used. We state the result here, which was found in Gershenzon et al. (1990), as well as the experiments described later in this thesis. The electron-phonon coupling is given by:

$$p_{out} = A(T_e^4 - T_{ph}^4), \tag{2.62}$$

where $A = 1-2\ 10^{10}\ W\ m^{-3}\ K^{-4}$ for $D = 1\ cm^2/s$. The electron-phonon time can be calculated to give:

$$\tau_{e-ph} = \frac{C}{G_{e-ph}} = \frac{\gamma T_e V}{dP_{e-ph}/dT_e} = \frac{\gamma T_e V}{4AT_e^3 V} = \frac{\gamma}{4AT_e^2}. \tag{2.63}$$

In order to account for this quantitatively, the diffusion equation 2.37 must be solved numerically. The diffusion equation can again be cast in dimensionless variables, and the result is:

$$-\left(\frac{dT'}{dx'}\right)^2 - T'\left(\frac{d^2T'}{dx'^2}\right) + \beta\left(T'^4 - 1\right) = p', \tag{2.64}$$

where

$$\beta \equiv \frac{AT_b^2L^2}{\mathcal{L}\sigma} = \frac{1}{4}\left(\frac{L}{L_{e-ph}}\right)^2. \tag{2.65}$$

Before discussing this quantitatively, the general characteristics of the solutions can be predicted. For devices which are very long compared with L_{e-ph}, the temperature profile will be flat except near (i.e. within L_{e-ph} of) the ends, where diffusion cooling will contribute somewhat. For devices which are much shorter than L_{e-ph}, the electron-phonon interaction will not contribute at all, as the electrons will diffuse out the ends before the electron-phonon interaction can contribute. Thus, the profile will be given accurately by equation 2.43. For intermediate length devices, both effects will be important. Note that L_{e-ph} is a temperature-dependent quantity, so that devices that are

less than L_{e-ph} for small heating may actually move into the intermediate limit if the temperature in the center becomes significantly larger than the bath temperature.

Since there is no analytical solution for equation 2.64, numerical methods must be used. The numerical code to solve equation 2.64 was written by Chalsani (1997). We plot in figure 2.5 several temperature profiles so generated, for bridges of length 6 L_{e-ph} and 20 L_{e-ph}. These should be contrasted with figure 2.3. The profiles are in agreement with the discussion of the previous paragraph. In a later chapter, these simulations will be used to compare with experimentally measured values of $< T_e >_x$ as a function of input power, using noise-thermometry.

2.3.5 AC heating in the presence of electron phonon interaction; strong AC heating

Based on the above results, we can come to the following conclusions regarding the temperature profile: For very long devices, in the presence of weak or strong dc or ac heating, the behavior should be that of a lumped element with a single time constant, τ_{e-ph}. For devices much shorter than πL_{e-ph} in the presence of weak ac heating, a lumped element is a good approximation, with a single time constant of $L^2/\pi^2 D$. A similar conclusion is expected to hold in the case of strong ac heating, without electron-phonon interactions, which has not yet been calculated. A numerical calculation of the time-dependent diffusion equation in the presence of electron-phonon interactions would be required to quantitatively evaluate the evolution of the behavior between the two regimes. However, we expect that the cooling rates should approximately add, and this approximation will be used in the remainder of this thesis.

2.4 Uniform vs. non-uniform dissipation of power

In the previous sections, the temperature profile of hot-electrons in the device was calculated for dc and ac heating assuming that the local power density was constant. However, the resistance varies with the local temperature, so if there is a constant current flowing through the device, the local power density varies. In order to calculate the temperature profile correctly as a function of input power, a self-consistent calculation would need to be done. The local temperature affects

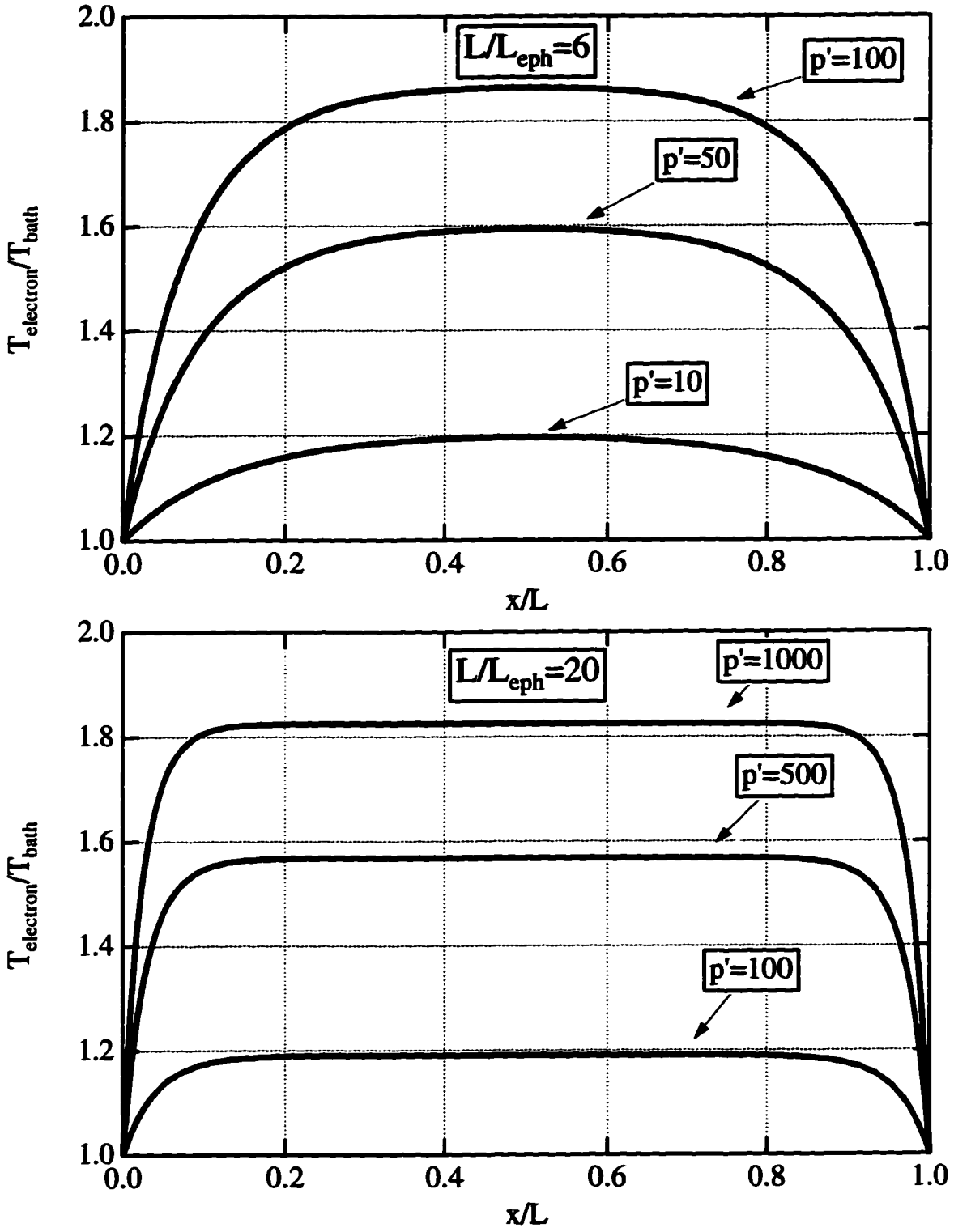

Figure 2.5: Temperature profile with electron-phonon interaction, for various values of the input power, $p' \equiv PR/T^2\mathcal{L}$, calculated by numerically solving equation 2.64, keeping $R = 100\ \Omega$. The code for the simulation was written by Chalsani (1997).

the local resistance which in turn affects the local power dissipation which feeds back to affect the local temperature. However, such a calculation would be of dubious significance for the shortest devices measured in this thesis, since the local temperature is not a meaningful concept for length scales shorter than L_{ee}. For this reason, the comparison of theory and experiment will neglect the non-uniform dissipation of power. The uniform-dissipation case will be used as a guide, but not expected to hold quantitatively. A more sophisticated theory will eventually need to be developed if the detailed response to ac and dc power is to be predicted.

The impedance of the device at frequencies above the gap frequency however ($\approx$ 700 GHz in bulk Nb) is constant and equal to the normal state impedance. Therefore, if a high frequency signal is applied above the gap frequency, then the dissipation of power *is* uniform. For the measurements presented in this thesis, all frequencies used were below the gap frequency. Experiments done at JPL used ac signals above the gap frequency. The two sets of results will be compared in chapter 6.

2.5 DC and ac differential impedance

The differential impedance of the device is an important quantity to know for circuit design purposes. In addition, measurements of the differential impedance can also test the underlying physical model. The simplest theoretical model available postulates that the differential impedance at frequencies well above τ_{th}^{-1} is simply V_{dc}/I_{dc}. At frequencies below τ_{th}^{-1}, the electron temperature can follow the (slow) change in dissipated power. However, at high frequencies the electron temperature cannot follow the fast power variation and so stays fixed. Thus, it is possible to measure the differential impedance of the electron system in the absence of self-heating. In this way, it is possible to measure the I-V curve if there were no power dissipated in the device. We call this underlying I-V curve the "isothermal" I-V curve. The isothermal I-V curve is expected to be simply a straight line with slope between 0 and R_n, with slope determined solely by the temperature of the electrons.

Based on the heat flow equation, the equivalent circuit shown in figure 2.6 can be derived (Elant'ev and Karasik 1989). This circuit diagram can be understood very easily. At low frequencies, the capacitance does not conduct current, and the differential impedance is simply $R_1 + R_2$. This is equal to the dc differential impedance, dV/dI. At high frequencies, the capacitance shorts R_2, so the differential impedance is R_1. This is equal to V_{dc}/I_{dc}, as discussed above. At high frequencies,

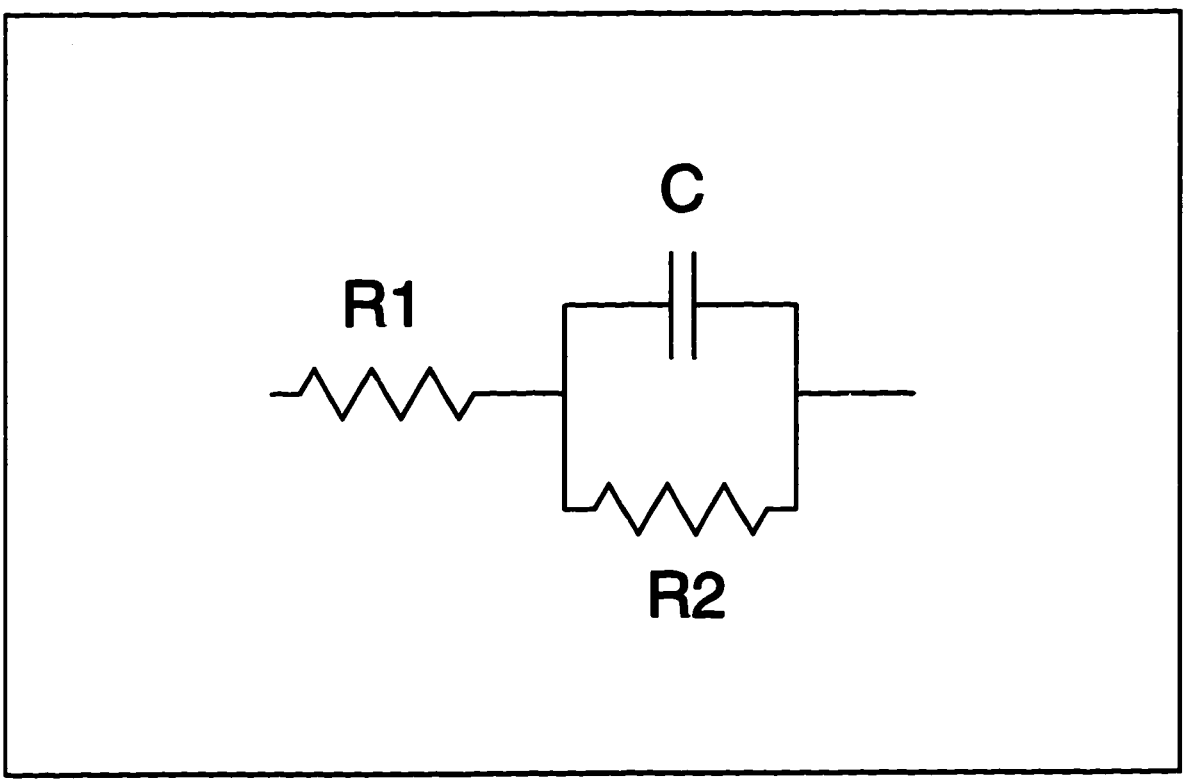

Figure 2.6: Equivalent circuit of bolometer.

the time-varying power dissipated in the devices causes a time-varying temperature of the electrons which lags the power. Since the electron temperature is out of phase with the power dissipated, the resistance is out of phase with the power dissipated. This thermal inertia gives rise to the effective capacitance in the model, whose value is set by the thermal time constant of the system. The parameters in the circuit model are:

$$R_1 = V_{dc}/I_{dc}, \tag{2.66}$$

$$R_1 + R_2 = \left(dV/dI\right)_{dc}, \tag{2.67}$$

$$R_2 C = \frac{\tau_{th}}{1-\alpha_0}. \tag{2.68}$$

2.6 Voltage dependence of gain and noise; α from I-V curve

When dc and ac power are applied to the device, the electron temperature is heated above the bath temperature to somewhere near the critical temperature. However, the temperature of the electron system is difficult to predict accurately. Since the value of dR/dT changes from 0 to its maximum value in the range of about 0.25 K, it is difficult to predict the value of dR/dT under operating conditions. This makes predictions of the conversion efficiency and output noise based on equations 2.13 and 2.28 difficult. There is, however, a way to determine the value of α_0 from the measured I-V curve, which allows predictions of the output noise and efficiency. The principle is simply this: An increase in bias voltage increases the power dissipated. This raises the electron temperature, which in turn causes an increase in resistance. Therefore, the quantity dR/dP can be measured. A derivation is given in Ekström et al. (1995) for the following formula:

$$I_{dc}^2 dR/dP = I_{dc}^2 dR/(G dT_e) = \frac{(dV/dI) - R}{(dV/dI) + R} \equiv \alpha_0. \tag{2.69}$$

Therefore, the measured dc I-V curve can provide a measurement of α_0. (It is straightforward to calculate α from the dc I-V curve once α_0 is known.) The predictions of equations 2.13 and 2.28 can be rewritten in terms of α and α_0 as

$$\eta(\omega_{IF}) = \frac{P_{LO}}{2\,P_{dc}} \frac{\alpha_0^2}{(1-\alpha)^2} \frac{1}{1+(\omega_{IF}\tau_{eff})^2} \eta_{IF}, \tag{2.70}$$

$$T_{out} = \frac{T_e^2}{P_{dc}} \frac{G}{(1-\alpha)^2} \frac{\alpha_0^2}{1+(\omega_{IF}\tau_{eff})^2} \eta_{IF}. \tag{2.71}$$

The values of P_{dc}, P_{LO}, G, and T_e can be estimated with reasonable accuracy, so that a prediction of device performance from the measured I-V curve should be possible.

Chapter 3

Experimental technique

In this thesis, the conversion efficiency and output noise were measured with rf and LO signals between 8 and 40 GHz. The goal was to measure the IF bandwidth and noise for devices of different lengths in order to determine if diffusion cooling could be used to increase the bandwidth, and to determine whether diffusion-cooled bolometers are competitive devices for THz heterodyne detection. Since the mixing process is thermal and depends only on heating of the electrons, the results of these measurements should be representative of device performance at THz frequencies. We expect that the bandwidth and output noise measured here should be very similar to results at 1 THz, but the detailed dependence on the dc and LO power may be different. These issues will be discussed in more detail in chapter 6, where the results presented in this thesis are compared with measurements on diffusion-cooled bolometers done at JPL at THz frequencies. The availability of variable frequency sources at THz frequencies is very limited, so for a systematic study of device performance as a function of frequency and other parameters, a lower frequency was used.

The experimental goal was to measure the conversion efficiency and output noise of several devices as a function of dc and LO power, and intermediate frequency. The measurements were done as follows: Two coherent signals (the LO and rf) were applied to the device, and the frequency of the rf signal was varied. The absolute power coupled to the device at each rf frequency used was calibrated as discussed in section 3.5. The power generated at the intermediate frequency was amplified and measured on a spectrum analyzer. By carefully calibrating the gain of the amplifier chain, the

absolute power generated by the device at the intermediate frequency was determined. Then, the (coupled) conversion efficiency (the ratio of the output power at the IF to the input power at the rf) was calculated. An important advantage of using coherent signals to measure the bandwidth and conversion efficiency is the large signal to noise ratio and the fact that the measurements demonstrate definitively that the device response is indeed heterodyne. An additional goal was to measure the output noise of the device as a function of temperature, dc and LO power, and intermediate frequency. For this, the noise generated by the device was amplified and measured on either a spectrum analyzer or on a broadband detector preceded by a band-pass filter. The noise of the amplifier itself was also amplified and detected, so this contribution had to be carefully calibrated and subtracted off in order to determine the contribution from the device itself. By knowing the output noise and the conversion efficiency, it was then possible to calculate the *mixer noise*, which is the important parameter for any detector. If the mixer noise is low enough, then the devices will be competitive THz mixers.

In this chapter, the technique used to measure the dc and rf properties of the devices studied in this thesis is described. First, the rf setup is described. Next, the dc electronics are described. Next, the thermometry is described. Then, the shielding and filtering techniques used are described. Finally, the rf calibrations are described.

3.1 RF setup

3.1.1 RF block diagram

The experimental setup used in this thesis consisted of the device which was mounted on a variable temperature stage in a vacuum can, as well as several rf components which were immersed in a liquid He bath which surrounded the vacuum can. The setup was unique in that it allowed the simultaneous measurement of many different high frequency properties of the devices, including the high frequency differential impedance, the high frequency output noise in both the normal and mixed states, and the conversion efficiency as a mixer as a function of dc power, LO power, LO and rf frequency, and temperature. A block diagram of the rf measurement system is shown in figure 3.1.

The rf and LO signals were coupled in weakly through a directional coupler[1]. The attenuators were in place to reduce blackbody radiation from room temperature, as well as to damp any frequency dependence of coupling to the device, i.e. standing waves. The attenuator in front of the amplifier was removed during most runs where the noise was measured. The cooled low-noise amplifier[2] was used to amplify any coherent signals generated by the device at the intermediate frequency, as well as noise generated by the device.

A hermetic feedthrough SMA connector[3] allowed dc and ac signals to be coupled to the device, which is mounted on a variable temperature stage inside a vacuum can. A 1" section of stainless steel (both inner and outer conductor) coax provided a weak thermal link between the He bath and the device mount, so that the temperature of the device mount could be independently varied from 1.8-20 K. (The rf loss of the stainless dc bias tee and hermetic connector combined was measured to be less than 1 dB below 10 GHz and less than 2.3 dB from 10-20 GHz at 4 K. The loss of the 1" section of stainless steel coax is less than 0.3 dB below 20 GHz.) By measuring the ratio of the intermediate frequency power generated by the device to the rf power delivered to the device, the (coupled) conversion efficiency could be measured. In addition, the amplified output noise generated by the device could be measured, and with a proper calibration, the absolute noise generated by the device could be measured. An isolator was sometimes placed between the device and the amplifier to reduce the effect of the change of impedance on the calibration coefficients. This will be described in more detail in a chapter 5.

Finally, the directional coupler allowed the device impedance to be measured: A weak signal sent in via the directional coupler will be reflected off of the device and amplified, then measured at room temperature on the spectrum analyzer. By biasing the device in the superconducting state, the impedance is essentially zero, so that all the power is reflected. This provides a (scalar) calibration of the coupling and gain, and allowed the (scalar) coupling to the 50 Ω system to be measured when the device is in the normal or intermediate state. This is important for measuring the conversion efficiency, as well as the noise, since the coupling factor must be included in the corrections to the

[1]TRM (Manchester, New Hampshire) model DCS-210. For later experiments, a broader-band (1-18 GHz) coupler was used, Mac Technology (Klamath Falls, OR) model CD 4238-20F.

[2]Miteq (Happauge, NY) model AFS3 00100800-32-CR-4. The amplifier was modified by the factory to be cryogenically coolable, and biased at 3 V to reduce power dissipation, instead of the recommended 6 V. The power dissipation in the amplifier was about 180 mW.

[3]M/A-COM (Waltham, MA) model 2098-3251-94, soldered into place with Sn/Pb solder.

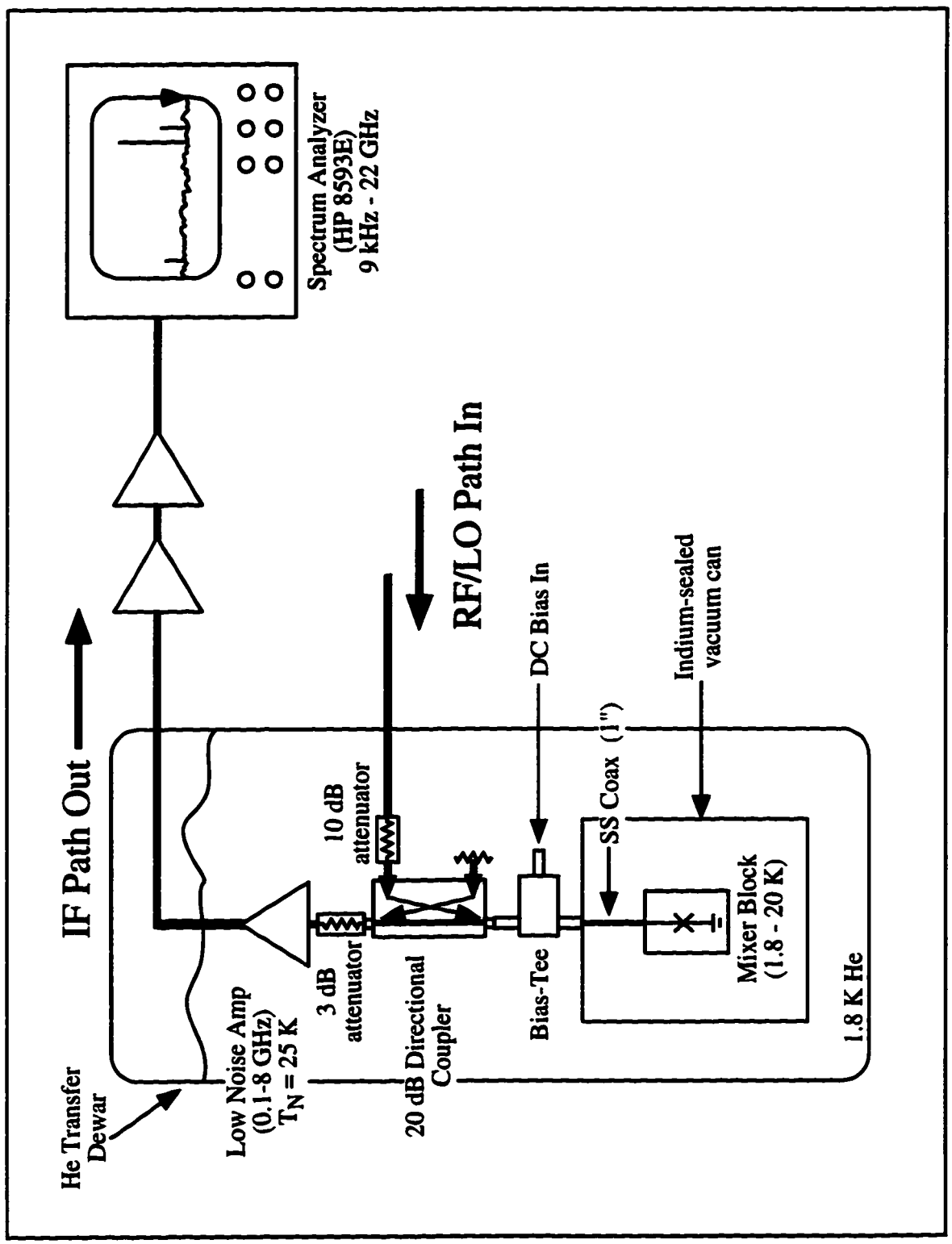

Figure 3.1: Block diagram of RF measurement system. All components are connected with SMA connectors.

data.

3.1.2 Mixer mount

The mount used to couple from the coax system to the device is shown in figures 3.2 and 3.3, and the lead geometry of the chip is shown in figure 3.4. The coax transmission line was fed into a microstrip transmission line, both having a characteristic impedance of 50 Ω. The microstrip was constructed of 0.025" thick copper plated teflon[4]. One side of the teflon was etched by a commercial circuit board company[5] to form the microstrip, and the other side was left plated. The Duroid was soldered onto the Cu block using low temperature solder. At the end of the microstrip, the device was "flip-chipped" into place: The chip was carefully placed upside down on the end of the microstrip with indium squashed between the chip and the microstrip to provide reliable electrical contact. A spring-loaded pogo pin applied pressure to keep the chip in place. This mounting technique was extremely robust. After each device was mounted, the whole block was dipped into liquid He and warmed to room temperature three times, while the I-V curve was monitored to ensure the electrical contact did not change. All mounted devices survived this ordeal, and were then carefully handled when being inserted in the experimental setup. Once a device was mounted at the end of the microstrip, it could be inserted and removed from the experimental apparatus simply by screwing it onto the SMA connector of the apparatus.

The coupling from the SMA connector of the mount to the device was measured by measuring the return loss of the device in the normal state, and found to be better than 90% between 50 MHz and 12 GHz. Additionally, a measurement of a chip resistor similarly mounted at room temperature showed a 90% or better coupling from 50 MHz to 40 GHz at room temperature. Thus, this method provides a ***broadband, resonance free coupling*** to a 50 Ω device from 50 MHz to over 40 GHz. Most mounting methods used to study mesoscopic electronic devices at cryogenic temperatures include some parasitic capacitance and inductance. The development of an ultra-broadband coupling scheme for the hot-electron bolometers was therefore a significant accomplishment.

[4]Rogers Corporation (Chandler, Arizona) model RT/Duroid 6010LM, $\epsilon = 10.2$.
[5]Tech Circuits (Wallingford, CT).

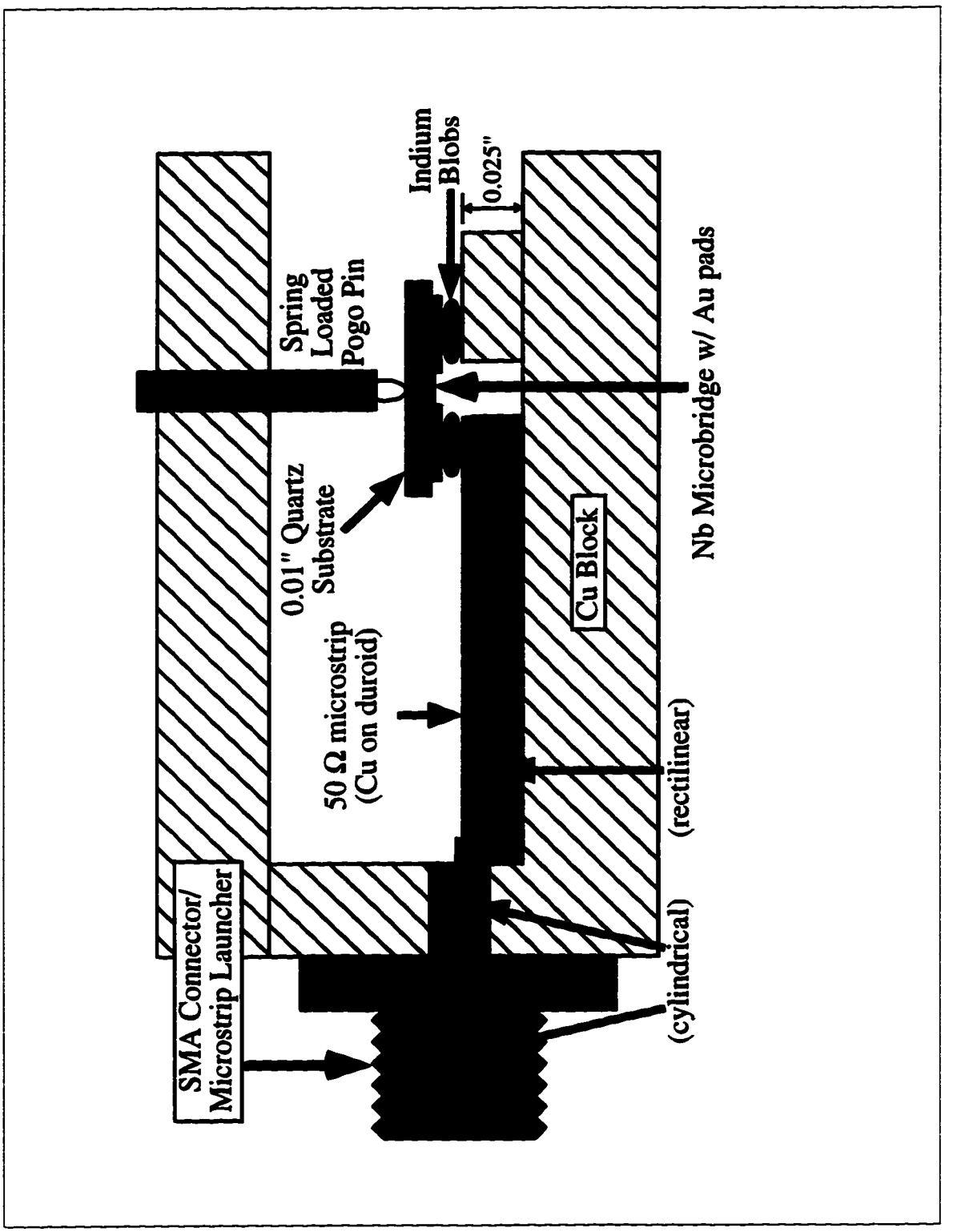

Figure 3.2: Mixer mount, side view (*not to scale*).

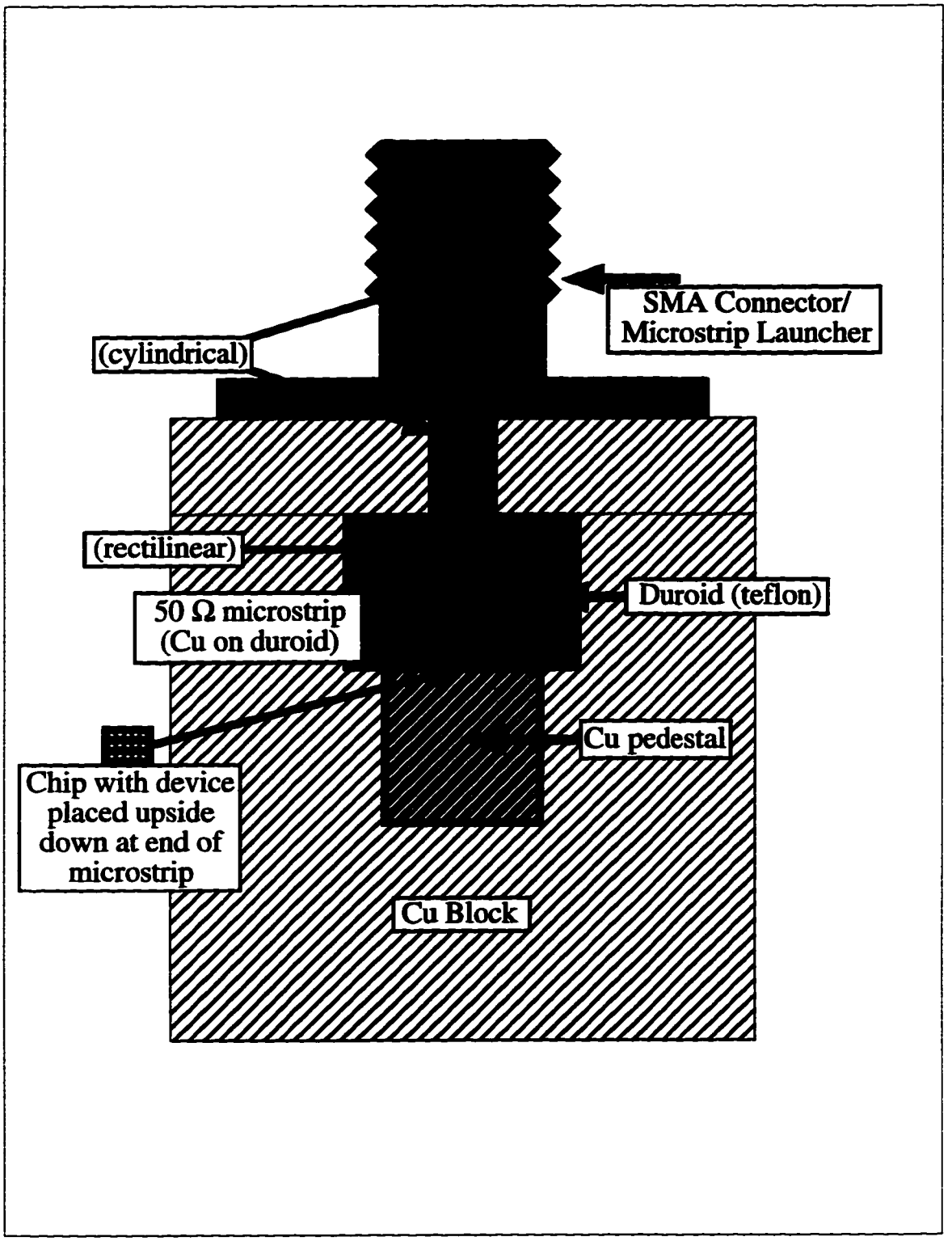

Figure 3.3: Mixer mount, top view (to scale, 5:1).

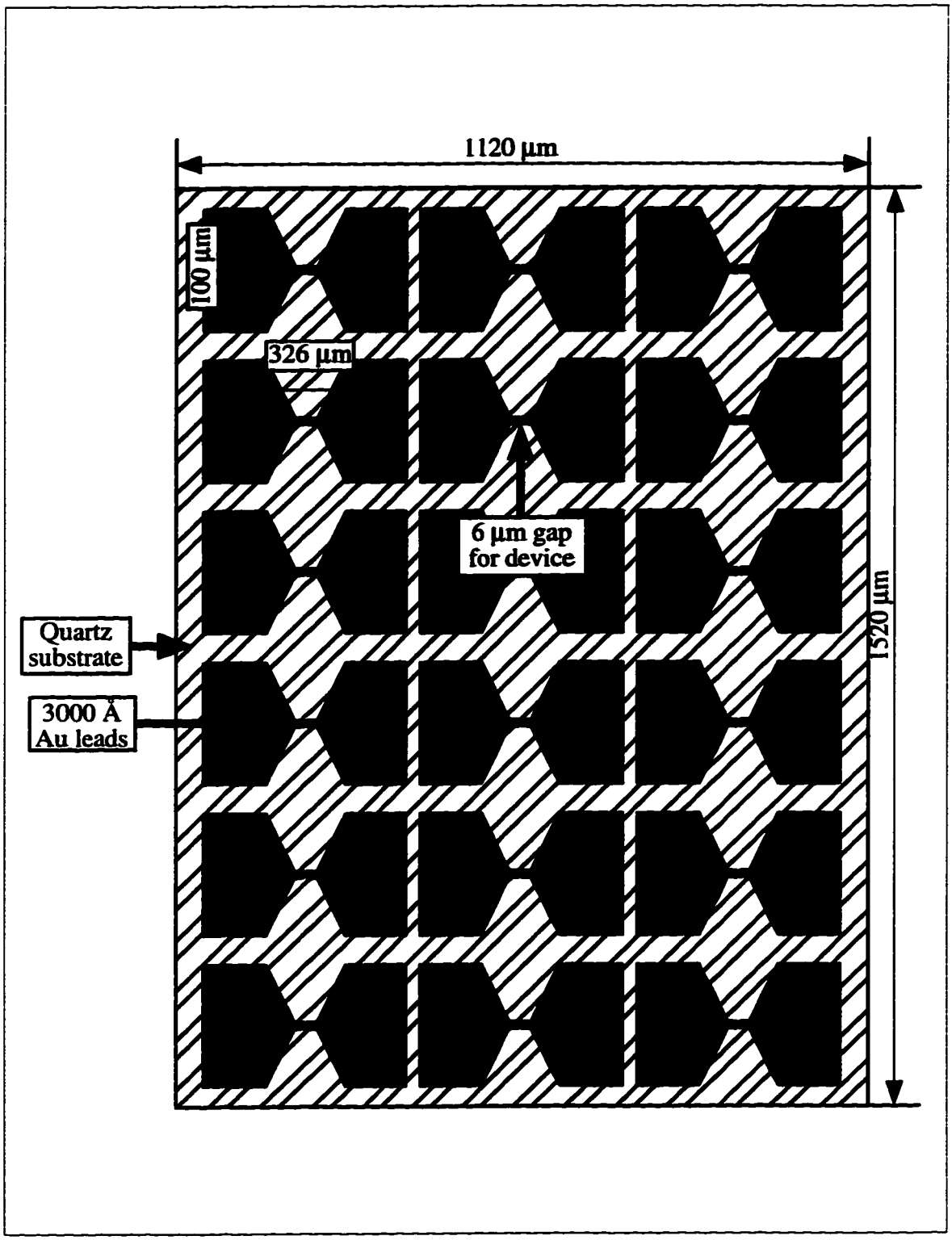

Figure 3.4: Lead geometry, to scale 100:1. (Electron beam lithography is used to define the device length inside of the 6 μm gap.)

3.2 DC electronics

The circuit diagram for the dc electronics is shown in figure 3.5. This is a versatile bias scheme. The voltage can be controlled externally by computer or through the internal oscillator and dc bias. The 10 Ω resistor in parallel with the device in combination with the 10 Ω resistor in series with the device gives rise to a load line of 20 Ω. The I and V outputs on the right are actually passed back through the rf filters, and through the adder box before being sent to the DVM or oscilloscope, which displays the I-V curve in real time. To switch to current bias, the 10 Ω resistor in parallel with the device can be disconnected, and R_{bias} is used as the current sense resistor with the first AD624 instrumentation amplifier. The connection from the bias box to the dc bias tee was all through semi-rigid coax with SMA connectors in order to avoid rf pickup. Additionally, a 2 MHz low pass filter[6] was placed at the output of the bias box. The readout circuit is a two-point measurement of the resistance. This was not a problem, since the the lead resistance was low, less than 1 Ω. This was measured by measuring the resistance when the device was biased in the superconducting state.

Of particular interest is the way the devices are connected and disconnected from the electronics to avoid damage due to electrostatic discharge. The procedure was as follows: Before connecting the dc bias line to the bias box, all electronics in the bias box were powered up. In the initial configuration, switches S1 were and S3 are closed, and switch S2 is open. (Switch S2 serves to connect or disconnect the device from all of the electronics inside the bias box.) After the device line is connected, switch S2 is closed, connecting the device to the electronics. Next, switch S1 (which so far insured the amplifier leads would not float to a non-zero potential difference) is opened. Finally, switch S3 is opened and the 10 kΩ potentiometer is slowly opened[7], allowing current from the electronics to slowly begin flowing through the device. In later experiments, switches S1 and S2 were rarely used, but switch S3 and the potentiometer were a sure way to ensure that when the coax was connected to the bias box, the center conductor would be at zero voltage. Only one of the six devices measured was damaged during the course of over fifty separate experiments that were performed on the devices described in this thesis.

[6] Mini-Circuits (Brooklyn, New York) model BLP-1.9

[7] Since the device resistance was only 50-100 Ω, the 10 kΩ is essentially an open circuit and draws little current.

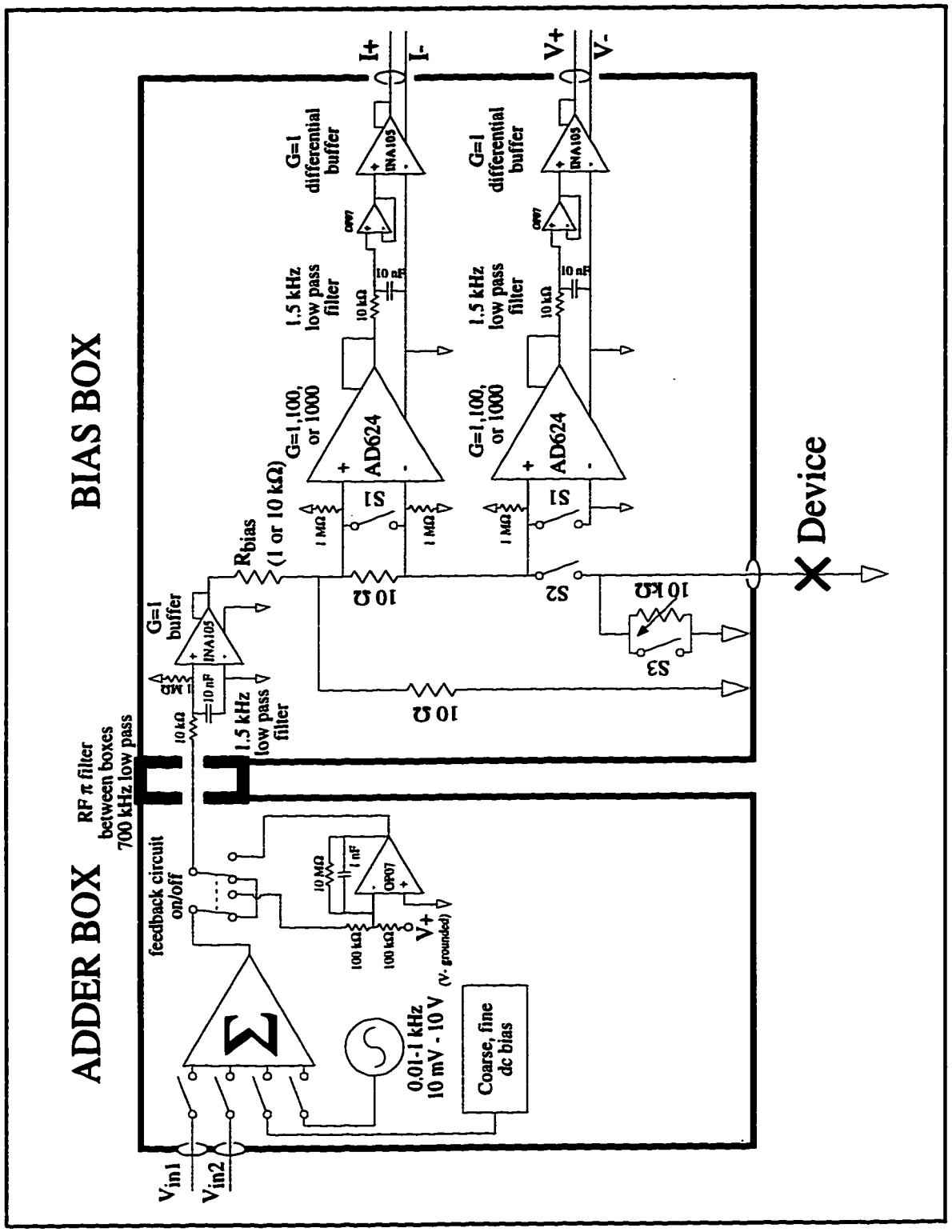

Figure 3.5: DC electronics schematic.

3.3 Cryogenic setup and thermometry

The temperature of the block the device was mounted on was monitored by a calibrated diode thermometer[8] whose case was screwed directly to the back of the Cu block. The temperature of the block was raised above the He bath temperature by applying current to a 1 kΩ resistor which was thermally anchored to the block. A commercially available feedback circuit[9] under computer control via a GPIB interface adjusted the heater power to regulate the temperature to a precision of about 10 mK. The thermal time constant for the entire Cu block was about 30 seconds.

Two consistency checks ensured that the thermometry was correct. In a separate series of experiments, the T_c of a Nb film fabricated by A.A. Verheijen with T_c of 8.6 K was measured in two separate setups. In the first setup, the mount described in figure 3.2 was used with the diode thermometer. This setup was used both with and without a coax connected in order to verify that the heat load of the center pin was not heating up the device. In the second setup, a different mount designed for dc measurements only was used, together with a different, carbon-glass calibrated resistance thermometer[10]. Both measurements of T_c agreed to within the specified accuracy of the diode thermometer of 50 mK. A second consistency check comes from measuring the Johnson noise as a function of indicated temperature, and will be discussed in section 3.5. There, the thermometry and the microwave amplifier gain calibrations are shown to be self-consistent.

3.4 Shielding and filtering

Shielding and filtering were required for two reasons: first, to avoid external heating of the device by spurious signals, and second to avoid confusing spurious signals from signals generated by the device. In this section, the shielding setup is first described, and then estimates and measurements of the effectiveness of these techniques are described.

The technique used was to ensure that all connections to the device were done through semi-rigid coax cables with SMA connectors. While the isolation of the cable itself is typically 130 dB or greater at rf frequencies, the SMA connectors used have specified isolation of at least 80 dB from

[8] Lakeshore model DT-470-BR-13 1.4L.
[9] Lakeshore model DRC-93 temperature controller.
[10] TRI Research model CC1000-5%.

dc to 18 GHz. On the dc bias out of the bias box, a 2 MHz low pass filter with loss greater than 40 dB from 5 MHz to 10 GHz was used. Therefore, the electromagnetic coupling to the device at all frequencies from dc to rf was well controlled. A similar scheme was used with the dc bias line for the cooled amplifier, but the last inch or so was twisted pair wiring due to the configuration of the commercial amplifier.

Experimentally, it was possible to estimate stray coupling from coherent signals such as cell phones and radio and TV stations as follows: Some fraction of the power coupled into the device would get reflected and fed into the input of the amplifier, whose gain was accurately characterized as described in section 3.5. Using this technique, it was determined experimentally that the largest absolute coherent signal coupled into the amplifier above about 100 MHz was due to cell phone signals at 900 MHz, with an absolute magnitude of less than 10^{-15} W. The power coupled to the device at 900 MHz was most likely of the same order of magnitude or less. This power will not provide any significant heating of the electrons since the thermal conductance to the bath is of order nW/K. Additionally, the coherent signals generated by the device during the experiments described in this thesis were between 0.1 pW and 100 nW, so that the low-level spurious signals were not important.

Stray coupling of incoherent signals such as 300 K black body and noise generated by the microwave oscillators was much more difficult to measure, and for this purpose room temperature and cooled attenuators were used wherever possible. The attenuation between the rf coax connector at the cryostat to the device was approximately 30 dB, so that the 300 K blackbody propagating down the coax would be attenuated to 0.3 K by the time it reached the device. Extraneous noise sources above 300 K from the microwave sources were carefully measured and attenuated down to below 300 K equivalent noise temperature.

3.5 Calibrations

Two separate techniques were used to calibrate the rf power coupled to the device, as well as the gain and noise of the amplifier, the first using coherent signals from a microwave generator as the source of power, and the second using Johnson noise generated by the device as an incoherent source of known spectral intensity. For the first set of experiments described in this thesis where only the

conversion efficiency was measured, the calibrations with a coherent signal were sufficient. However, for the second set of experiments where both the noise and the conversion efficiency were measured, it was necessary to use the calibration coefficients determined using the Johnson noise of the device.

3.5.1 Calibrations using a coherent signal

In one technique, a coherent signal was used as a source, and the ratio of the input power at a fixed frequency to the output power at a fixed frequency was measured in order to determine the amplifier gain and the rf coupling to the device. Using this technique, it was possible to calibrate the coupling from the rf input connector of the cryostat to the connector on the bias tee which fed directly through the hermetic feedthrough and 1" section of SS coax to the device mount. The loss of the bias tee, the hermetic SMA feedthrough, the 1" section of SS coax, and the on-chip microstrip was neglected in these measurements. The coherent calibration method required several sets of measurements of cold components and cables, which were then used as the coupling coefficients for the rest of the experiments. A disadvantage of this technique is that it cannot be used to measure the noise of the amplifier, and it is does not account for run to run variation in the performance of the system. In a separate experiment, the drift of the calibration coefficients as a function of time during the run was measured to be less than 1 dB over the course of the run. Due to this and other errors, the estimated error on the measured conversion efficiency is 2 dB.

The calibration coefficients determined using a coherent source are plotted in figure 3.6. The top graph displays the loss between the connector at the entrance to the cryostat and the cooled directional coupler, as well as the coupling through the directional coupler to the device port. The rf power coupled to the device was measured by measuring the power generated by the source on the spectrum analyzer at each frequency, and then subtracting the coax cable loss and coupling of the directional coupler. The lower graph shows the gain of the amplifier chain used.

3.5.2 Calibrations using incoherent signals

In order to calibrate the amplifier gain *and* noise, the device itself in the normal state was used as a source of known spectral intensity. If there is no current flowing through the device, then the fluctuation-dissipation theorem guarantees that the spectral intensity of the power radiated by the

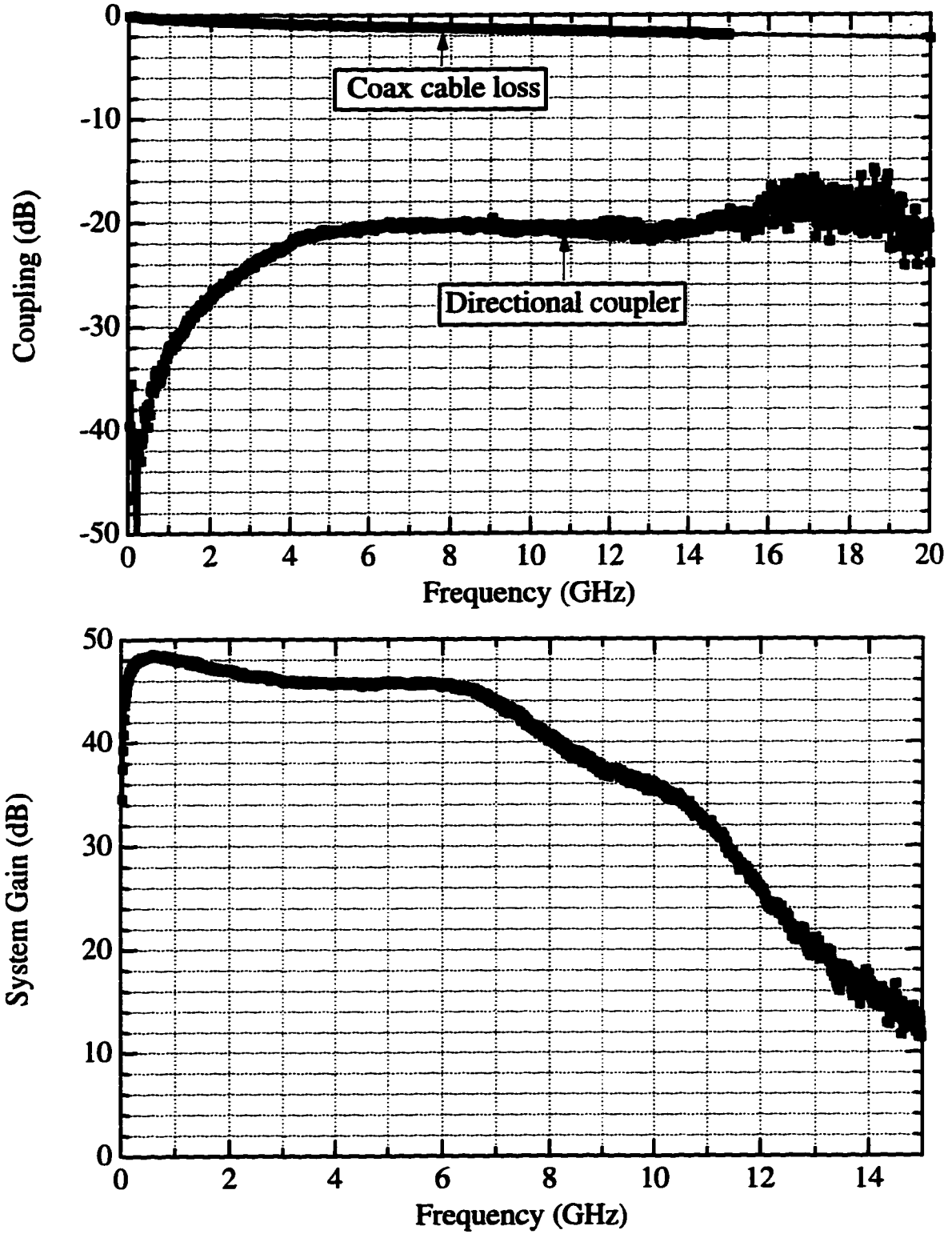

Figure 3.6: Calibrations coefficients determined using a coherent source.

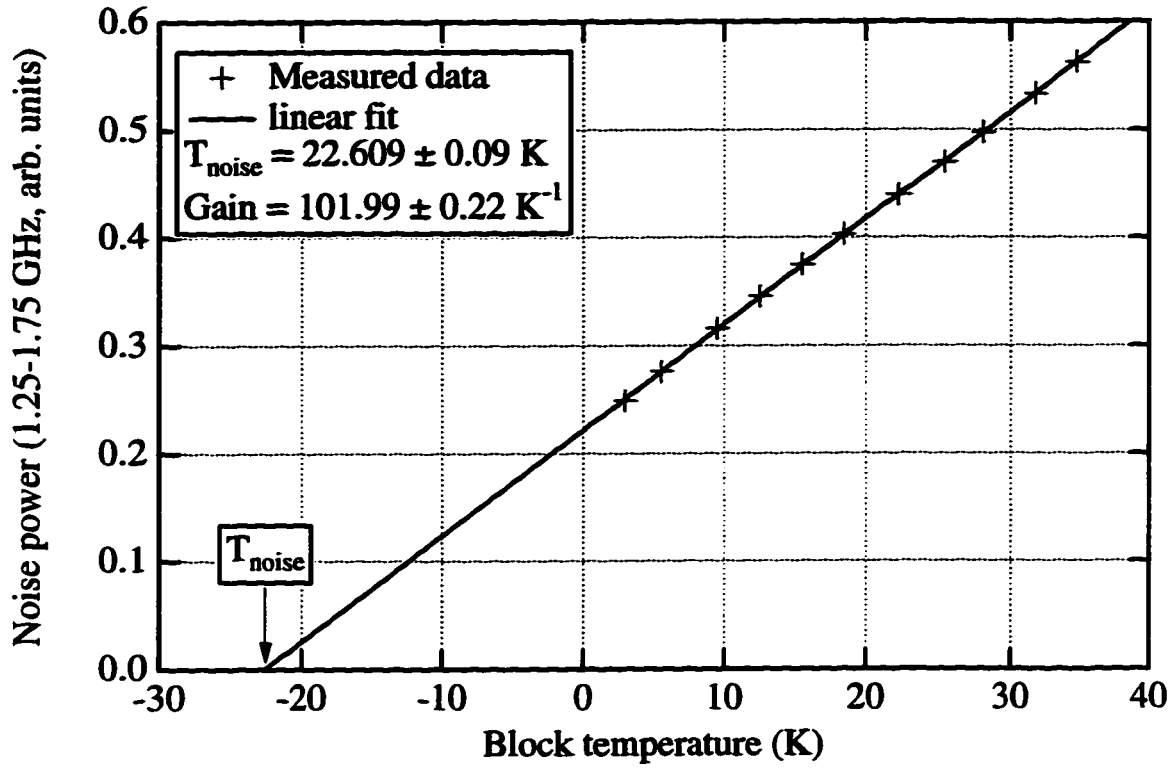

Figure 3.7: Calibration at fixed frequency of amplifier gain and noise.

device into a matched load is simply $k_B T$, where T is the temperature of the device. By varying the temperature of the device and measuring the output power of the amplifier, it is possible to simultaneously determine the gain and noise of the entire amplifier system referred to the terminals of the device. In figure 3.7, the measured amplified noise power in the 1.25-1.75 GHz band (in units of volts on the detector) is plotted against the mixer block temperature, which is equal to the device temperature since there is no current flowing in the device for this experiment. For this plot, the data were taken at two minute intervals in order to assure that the mixer block temperature had stabilized before taking the next point, for a total sweep time of about 25 minutes. The line would intercept zero if the amplifier were noiseless; the non-zero intercept is the amplifier noise temperature, and the slope is the gain of the amplifier system. This technique assumes that the device is well-matched to the 50 Ω input impedance of the amplifier, which is indeed the case as was measured in separate series of experiments to be discussed later.

The technique of measuring the amplifier noise and gain can be applied at all frequencies, and

this was done in many of the experiments described below. Since the statistical variation in the noise power measured during a time t in a bandwidth of B is proportional to $1/\sqrt{Bt}$, it is better to integrate as long as possible, and to use as wide of a bandwidth as possible. The practical constraint is that the liquid He only lasts a few hours, and the gain and noise drift on a slow timescale. The compromise used when measuring the amplifier gain and noise as a function of frequency was as follows: The spectrum analyzer was set to a resolution bandwidth of 3 MHz[11], and an integration time per point of 0.16 μs. 1000 traces were averaged, giving an effective integration time of 0.16 ms, and then the data were smoothed over a 100 MHz bin. Therefore, the measured gain and noise were actually the average gain and noise over a 100 MHz bin, this poor spectral resolution being a disadvantage of the technique over using a coherent signal. This is especially a disadvantage when trying to measure the gain of the amplifier at frequencies below a few hundred MHz, where the gain is dropping rapidly to zero for the amplifiers used in these experiments. The gain of the amplifier system determined using the two separate techniques described above is plotted against frequency in figure 3.8. The disagreement (averaging 3 dB from 0.1 to 6 GHz) is probably due to two factors: First, the spectrum analyzer used has a rated accuracy of $\pm$ 1 dB at the powers levels measured (1 nW), and second, there is $\approx$ 1 dB of loss between the device and the input of the amplifier, which is not accounted for in the coherent calibration. (The amplifier gain from the incoherent calibration was consistent within 0.5 dB over four runs on three separate devices.) An additional calibration of the microwave amplifier at a fixed frequency was done with a (macroscopic) chip resistor, and the results obtained there were consistent with the results obtained when using the device itself as a source of incoherent power of known spectral intensity. Since the measurement of the device noise relies only on the thermometry, the incoherent calibrations were used for determining the device output noise. However, the absolute gain determined using a coherent source was more reliable for measuring the absolute conversion efficiency of the device, so the gain determined using a coherent signal was used in that case.

The gain of the amplifier system when configured to use the Johnson noise of the device to calibrate the gain and noise is much higher than that plotted in figure 3.6, in order to insure that the amplified Johnson noise overcomes the input noise ($\sim 100,000\ K$) of the spectrum analyzer

[11]This was the widest available resolution bandwidth. If enough rf equipment were available, a better and more efficient technique would have been to construct a custom spectrum analyzer with a much wider resolution bandwidth.

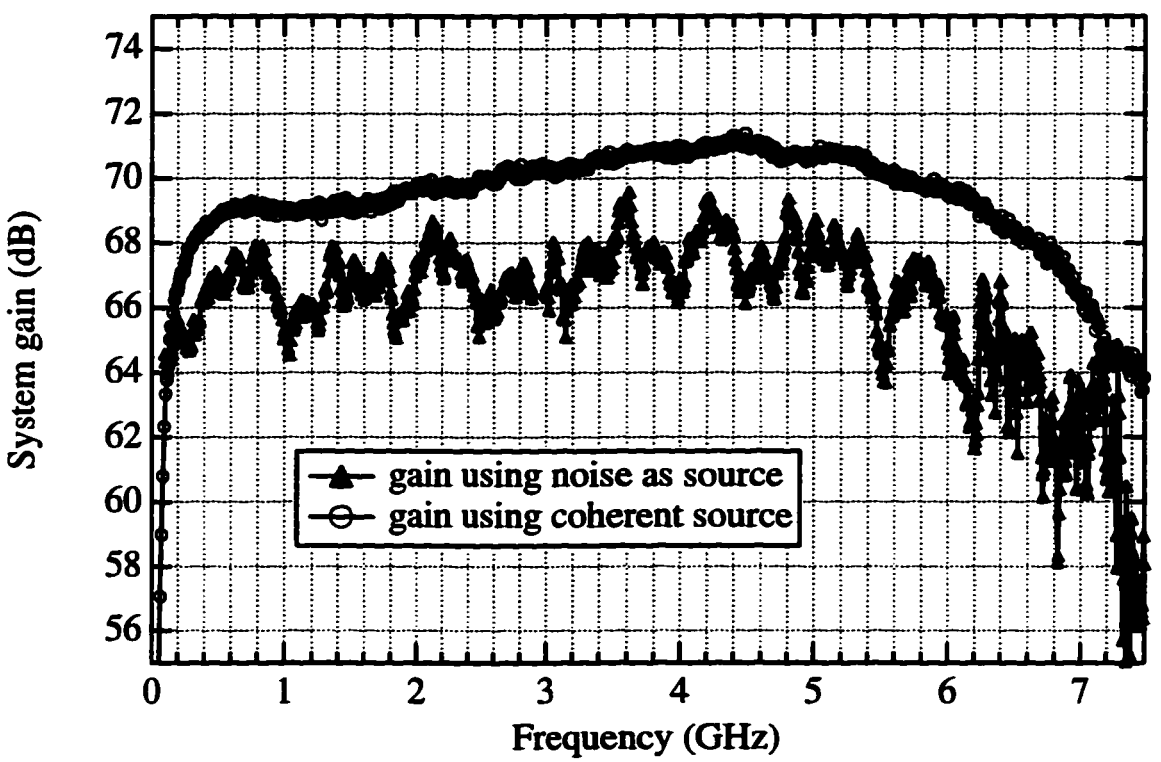

Figure 3.8: Calibration of amplifier gain using coherent vs. incoherent source.

used[12]. The final amplifier has a 1 dB saturation point of typically 1 mW, so the gain must be less than 85 dB to ensure that the amplified noise of the first amplifier ($\approx 25\ K$ over a 10 GHz band) does not saturate the last amplifier.

It was also possible to measure *in-situ* the the absolute power coupled into the device using a coherent source. This was done using a combination of noise-thermometry and the method of dc substitution as follows: First, the amplifier gain and noise was calibrated as discussed above. Next, dc power was applied to the device to heat the electrons while it was in the normal state. The heated electrons have a higher Johnson noise, and the rise in electron temperature with applied dc power was measured. Finally, the dc power was turned off and ac power was applied. Figure 3.9 shows the rise in electron temperature as a function of dc power and ac power calibrated using the (separate) technique of coherent signals discussed above. (The discontinuous change in the response to the ac power is due to a range-change on the microwave generator, which was not accounted for in the corrections.) This figure shows that the two methods for calculating the ac power agree fairly well. Therefore, it was later *assumed* that they agree, and the method was used to calculate how much power was coupled into the device as a function of frequency while in the normal state, in absolute units. The advantage of this technique for calibrating the rf power coupled to the device is that it is *in-situ*, accounting for all loss up to the terminals of the device, and that it accounts for run to run variations in calibration coefficients.

3.5.3 Drift of calibrations during run

The drift of the gain and noise temperature of the amplifier during the course of the run was measured during a separate run in order to determine its magnitude. A three-temperature (incoherent) calibration was done every 10 minutes to monitor the gain and noise, using the spectrum analyzer and a detector preceded by a 1.25-1.75 GHz band-pass filter. The percent variations vs. time are plotted in figure 3.10, and are shown to be approximately 5%. The reason for the drift could be due to many factors which have not been analyzed in detail. Additionally, it is clear that the spectrum analyzer technique drifts more than using a direct detector, presumably because the power detection circuits within the spectrum analyzer itself are not as stable as the direct detector used.

[12]Hewlett-Packard model HP8593E.

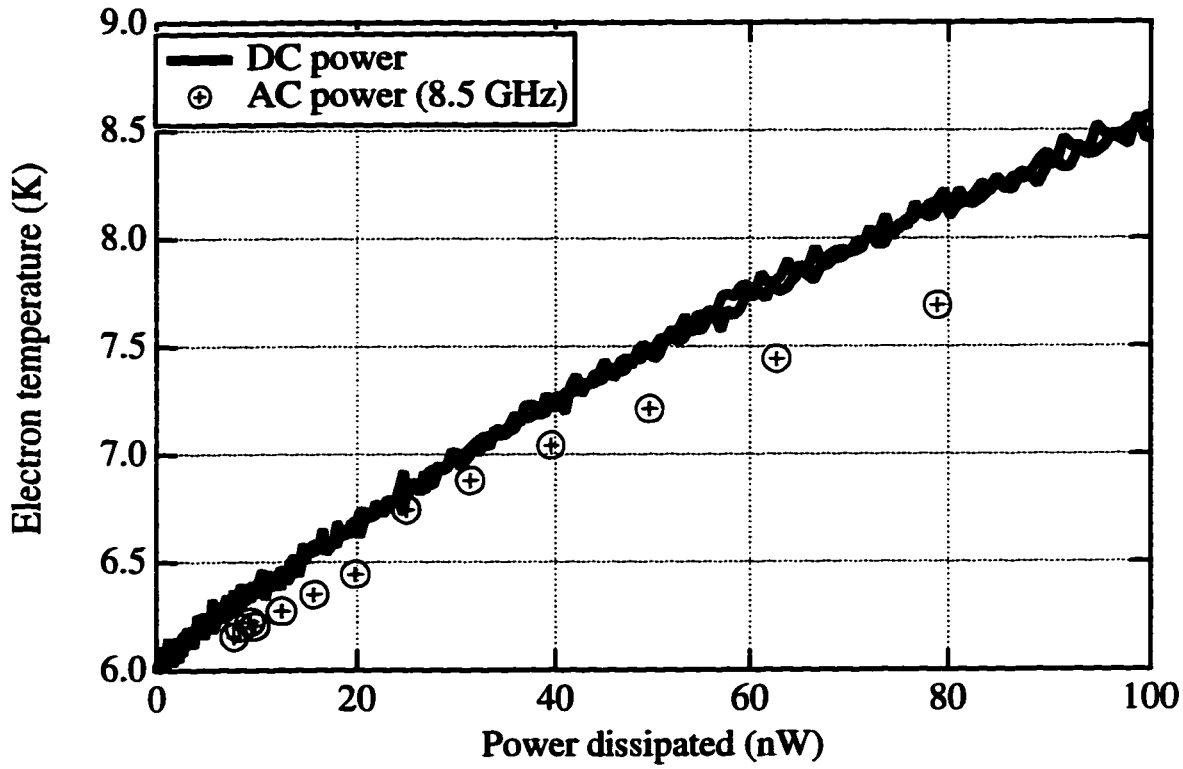

Figure 3.9: Electron temperature vs. applied power, dc and ac.

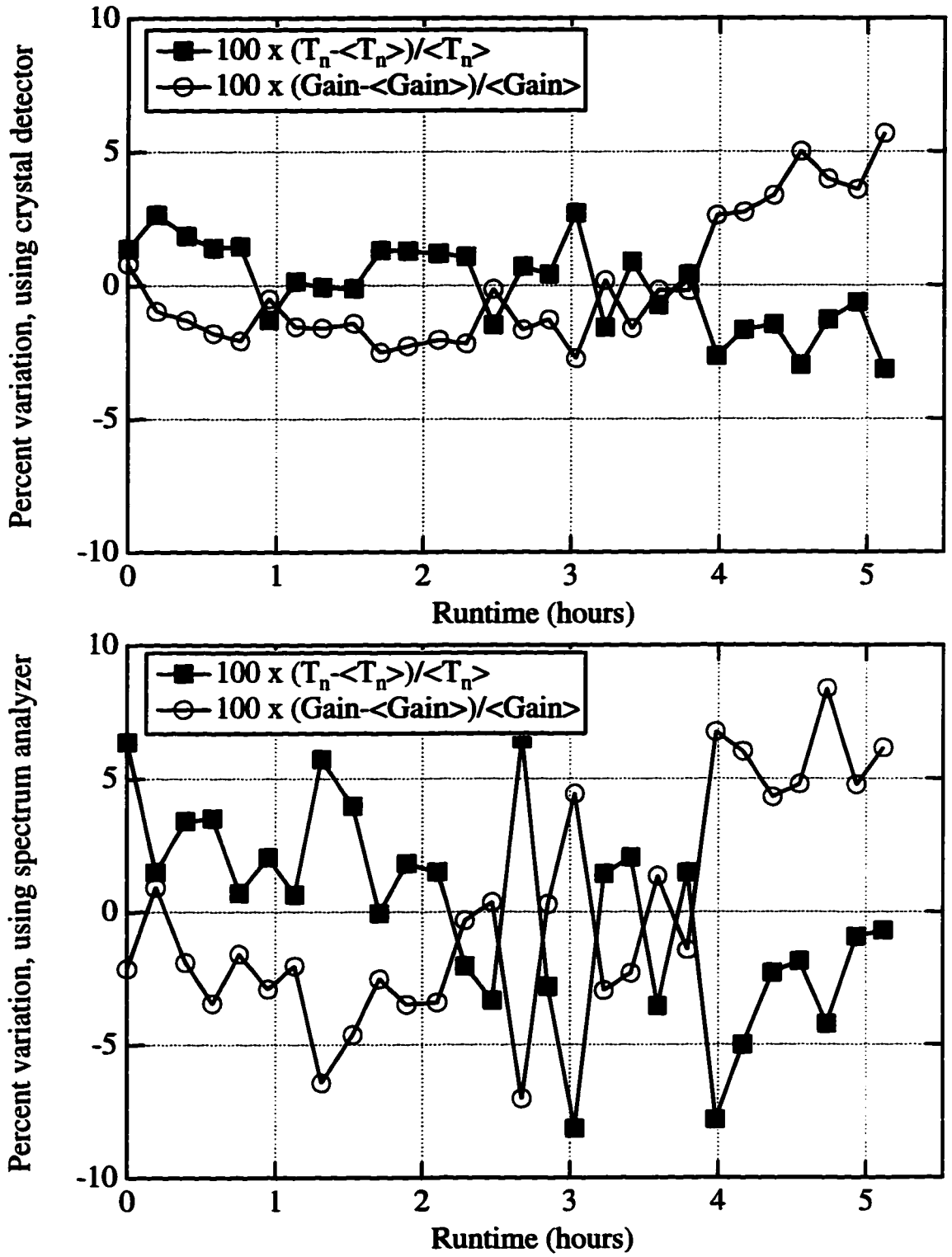

Figure 3.10: Drift of gain and noise with time in the 1.25-1.75 GHz band.

Chapter 4

Device geometries and dc properties

In this chapter, the geometry and dc properties of the devices studied in this thesis are described. The geometry and fabrication are discussed in the first section. In the second section, measurements of resistance vs. temperature are discussed. In the third section, the general characteristics of the I-V curves are discussed.

4.1 Fabrication and geometry

The devices studied in this thesis were fabricated at the Center for Space Microelectronics Technology, Jet Propulsion Laboratory (JPL) by Bruce Bumble and H. G. LeDuc. Devices were fabricated for the tests described in this thesis, as well as the 500 GHz, 1.2 THz, and 2.5 THz tests in the research group of W.R. McGrath at JPL. The goal was to test devices from the same fabrication batch at JPL and Yale at different frequencies in order to allow quantitative comparison of results. In practice, devices from different batches were measured[1], and the comparisons will be discussed in chapter 6.

Here, a brief summary of the fabrication details are given, since they are important to the

[1] For this thesis, devices from fabrication batch 08/31/95 were used.

interpretation of the results. For more detail, the reader may consult Bumble and LeDuc (1997). The finished device consisted of a 10 nm thick Nb bridge which was connected to thick, wide gold leads. The 10 nm Nb film extended under the entire gold lead, and this was made possible by a self-aligning fabrication process developed by B. Bumble. The Nb under the thick gold is assumed to be in the normal state due to the proximity effect, so that the leads consist only of normal metals.

In the first step, a uniform 10 nm Nb film is magnetron sputtered, followed *in-situ* by a uniform coating of 15 nm of gold. This ensured that no oxide layer forms on the Nb film, and that the contact resistance to the Nb is small. Next, electron-beam lithography is used to pattern a 25 nm thick gold line which is later used as an etch mask to define the width of the Nb bridge. Next, a 150 nm thick gold etch mask which defines the length of the Nb bridge is patterned, again using electron beam lithography. A three-step reactive ion etch process is then used. In the first etch, the gold over the Nb film and some of the gold over the bridge is etched. In the second etch, the Nb film everywhere but the bridge is etched using a process that selectively etches Nb. In the third etch, after the leads are deposited and patterned using optical lithography, the remaining gold on the bridge (as well as some from the leads) is etched, leaving the desired geometry. An SEM of a finished bridge is shown in figure 4.1. The length and width of the devices measured in this thesis were determined by inspecting the SEM image of different devices with the same design length in the same fabrication run. The estimated error using this technique is approximately $\pm 0.05\ \mu m$. The devices measured in this thesis were not measured in an SEM, in order to avoid electrical damage.

The device geometries and dc resistances are documented in table 4.1. In order for diffusion cooling to be efficient, it is important that the out-flow of heat into the thick gold leads be unimpeded. By biasing the device in the superconducting state, it was possible to estimate the contact resistance. The contact resistance was less than 1 Ω for all the devices measured, which is small enough compared to the bridge resistance to be neglected for the purposes of the work described in this thesis. The lengths fabricated range from well above L_{eph} to well below L_{eph} in order to allow the crossover from phonon dominated to diffusion dominated behavior to be investigated. The length to width ratio was designed to achieve the same normal state resistance for each device, so that electro-thermal feedback effects would be the same for each device, and only the length would affect the time constant. As can be seen from the table, the resistances are all within about 50% of one another. The sheet

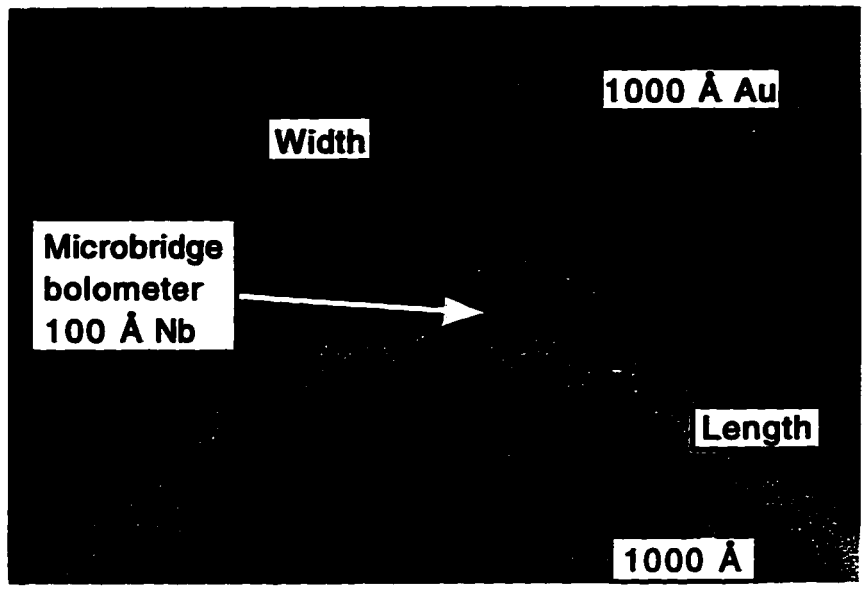

Figure 4.1: SEM of a Nb microbridge with gold pads.

resistance is determined using device E, where the relative errors in the geometry are small, and is approximately 29 Ω, corresponding to a resistivity of 29 $\mu\Omega$-cm.

For metals, the normal state conductivity is related to the diffusion constant by the Einstein relationship, the constant of proportionality depending on the Fermi velocity. It is important to know the diffusion constant, since this determines the diffusion cooling rate. In Gershenzon et al. (1990), the constant of proportionality between the conductivity and the diffusion constant was determined for 10 nm Nb films by measuring the conductivity from the geometry and the diffusion constant from the slope of dH_{c2}/dT near H=0, which gives the diffusion constant from a standard result of the BCS theory of superconductivity. For the resistivity of the devices measured in this thesis, using the results of Gershenzon et al. (1990), D $\approx$ 1 cm^2/s.

4.2 Resistance vs. Temperature

The resistance as a function of temperature was measured for the devices in order to determine dR/dT_e as well as T_c. These are plotted in figure 4.2. For a bulk superconducting sample, the transition width should be very narrow, but for the samples studied here, the transition width is

Device:	Length (μm)	Width (μm)	$R_N(\Omega)$	dR/dT (Ω/K)
A1	0.08	0.08	56	140
A2	0.08	0.08	56	-
B	0.16	0.08	80	200
C	0.24	0.08	96	250
D	0.6	0.2	93	-
E	3	1	86	-

Table 4.1: Device geometries and dc resistances.

approximately 0.1 to 0.5 K. So far, no microscopic model which explains the finite transition width is available. There are two possible sources for the finite width. First, the critical temperature may vary spatially along the length of the bridge. Second, regions of the bridge may be fluctuating in and out of the superconducting state, at a rate which depends on the temperature. This second source of broadening might also contribute excess noise, but with a different time scale than τ_{diff}. Thus, our noise measurements tend to rule out this second explanation of the broadening.

4.3 Current-Voltage Characteristics

Figure 4.3 shows a typical dc I-V curve for a diffusion-cooled device measured at a bath temperature of 2 K. For small bias voltages, there is no dissipation since the resistance is zero. At very large bias voltages, the dc power being dissipated heats most of the electrons significantly above T_c. If the region near the ends is still superconducting, there will always be a little bit of excess current (compared to the normal state I-V curve), and this is indeed found to be the case. Finally, the region near the "dropback" is where the electrons are near T_c, and the I-V curve is no longer linear. This non-linearity is presumably due at least in part to dc heating, and is the effect which allows the bridge to be used as a detector. While these general characteristics are understood, there is as yet no theory which allows quantitative predictions of the shape of the I-V curves. By applying ac power, it is possible to drive the whole bridge into the normal state, so that the I-V curve becomes

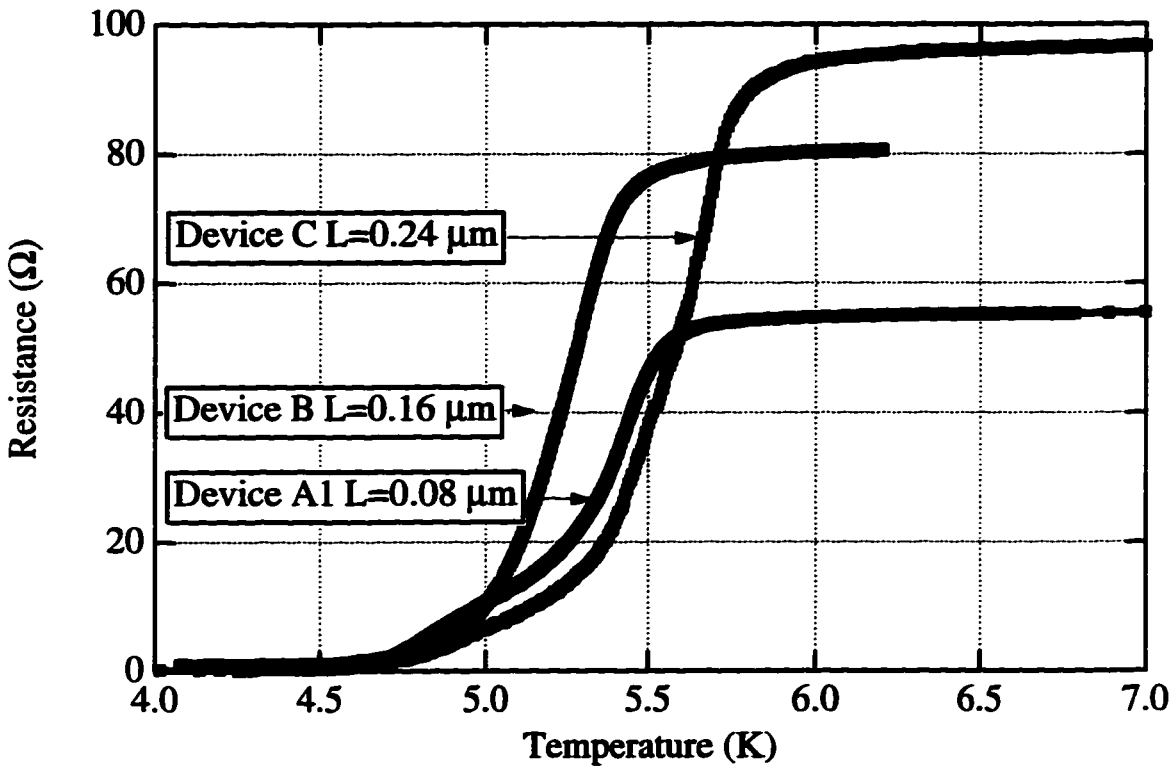

Figure 4.2: Resistance vs. temperature curves for diffusion-cooled devices.

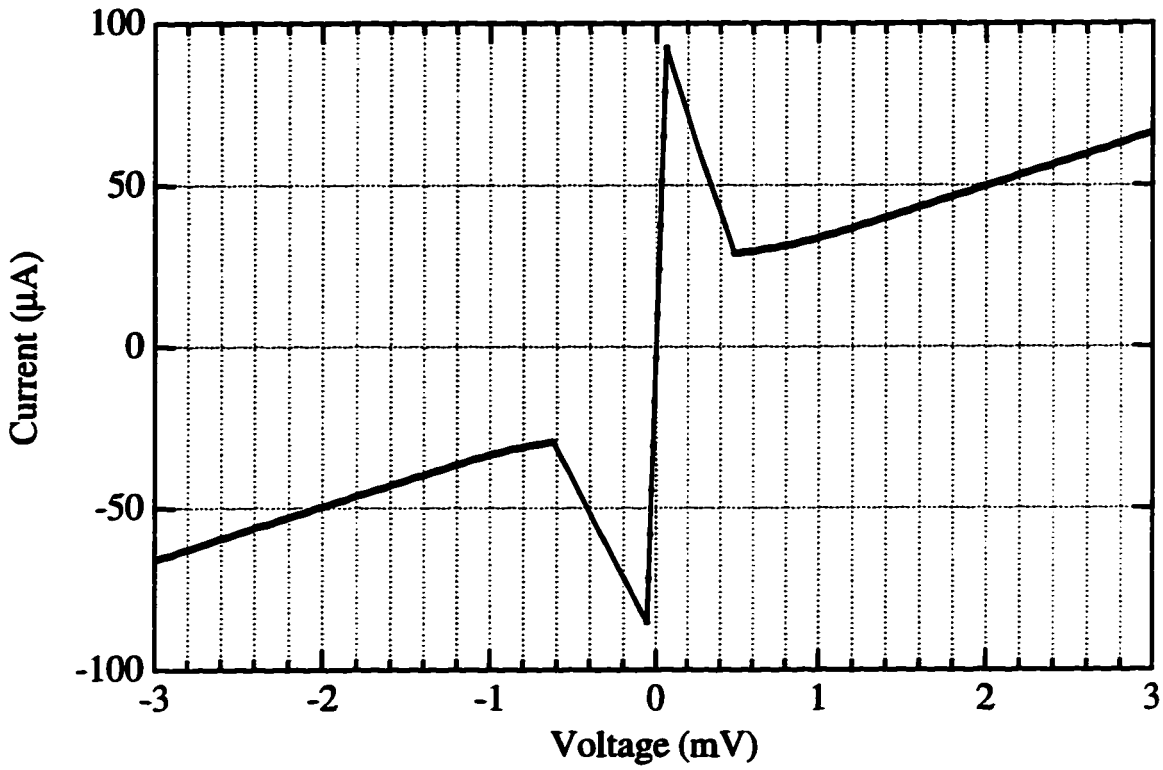

Figure 4.3: I-V curve for device A1, no ac power applied, for bath temperature of 2 K. The slight asymmetry is due to the sweep direction; points of unstable bias between the origin and 0.5 mV are not plotted. The slight slope of the superconducting branch is due to the lead and contact resistance.

a straight line with slope R_N.

Chapter 5

Measurement of gain, noise, and bandwidth

This chapter contains most of the experimental results presented in this thesis. The measurements of the noise and conversion efficiency presented in the first section demonstrate that diffusion cooling can be used to increase the intermediate frequency bandwidth to larger than 6 GHz, which is large enough for the use of hot-electron bolometers in THz receivers. The measurements of the output and mixer noise also indicate that the device is very sensitive, and indeed indicates the hot-electron bolometers will be the most sensitive devices for THz frequencies. In addition to measuring the performance as a practical device, the high-frequency impedance of the devices was also measured in order to test the physical model presented in chapter 2. These measurements are presented in the second major section, and indicate that the devices were all well coupled to the 50 Ω rf system, in accordance with theoretical predictions. In a separate, but related set of experiments, noise thermometry was used to independently determine the response of the devices to ac and dc power when in the normal state. This allowed the crossover from diffusion-cooled to phonon-cooled behavior to be determined in a separate set of experiments, thus substantiating the conclusions of the first section. In the final section of the chapter, the device output noise and conversion efficiency are compared to theoretical predictions based on chapter 2. It is important to understand the device performance in order to predict the optimum mixer noise that can be attained, and how to obtain it.

While there is qualitative agreement between the basic theoretical predictions and the experimental results, a theory which quantitatively predicts device performance under a wide variety of operating conditions is still lacking.

5.1 Gain and noise

The measured gain, output noise, and mixer noise all depend on several parameters under experimental control for a given device, including the LO power, dc power/voltage, temperature, and intermediate frequency. Therefore, this section is divided into four subsections, in order to illustrate the dependence of the gain and noise on the different parameters. In the first subsection, the variation of the dc I-V curve itself with temperature and LO power will be presented. Next, the dependence of the gain, output noise, and mixer noise on the LO power and dc voltage is presented. Third, the dependence of the gain on intermediate frequency is presented, together with the dependence of the bandwidth on device length. In the fourth subsection, the dependence of the output noise on intermediate frequency is presented. In the final subsection, the dependence of the noise on the LO frequency is presented.

5.1.1 I-V curves vs. bath temperature, LO power

In figure 5.1, I-V curves are plotted for device A1 under several different bath temperatures. Very near T_c, there is no hysteresis, although there is negative differential resistance. As the bath temperature is lowered, a supercurrent branch develops. There, the power dissipated is zero since the voltage is zero. (The finite slope is due to resistance in the on-chip as well as off-chip leads.) Since there is no dissipation of power, the electronic temperature is equal to the bath temperature. The amount of current that can flow without a voltage drop is not infinite. Therefore, there is a branch of the I-V curve where the power dissipated is enough to heat the electrons substantially above the bath temperature, hence bringing them (mostly) into the normal state. We have termed the finite-voltage region of the I-V curve near the point of switching the "dropback" region. It is here that just enough power is being dissipated to heat the electrons to near T_c.

There is a simple theoretical model which predicts the shape of the I-V curves more quantitatively,

but the agreement with the experimental data in this thesis is marginal. The curve can be predicted as follows: assume that the electrons are a given temperature near or above T_c, and then infer the dc resistance from that temperature based on the resistance vs. temperature curve measured separately with small enough current to avoid self-heating. Given the assumed temperature, calculate the dc power necessary to heat the electrons above the bath temperature using knowledge of the thermal conductance. Then, from the dc power and resistance, infer the voltage by equating P_{dc} to V^2/R. The current will simply be V/R. This method requires quantitative knowledge of the amount of power required to heat the electrons above the bath temperature, as well as a knowledge of the temperature profile along the length of the bridge, if it is not uniform.

This theoretical model successfully predicts the gross features of the I-V curve. It predicts that for large dc power (i.e. large bias voltages), the electrons are heated well above T_c, and the I-V curve approaches the normal state (linear) I-V curve at high bias. Experimentally, we find that the curves never meet, which may be due to the fact the some fraction of the electrons near the ends of the device are below T_c, so that the resistance is always less than the normal state resistance by some fraction. The theory also predicts a supercurrent branch, where there is no dc power dissipated, hence no heating. (The model does not, however, predict the value of the critical current.) Finally, the model predicts that near the dropback region, the electrons are near T_c. Since the change in resistance with temperature is largest at T_c, the device is expected to have the best conversion efficiency in this region. This is indeed found to be the case experimentally, as will be discussed further below.

The model fails to give quantitative agreement with the experimental data for several reasons. In the case of devices longer than the electron-phonon interaction length L_{e-ph}, the temperature profile is expected to be uniform, and the relationship between the electron temperature, bath temperature, and input power in the normal state can be measured using noise-thermometry, as discussed in section 5.3. However, for the long device measured in this thesis, the I-V curve is not smooth at any temperature. An example of this can be seen in figure 5.37. There, "kinks" in the I-V curve are very suggestive of the formation of local "hot-spots" (Skocpol et al. 1974). It is postulated that some regions of the device are in the normal state, hence dc power is dissipated there, sustaining an elevated temperature. Other regions may be superconducting. Since no power is dissipated in

those regions, the electrons remain at the bath temperature and hence remain superconducting. It is also possible that the kinks are due to phase slip centers (Skocpol 1974), which normally occur in one dimensional superconducting wires. Since the width of the devices studied in this thesis is larger than the superconducting coherence length, they are classified as two dimensional superconductors, making the analysis of the current density and critical current much more complicated, especially under non-equilibrium conditions.

For the devices shorter than L_{e-ph}, the temperature profile is expected to be non-uniform. The ends are expected to be near the bath temperature, and the center is at or above T_c if the device is biased at non-zero voltage. Therefore, in order to accurately predict the I-V curve, the temperature profile would need to be self-consistently calculated. Presumably, such a calculation would need to include the assumption that dc power is only dissipated in normal regions, and that regions below T_c would not be heated. An additional complication arises from the fact that the devices with length less than L_{e-ph} are only 1-5 x L_{ee} in length, so that a local temperature could only be defined over 1-5 "pixels." A quantitative prediction of I-V curves remains an unsolved problem for future research.

The electrons can be heated above the bath temperature with ac power as well as dc power. In figure 5.2, the I-V curve at a fixed bath temperature of 2 K is plotted for various LO powers. The LO frequency was 20 GHz, which is too fast for the electronic system to follow. Therefore, there is a net rise in the electron temperature, but no substantial oscillatory component. With sufficiently large LO power, all the electrons can be heated above T_c into the normal state, and the I-V curve becomes linear. (This case is not illustrated in figure 5.2.) The critical current (i.e. the maximum current the device can sustain with no voltage drop) decreases with increasing in LO power. This trend is not continuous, and at a certain LO power, the critical current jumps discontinuously to zero, and the I-V curve is no longer hysteretic. We have termed the case where just enough LO power is applied to completely suppress the critical current the "overpumped" case. This is because the LO power required for optimum gain is 2-3 dB *less* than that required to completely suppress the critical current.

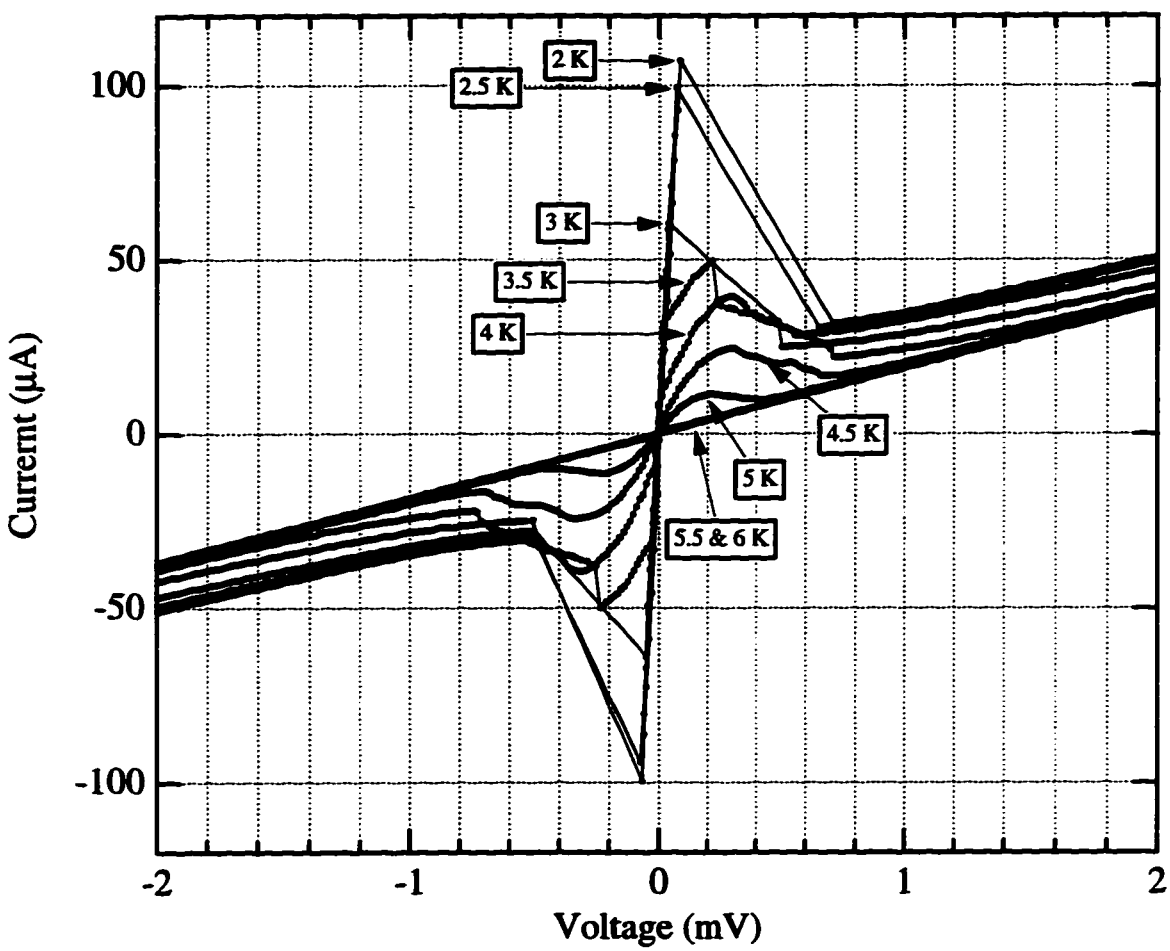

Figure 5.1: I-V curves at different bath temperatures for device A1, with no LO power applied.

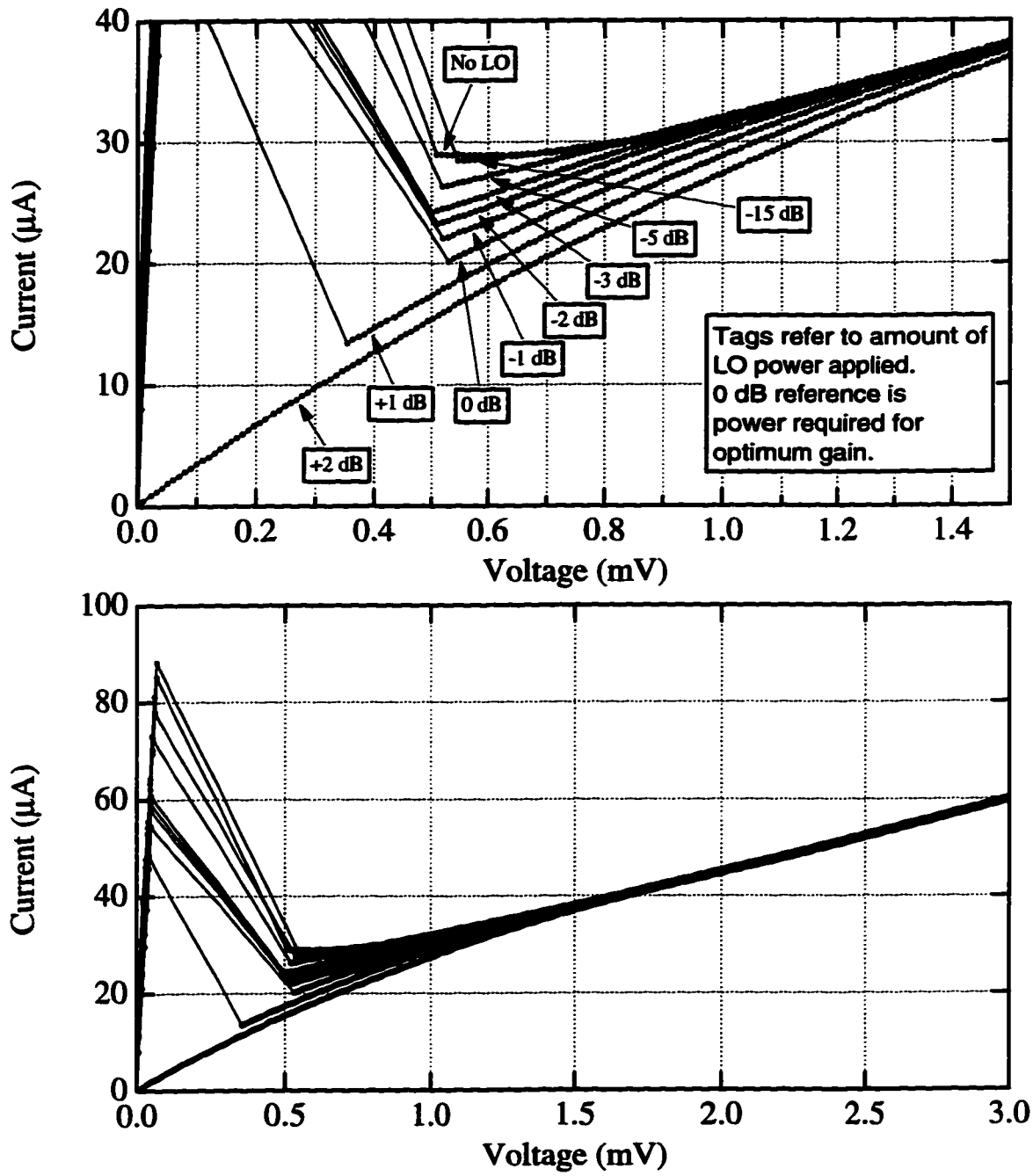

Figure 5.2: I-V curves under different LO powers for device A1. The bath temperature was 2 K.

5.1.2 Gain and noise vs. voltage, LO power

The measurements of the gain and noise were all performed at a bath temperature of 2 K, for several reasons. First, it was found that the conversion efficiency improved by about 1 dB for devices A1 and B upon reducing the temperature from 4.2 K to 2 K. Second, the conversion efficiency and noise both had very non-uniform dependence on the dc bias voltage until the temperature was reduced to below approximately 3 K. The I-V curves were also smooth below that temperature, but developed kinks above that temperature, as can be seen in figure 5.1. (This was not the case for device E, which had kinks in the I-V curves at all temperatures measured, from 2 K to T_c.) This would have complicated the analysis as well as the search for optimum bias points at a given temperature. It was also desired to compare different devices under nominally similar conditions, which was much simpler using the smooth I-V curves below 3 K. Finally, experiments at JPL at 500 GHz on very similar diffusion-cooled devices found an improvement in the receiver noise temperature by about a factor of two for the same reduction in bath temperature from 4.2 K to 2 K (Skalare et al. 1996). This is in accord with the theoretical prediction of equation 2.31, since more LO power is required to heat electrons to T_c from a lower bath temperature, and the thermal conductance is reduced linearly with the bath temperature for diffusion cooling. (The electron temperature is presumed to be near T_c for mixing to occur.) Therefore, unless otherwise specified, the measurements in this thesis were undertaken with a bath temperature of 2 K.

The (relative) conversion efficiency, output noise, and mixer noise are plotted as a function of LO power for fixed dc voltage in figure 5.3 for device A1. There are two cases of LO power which are of interest. We refer to the LO power required to maximize the (coupled) conversion efficiency as the "optimum gain" case. Note that the conversion efficiency and output noise peak at different LO powers, for a fixed bias voltage. However, the *mixer* noise is relatively constant near its minimum, even though the efficiency and output noise are changing very rapidly with LO power there. The second qualitative case is the "overpumped" case, where the critical current is suppressed. In that case, the output noise is drastically suppressed relative to its maximum value. The conversion efficiency is also somewhat lower than its maximum value. However, the mixer noise does not change much between the "optimum gain" case and the "overpumped" case. It is possible to explain this as consistent with equations 2.13 and 2.28. The efficiency is proportional to the LO power, while the

output noise does not depend on it directly. Therefore, it is conceivable that the efficiency peaks at a higher LO power than the output noise. The overpumped case is of practical interest because the output noise and efficiency are less sensitive to the dc bias voltage, which will be discussed next. The general behavior indicated in figure 5.3 was observed in all the devices measured. With the exception of device E, the *mixer* noise in the overpumped case at the dc bias that minimized the mixer noise was lower than the mixer noise in the optimum gain case at the dc bias that minimized the mixer noise.

An important practical issue is the input power which saturates the detector. In figure 5.4, the relative gain is plotted as a function of input power for device B. The 1 dB gain compression point is approximately 1/3 of the LO power, and the curve indicates that the device saturates very smoothly with increasing signal power. Although the saturation curve was not measured for each of the devices studied in this thesis, it is reasonable to postulate a scaling law for the saturation power. The LO power (in addition to the dc power) provides an indication of how much power must be applied to bring the electron temperature to T_c. It is then plausible that the saturation signal power is approximately 1/3 of the LO power for all devices.

In order to investigate the dependence of the gain and noise on dc bias, the output noise and conversion efficiency were measured as a function of dc bias for two different LO powers (optimum gain, and overpumped) for each device. The I-V curve was also simultaneously measured. The resultant mixer noise was calculated by taking the ratio of the output noise to the conversion efficiency. The measurements were done at an intermediate frequency that is low enough to be representative of the zero IF limit of the device performance. The results are plotted in figures 5.5-5.24. The differential and absolute resistance are also plotted with the corresponding I-V curves, since they will be needed for the data analysis. (Note that both quantities are between 20 Ω and 130 Ω for all of the devices, except E. This means they were all well coupled to the rf and IF system. This point will be discussed in more detail in section 5.2.) The immediate conclusion in these graphs is that the mixer noise is *very low*, varying from $\approx$ 100 to 500 K (DSB) for all of the data. Since the mixing process is thermal and depends only on heating of the electrons, similar results are expected to be achievable at THz frequencies. This indicates that the achievable receiver or system noise is at least an order of magnitude below existing technologies for frequencies above $\approx$ 1 THz.

Excellent results at THz frequencies have already been achieved in experiments on diffusion-cooled hot-electron bolometers, and these will be discussed further in chapter 6.

In addition to the low mixer noise, we have observed two general trends. First, in the optimum gain case, the conversion efficiency and output noise rise sharply near the point of instability where the device can switch to the supercurrent branch. The *mixer* noise gets slowly lower, the closer one can bias near the region of instability. Second, in the overpumped case, the output noise and conversion efficiency are reduced compared to the optimum gain case, and the *mixer* noise is usually lower. Additionally, since the I-V curve is non-hysteretic, the device cannot switch into the superconducting branch and the efficiency and noise depend smoothly on the dc bias. (Note that in the overpumped case the device sometimes switches into the superconducting state because not quite enough LO power was applied.) In section 5.4, these data will be compared with theoretical predictions based on chapter 2.

The measured output noise (from 175-215 MHz) for device A1 in figures 5.5 - 5.7 was done with an LO frequency of 18 GHz. When the output noise was measured for the same device with an LO frequency of 20 GHz over a broader band, the output noise was about a factor of 2 higher in the optimum gain case, but a factor of 2 lower in the overpumped case. Additionally, the conversion efficiency plotted in figures 5.5 - 5.7 was measured with an LO frequency of 18 GHz as a *relative* quantity. It has been normalized to agree with the conversion efficiency measured over a broader IF band with an LO of 20 GHz. (The conversion efficiency measured with a 20 GHz LO was also calibrated in a slightly different manner than the other devices: incoherent calibrations were used to determine the coupled rf power as well as the gain of the IF amplifiers.) Therefore, the mixer noise and conversion efficiency for device A1 in figures 5.5 and 5.7 are valid as relative quantities, but have been normalized in an indirect manner, and are therefore less trustworthy. Additionally, the periodic variation of the output noise and efficiency with bias voltage is *not* an experimental artifact. The period is approximately 35 μV, which corresponds to a frequency of 8.5 GHz (using $\hbar\omega = eV$). However, the spacing of the peaks did not scale with the applied LO frequency. The periodicity in the *mixer noise* may be an experimental artifact, since the offset voltage in the dc electronics may have shifted by an amount comparable to the periodicity between the measurements of the conversion efficiency and the measurements of the output noise. This behavior was only observed

for device A1[1], and so may be a mesoscopic effect related to the fact that the length of the device was comparable to L_{ee}.

[1]The bias voltage dependence of the gain and noise for device A2 was not carefully measured.

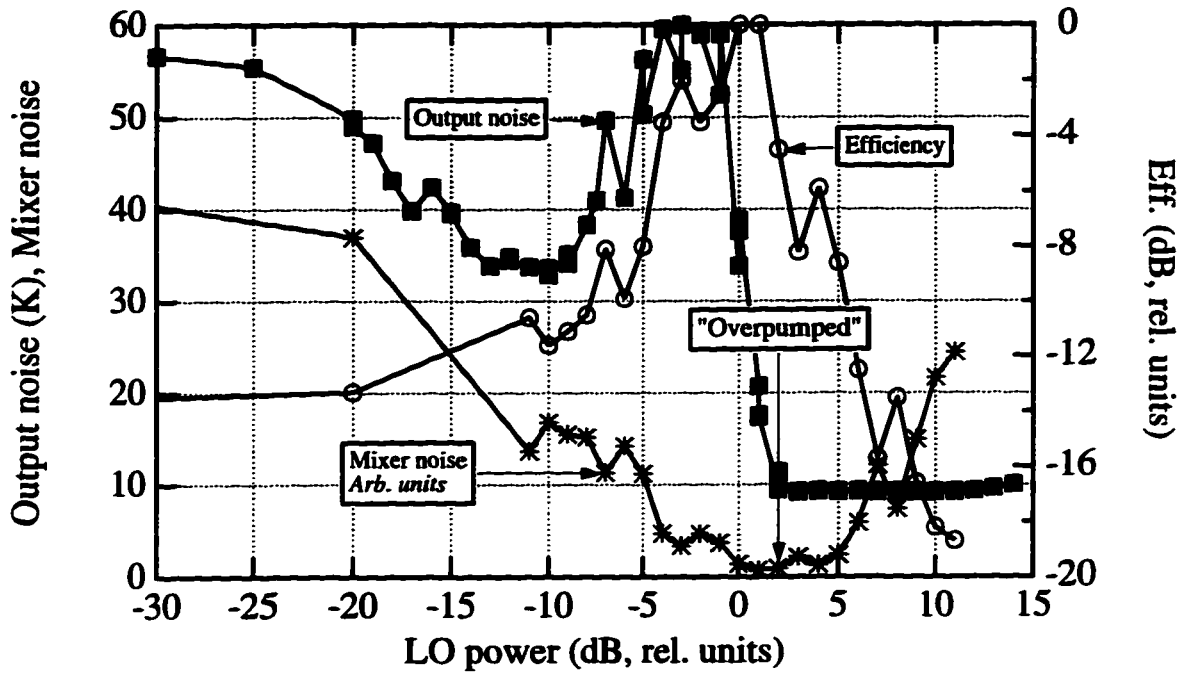

Figure 5.3: Efficiency, output and mixer noise for device A1 vs. LO power. The optimum gain occurs at $P_{LO} = 0$ dB. Bias voltage = 0.6 mV. Noise and efficiency measured at IF = 1.25-1.75 GHz.

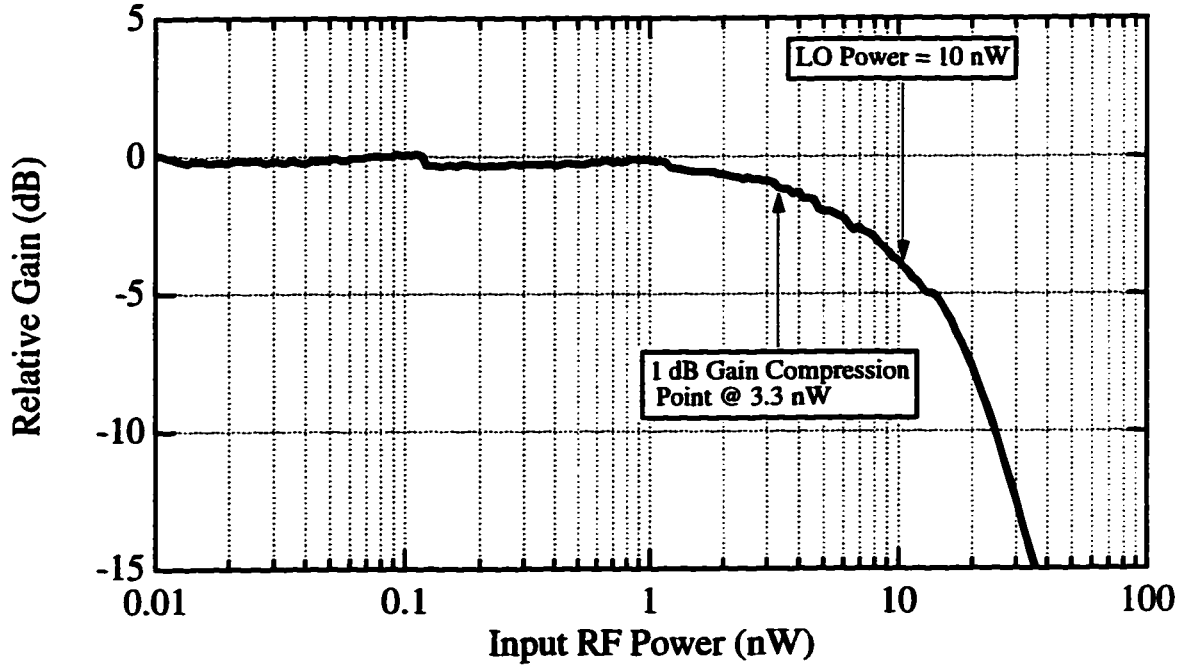

Figure 5.4: Saturation curve for device B.

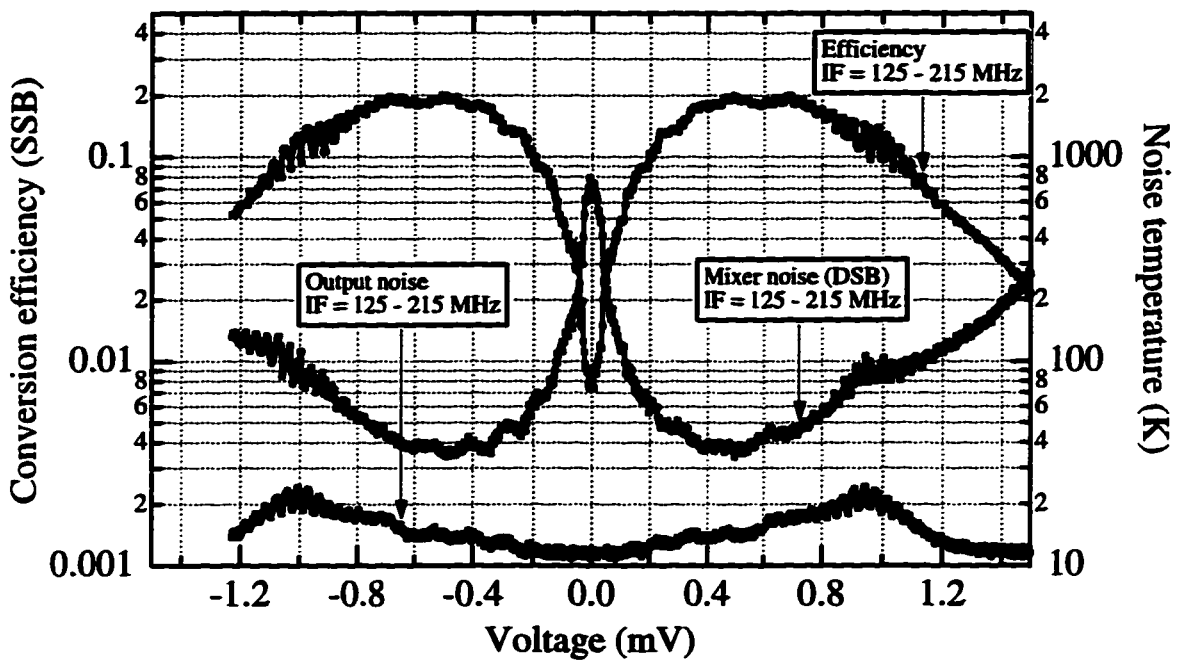

Figure 5.5: Gain and noise vs. voltage for device A1 in overpumped case.

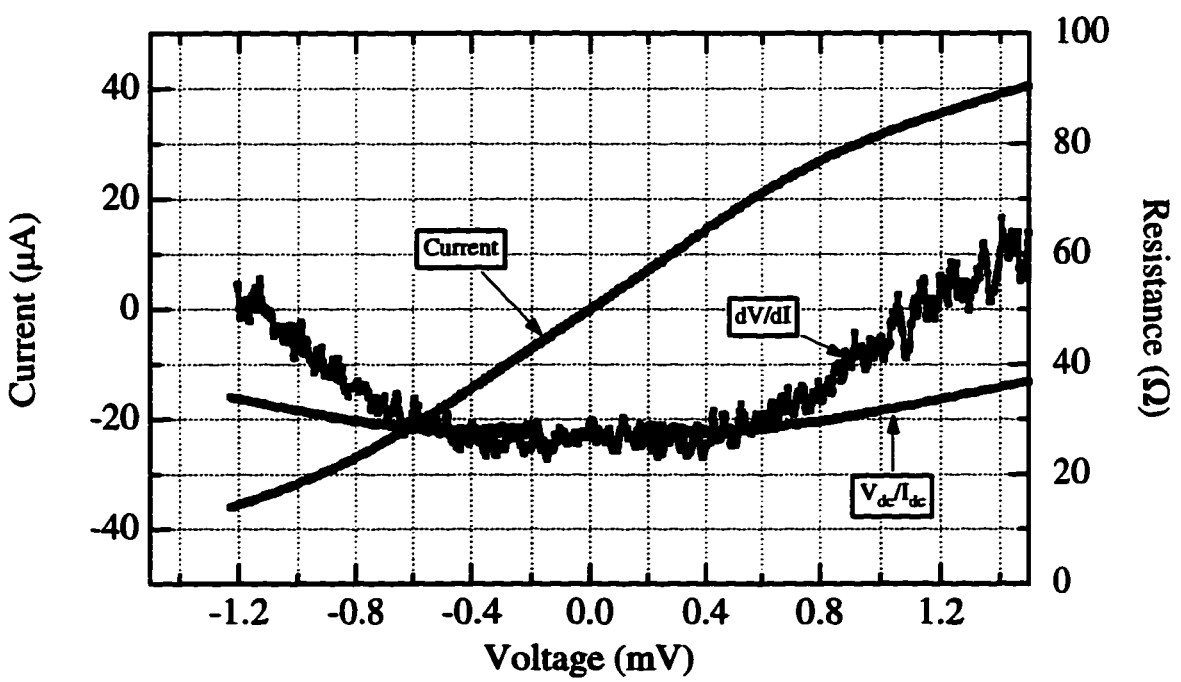

Figure 5.6: Current vs. voltage for device A1 in overpumped case.

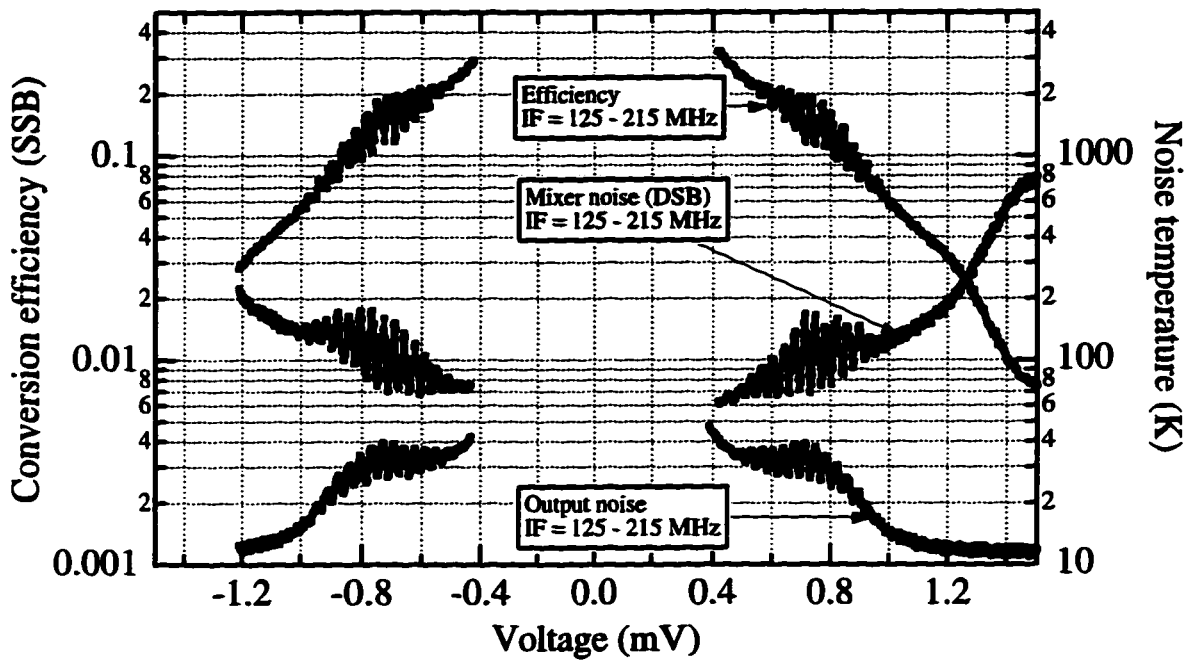

Figure 5.7: Gain and noise vs. voltage for device A1 in optimum gain case.

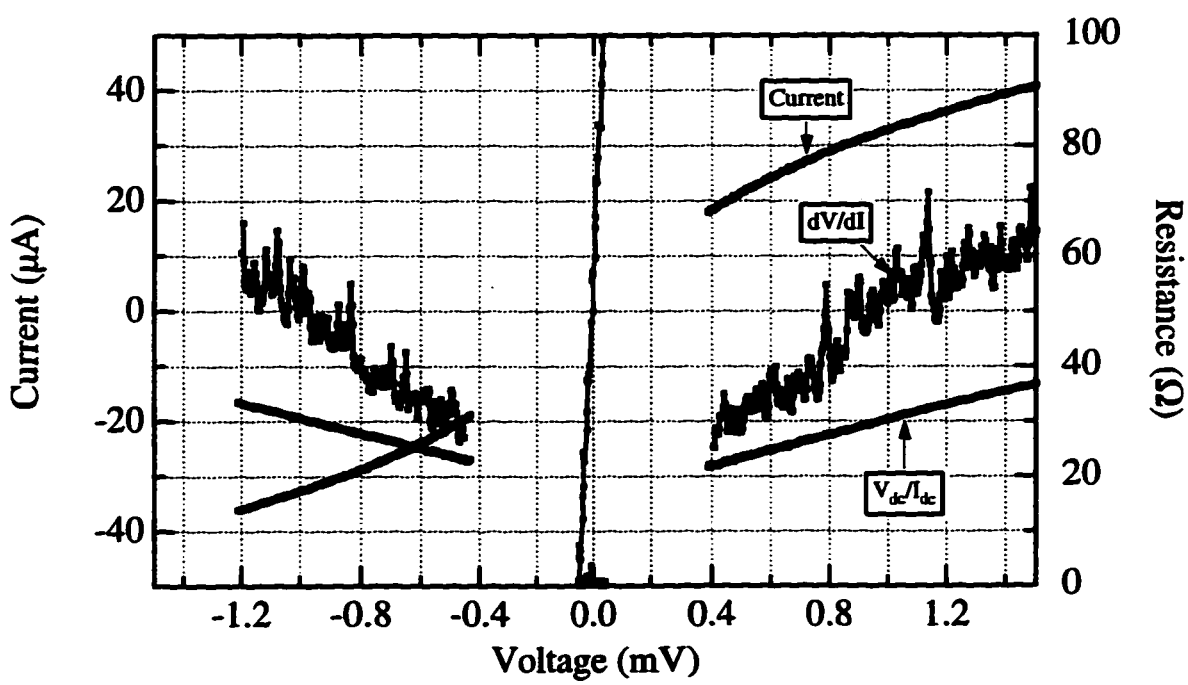

Figure 5.8: Current vs. voltage for device A1 in optimum gain case.

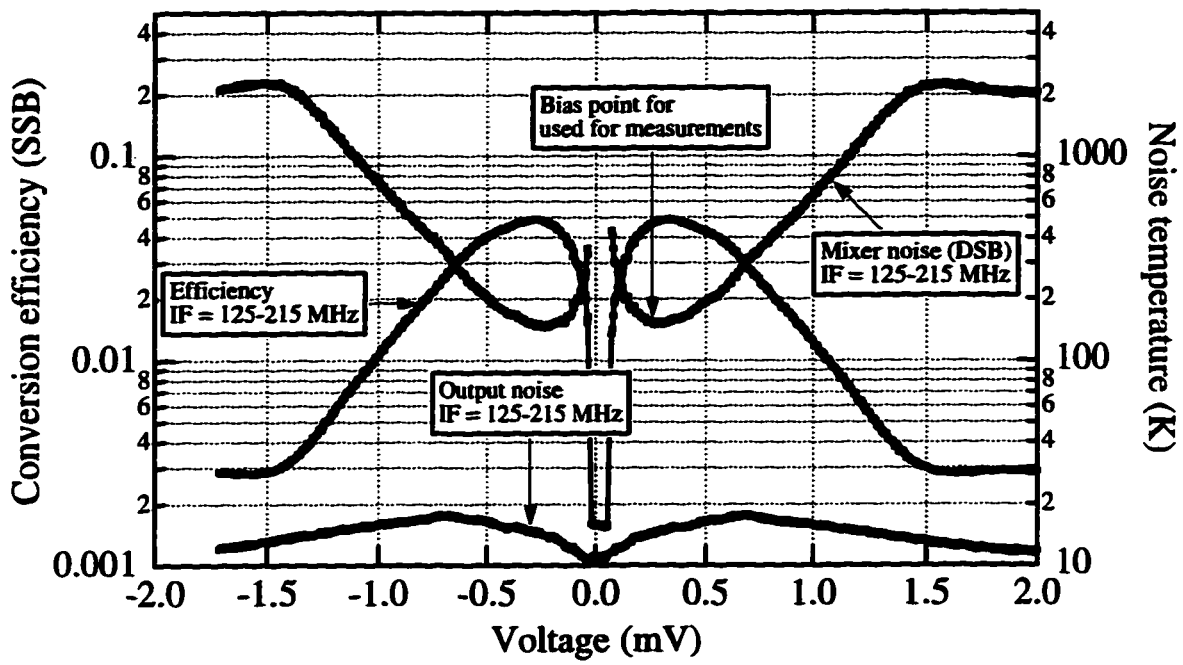

Figure 5.9: Gain and noise vs. voltage for device B in overpumped case.

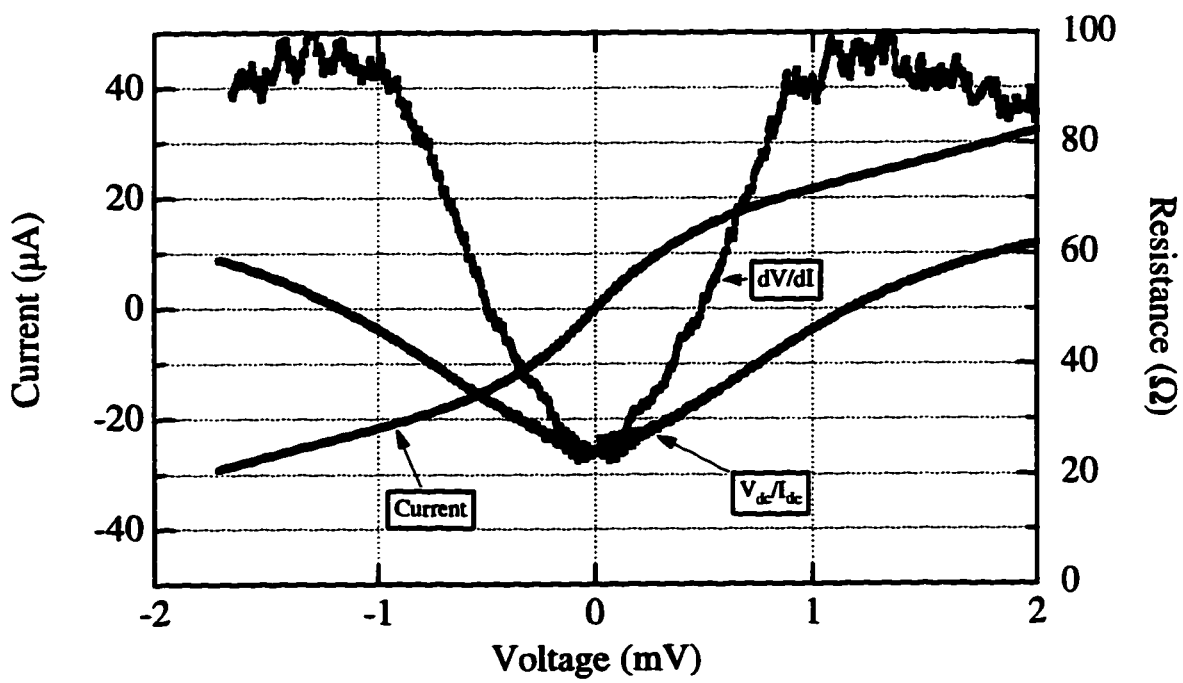

Figure 5.10: Current vs. voltage for device B in overpumped case.

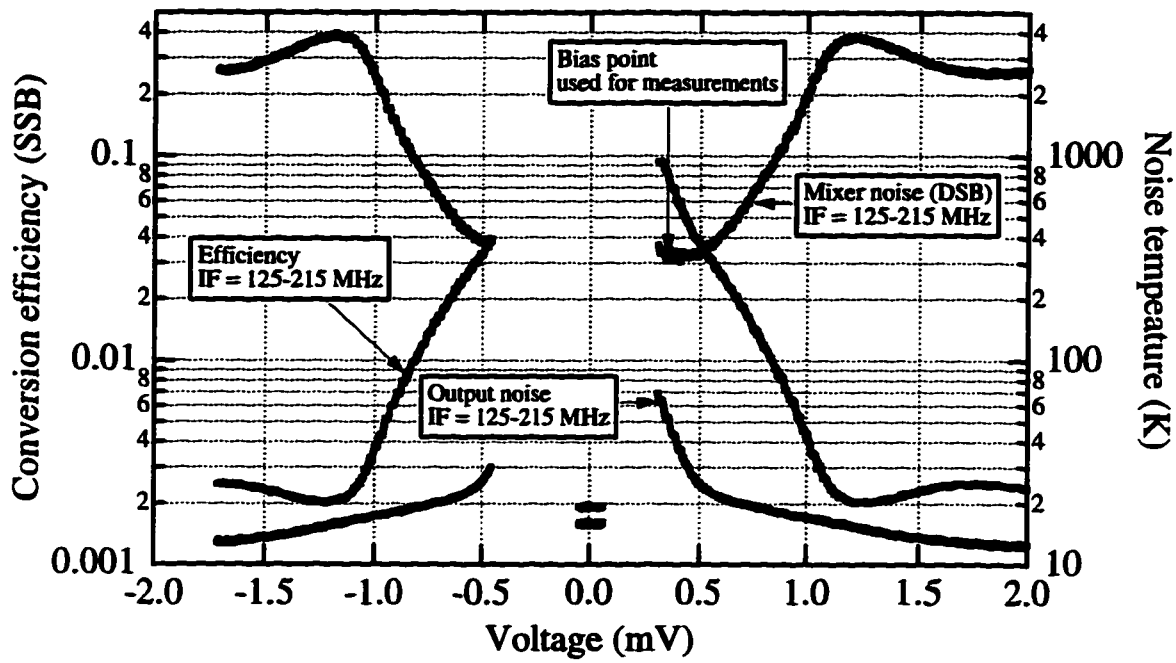

Figure 5.11: Gain and noise vs. voltage for device B in optimum gain case.

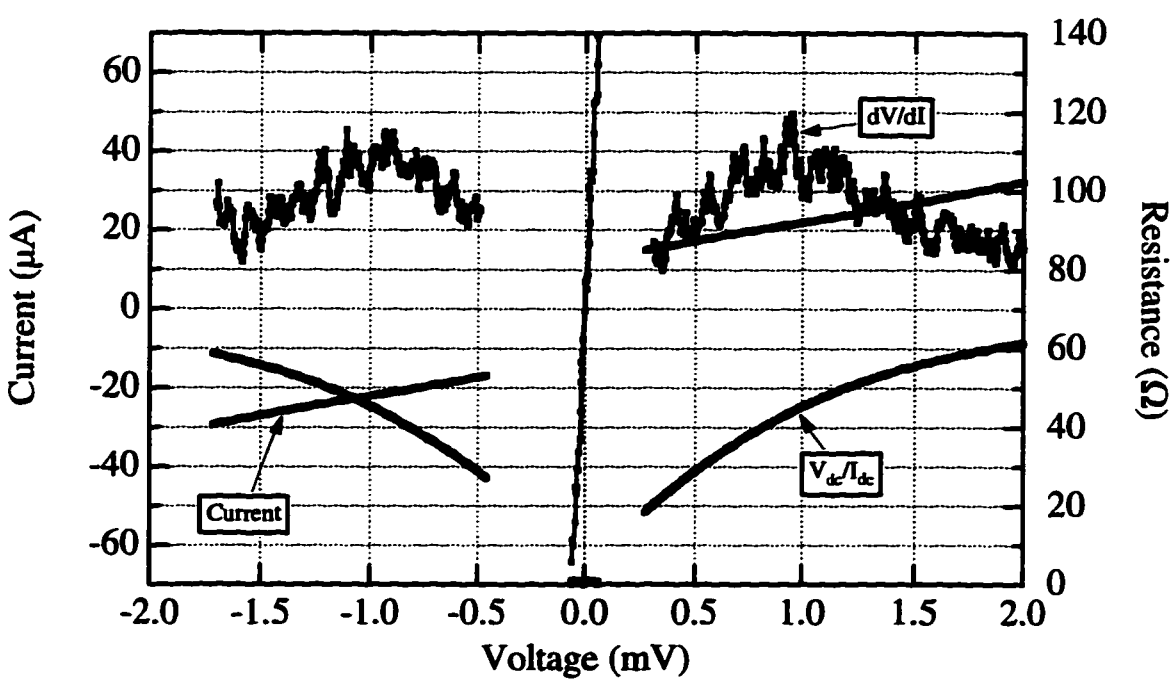

Figure 5.12: Current vs. voltage for device B in optimum gain case.

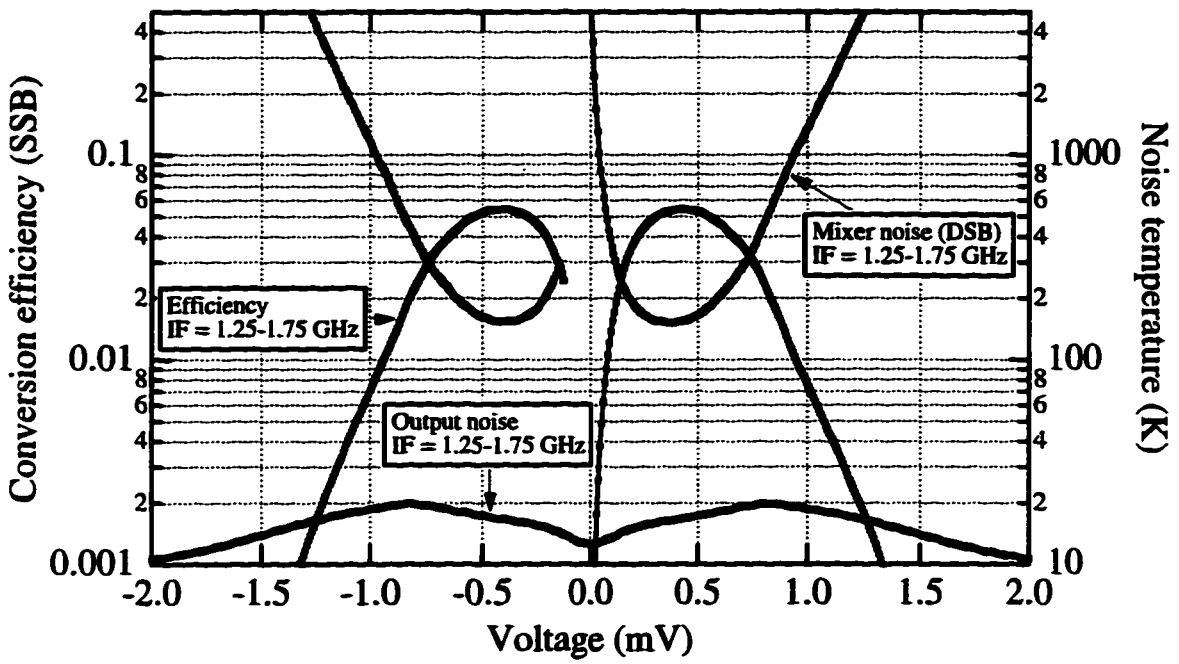

Figure 5.13: Gain and noise vs. voltage for device C in overpumped case.

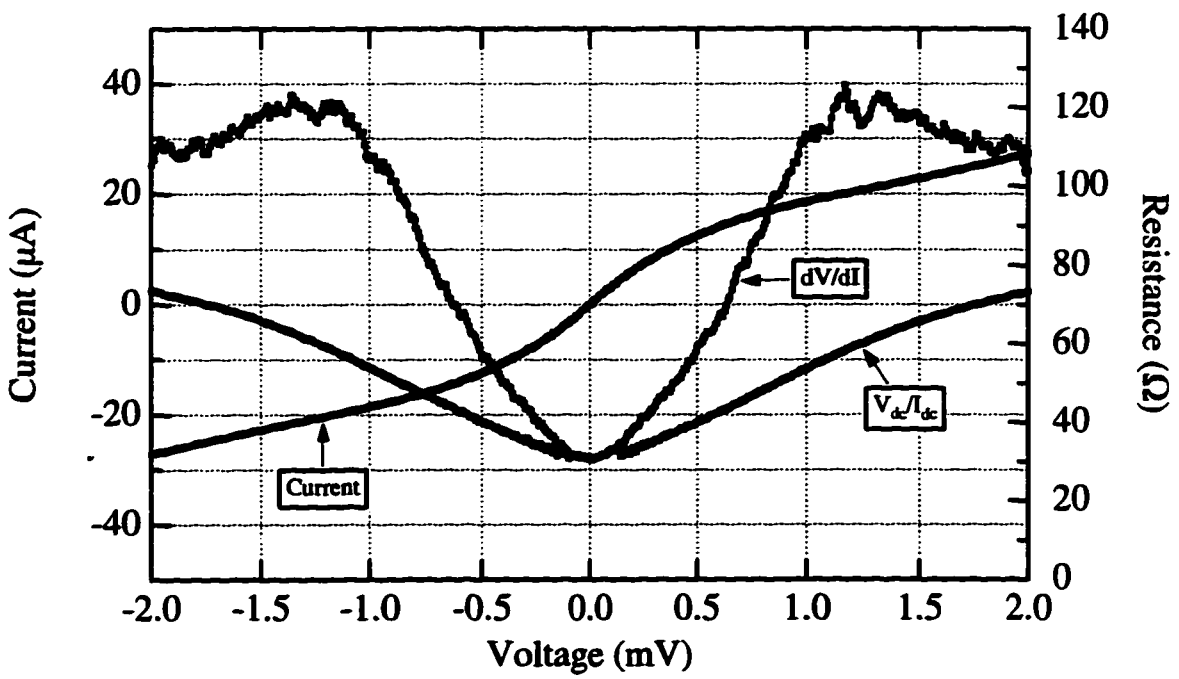

Figure 5.14: Current vs. voltage for device C in overpumped case.

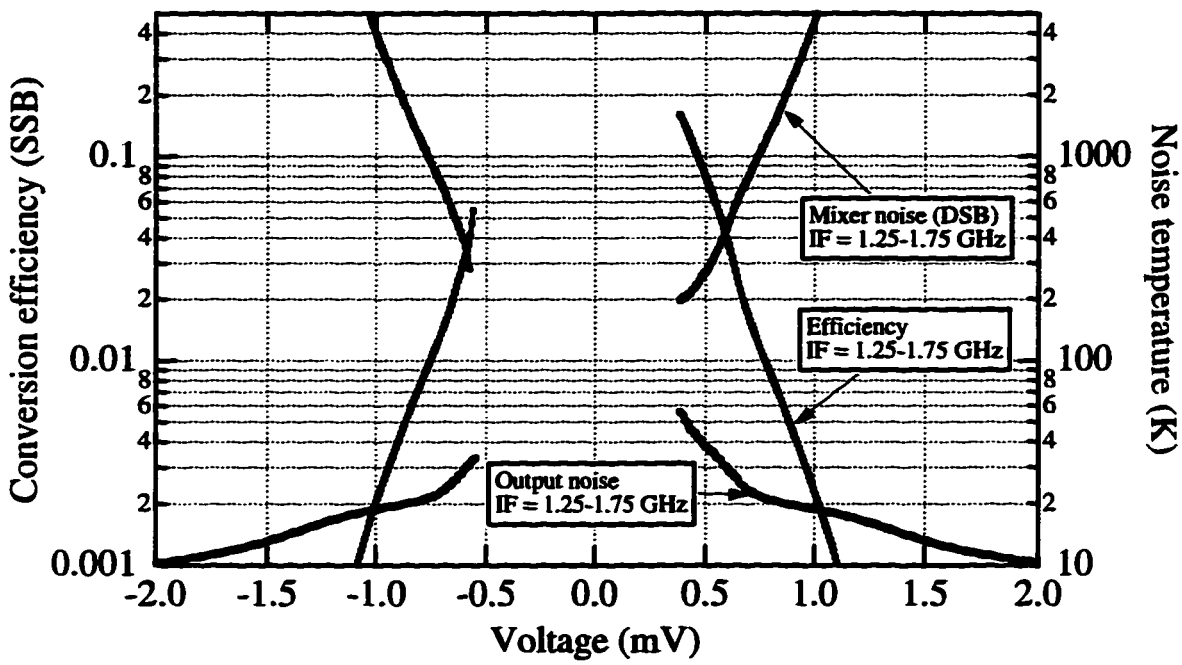

Figure 5.15: Gain and noise vs. voltage for device C in optimum gain case.

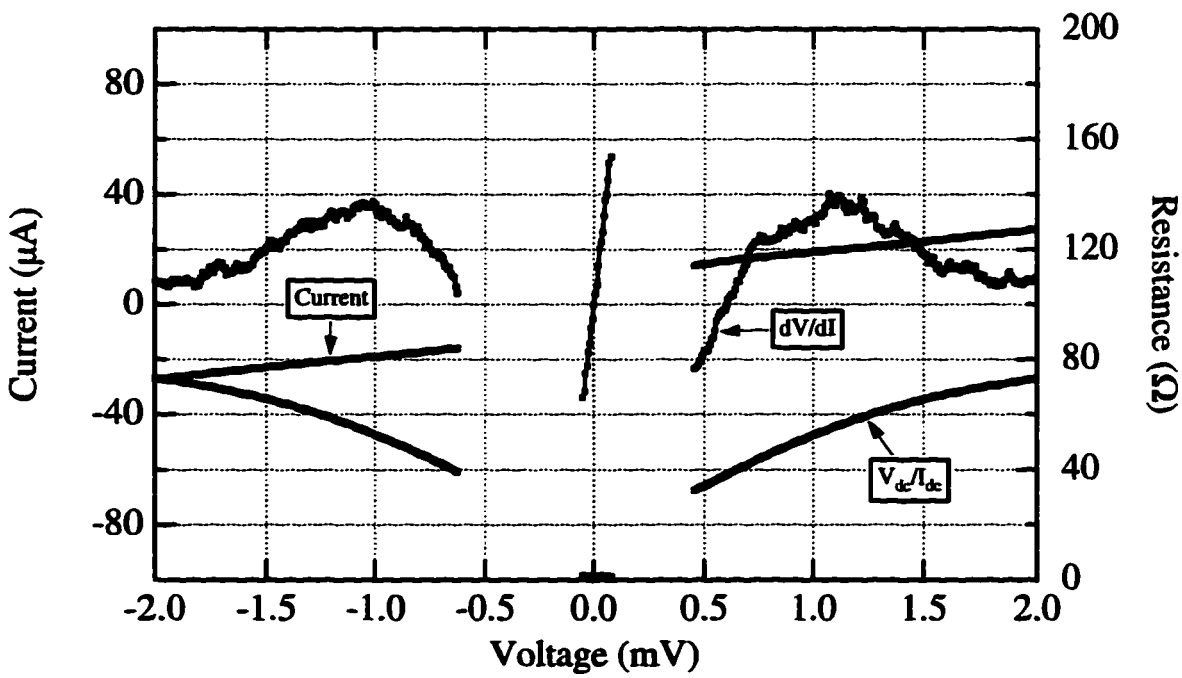

Figure 5.16: Current vs. voltage for device C in optimum gain case.

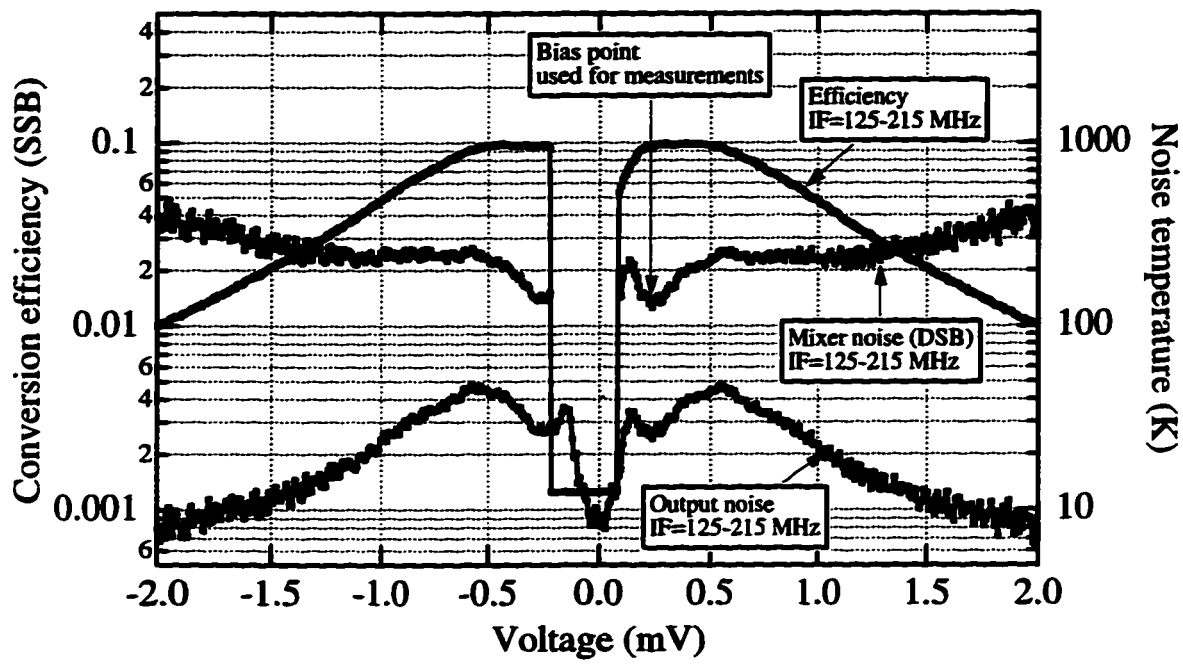

Figure 5.17: Gain and noise vs. voltage for device D in overpumped case.

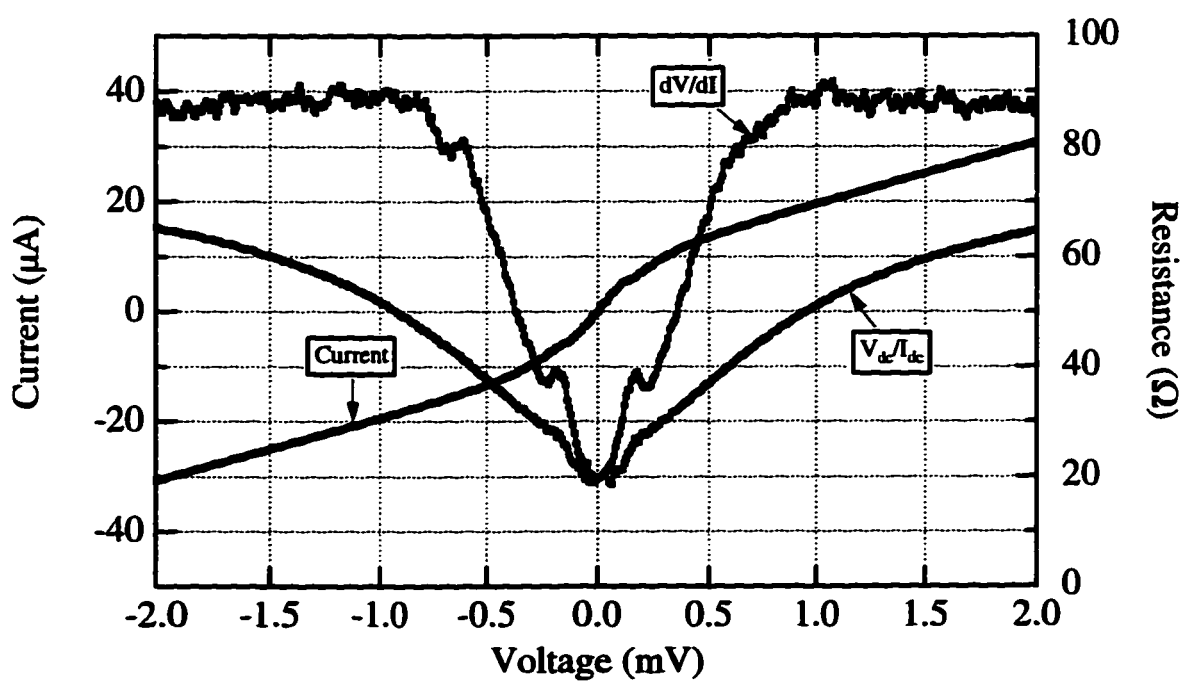

Figure 5.18: Current vs. voltage for device D in overpumped case.

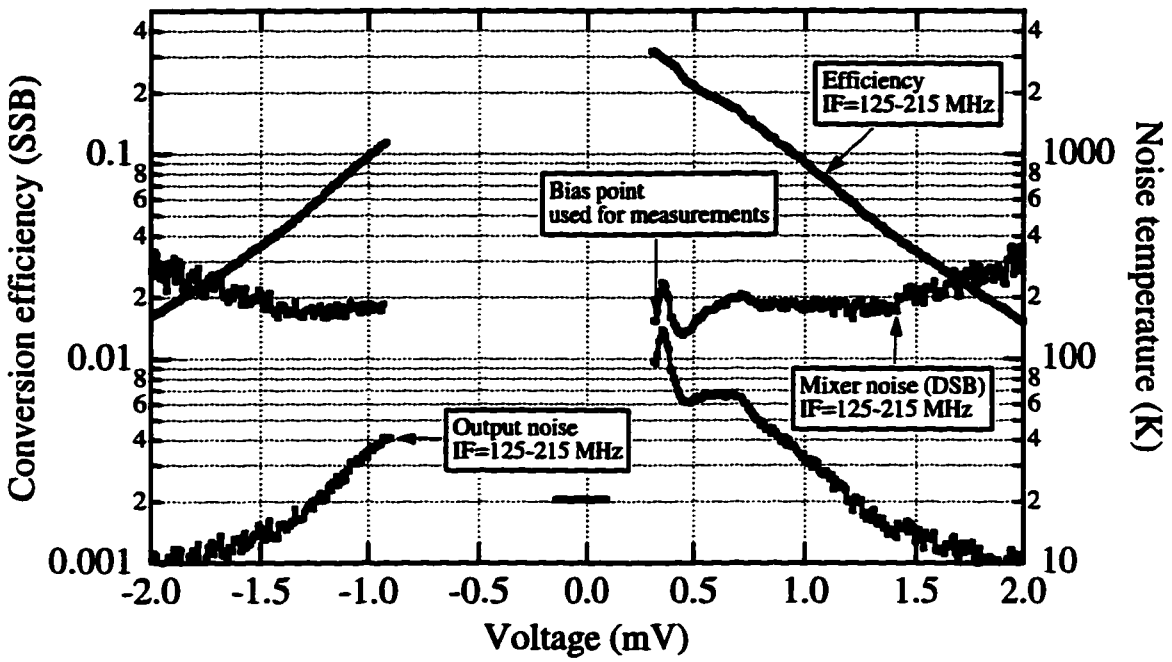

Figure 5.19: Gain and noise vs. voltage for device D in optimum gain case.

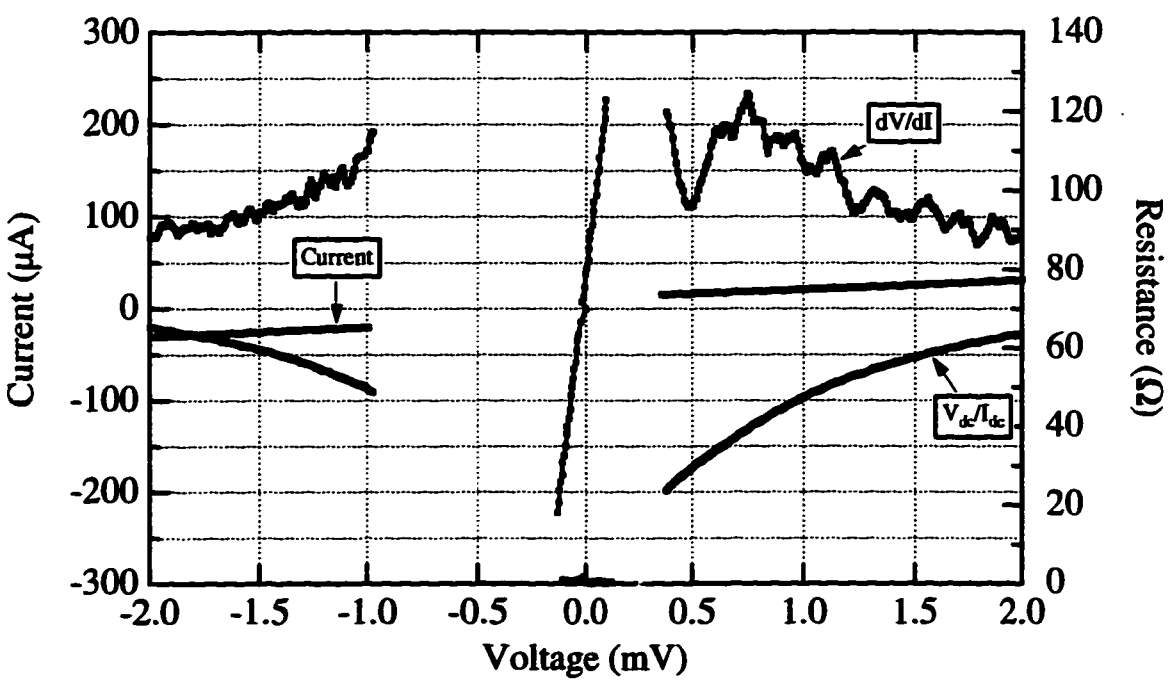

Figure 5.20: Current vs. voltage for device D in optimum gain case.

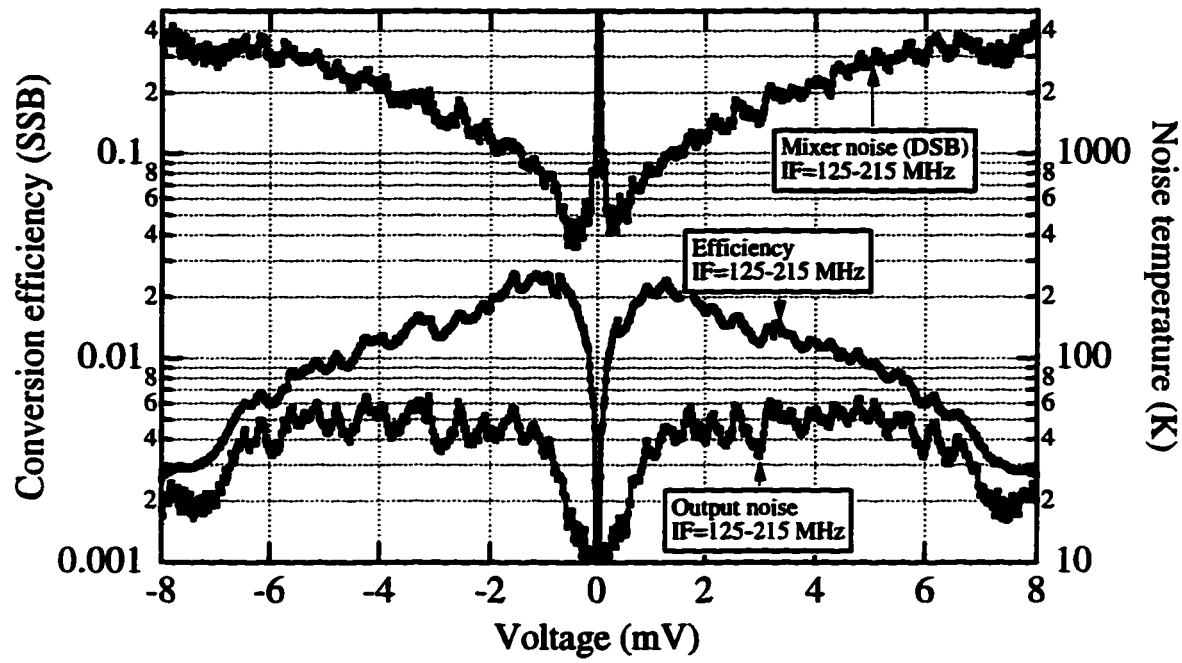

Figure 5.21: Gain and noise vs. voltage for device E in overpumped case.

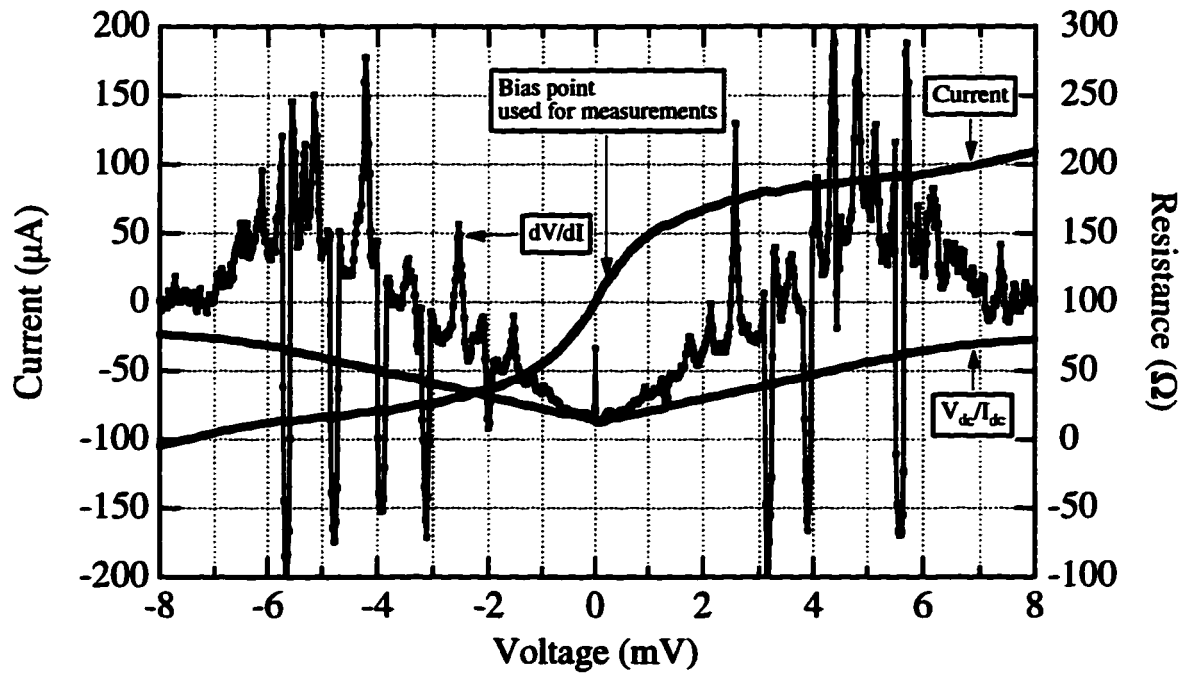

Figure 5.22: Current vs. voltage for device E in overpumped case.

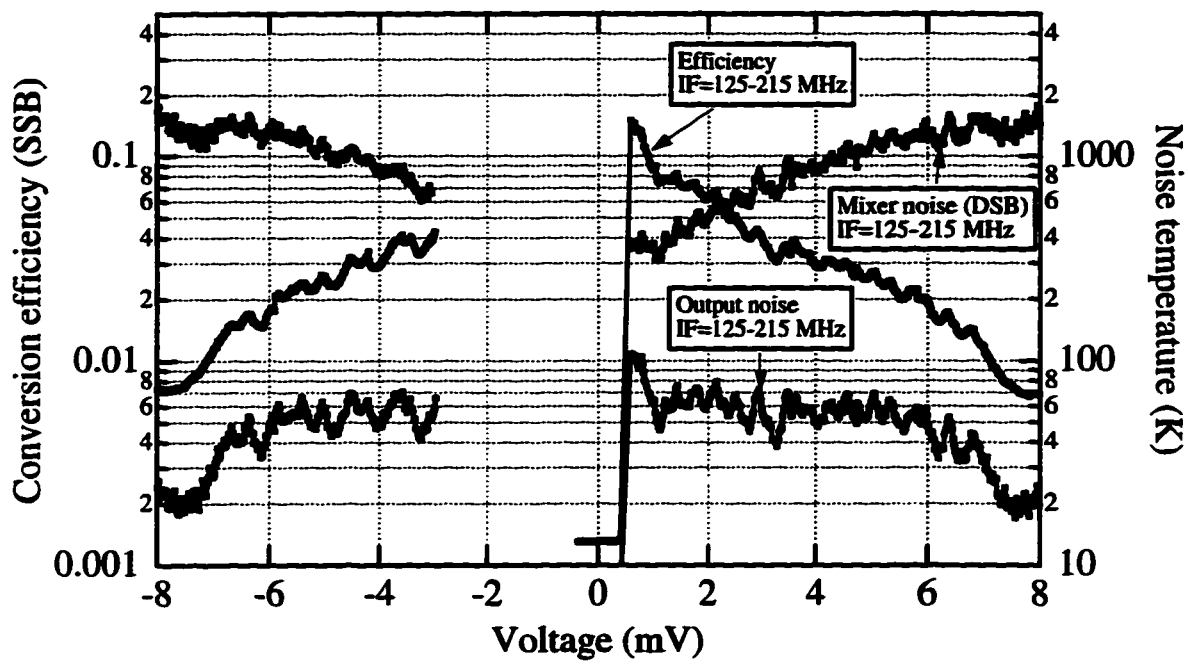

Figure 5.23: Gain and noise vs. voltage for device E in optimum gain case.

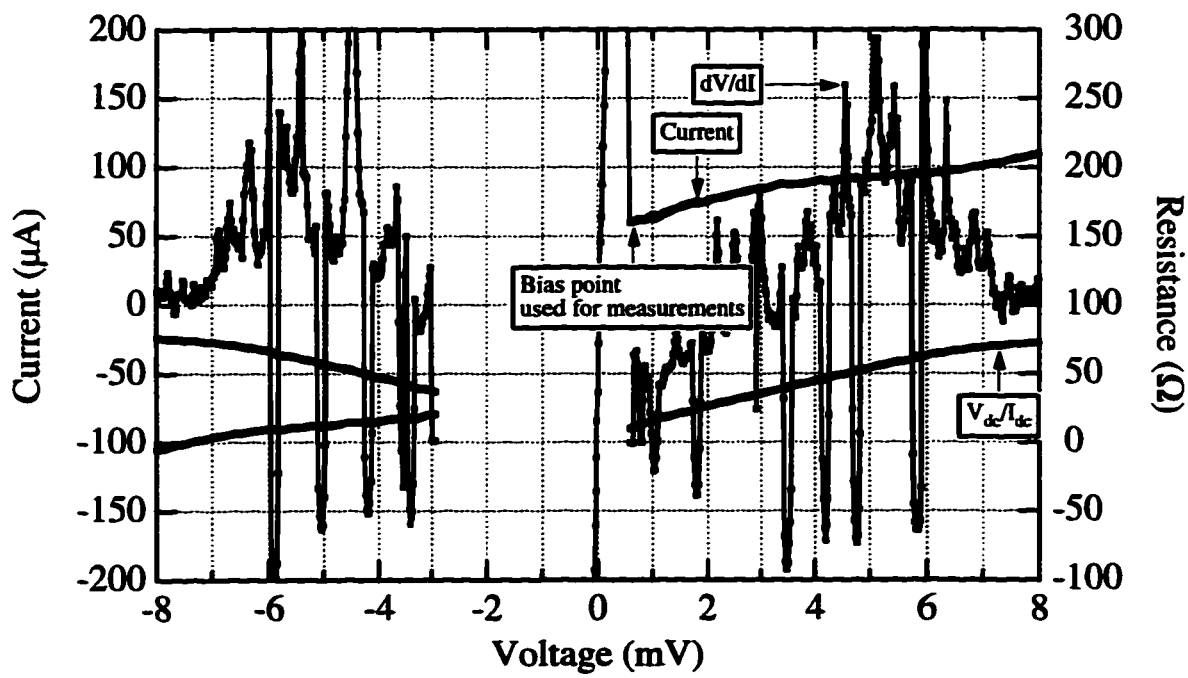

Figure 5.24: Current vs. voltage for device E in optimum gain case.

5.1.3 Gain vs. intermediate frequency

One of the most important goals of this work was to investigate the dependence of the conversion efficiency on the intermediate frequency and determine the time constant as a function of device length. The dependence of the conversion efficiency on intermediate frequency is plotted for all the devices measured in figure 5.25. The absolute conversion efficiency will be discussed further in section 5.4. However, in order to compare the relative frequency response of each device, the relative frequency dependence is plotted in figure 5.25. The theoretical fits to equation 2.13 are also shown. The frequency dependence of the conversion efficiency is indeed well-described by equation 2.13. Note that there are two devices of the shortest length plotted, and the data are very consistent. The close agreement between the theory and experiment provides strong confirmation of the theoretical model over two orders of magnitude in frequency and conversion efficiency.

The fitted time-constant is plotted in figure 5.26 as a function of length. This plot is the central result of this thesis. When the device length L is much larger than $\pi\ L_{e-ph}$ ($\approx 1\ \mu$m at 4.2 K), the bandwidth is expected to be independent of length. The dashed line indicates this phonon cooling limit. Device E is in this limit. For $L \ll \pi\ L_{e-ph}$, the dominant cooling mechanism should be diffusion, and the dotted line shows the expected L^{-2} dependence. The solid line shows the prediction for the net effect of both phonon and diffusion cooling mechanisms, assuming the thermal conductances add. The theoretical prediction for the diffusion cooling based on equation 2.57 is that $\tau_{th}(ns) \approx L^2$, with L in μm. We find experimentally that $\tau_{th}(ns) \approx 1.8\ L^2$. This discrepancy appears to be within the uncertainties in the predicted as well as the measured prefactor. While the prediction for τ_{th} is exact for a non-superconducting bridge, it also can be used below T_c because the quasiparticle excitations which carry away heat have energy $\sim kT$ which is much larger than the gap energy near T_c. The measured bandwidth of 6 GHz is the largest bandwidth yet obtained in a low-T_c bolometric mixer, as of the writing of this thesis. The value of 6 GHz is actually a lower limit, since since the conversion efficiency changes with IF by an amount comparable to the experimental uncertainties for the IF frequencies used.

It is possible that the measured time constant is modified by electro-thermal feedback effects, and that the "bare" time constant is different from the measured one. However, in section 5.4, the "slowing factor" (α) is estimated, and for all the devices it is less than 0.25, with the exception of

device E. For device E, α is 0.46 in the optimum gain case. Therefore, the inferred time constant is approximately equal to τ_{th}.

5.1.4 Noise vs. intermediate frequency

In the previous subsection, it was demonstrated that diffusion cooling could be used to increase the conversion efficiency bandwidth by a factor of 50. An additional quantity of practical interest is the mixer noise, i.e. the noise referred to the input. If the output noise decreases with intermediate frequency in the same way as the conversion efficiency, then the mixer noise will be independent of the intermediate frequency. For this reason, the spectrum of the output noise was measured under identical conditions as the conversion efficiency.

Measurements at microwave frequencies of noise are usually performed with an isolator between the device under test and the amplifier. The isolator serves to insure that noise generated by the amplifier does not get reflected off of the device under test back into the amplifier input, and mistaken as noise from the device. Broadband, coolable isolators are not available, so most of the measurements presented in this section were done without an isolator. The reflection coefficient of each device was measured under the same conditions that the noise was measured under, and the devices were found to be well coupled in all cases, except for device E at frequencies below 100 MHz. (The reflection measurements are discussed in more detail below in section 5.2.) Therefore, the lack of an isolator should not introduce significant errors into the measurement process. However, in several cases an isolator was used in order to confirm that the measured noise with and without an isolator agreed. This is addressed in figure 5.27, where the noise in the band 5-7.5 GHz is plotted vs. dc bias, measured in two separate experiments, one with an isolator and one without. The results agree, and it was found that the drift in the calibration coefficients was a larger source of uncertainty than that introduced by not using an isolator.

The output noise for each device was measured as a function of frequency in the case of optimum gain and in the overpumped case. In both cases, the dc bias was chosen to minimize the mixer noise. The calibration technique was described in section 3.5. The output noise was measured under identical conditions (usually during the same experiment) as the conversion efficiency. Then, the mixer noise was calculated by dividing the measured output noise at each frequency by the conversion

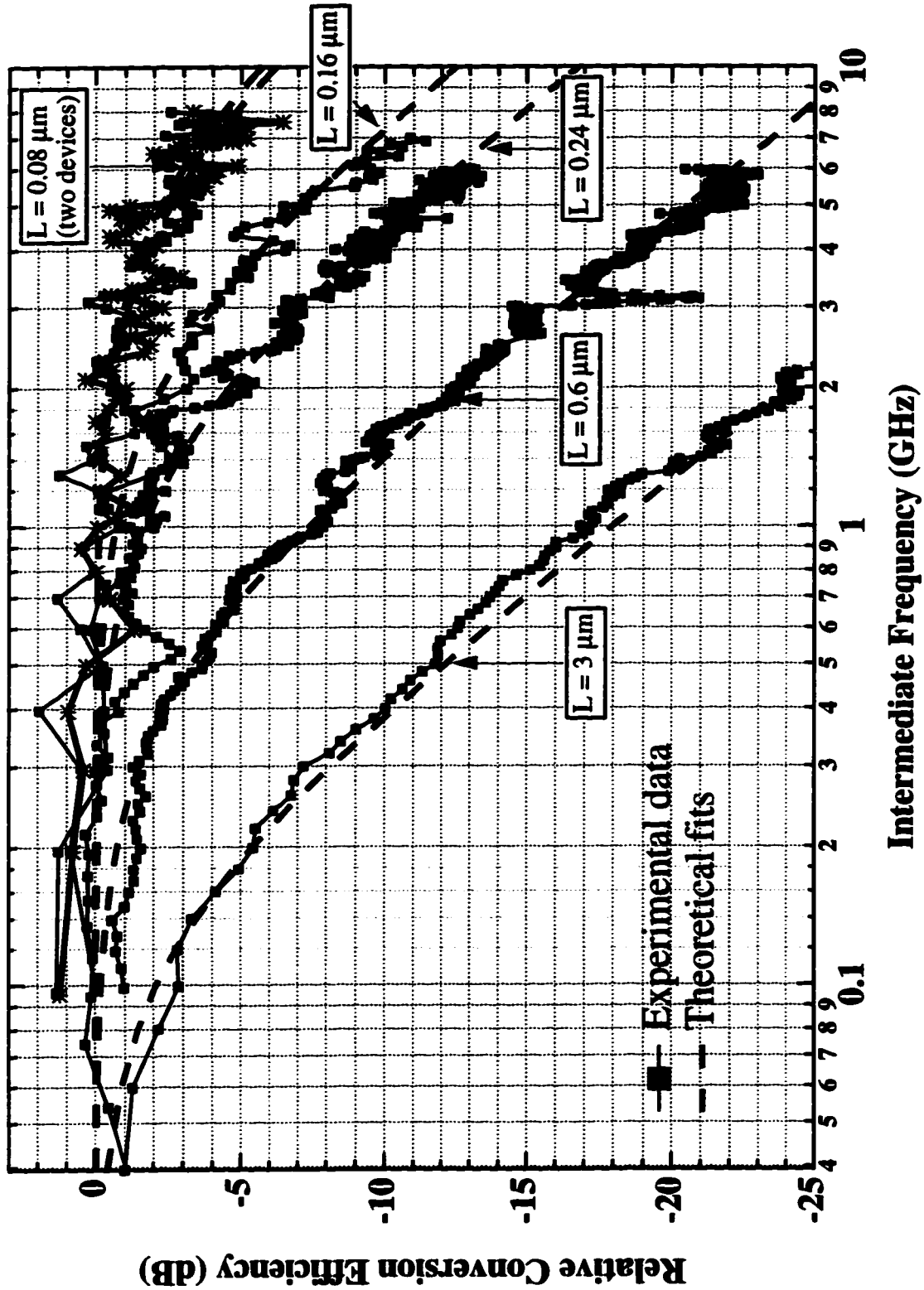

Figure 5.25: Relative conversion efficiency vs. intermediate frequency for devices of different length.

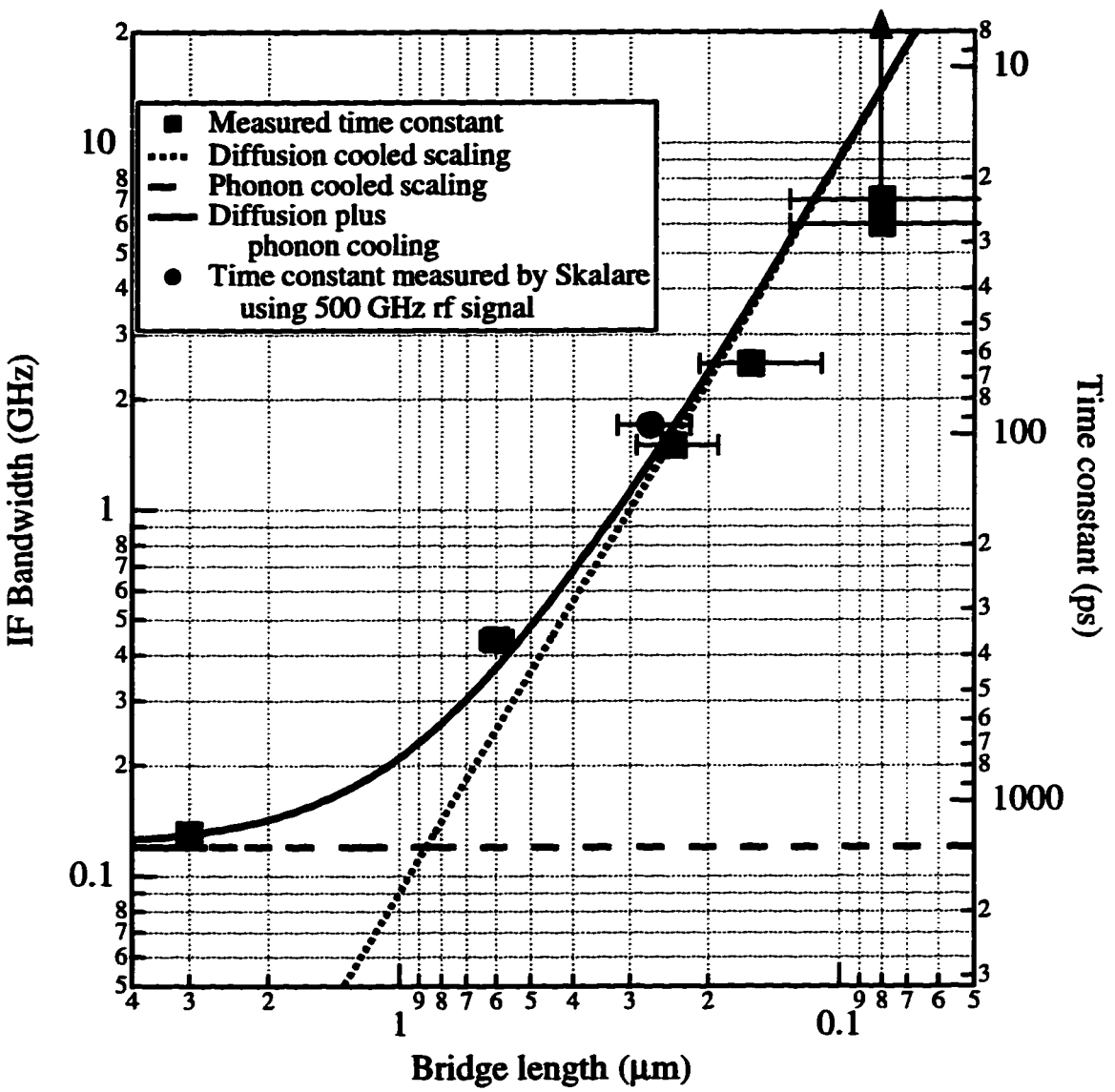

Figure 5.26: Bandwidth vs. device length.

efficiency at that frequency. The results of these measurements are plotted in figures 5.28-5.35. The points for frequencies above 1 GHz are averaged over a 500 MHz bin, and the points for frequencies below 1 GHz are averaged over a 100 MHz bin. Additionally, theoretical fits to the functions

$$T_{out}(\omega_{IF}) = T_{John.} + \frac{T_{T.F.}(0)}{1 + (\omega_{IF}\tau_{effNOISE})^2} \tag{5.1}$$

and

$$T_{mix}(\omega_{IF}) = a + b\omega_{IF}^2 \tag{5.2}$$

are plotted. Note that the 3 dB gain bandwidth (i.e. the frequency at which the gain falls by a factor of 2) is predicted to be $(2\pi\tau_{eff})^{-1}$, and the frequency at which the thermal fluctuation noise component of the output noise falls by a factor of two is predicted to be the *same*, i.e. $(2\pi\tau_{eff})^{-1}$. In order to test this prediction experimentally, both quantities were varied in the fits to the measured conversion efficiency and output noise. The results of these fits are summarized in tables 5.1 and 5.2. The relative spectrum of the output noise behaves similarly with frequency as the conversion efficiency, as can be seen by comparing the fitted time constant for the conversion efficiency and output noise. This implies that the 3 dB noise bandwidth is larger than the 3 dB gain bandwidth, which is also indicated by comparing the two quantities in tables 5.1 and 5.2. The noise bandwidth is larger than the gain bandwidth by a factor of 1.4-9.4. The fitted white component of the output noise should be approximately the electron temperature, which is presumed to be near $T_c \approx 5.5\ K$. However, the fitted value is larger than this, from 8-25 K. For the diffusion cooled devices, it is difficult to determine the white portion accurately, since the frequency-dependent thermal fluctuation noise is a significant component of the total output noise at all frequencies within the measurement band. However, for device E it was possible to measure the output noise at 4.75-7.25 GHz, which is higher than the thermal time constant of $\sim$ 100 MHz for that device. There, the dominant noise should no longer be the thermal fluctuation noise.

In figure 5.36, the output noise (measured with an isolator) from 4.75-7.25 GHz is plotted vs. bias voltage for a bath temperature of 2 K, and a bath temperature of 7 K. For the 7 K data, the device is in the normal state, and the increase in noise with increasing bias voltage is due to the fact that the electron temperature (and hence the Johnson noise) rises with increasing dissipated

dc power. The 2 K data shows very similar behavior with bias voltage, except near the dropback. Near the dropback, the thermal fluctuation noise is evident, but only at the level of about 0.5 K. The other component of the noise is interpreted as Johnson noise, due to the fact that the electrons are hotter than the bath. Therefore, it appears that the high-frequency (i.e. $f \gg \tau_{th}^{-1}$) component is indeed only due to Johnson noise, and not some other noise source.

In figure 5.34, where the output noise for device E is plotted against the intermediate frequency, it is clear that the output noise is still rising below 100 MHz, the lowest frequency measured in that experiment. Therefore, in a separate experiment the noise of device E was measured from 18-25 MHz. (The noise temperature of the first amplifier was 300 K at that frequency.) In figure 5.37, the output noise at 20 MHz is plotted vs. bias voltage. In contrast to the other devices, the output noise depends very sensitively on the bias voltage. The peaks in the output noise correspond in many cases to regions of negative differential resistance on the I-V curve, which is also plotted in figure 5.37. The spectrum of the output noise at bias points near regions of negative differential resistance was not white, indicating that the device may be oscillating in the MHz frequency region. The measured (amplified) noise power, including the amplifier input noise, is plotted vs. frequency in figure 5.38. There, it is clear that the output noise is not white; this behavior was not observed for any of the other devices. Thus, since device E has regions of negative differential resistance on the I-V curve, it tends to oscillate, which can dominate the thermal fluctuation noise at frequencies below τ_{th}^{-1} for that device. The physical mechanism for the negative differential resistance is an open subject for future research.

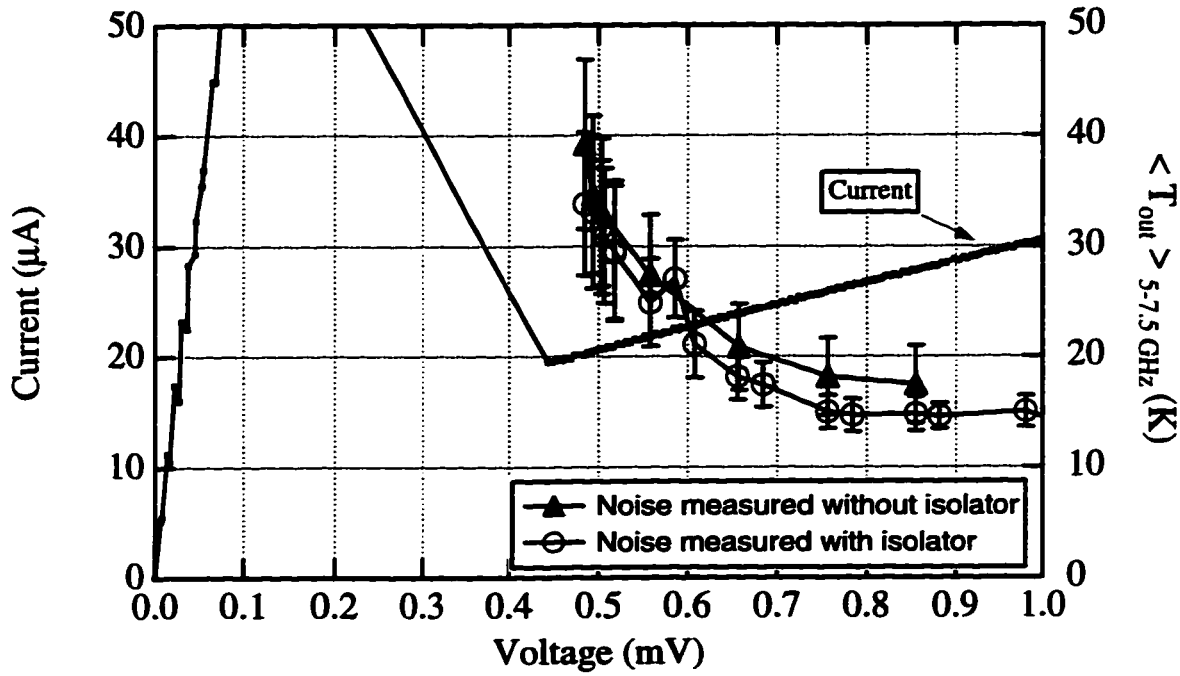

Figure 5.27: Output noise vs. bias voltage for device A1, with and without isolator, in optimum gain case. The error bars are the variances in the output noise across the band.

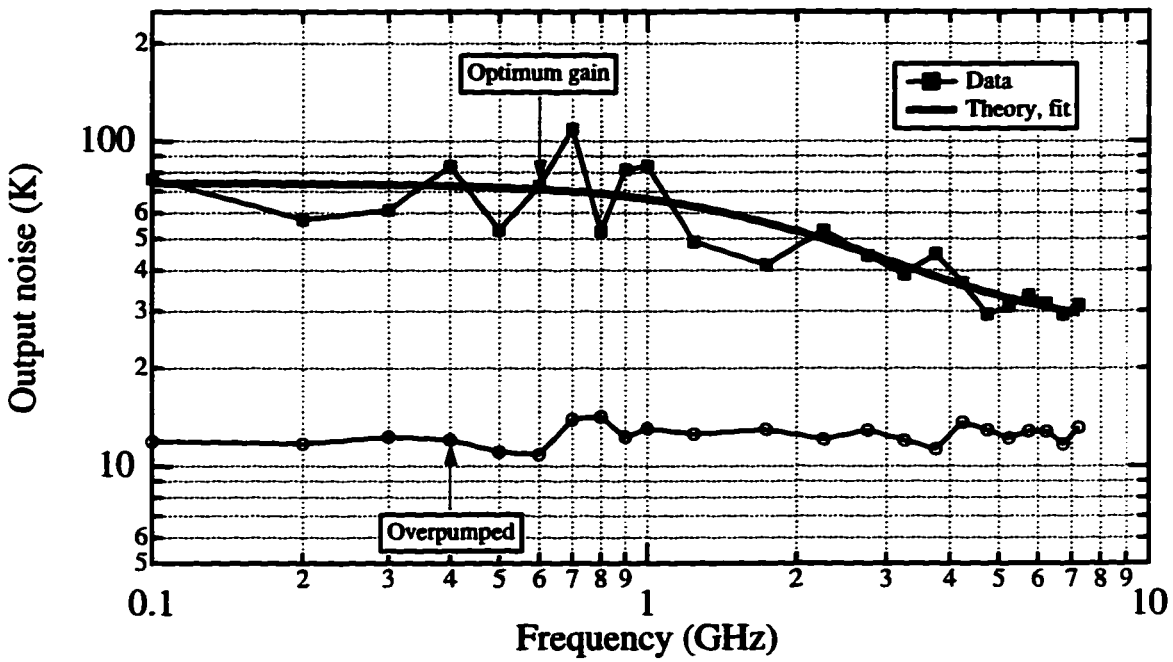

Figure 5.28: Output noise vs. frequency for device A1. In the overpumped case, the output noise was measured at the bias voltage which maximized T_{out}; the conversion efficiency was not measured in the overpumped case.

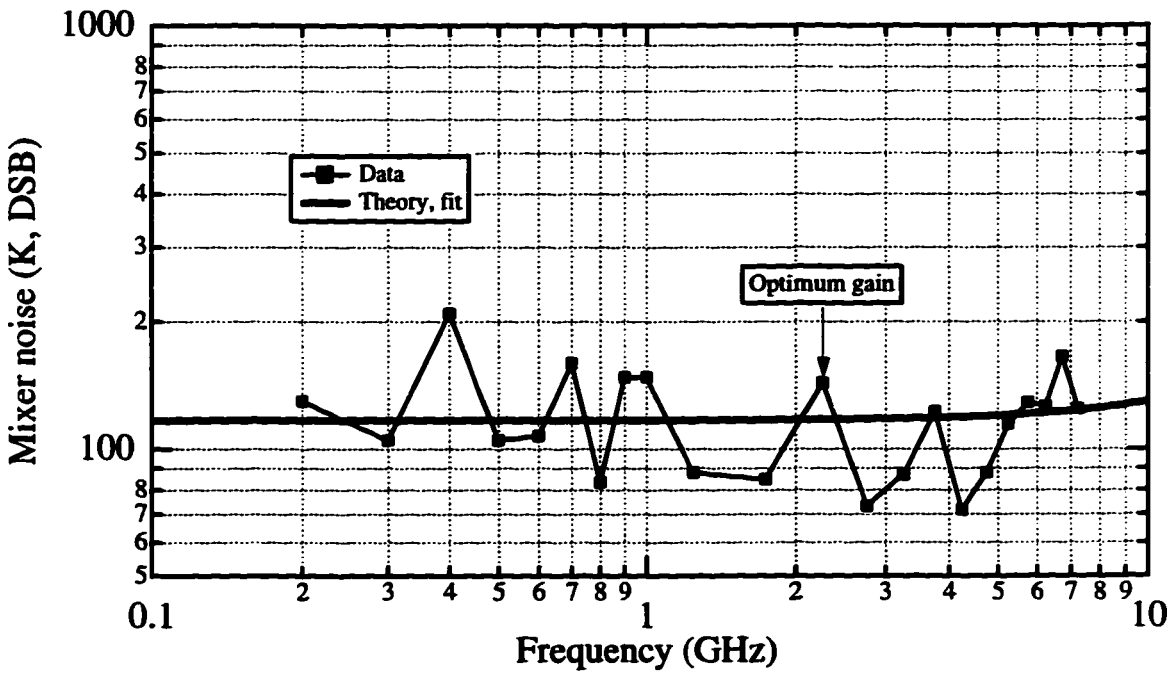

Figure 5.29: Mixer noise vs. frequency for device A1.

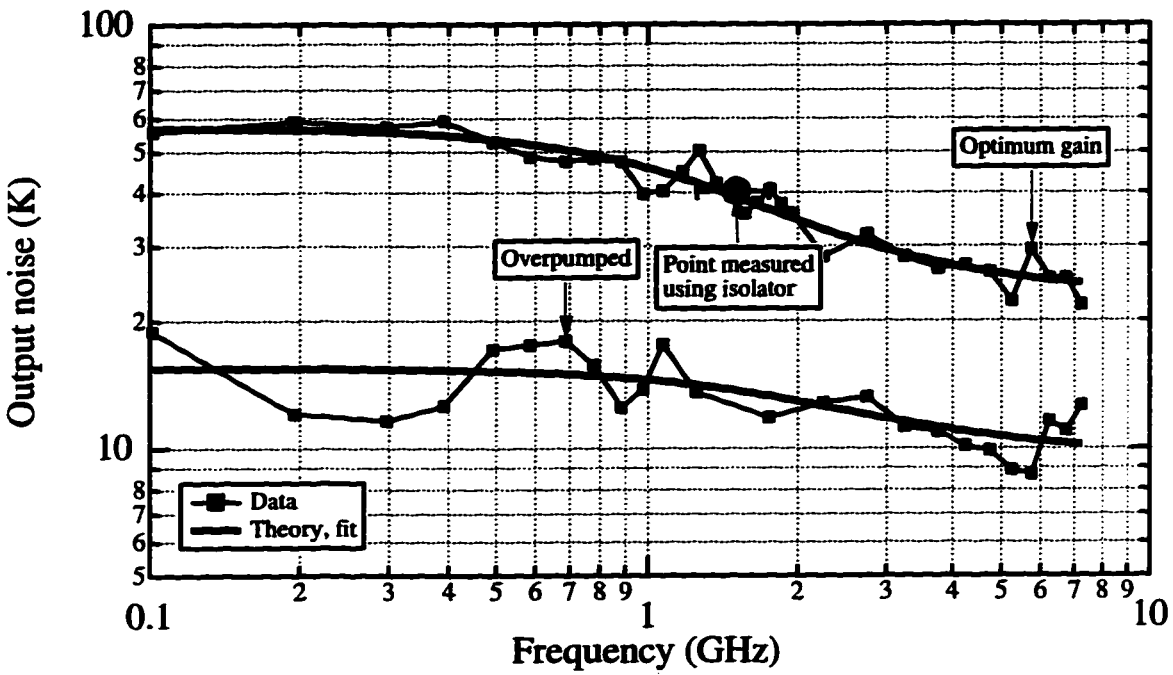

Figure 5.30: Output noise vs. frequency for device B.

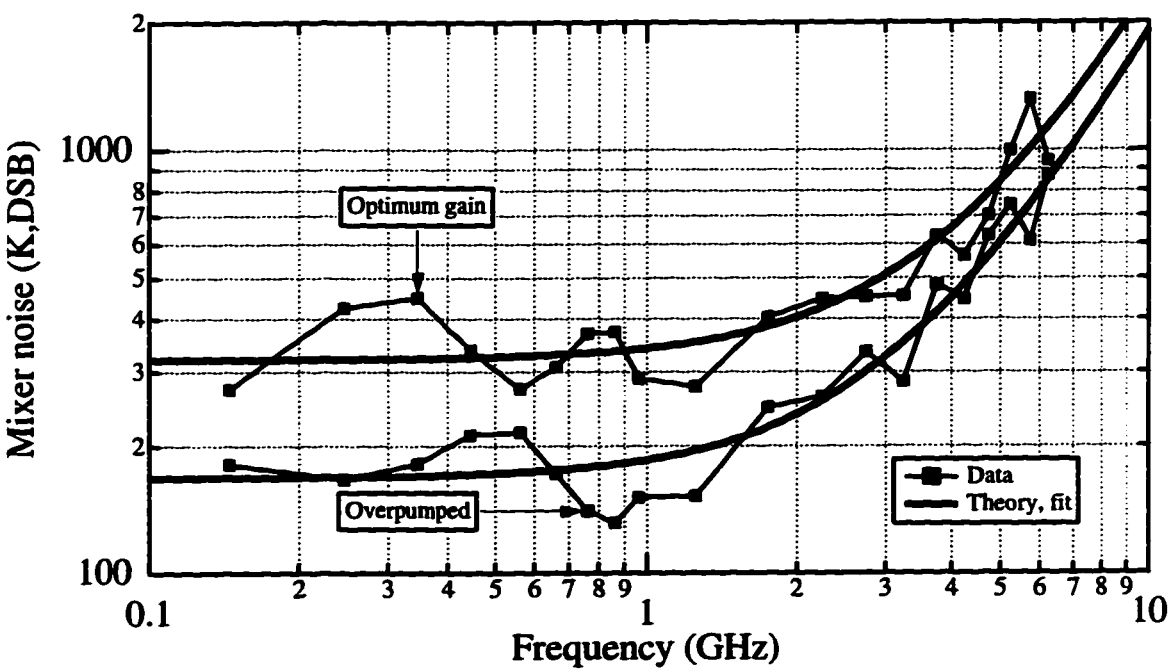

Figure 5.31: Mixer noise vs. frequency for device B.

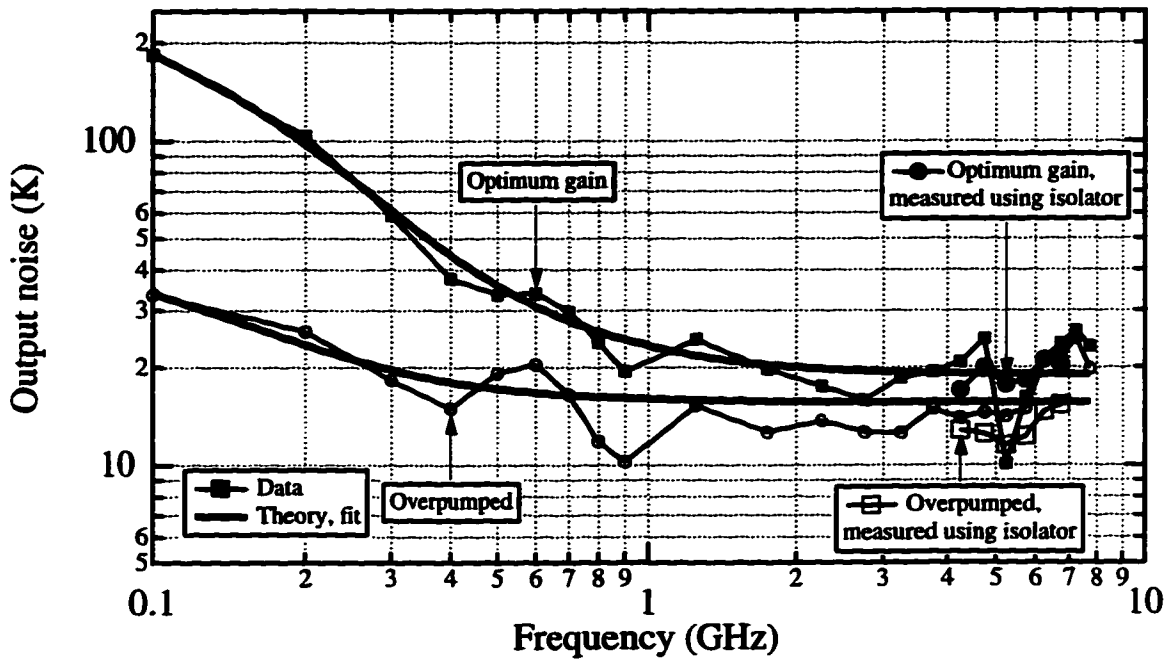

Figure 5.32: Output noise vs. frequency for device D.

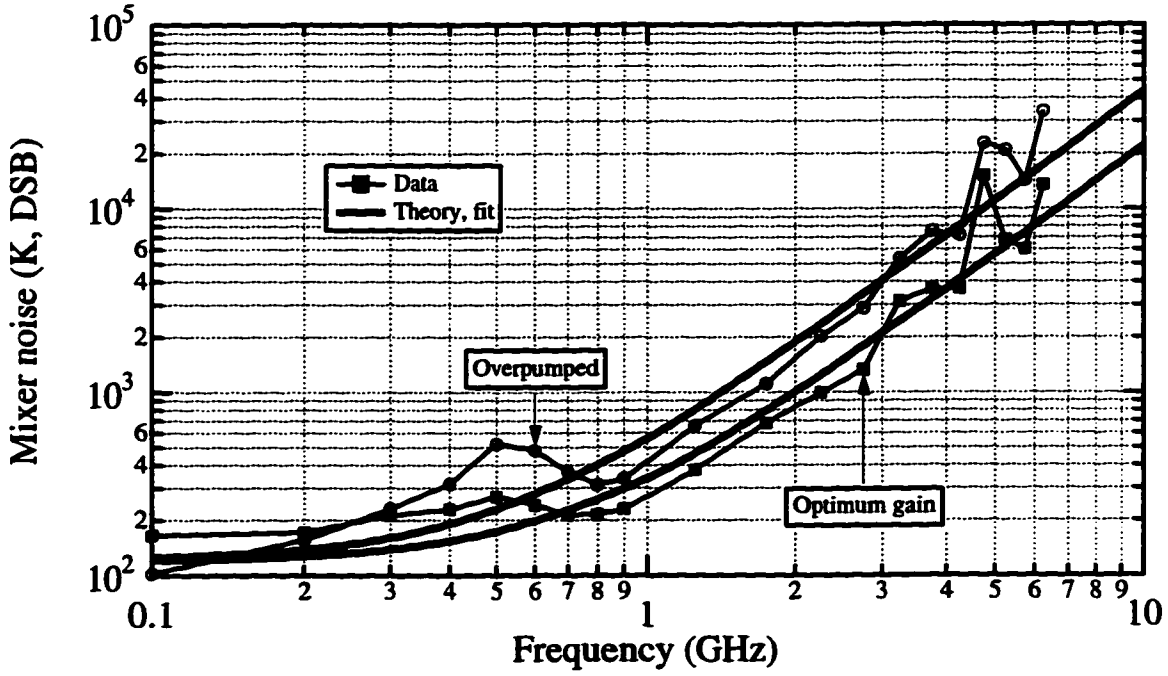

Figure 5.33: Mixer noise vs. frequency for device D.

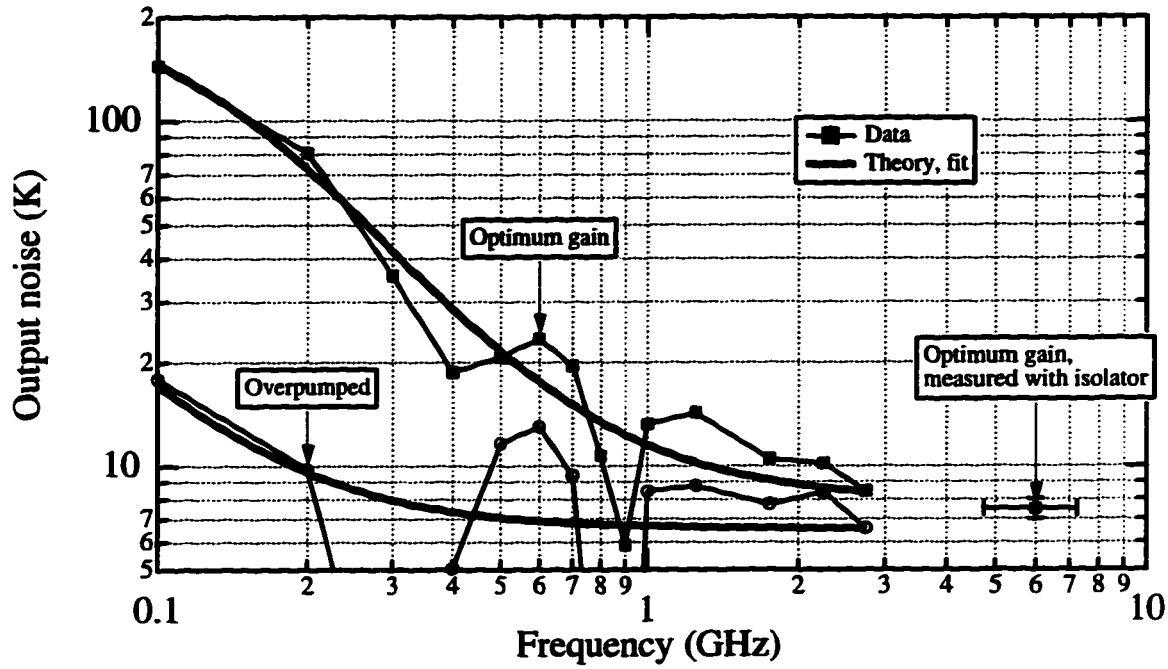

Figure 5.34: Output noise vs. frequency for device E.

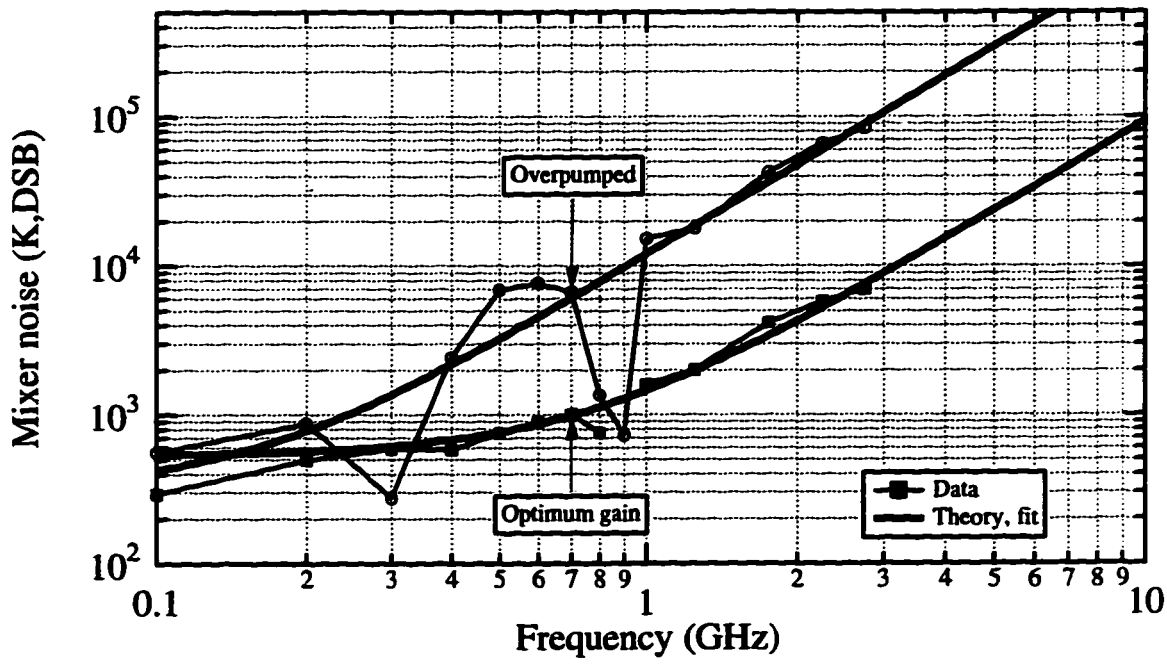

Figure 5.35: Mixer noise vs. frequency for device E.

Device	L (μm)	Gain BW (GHz)	$T_{out}(0)$ (K)	$\eta(0)$ (dB)	$T_{mix}(0)$ (K,DSB)	$\frac{1}{2\pi\tau_{eff NOISE}}$ (GHz)	Noise BW (GHz)	$T_{John.}$ (K)
A1	0.08	>6	49	-5.6	120	2.3	30	25
A2	0.08	>6	-	-	-	-	-	-
B	0.16	2.4	57	-11	320	1.4	3.9	23
C*	0.24	1.5	55	-8	200	-	-	-
D	0.6	0.3	281	-4.1	120	0.13	0.73	19
E	3	0.08	231	-2†	530	0.13	0.75	8

Table 5.1: Fitted gain and noise bandwidths, optimum gain case.
* 1.25-1.75 GHz. The spectrum was not measured for this device.
† The lowest efficiency measured was only -4 dB, but the fit returned a value of -2 dB because the lowest IF measured for this particular experiment was only 100 MHz.

Device	L (μm)	Gain BW (GHz)	$T_{out}(0)$ (K)	$\eta(0)$ (dB)	$T_{mix}(0)$ (K,DSB)	$\frac{1}{2\pi\tau_{eff NOISE}}$ (GHz)	Noise BW (GHz)	$T_{John.}$ (K)
A1	0.08	>6	13	-7	-	-	-	-
A2	0.08	-	-	-	-	-	-	-
B	0.16	2.25	16	-13.5	170	2.3	3.1	10
C*	0.24	1.5	16	-12.7	160	-	-	-
D	0.6	0.38	49	-10.4	120	0.11	0.53	16
E	3	0.064	69	-11.7	310	0.045	0.16	7

Table 5.2: Fitted gain and noise bandwidths, overpumped case.
* 1.25-1.75 GHz. The spectrum was not measured for this device.

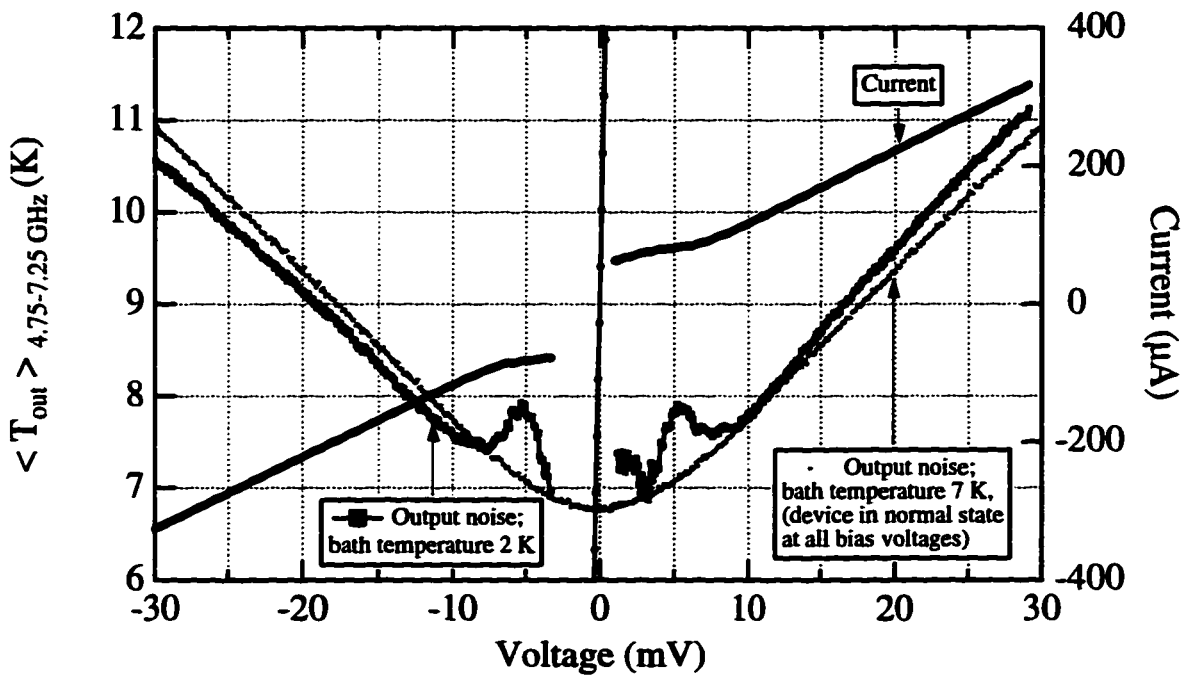

Figure 5.36: Output noise vs. voltage at 6 GHz for device E. (The slight skew of the 2 K data is probably due to drift of the calibrations during the measurement.) The measurements were done with no LO applied, but the application of LO power did not change the results taken at a bath temperature of 2 K by more than 1 K at any bias voltage.

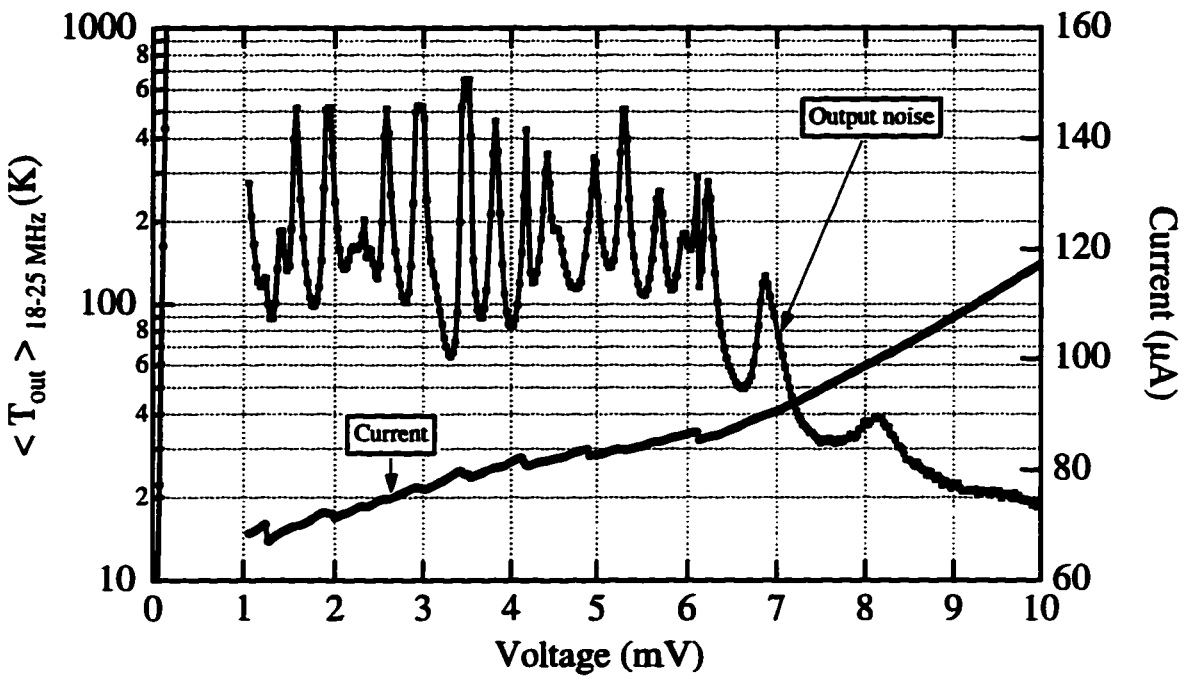

Figure 5.37: Output noise vs. voltage at 20 MHz for device E.

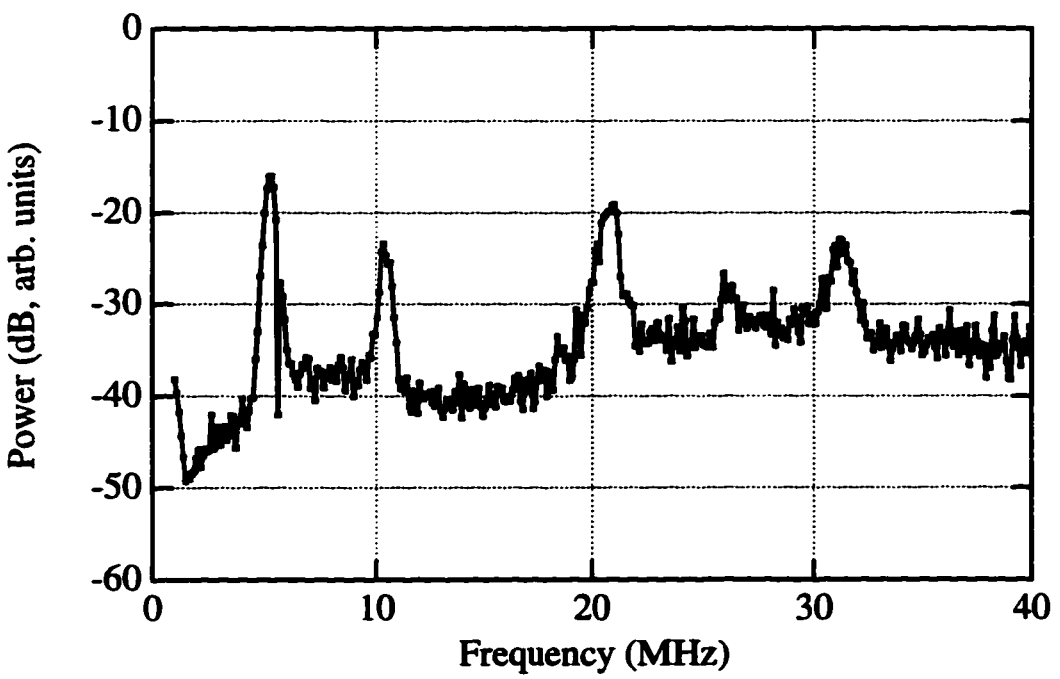

Figure 5.38: Output noise vs. frequency below 40 MHz for device E.

5.1.5 Noise vs. LO frequency

Since the LO frequency was under experimental control, the output noise was measured when the applied LO signal frequency was both above and below $(2\pi\tau_{th})^{-1}$. If the LO signal frequency is higher than $(2\pi\tau_{th})^{-1}$, the electron temperature will not vary with time. Rather, there will be a net increase in the temperature. On the other hand, if the LO signal frequency is lower than $(2\pi\tau_{th})^{-1}$, then the electron temperature may vary with time. The theoretical description of the thermal fluctuation noise in this case has not been developed, but was measured experimentally nonetheless.

The measured output noise at 1.25-1.75 GHz vs. bias voltage is plotted in figure 5.39 in the overpumped case for LO frequencies between 4 and 40 GHz for device A1. (At each LO frequency, just enough LO power was applied to completely suppress the critical current.) It is clear from this figure that the LO power causes an enhancement of the noise for frequencies below $\approx$ 10 GHz, and a suppression of the noise at frequencies above $\approx$ 10 GHz. In order to indicate the dependence of the output noise on the applied signal frequency, we have plotted the output noise (at the dc bias which maximized the output noise) as a function of the applied LO frequency in figure 5.40 for devices A1 and B. For device B, there is no increase in the output noise for LO frequencies above 8 GHz. Note that 8 GHz is already 3 times larger than $(2\pi\tau_{th})^{-1}$ for device B. Therefore, for both devices, the output noise is suppressed when a large signal with frequency higher than $(2\pi\tau_{th})^{-1}$ is applied. Additionally, the noise is dramatically enhanced for device A1 when a large signal with frequency lower than $(2\pi\tau_{th})^{-1}$ is applied.

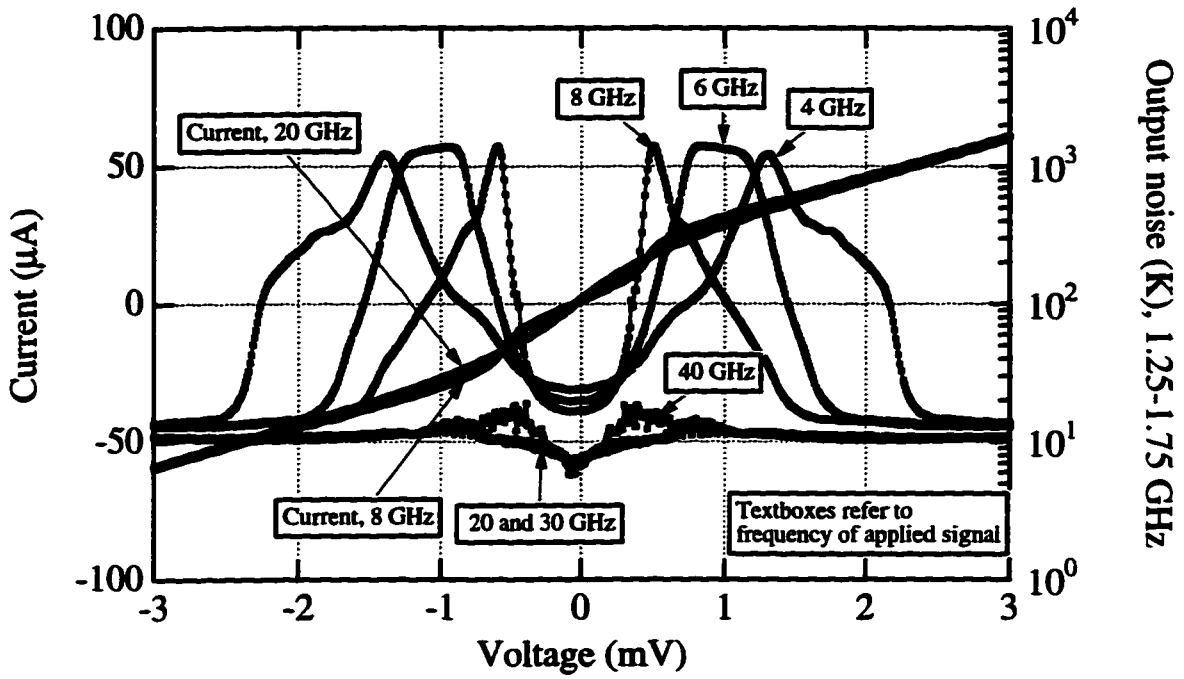

Figure 5.39: Output noise vs. bias voltage for device A1 in the overpumped case, for different LO frequencies.

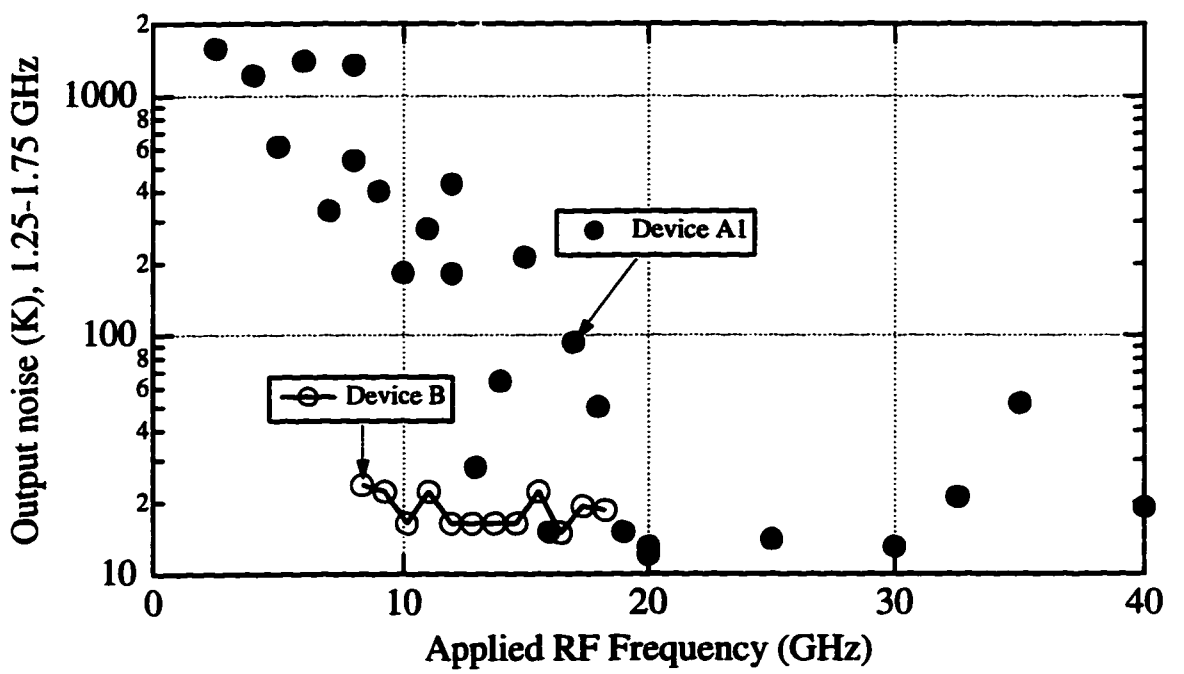

Figure 5.40: Output noise vs. LO frequency for devices A1 and B in overpumped case.

5.2 Device impedance measurements

In this section, the impedance measurements of the device in the mixed state are described. The results of these measurements are important for several reasons. First, the coupling between the device and the amplifier depends on the device impedance. The calibration technique used for the noise measurements are especially sensitive to the device impedance. Second, it is important to test the theoretical prediction for the device impedance discussed in section 5.2, which is the most fundamental aspect of the theory of hot-electron bolometers. Third, impedance measurements of the device in the normal state provide information about the electromagnetic coupling to the device from the 50 Ω system. This should be resonance free if frequency-dependent device parameters are to be studied.

The quantity actually measured in this thesis is the return loss off of the device, i.e. the (power) reflection coefficient of an ac signal propagating down toward the device. The (voltage) reflection coefficient Γ is related to the load impedance of the device terminating a transmission line by the well known formula:

$$\Gamma = \frac{Z_L - Z_0}{Z_L + Z_0}, \tag{5.3}$$

where Z_L is the load (i.e. device) impedance, and Z_0 is the characteristic impedance of the transmission line, which was 50 Ω for the systems used in this thesis work. The return loss, i.e. the ratio of the power incident on the device to the power reflected off of the device, is usually expressed in decibels as:

$$RL = -20\ log|\Gamma|\ (dB). \tag{5.4}$$

In this measurement, a directional coupler (see figure 3.1) allows a weak signal to be propagated down toward the device. When the device is biased in the superconducting state, all of the power is reflected off of the device, coupled into the amplifier, amplified, and then measured on the spectrum or network analyzer. This serves as a reference calibration. The ratio of the amplified and reflected power so measured on the spectrum analyzer when the device is in the intermediate state to the power so measured when the device is in the superconducting state provides a measure of the power reflection coefficient. This technique neglects the imperfections of the coax connectors and the directional coupler, and so is only approximate. An exact calibration would require a more

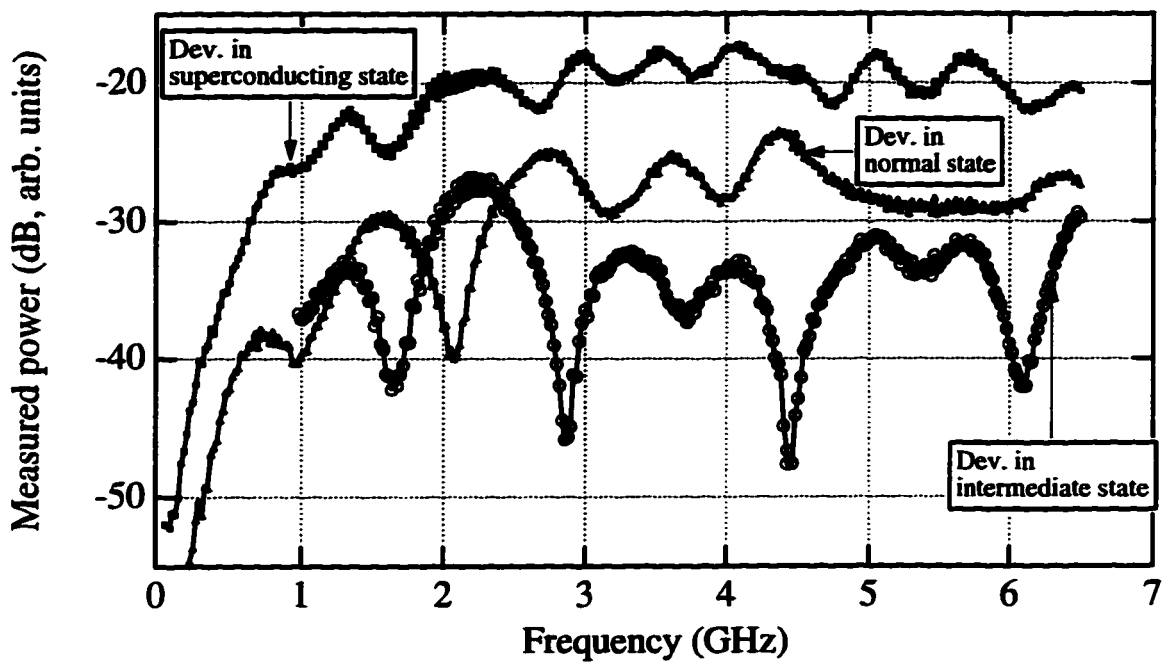

Figure 5.41: Measured reflected power for return loss.

sophisticated treatment of the non-idealities of the system[2]. Additionally, this method was only a *scalar* method, since only the magnitude of the reflection coefficient was measured, and not the phase.

In order to illustrate the technique, the raw measured powers are plotted in figure 5.41, measured using device D. These are the uncorrected data, and the ratio is calculated using these data to determine the return loss. The strong frequency dependence of the data below 1 GHz is a convolution of the strong frequency dependence of the coupling through the directional coupler and the gain of the amplifier chain. This makes the measurements below 1 GHz less accurate than the measurements above 1 GHz.

The results of the return loss measurements are plotted in figures 5.42 - 5.47. The results are plotted both for the device in the normal state, as well as in the intermediate state in the overpumped and optimum gain cases. From these plots, two important conclusions can be drawn.

[2]A *vector* open, short, load calibration treatment was attempted, where the open, short, and load were placed at the end of the 1" section of stainless steel coax, cooled, and measured. The calibration was not reliable since the microwave properties of the system changed on thermal cycling. A more concerted effort would have been needed to solve these and other associated calibration problems.

First, the devices are all well coupled in a broadband, resonance free manner to the 50 Ω system in the normal state. (A 10 dB return loss corresponds to a 90% power coupling of an incoming signal to the device.) This means that the mounting technique used provides a good 50 Ω transmission line system up to the device, without any unwanted parasitic capacitance or inductance. This is important because the main purpose of this thesis is to investigate the frequency dependence of the gain and noise in order to extract information about the underlying physical processes occurring in the device.

The second conclusion is that, with the possible exception of device E, all of the devices were well-coupled to the 50 Ω system when in the intermediate state. (Although the plots are only for one particular dc bias voltage, it was found that the dependence of the return loss on the bias voltage was very weak.) Additionally, these measurements are in accord with the theoretical prediction[3] which states that the device impedance at $f < (2\pi\tau_{th})^{-1}$ should be dV/dI, and at $f > (2\pi\tau_{th})^{-1}$ V_{dc}/I_{dc}. The values of these two parameters and the predicted and measured return loss are summarized in tables 5.3 and 5.4. The values of V_{dc}/I_{dc} and dV/dI fall within the range of 23-100 Ω, which is close enough to 50 Ω according to equation 5.4 to allow power coupling of approximately 90%. Device E had values of V_{dc}/I_{dc} between 10 and 20 Ω, so that the power coupling to the 50 Ω system was only between 50 and 80%, theoretically as well as experimentally. The frequency dependence of this coupling was still smooth enough for the studies carried out in this thesis.

Finally, the coupling to the device at frequencies above $\approx$ 12 GHz was more difficult to measure because the gain of the amplifier used dropped rapidly above that frequency. However, a separate measurement of the return loss off of a 50 Ω chip resistor in a similar mounting configuration at room temperature showed a resonance free coupling better than 90% from 50 MHz to 40 GHz. Although that configuration was slightly different, it seems reasonable to assume that the devices were well coupled to the 50 Ω system up to 40 GHz.

[3]In this section, we neglect the difference between τ_{th} and $\tau_{th}/(1-\alpha_0)$, which is the correct quantity to use for the frequency of interest regarding the device impedance.

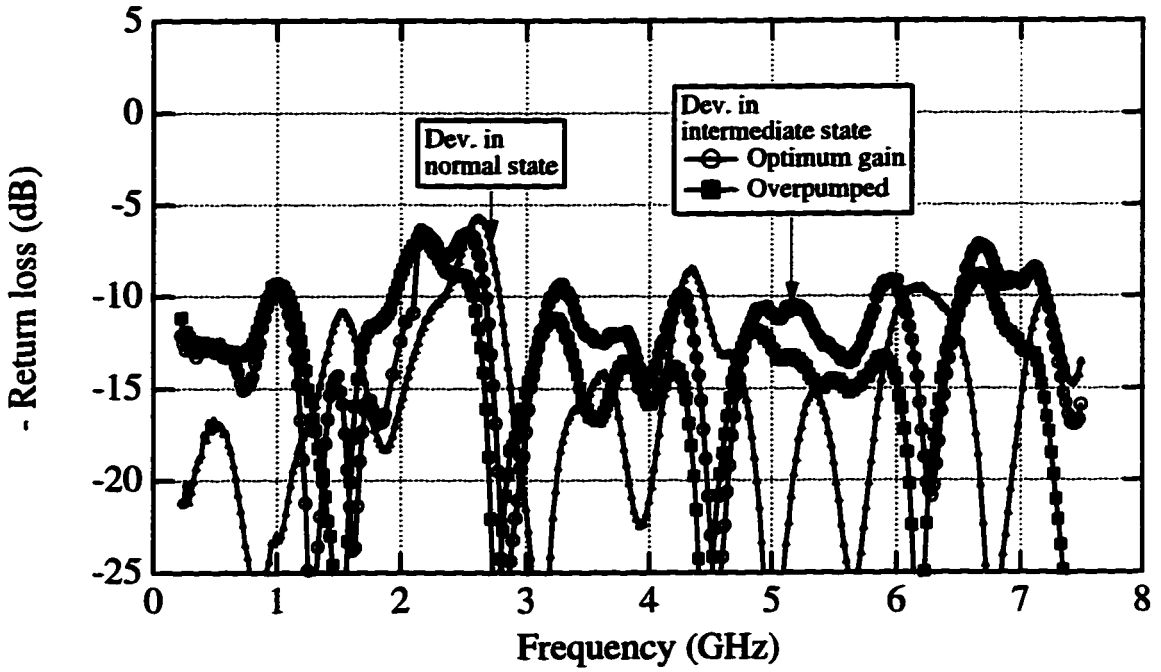

Figure 5.42: Measured return loss for device A1.

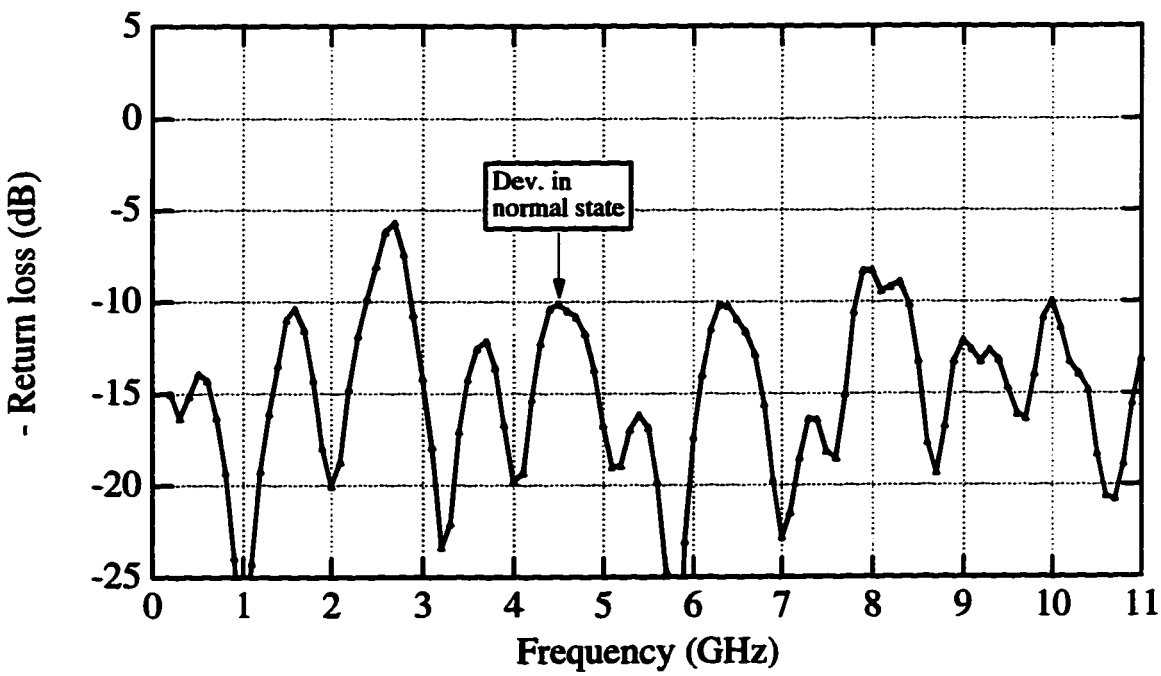

Figure 5.43: Measured return loss for device A2.

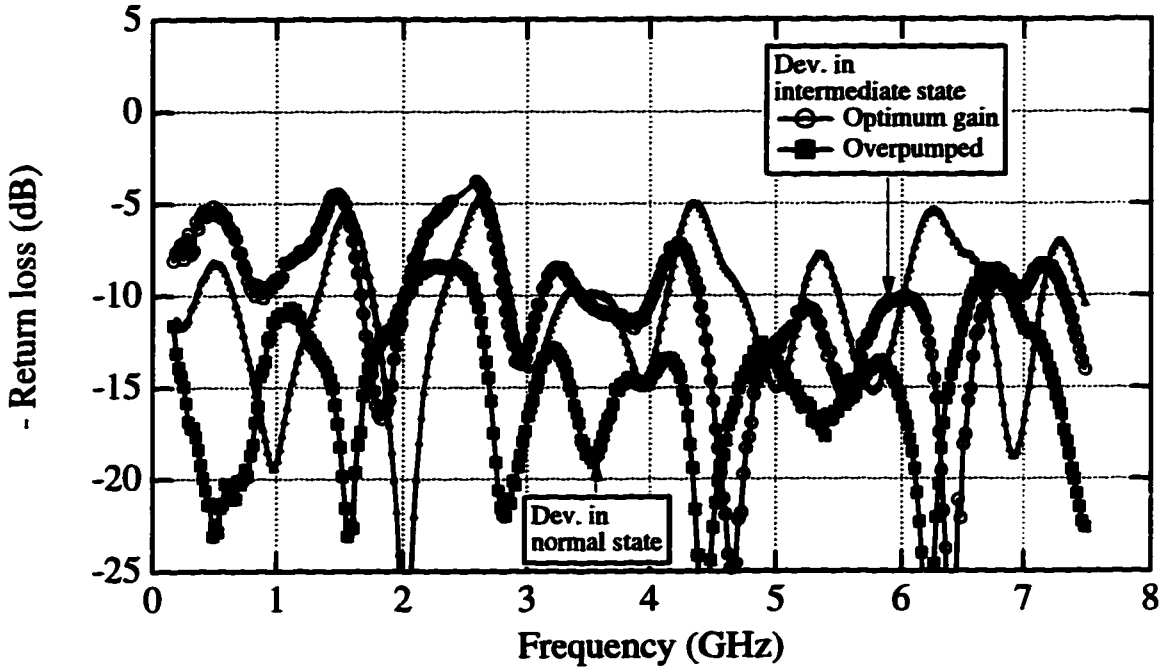

Figure 5.44: Measured return loss for device B.

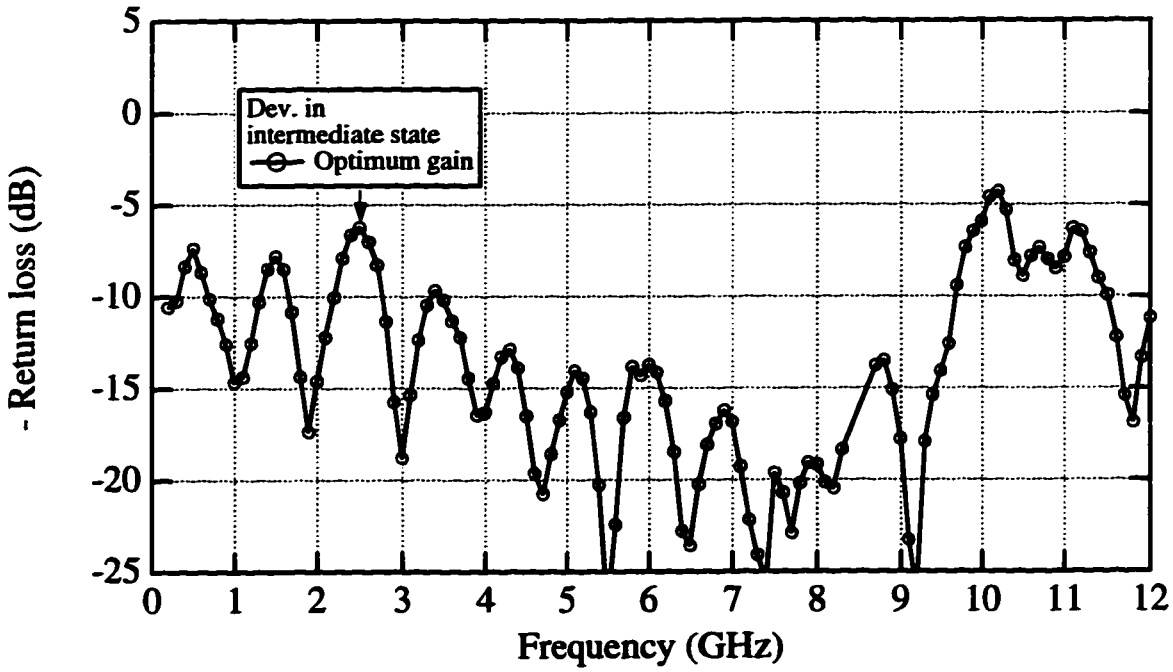

Figure 5.45: Measured return loss for device C.

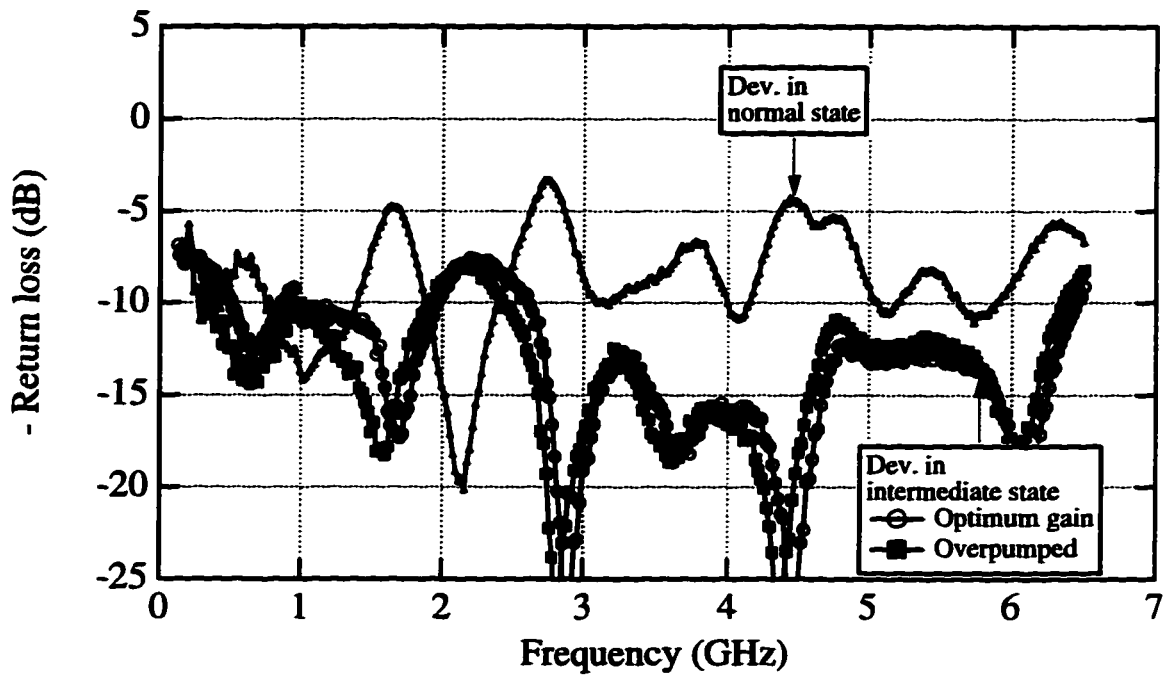

Figure 5.46: Measured return loss for device D.

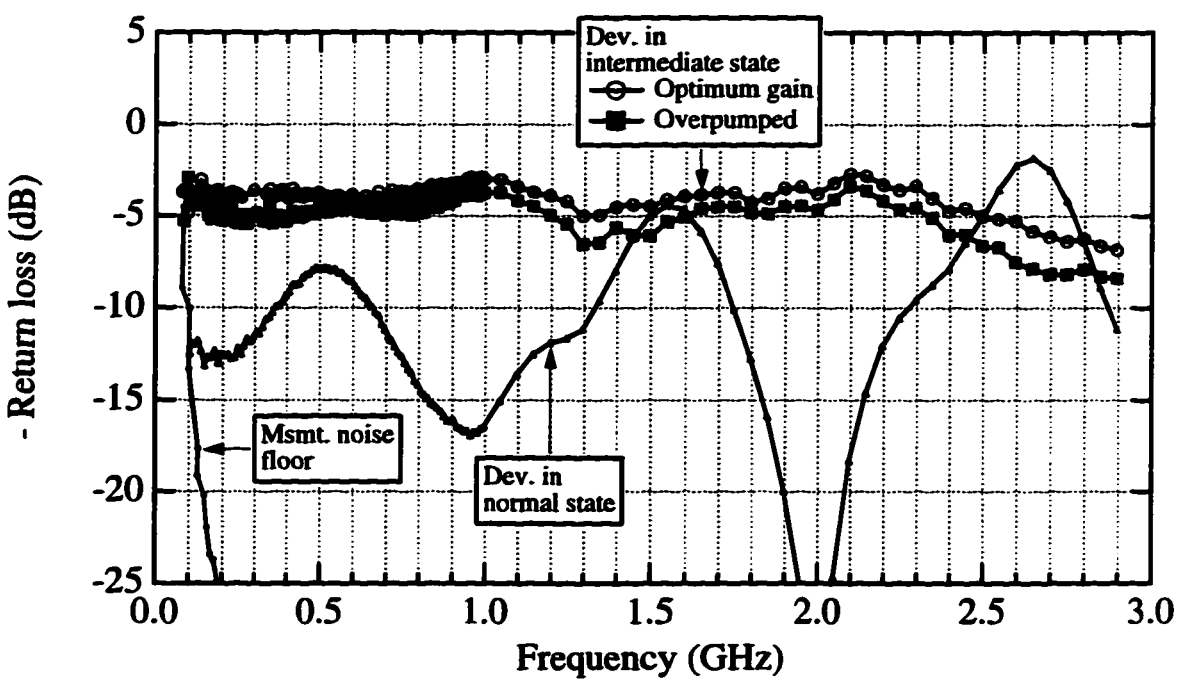

Figure 5.47: Measured return loss for device E.

Device	L (μm)	R_N (Ω)	dV/dI (Ω)	RL theory (dB) $\omega < \tau_{th}^{-1}$	RL expt. (dB) $\omega < \tau_{th}^{-1}$	V_{dc}/I_{dc} (Ω)	RL theory (dB) $\omega > \tau_{th}^{-1}$	RL expt. (dB) $\omega > \tau_{th}^{-1}$
A1	0.08	56	32	13	>10	23	9	>10
B	0.16	80	90	11	>10	28	11	>10
C	0.24	96	100	10	>10	40	19	>10
D	0.6	93	83	12	8	28	11	>10
E	3	86	65	18	-	11	4	4

Table 5.3: Device dc and ac differential impedances in optimum gain case. The return loss for device E could not be measured below $(2\pi\tau_{th})^{-1}$ (100 MHz for that device), and the I-V curve was not smooth, in contrast to the other devices measured.

Device	L (μm)	R_N (Ω)	dV/dI (Ω)	RL theory (dB) $\omega < \tau_{th}^{-1}$	RL expt. (dB) $\omega < \tau_{th}^{-1}$	V_{dc}/I_{dc} (Ω)	RL theory (dB) $\omega > \tau_{th}^{-1}$	RL expt. (dB) $\omega > \tau_{th}^{-1}$
A1	0.08	56	29	12	>10	29	12	>10
B	0.16	80	35	15	>10	28	11	>10
D	0.6	93	38	17	8	28	11	>10
E	3	86	18	7	-	14	5	4

Table 5.4: Device dc and ac differential impedances in overpumped case. The return loss for device E could not be measured below $(2\pi\tau_{th})^{-1}$ (100 MHz for that device), and the I-V curve was not smooth, in contrast to the other devices measured.

5.3 Normal state noise thermometry measurements

In section 5.1, the crossover from cooling behavior dominated by electron-phonon interaction to cooling behavior dominated by out-diffusion was demonstrated by measuring the thermal time constant as a function of device length. However, because of possible complications due to non-equilibrium superconducting and non-uniform heating effects, it is desirable to investigate this cross-over under more well-understood conditions. Additionally, the crossover from phonon dominated to diffusion dominated behavior must be understood if the crossover from dissipative to non-dissipative transport in electronic conductors generally is to be understood. (In addition to the work described in this thesis, the crossover from phonon dominated to diffusion dominated to dissipationless transport has been investigated and discussed in de Jong (1995), Kanskar and Wybourne (1994), Prober et al. (1995), Steinbach et al. (1996), Karasik et al. (1996), and Pothier et al. (1997).)

The experimental setup described in this thesis is well-optimized to measure the noise generated by the devices very quickly and accurately, as long as the device impedance is not different from the device impedance when it is used to do the calibration. The fluctuation-dissipation theorem guarantees that the output noise generated by the device when it is in the normal state and biased at zero voltage is simply $k_B T$ per unit bandwidth, as long as it is well-matched to the input impedance of the amplifier. (The match was shown to be very good in the previous section, where the differential impedance was measured in the normal state.) When the device is in the normal state, an increase in bias voltage does not change the differential impedance significantly, so that the calibrations done under zero bias conditions can be used with impunity. Additionally, since the frequency band is typically 500 MHz, an integration time of only 2 ms can allow a measurement of the output noise with a statistical uncertainty of only 0.1%. Therefore, it is possible to quickly and accurately measure the increase in the electron temperature (averaged over the length of the device) as a function of applied power. The calibration technique described in section 3.5 allows the amplifier contribution to be accurately subtracted off, and the temperature of the device measured using noise-thermometry with an accuracy equal to that of the independent thermometer, which was 50 mK in this case.

The output noise and hence electron temperature was measured as a function of applied dc power at a bath temperature above T_c, at 6 or 6.5 K, for several of the devices used in this thesis. The results of these measurements are plotted for four devices in figure 5.48. We consider first device E, the

longest device. Since the length of this device is much longer than L_{e-ph}, the temperature profile is uniform over most of the length of the bridge, except within L_{e-ph} of the ends. We can safely neglect the end-effect in this case. Plotting the increase in temperature with input power (as is shown in the last graph of figure 5.48) allows determination of the strength and temperature-dependence of the electron-phonon interaction. The power-law of the temperature dependence of the electron-phonon interaction for this device is well-described by equation 2.62, with $A = 2.34\ 10^{10}\ Wm^{-3}K^{-4}$. This value is reasonably consistent with the value of $A = 0.98\ 10^{10}\ Wm^{-3}K^{-4}$ found in Gershenzon et al. (1990) for samples of the same material, thickness, and diffusion constant.

In the first graph in figure 5.48, the electron temperature vs. input dc power is plotted for device A1, together with the analytical prediction of equation 2.45 derived in chapter 2 by neglecting the electron-phonon interaction. Since device A1 is sufficiently shorter than L_{e-ph}, this analytical solution describes the data very well. Additionally, a numerical solution to the diffusion equation was performed in Chalsani (1997) which included the electron-phonon interaction, with strength given by equation 2.62. The results of this simulation are also plotted.[4] The simulation agrees with the analytical solution since the electron-phonon interaction can be safely neglected for this device length.

The electron temperature vs. input dc power is plotted for device B in the second graph of figure 5.48, in addition to results of the numerical simulations and the analytical solution neglecting the electron-phonon interaction. At temperatures below $\approx$ 8 K, the electron-phonon interaction is not significant, and the device is still in the diffusion-cooled regime. This is evident because the numerical simulation which includes the electron-phonon interaction agrees with the analytical solution which neglects the electron-phonon interaction, and both agree with the data. Above 8 K, the simulations and data deviate from the analytical solution, indicating that the electron-phonon interaction is becoming important. The crossover from diffusion dominated to the intermediate behavior where the electron-phonon interaction is significant can occur in the same device because the electron-phonon length L_{e-ph} varies with temperature. As was discussed in section 2.3, it is the ratio of the device length L to L_{e-ph} which determines the relative importance of diffusion

[4]The Lorenz number was varied in Chalsani (1997) for the simulations and analytical solutions plotted in figure 5.48 in order to obtain the agreement shown. The free electron value of $\mathcal{L} = 2.45\ 10^{-8}\ W\Omega K^{-2}$ was adjusted to $3.3\ 10^{-8}\ W\Omega K^{-2}$, which is acceptable since experimentally determined values of $\mathcal{L}$ generally depend on temperature and material.

and the electron-phonon interaction. The electron temperature vs. input dc power is plotted for device D in the third graph of figure 5.48, as well as results of the numerical simulations and the analytical solution neglecting the electron-phonon interaction. For this device, the analytical solution neglecting the electron-phonon interaction is not valid at any temperature, so that the device is not in the diffusion-cooled regime at any temperature. Diffusion still contributes significantly to the cooling, and it is not until device E that the diffusion can be neglected altogether.

Thus, the crossover from diffusion-cooled to phonon-cooled behavior has been demonstrated in two ways using noise thermometry, in addition to the crossover demonstrated in section 5.1 by measuring the thermal time constant. At a fixed temperature of 6 K, varying the device length changes the behavior from phonon to diffusion-cooled. For fixed device length, varying the temperature changes L_{e-ph}, which changes the relative importance of diffusion and the electron-phonon interaction within the same device in a clearly measurable way. Numerical simulations which include both the effects of diffusion and the electron-phonon interaction agree with all the data by adjusting only two parameters, the Lorenz number and the electron-phonon coupling constant.

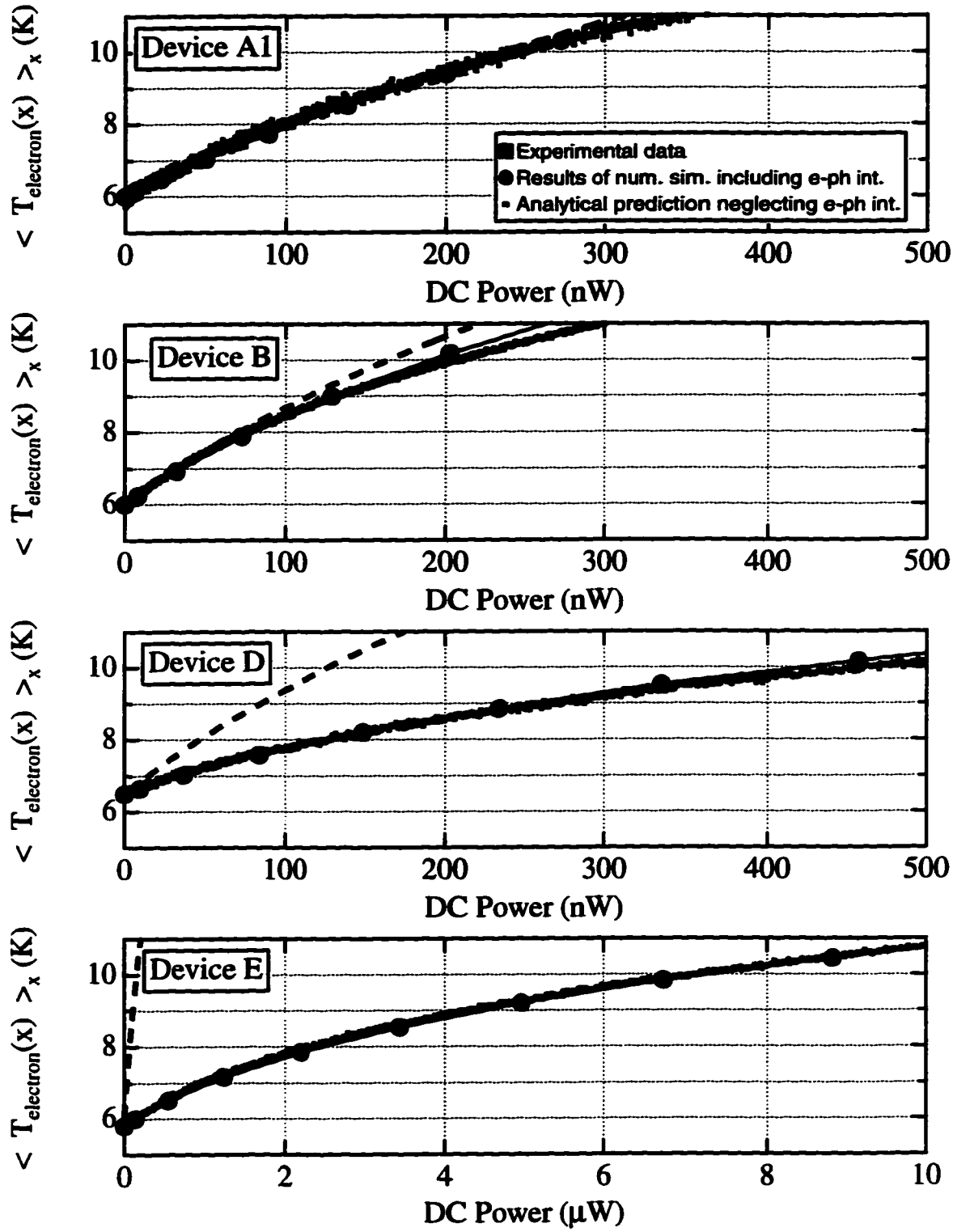

Figure 5.48: Measured electron temperature vs. dc power using noise thermometry. Note the change in units on the abscissa for device E.

5.4 Comparison with theory

In this section, we compare the measured results of the *coupled* output noise and *coupled* conversion efficiency with the theoretical predictions presented in chapter 2. (Later in this section, the difference between the coupled and available conversion efficiency and noise is calculated to be small, typically less than 10%.) There, a simple lumped-element thermal model was developed which neglected the effect of the non-uniform temperature profile and non-uniform dissipation of power. This simple model allows a prediction of the output noise and conversion efficiency in terms of the electron temperature, the device resistance, the thermal conductance from the electrons to the bath, the dc current, the LO power, and slope of the R vs. T curve, i.e. dR/dT_e. It is possible to measure or estimate all of the above parameters except dR/dT_e under the operating conditions.

If the electron temperature could be accurately determined, then the instantaneous value of dR/dT_e (which depends strongly on the electron temperature near T_c) could be determined. However, there is no clear way to accurately determine the electron temperature, which makes comparison of theory and experiment difficult. Both the conversion efficiency and the output noise increase as the square of dR/dT_e, so that an upper limit on both of these parameters can be calculated based on the maximum value of dR/dT_e. There are two possible solutions to determining dR/dT_e, and both depend on the assumption that the I-V curve is determined entirely by the heating process.

The physical model is the following. DC (and possibly ac) power heats the electrons above the bath temperature. This causes the resistance to fall somewhere between zero and R_n, depending on the value of the electron temperature. Here "resistance" is interpreted as V_{dc}/I_{dc}. The differential resistance will be different from V_{dc}/I_{dc} since increasing the current or voltage increases the power dissipated, which in turn increases the temperature, which in turn increases the resistance, which in turn changes V_{dc}/I_{dc}. A temperature well above T_c would cause the resistance to be equal to R_n. A temperature in the middle of the transition would cause a resistance of approximately 1/2 R_n, and so forth. Since the R vs. T curve can be (and was) measured under conditions of negligible self-heating, by measuring the resistance, one can determine the electron temperature, and hence the instantaneous value of dR/dT_e.

The predicted conversion efficiency and output noise based on equations 2.13 and 2.28 was calculated for each device by using the maximum value of dR/dT_e, as well as the value of dR/dT_e

determined using the method described above[5]. This method was carried out for the dc bias voltage used which minimized the mixer noise in both the overpumped and optimum gain cases. The parameters for the theoretical calculations are shown in tables 5.5 and 5.6. The results of the calculated conversion efficiency based on this method and equations 2.13 and 2.28 are presented in tables 5.7 - 5.8. When the maximum value of dR/dT_e is used, the conversion efficiency is overpredicted by 6 - 13 dB in all cases. The output noise is also overpredicted by a factor of at least 3-19 for all cases. (The measured noise also includes a component of the Johnson noise.) When the value of dR/dT_e is estimated by inferring the electron temperature from V_{dc}/I_{dc}, the predicted conversion efficiency and output noise is lower than that predicted when the maximum value of dR/dT_e is used. For the conversion efficiency calculated in this way, the predicted conversion efficiency is still 7-13 dB higher than that measured, with the exception of device A1 in the optimum gain case, where the agreement is very good. The output noise estimated using the local value of dR/dT_e is also still overestimated by a factor of 1.5-8, again with the exception of device A1 in the optimum gain case, where the agreement is very good. Thus, while using the local value of dR/dT_e to estimate the output noise and efficiency improves the agreement, the theory still overpredicts both quantities by a large factor.

There is a second way to estimate the local value of dR/dT_e, which also could be expected to include the effects of the non-uniform temperature profile. The method requires only a measurement of the differential resistance at low frequencies (which can be calculated from the measured I-V curve), and a measurement of the dc current and voltage. An increase in bias voltage increases the power dissipated, hence the electron temperature, hence the resistance. The quantity $\alpha_0 \equiv \frac{I_{dc}^2 dR/dT_e}{G}$ can thus be measured. In section 2.6, the prediction for the conversion efficiency and output noise was expressed in terms of α_0, the electron temperature, the thermal conductance, and the dc and LO power. Therefore, the prediction of the conversion efficiency and output noise can be done using a value of dR/dT_e effectively determined directly from the measured I-V curve. This procedure has the additional advantage that the dc bias dependence of the gain and noise can also be related to the I-V curve, since α_0 can be calculated at each bias point. This procedure has been carried out, and the resultant theoretical predictions for the gain and noise are compared to the experimental

[5]The mismatch factor η_{IF} has been calculated assuming an IF amplifier load impedance of 50 Ω. For all devices measured, it varies from 0.87 to 1, with the exception of device E, where it varies from 0.58 to 0.68.

results for all five devices measured in the optimum gain and overpumped cases in figures 5.49 - 5.68. Since the predictions depend on the calculated values of α and α_0, these are also plotted with the I-V curves for each device in the appendix.

For the optimum gain case, the efficiency and output noise due to thermal fluctuations are predicted to increase monotonically as the dropback region is approached, which is in agreement with the experimental data. This is intuitively plausible for the following reason: at high bias voltages, the electron temperature is much higher than T_c, so that the local value of dR/dT_e is expected to be low, and hence the conversion efficiency and output noise due to thermal fluctuations also. As the bias voltage is reduced, the electron temperature gets closer and closer to T_c, where dR/dT_e is large. There, the conversion efficiency and output noise due to thermal fluctuations are expected to be larger. Therefore, the qualitative agreement is good, but the quantitative agreement is poor. For device A1, the qualitative agreement is not good, either.

In the overpumped case, there is also qualitative agreement with the voltage dependence of the conversion efficiency and output noise. At zero voltage, the resistance is low but non-zero. This is due to the fact that the LO power has heated the electrons up close to T_c, but not above it. As dc power is applied, the electrons get closer to T_c, thus increasing the resistance. When the electrons get close to T_c, the local value of dR/dT_e increases, causing the conversion efficiency and output noise due to thermal fluctuations to increase. As more dc power is applied, the electrons get heated well above T_c, causing the local value of dR/dT_e to decrease, and hence the conversion efficiency and output noise due to thermal fluctuations to decrease. Thus, there is a voltage at which the conversion efficiency and output noise due to thermal fluctuations are maximized, and this is predicted theoretically as well as observed experimentally. In the overpumped case, there is again qualitative agreement between the theory and experiment, but the quantitative agreement is only marginal.

The theory presented in chapter 2, to which we have been comparing the experimental data, is a simplified phenomenological model of a more complicated physical system. It treats the application of ac and dc power as equivalent, and it treats the system as a lumped-element, neglecting any spatial distribution of energy and temperature. Additionally, the physical mechanism of the resistance vs. temperature curve is not included in the theoretical description. A full theoretical explanation for the

broadened transition width has not yet been developed. An understanding of physical mechanisms that cause the finite width of the superconducting transition would need to be developed before a more complete theory of device performance could be achieved. Then, a proper treatment of the problem would need to include the non-equilibrium superconducting dynamics of the system, with the inclusion of the spatial dependence of the local energy distribution function, and the implications of this for the dc and ac voltages developed at the intermediate, rf and LO frequencies, as well as the response to such voltages being applied.

The approach taken for the research described in this thesis has been to measure the conversion efficiency and output noise, and its dependence on the intermediate frequency, dc and LO powers, and device length. The absolute value of the conversion efficiency and noise are not quantitatively predicted by the model presented in chapter 2, where a local temperature is defined and assumed to determined the resistance. This clearly motivates the need for experimental work to test theoretical assumptions. In contrast, the frequency dependence of the output noise and conversion efficiency *do* agree with the theory presented in chapter 2, in addition to the length-dependence of the relevant thermal time constant. The *mixer noise* is actually low, and therefore the diffusion-cooled hot-electron bolometer is an excellent device for use in ultra-sensitive THz receivers.

Dev.	V_{dc}/I_{dc} (Ω)	I_{dc} (μA)	V_{dc} (mV)	P_{dc} (nW)	P_{LO} (nW)	dR/dT_e (Ω/K) loc./max.	G* (nW/K) Exp.(thy.)	$\alpha_0^\dagger$	$\alpha^\dagger$	$\eta_{IF}^\ddagger$
A1	22	20	0.45	9	13	68/140	40 (29)	0.16	0.06	0.86
B	22	15.7	0.35	5.5	5	135/200	30(20)	0.56	0.22	0.85
C	32	14.1	0.46	6.4	8	144/250	-(17)	0.41	0.086	0.95
D	24	15.2	0.38	5.6	15	-/250°	44(-)††	0.66	0.24	0.87
E	11	60	0.65	39	85	-/250°	520(-)†††	0.71	0.46	0.58

Table 5.5: Device parameters in optimum gain case.
† Determined from measured I-V curve using equations 2.15 and 2.69.
‡ Calculated from equation 2.16.
* Measured value at 6 K or 6.5 K extrapolated to 5.5 K. (Theoretical value calculated using R_N and equations 2.47.) See section 5.3 for the method of determining G experimentally.
° Not actually measured. Estimated based on device C, which has the same normal state resistance as devices D,E.
†† Expt. value @ 6.5 K was 65 nW/K. 20.5 nW/K was due to diffusion cooling and scaled linearly in temperature to 5.5 K. The remaining 44.5 nW/K was due to diffusion cooling and scaled as T^3 to 5.5 K. The resultant net thermal conductance at 5.5 K is thus estimated to be 44 nW/K.
††† Expt. value @ 6 K was 675 nW/K. This was scaled as T^3 to 5.5 K in order to estimate the value at T_c, resulting in 520 nW/K.

Dev.	V_{dc}/I_{dc} (Ω)	I_{dc} (μA)	V_{dc} (mV)	P_{dc} (nW)	P_{LO} (nW)	dR/dT_e (Ω/K) loc./max.	G* (nW/K) Exp.(thy.)	$\alpha_0^\dagger$	$\alpha^\dagger$	$\eta_{IF}^\ddagger$
A1	28	18.1	0.5	9	26	103/140	40 (29)	-0.025	-0.007	0.92
B	28	9.1	0.25	2.3	10	163/200	30(20)	0.095	0.028	0.92
C	37	10.5	0.4	4.3	16	164/250	-(17)	0.15	0.021	0.98
D	28	8.2	0.23	1.9	30	-/250°	48(-)††	0.13	0.037	0.92
E	14	14.4	0.2	2.9	170	-/250°	520(-)†††	0.13	0.076	0.68

Table 5.6: Device parameters in overpumped case.

† Determined from measured I-V curve using equations 2.15 and 2.69.

‡ Calculated from equation 2.16.

* Measured value at 6 K or 6.5 K extrapolated to 5.5 K. (Theoretical value calculated using R_N and equations 2.47.) See section 5.3 for the method of determining G experimentally.

° Not actually measured. Estimated based on device C, which has the same normal state resistance as devices D,E.

†† Expt. value @ 6.5 K was 65 nW/K. 20.5 nW/K was due to diffusion cooling and scaled linearly in temperature to 5.5 K. The remaining 44.5 nW/K was due to diffusion cooling and scaled as T^3 to 5.5 K. The resultant net thermal conductance at 5.5 K is thus estimated to be 44 nW/K.

††† Expt. value @ 6 K was 675 nW/K. This was scaled as T^3 to 5.5 K in order to estimate the value at T_c, resulting in 520 nW/K.

Device	η (dB) calc. from eq. 2.13 max./local dR/dT used	η (dB) calc. from eq. 2.70	η (dB) expt.	$T_{T.F.}$ (K) calc. from eq. 2.29 max./local dR/dT used	$T_{T.F.}$ (K) calc. from eq. 2.71	T_{out} (K) expt. (incl. $T_{John.}$)
A1*	+1.0/-5.3	-17.5	-5.6	232/55	3.5	37
B	+0.2/-3.2	-7	-11	384/175	73	51
C**	+0.7/+0.2	-9.4	-9.9	656/218	15	44
D	+0.3/-	-0.5	-5.4	360/-	174	118
E	+0.3/-	0.0	-8.6	690/-	404	105

Table 5.7: Predicted and experimental conversion efficiency and output noise in optimum gain case. The measured quantities are for IF=125-215 MHz. Theoretical predictions are for IF=0. This is only a significant difference for devices D,E. Efficiencies are SSB. No electro-thermal feedback correction was applied for calculations of efficiency and noise using eqs. 2.13 and 2.29, respectively. For devices C and D, the bias voltage used was not exactly where η was maximized in order to allow dV/dI to be calculated.

* I-V was pumped with 18 GHz LO; T_{out} quoted for 18 GHz LO. η was measured relative with 18 GHz LO and normalized to measured value with 20 GHz LO.

** 1.25-1.75 GHz. Spectrum not measured.

Device	η (dB) calc. from eq. 2.13 max./local dR/dT used	η (dB) calc. from eq. 2.70	η (dB) expt.	$T_{T.F.}$ (K) calc. from eq. 2.29 max./local dR/dT used	$T_{T.F.}$ (K) calc. from eq. 2.71	T_{out} (K) expt. (incl. $T_{John.}$)
A1*	+2.3/0.0	-31	-7	160/86	0.1	14
B	-2.2/-4.0	-17.2	-13.5	110/73	3.5	14
C**	+0.7/+0.2	-13.8	-12.7	325/140	2.6	17
D	0.0/-	-8.8	-10.4	87/-	12	26
E	-7.0/-	-3.7	-20	37/-	78	10

Table 5.8: Predicted and experimental conversion efficiency and output noise in overpumped case. The measured quantities are for IF=125-215 MHz. Theoretical predictions are for IF=0. This is only a significant difference for devices D,E. Efficiencies are SSB. No electro-thermal feedback correction was applied for calculations of efficiency and noise using eqs. 2.13 and 2.29, respectively.

* I-V was pumped with 18 GHz LO; T_{out} quoted for 18 GHz LO. η was measured relative with 18 GHz LO and normalized to measured value with 20 GHz LO.

** 1.25-1.75 GHz. Spectrum not measured.

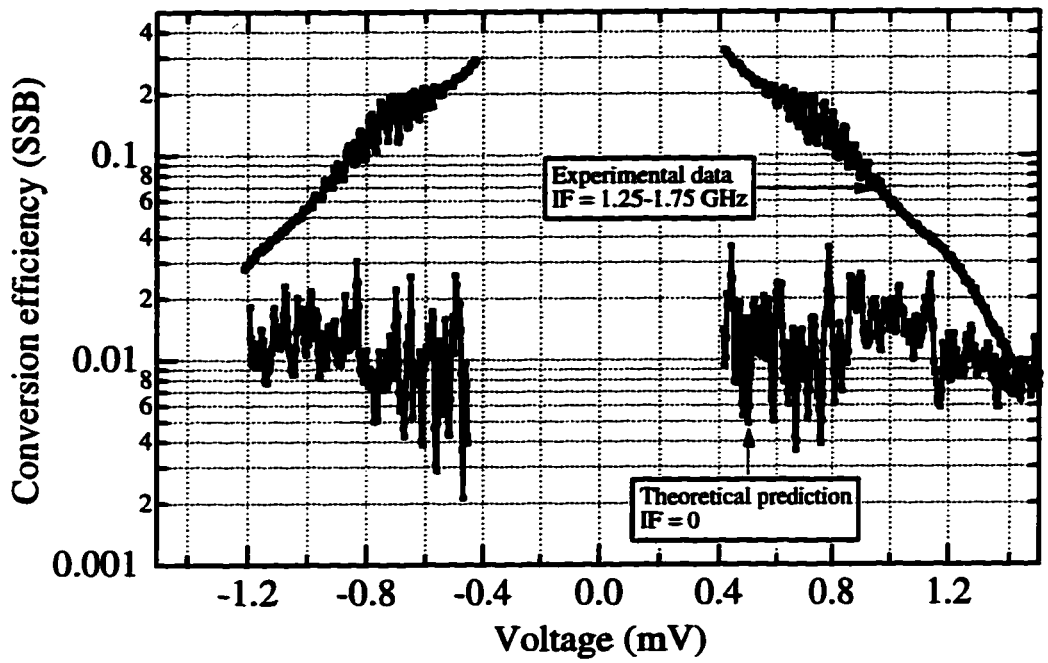

Figure 5.49: Comparison of theoretical and experimental efficiency for device A1 in optimum gain case.

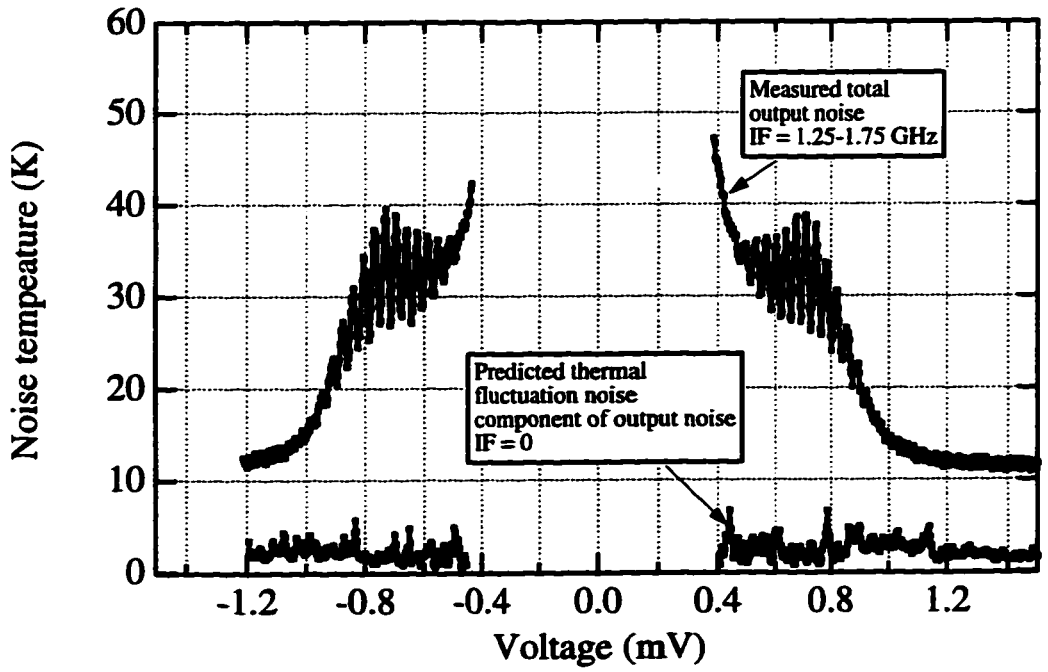

Figure 5.50: Comparison of theoretical and experimental output noise for device A1 in optimum gain case.

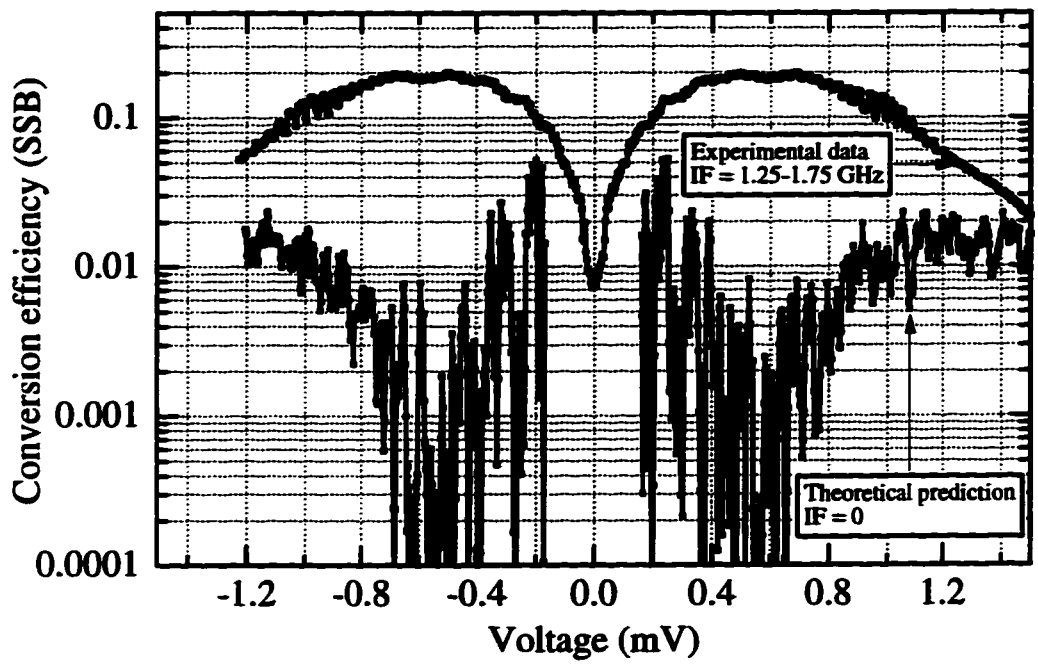

Figure 5.51: Comparison of theoretical and experimental efficiency for device A1 in overpumped case.

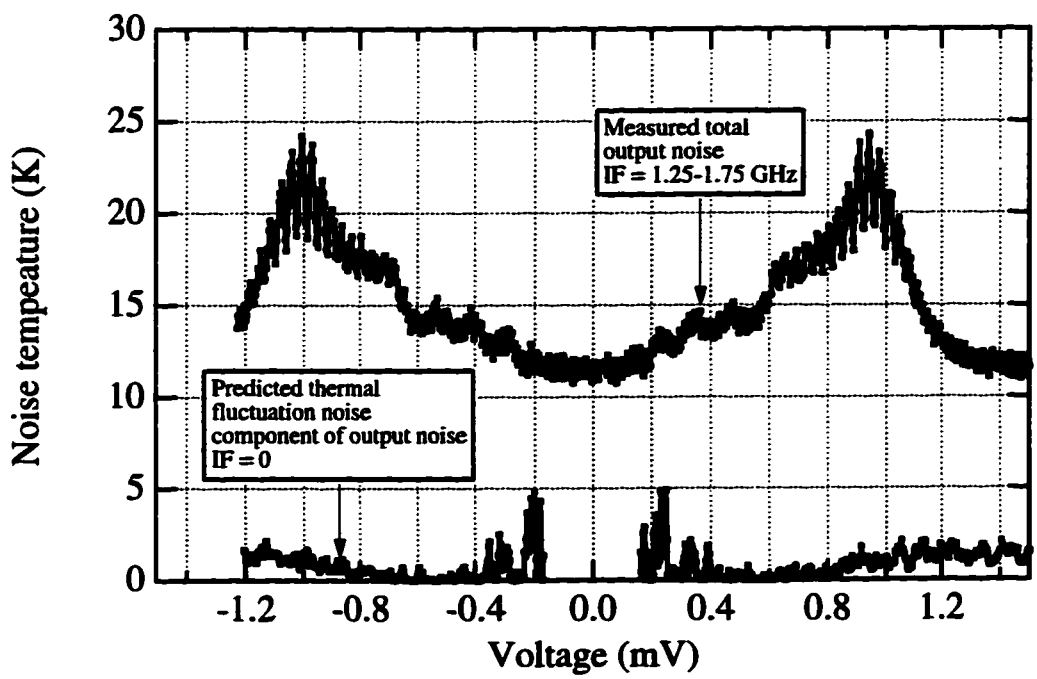

Figure 5.52: Comparison of theoretical and experimental output noise for device A1 in overpumped case.

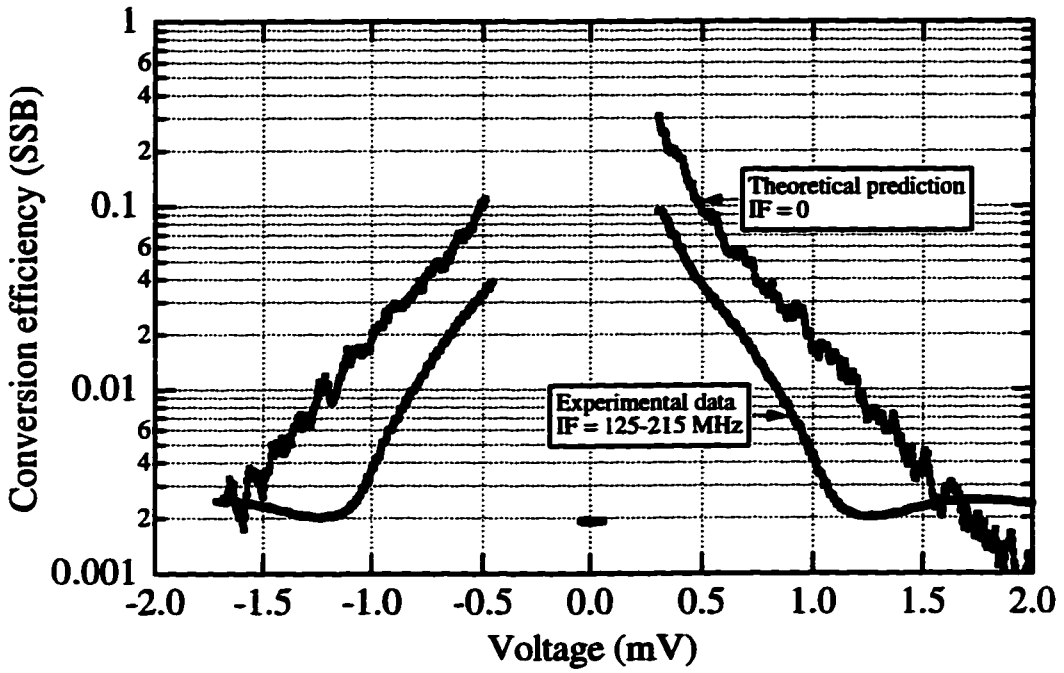

Figure 5.53: Comparison of theoretical and experimental efficiency for device B in optimum gain case.

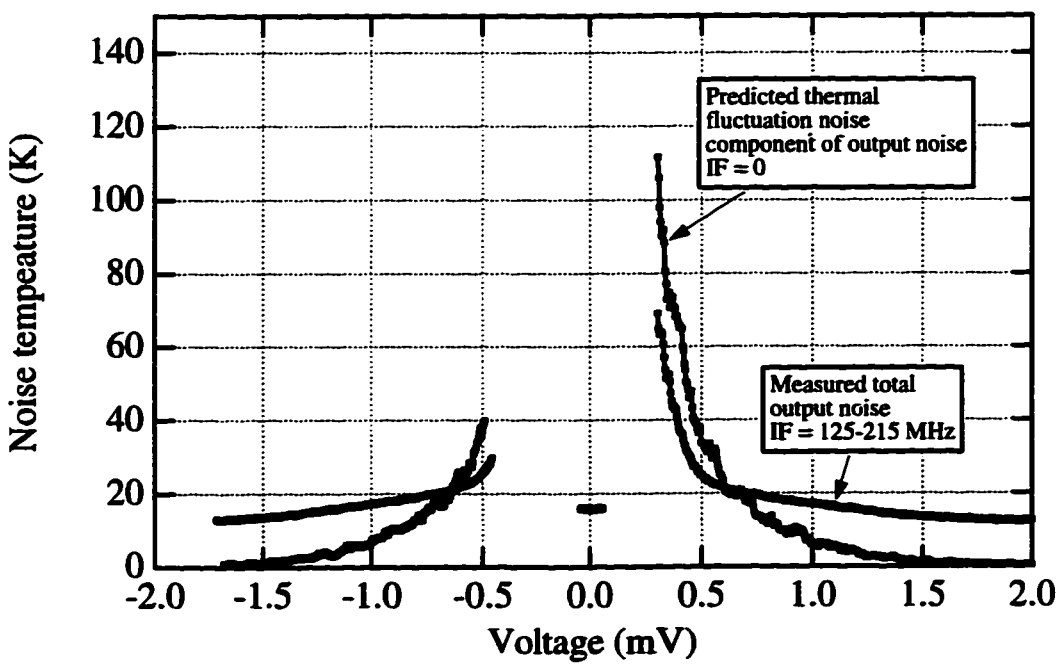

Figure 5.54: Comparison of theoretical and experimental output noise for device B in optimum gain case.

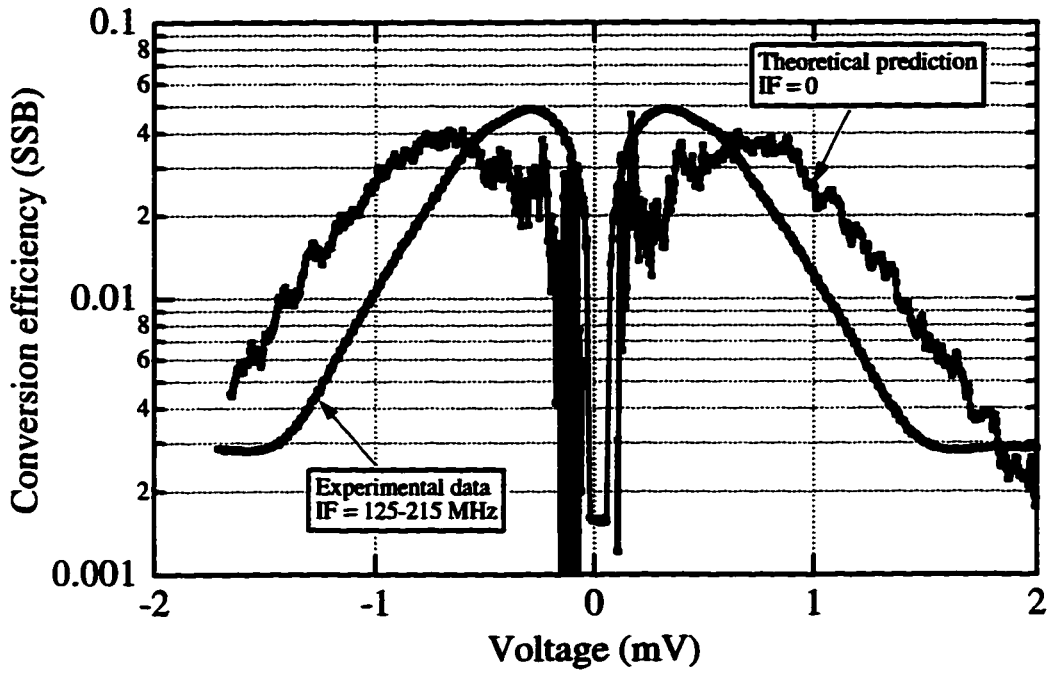

Figure 5.55: Comparison of theoretical and experimental efficiency for device B in overpumped case.

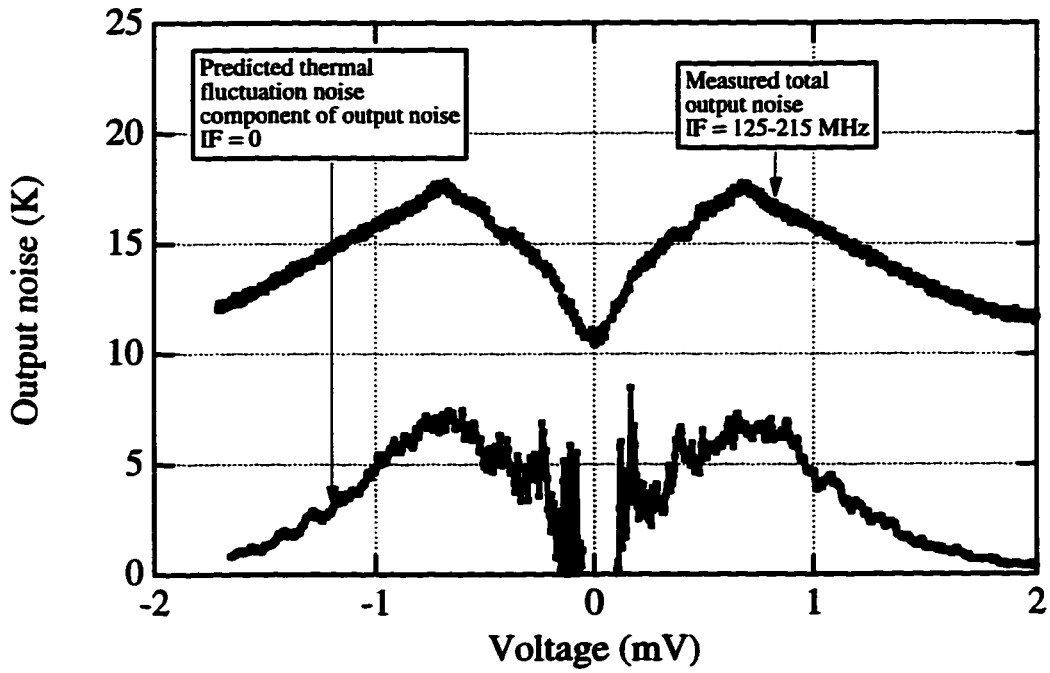

Figure 5.56: Comparison of theoretical and experimental output noise for device B in overpumped case.

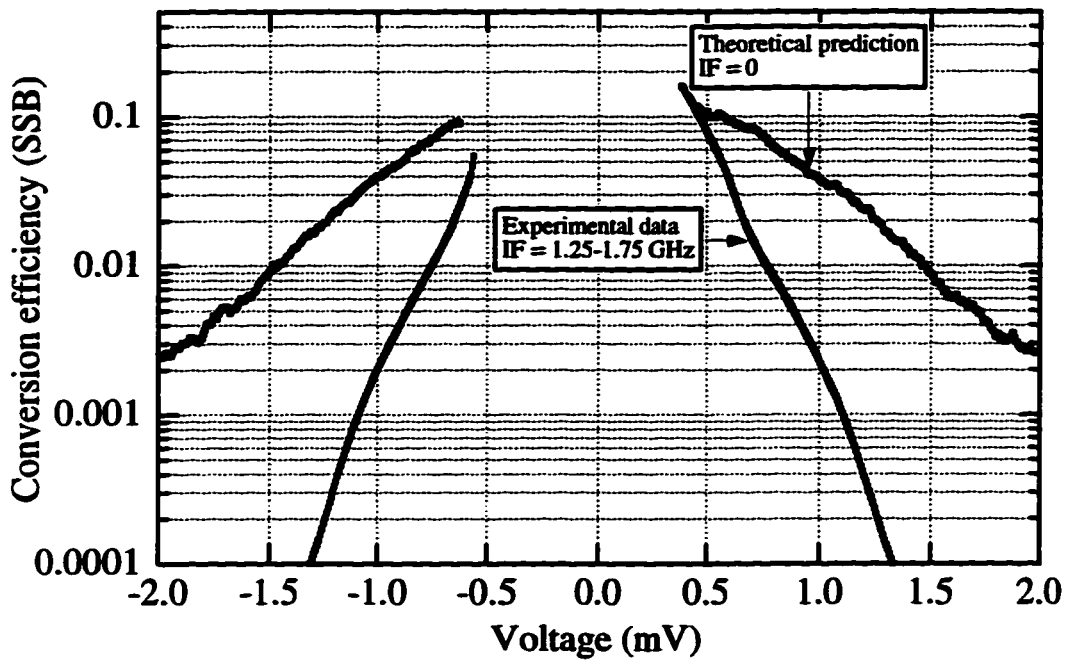

Figure 5.57: Comparison of theoretical and experimental efficiency for device C in optimum gain case.

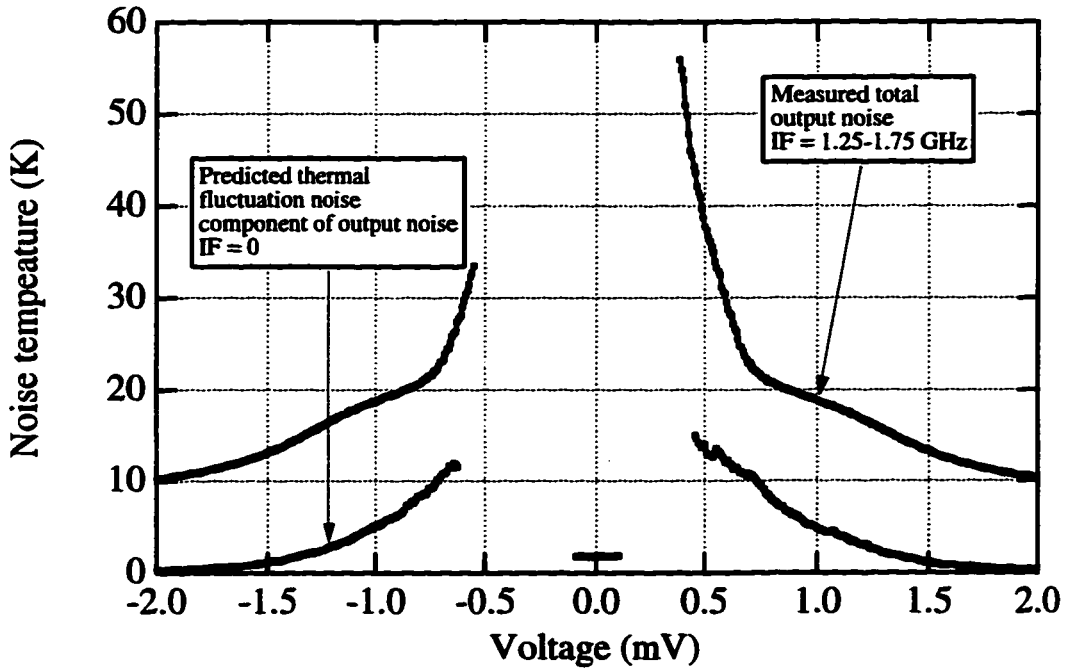

Figure 5.58: Comparison of theoretical and experimental output noise for device C in optimum gain case.

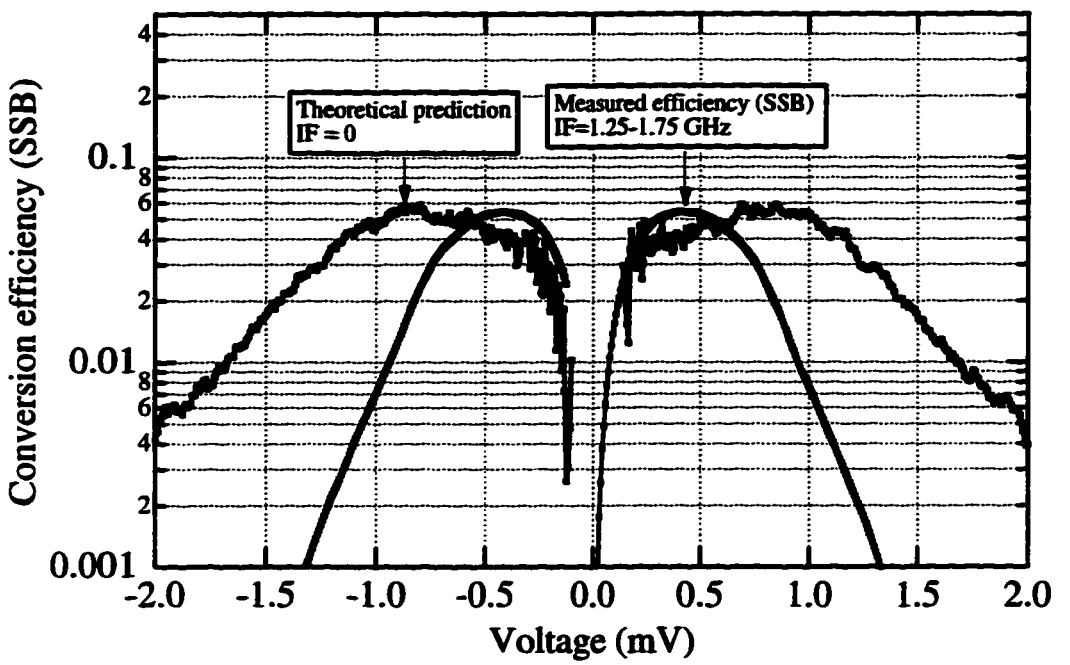

Figure 5.59: Comparison of theoretical and experimental efficiency for device C in overpumped case.

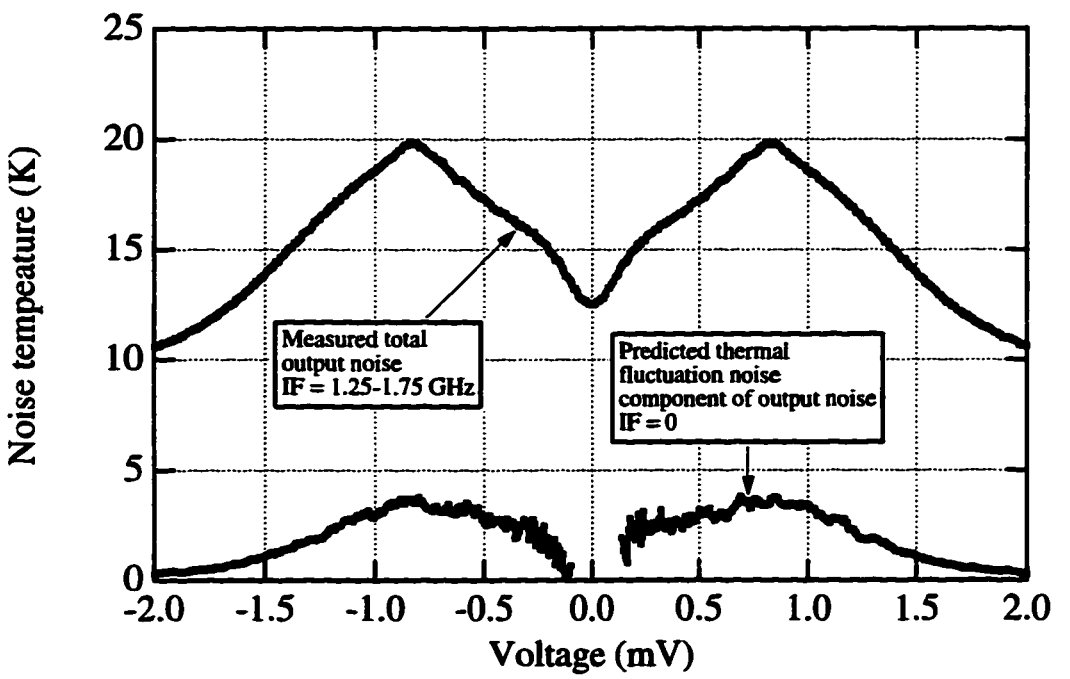

Figure 5.60: Comparison of theoretical and experimental output noise for device C in overpumped case.

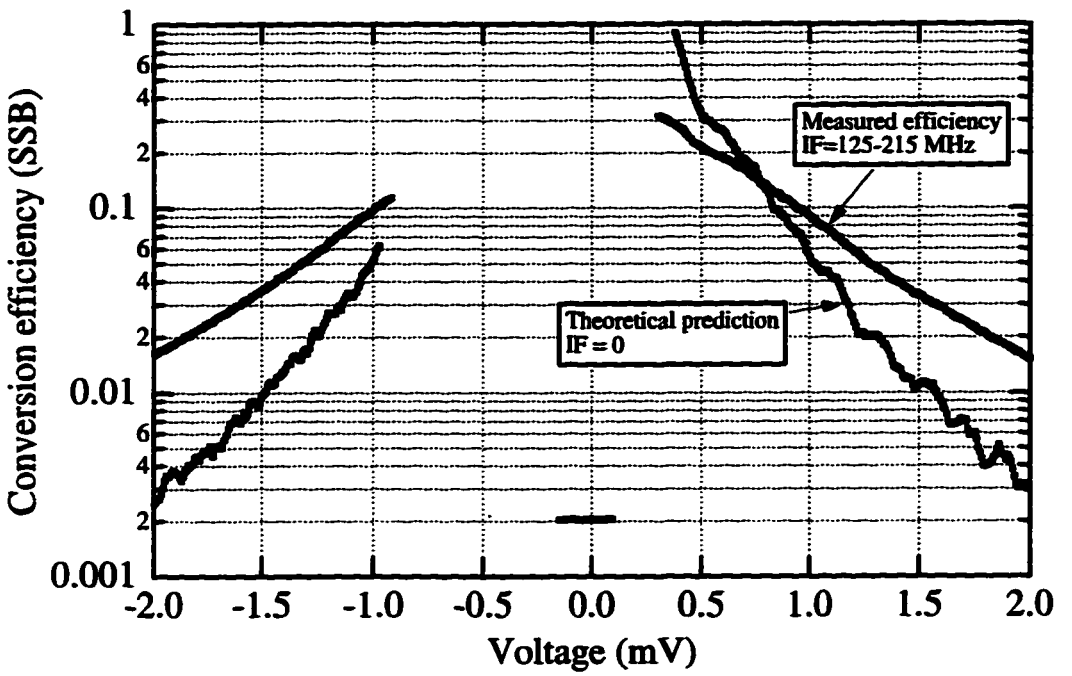

Figure 5.61: Comparison of theoretical and experimental efficiency for device D in optimum gain case.

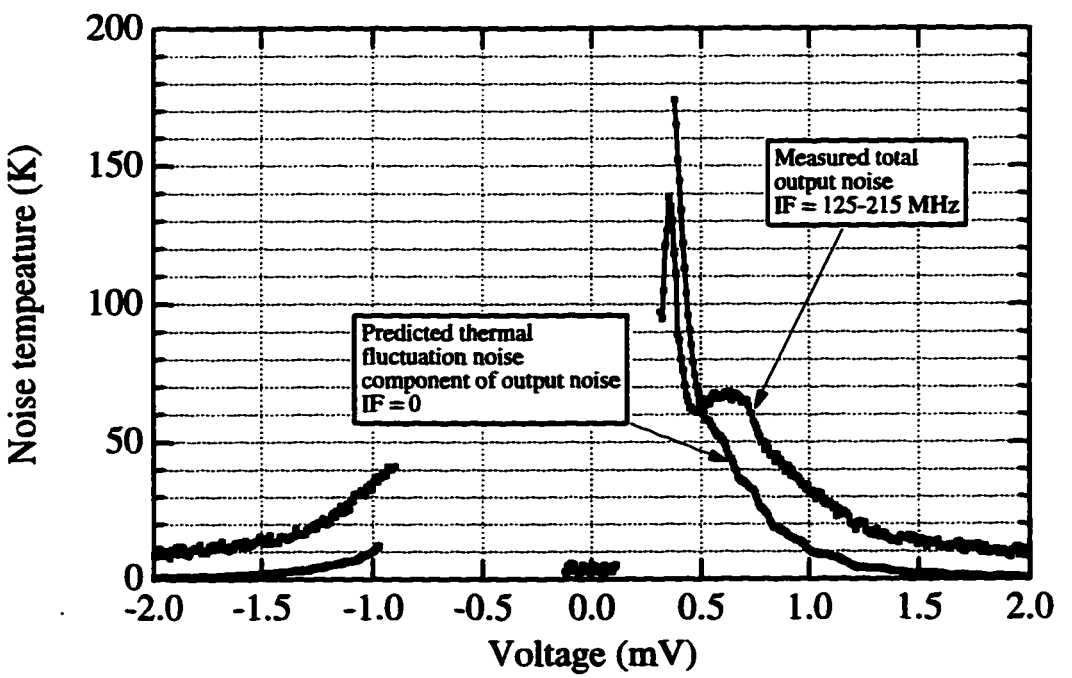

Figure 5.62: Comparison of theoretical and experimental output noise for device D in optimum gain case.

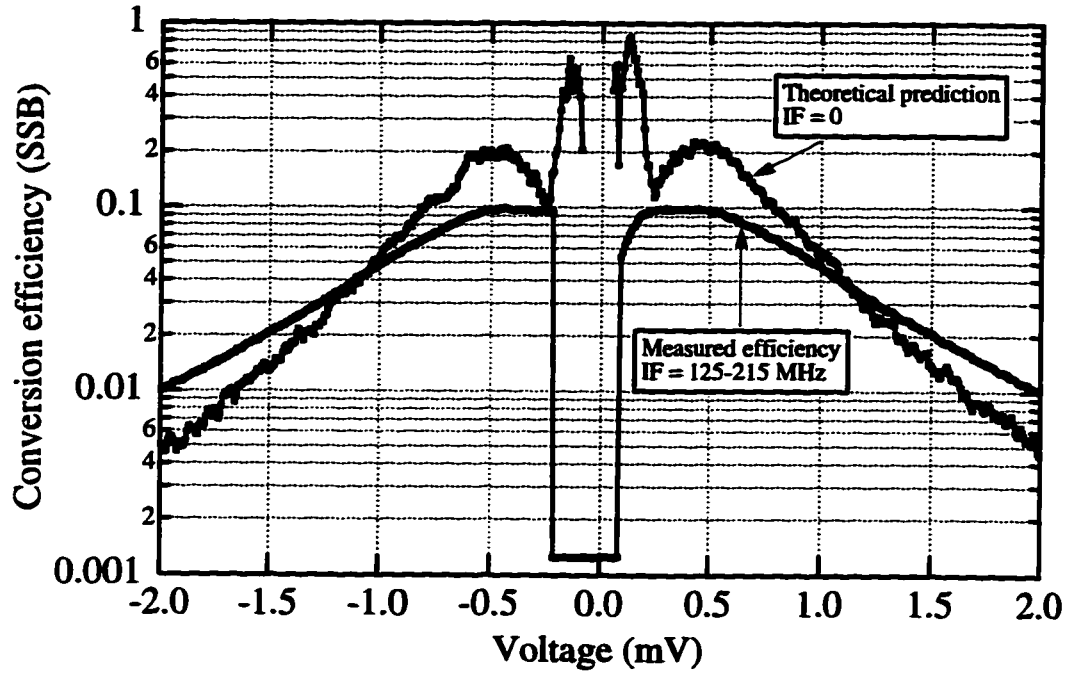

Figure 5.63: Comparison of theoretical and experimental efficiency for device D in overpumped case.

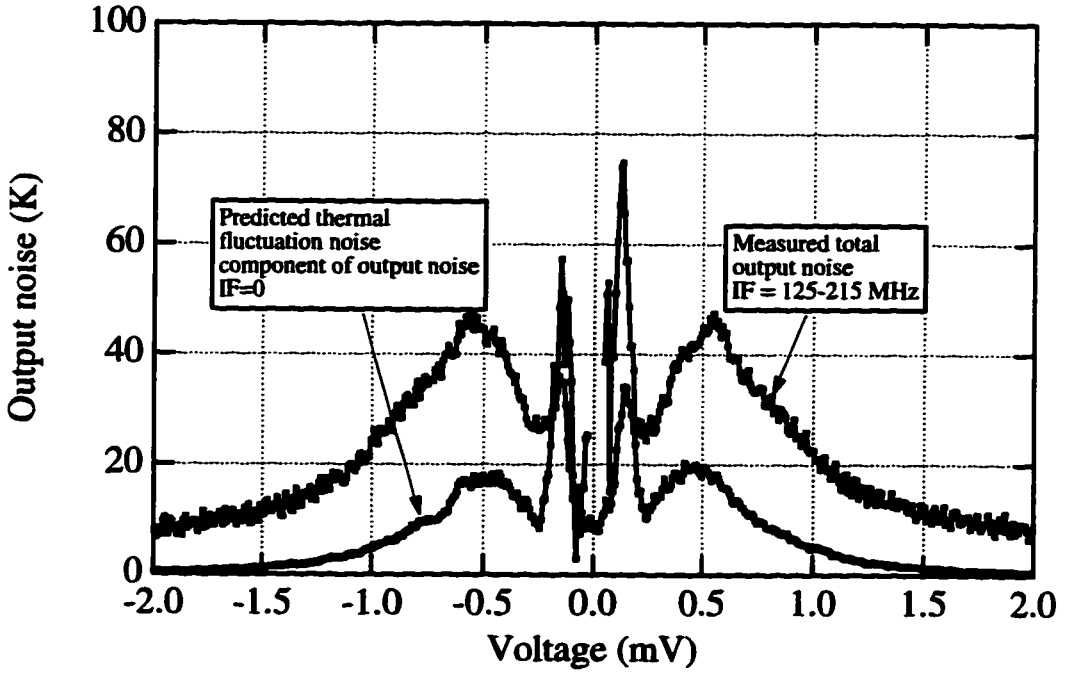

Figure 5.64: Comparison of theoretical and experimental output noise for device D in overpumped case.

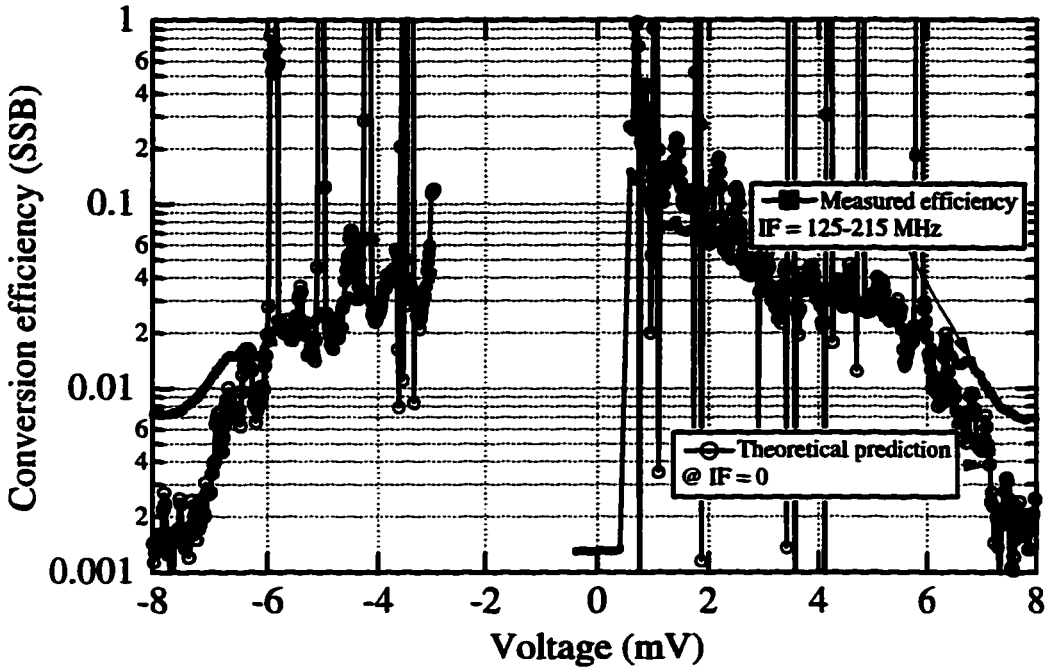

Figure 5.65: Comparison of theoretical and experimental efficiency for device E in optimum gain case.

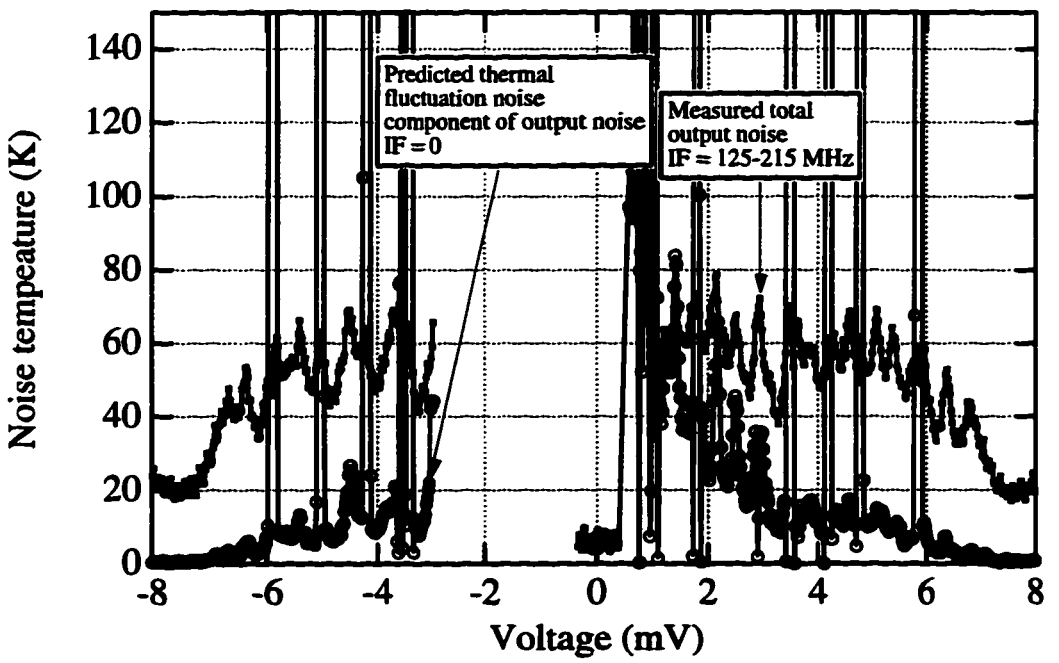

Figure 5.66: Comparison of theoretical and experimental output noise for device E in optimum gain case.

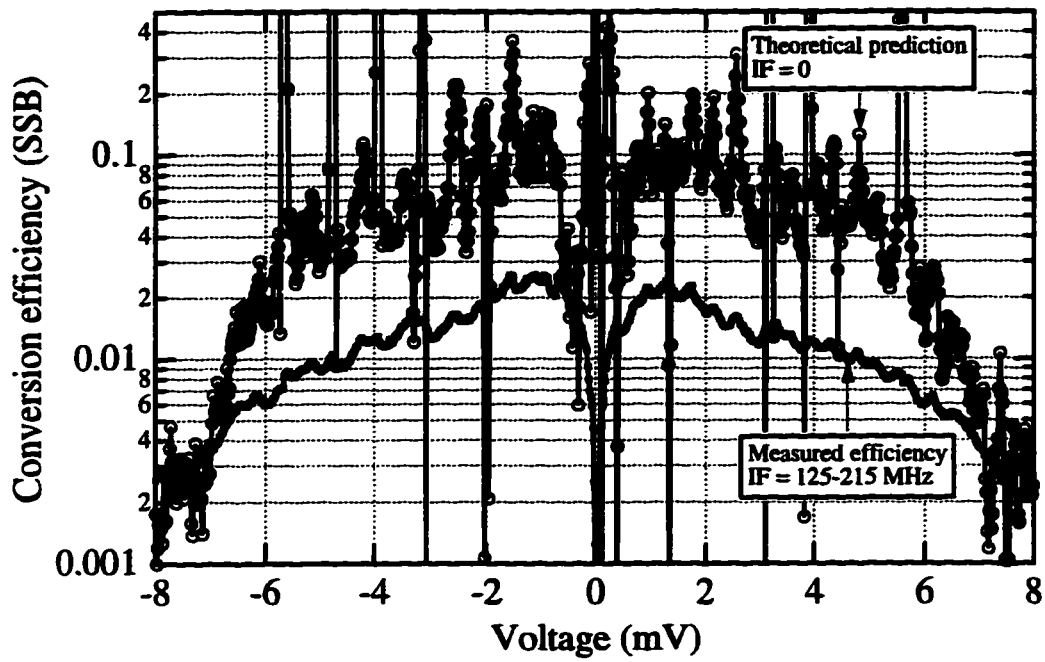

Figure 5.67: Comparison of theoretical and experimental efficiency for device E in overpumped case.

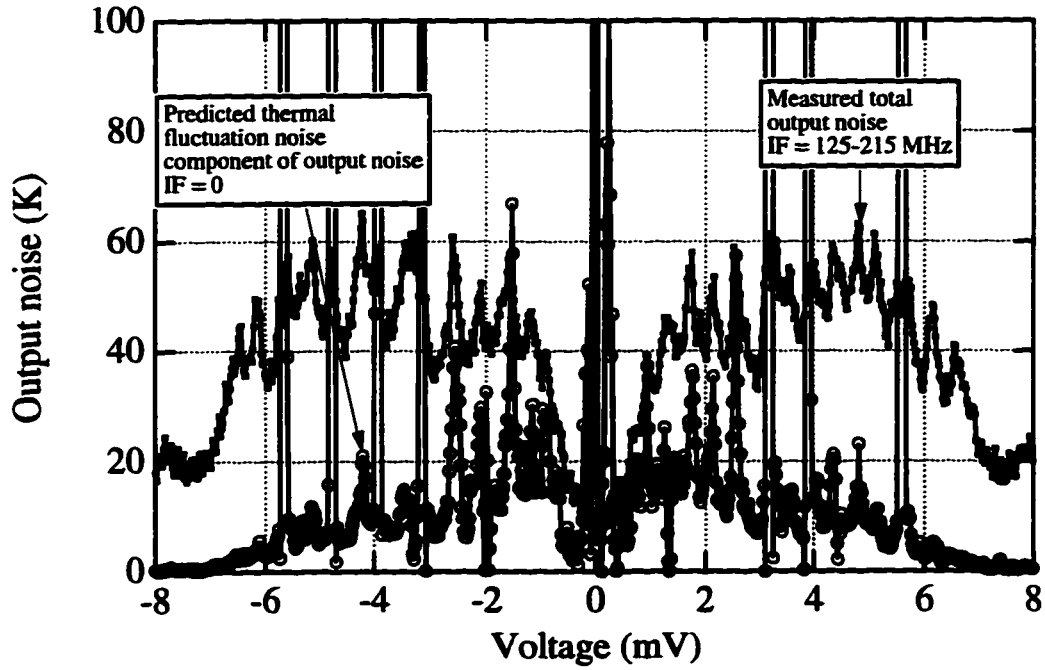

Figure 5.68: Comparison of theoretical and experimental output noise for device E in overpumped case.

Chapter 6

Comparison to JPL THz Receiver Measurements

The motivation for the work described in this thesis is the ultimate development of an ultra-low noise THz receiver. The experiments performed with 20 GHz signals were designed to investigate the physical processes which determine the behavior of the device. In this chapter, we compare the results presented in this thesis with results on similar devices measured in the research group of W.R. McGrath at JPL with 500 GHz (Skalare et al. 1996), 1.2 THz (Skalare et al. 1997), and 2.5 THz (Karasik et al. 1997) signals in order to determine the relevance of the measurements presented in this thesis to actual THz receivers. From first principles, there are three main frequency scales in the problem which may be important. The first frequency scale is the inverse of the thermal time constant, and this issue has already been extensively discussed. The second frequency scale is the gap frequency, which is approximately 740 GHz for bulk Nb. The most important issue regarding the gap frequency scale is whether the device responds to ac power below the gap frequency in the same way as it does to ac power above the gap frequency, i.e. is the conversion efficiency measured in this thesis with 20 GHz signals indicative of what can be achieved with THz signals? An additional frequency scale is the inverse of the momentum-relaxation rate, which is approximately 100 THz for the dirty films measured in this thesis. If the ac voltage changes faster than this frequency, an inductive component of the device impedance develops, which decreases the absorption of rf power,

and hence the conversion efficiency. Experiments done by Gershenzon et al. (1982) indicate that the absorption of power is constant in thin-film Nb up to approximately 100 THz, and this frequency scale is not approached by the experiments done at Yale and JPL.

If a voltage is applied to the device with a frequency above the gap frequency, then the power dissipated in the device is uniform along the length of the device, regardless of whether it is in the superconducting, normal, or intermediate state. (This is because an rf photon has enough energy to break a Cooper pair, which results in the absorption of rf power.) In contrast, voltages applied below the gap frequency cause dissipation of power only where the electrons are in the normal or intermediate state, which is generally not spatially uniform for the devices studied in this thesis. For the thin-film Nb used in the Yale and JPL experiments, the gap frequency is lower then the bulk value since T_c is lower. For a T_c of 5.5 K, the gap frequency is approximately 440 GHz. Near T_c the energy gap is suppressed, and for bulk superconductors the energy gap (and hence the frequency scale associated with it) approaches zero as the temperature approaches T_c. Since the devices studied here are operated very near T_c (which is not well-defined due to the finite-transition width), it is possible that the dissipation of power *is* uniform, in which case there should be no difference between the response to 10 GHz signals and THz signals. Since there is no clear theoretical prediction, the issue must be investigated experimentally.

Experiments performed at JPL were done on thin film Nb devices which were fabricated using the same process as the devices studied in this thesis.[1] In the 500 GHz JPL experiments, the rf coupling to the device was accomplished with a waveguide with two adjustable tuning elements, which allow for variation of the rf and LO source impedance to optimize the rf coupling from the receiver input to the device. The 1200 GHz and 2.5 THz experiments were done quasi-optically with antennas integrated onto the substrate, so that the rf coupling to the device could not be adjusted. In all the JPL experiments, the rf coupling efficiency to the device was estimated in order to deconvolute the rf coupling loss from the intrinsic device conversion efficiency. The output noise was also measured in the JPL experiments over the 1.25-1.75 GHz frequency range.

A summary of the conversion efficiency and output noise measured at Yale and JPL is presented in table 6. The device parameters are also presented. The devices measured at JPL included normal

[1]The devices used in the 500 GHz experiments performed at JPL were not fabricated using the self-aligned process described in chapter 3, but with a similar process.

state resistances that were both larger and smaller than those measured at Yale, and the device lengths of the JPL devices was similar to those measured at Yale. The bias conditions for the Yale results presented are those of optimum gain. The data from the JPL experiments was not easily classified into the "optimum gain" and "overpumped" cases, and further experiments will need to be done to clarify if a similar classification scheme is valid for the response to THz signals. Therefore, the data presented in table 6 was for the bias conditions which minimized the system or receiver noise performance. These conditions resemble the "optimum gain" case for the 500 GHz experiments, in that the I-V curve was hysteretic. However, for the 1200 GHz and 2.5 THz experiments, the I-V curve did not clearly resemble the I-V curves presented in this thesis.

The measured conversion efficiency at Yale was between -6 dB and -11 dB, while the JPL results find between -14 dB and -18 dB. This suggests that the measured conversion efficiency at 20 GHz may be larger than that to be expected at THz frequencies, by 7-8 dB. The output noise measured at JPL varied from 10-41 K, while the Yale results found a between 49 K and 55 K. It is difficult to draw conclusions from these data, since the output noise depends on the dc and lo power applied in all experiments. For this reason, the output noise measured in the absence of any applied ac power is also indicated in table 6 for those cases in which the data are available. Here, in both cases, the output noise is maximum when the dc bias is very close to the point of instability, as in the "optimum gain" case. The JPL data fall between 12 K and 37 K, while the Yale data fall between 30 K and 57 K. Thus, the JPL data are somewhat smaller. This may be due to the fact that the devices measured at JPL had a slightly different R vs. T characteristic since they were fabricated from different films than the devices measured at Yale. Since the measured output noise is different when no LO power is applied, it should not be expected to be the same when LO power is applied. The output noise, then, is similar but not exactly the same, and the conversion efficiencies measured at JPL are also smaller. The estimated mixer noise for the Yale experiments is between 120 K and 320 K (DSB), while it is between 210 K and 560 K for the JPL experiments. Thus, it is possible that the value of dR/dT for the JPL devices was smaller, causing a smaller efficiency and output noise, but a similar mixer noise.

The gain bandwidth has been carefully measured at JPL in the 500 GHz experiments, and it is found to be 1.9 GHz. This point is included in the plot of bandwidth vs. length in figure 5.26.

Frequency (GHz)	Eff. (dB,SSB)	T_{out} (K)	T_{mix} (K,DSB)	T_{out} (K) (no LO pwr.)	L (μm)	R_N (Ω)	R_{sheet} (Ω)	Gain BW (GHz)
20*	-5.6	49	120	57	0.08	56	29	> 6
20*	-11	57	320	-	0.16	80	29	2.4
20*	-8	55	200	30.6	0.24	96	29	1.5
533	-14.4±3°	41°	560°	36.7	0.27	20	10.4	1.7
1267	-13±3†	16.6†	166†	13.7	0.3	140	70	-
2500	-18.5±3‡	10‡	350‡	< 12	0.3	23	11.5	-

Table 6.1: Comparison of JPL and Yale mixer results. The upper half of the table represents the results presented in this thesis measured at Yale, while the lower half represents the JPL data (Skalare 1997; Karasik 1997). The contribution of the IF amplifier has been subtracted off.
* Eff. referred to device. Bias conditions for optimum gain used. Output noise is extrapolated to f = 0. Sheet resistance determined from larger device on wafer.
° Referred to dewar input, incl. 1 dB cplg. loss. Output noise is at 1.24-1.56 GHz.
† Referred to device, does not incl. 9.1 dB cplg. loss. Output noise is at 1.24-1.56 GHz.
‡ Referred to device, does not incl. 8.5 dB cplg. loss. Output noise is at 1.5 GHz. The 2.5 THz measurements were done at a bath temperature of 4.2 K, in contrast to the other data in the table where the bath temperature was approximately 2 K.

There, the JPL measurement is in good agreement with the data presented in this thesis. Since the sheet resistance for the JPL device is approximately 3 times smaller for the JPL device than the Yale devices, the agreement should not be as good as it is. However, errors in the estimate of the sheet resistance due to errors in the estimate of the film thickness could account for some of the discrepancy. It is possible that the electro-thermal slowing factor is different in the JPL and Yale experiments, but this would not account for a factor of 3 discrepancy. This may indicate that more complicated non-equilibrium processes conspire to enforce the scaling law that we find experimentally in this thesis, regardless of the sheet resistance.

In figure 6.1, the system noise temperature is plotted as a function of rf frequency for several different detector technologies. From this graph, it is clear that the hot-electron bolometers are already the lowest-noise mixers available for rf frequencies above approximately 1 THz.

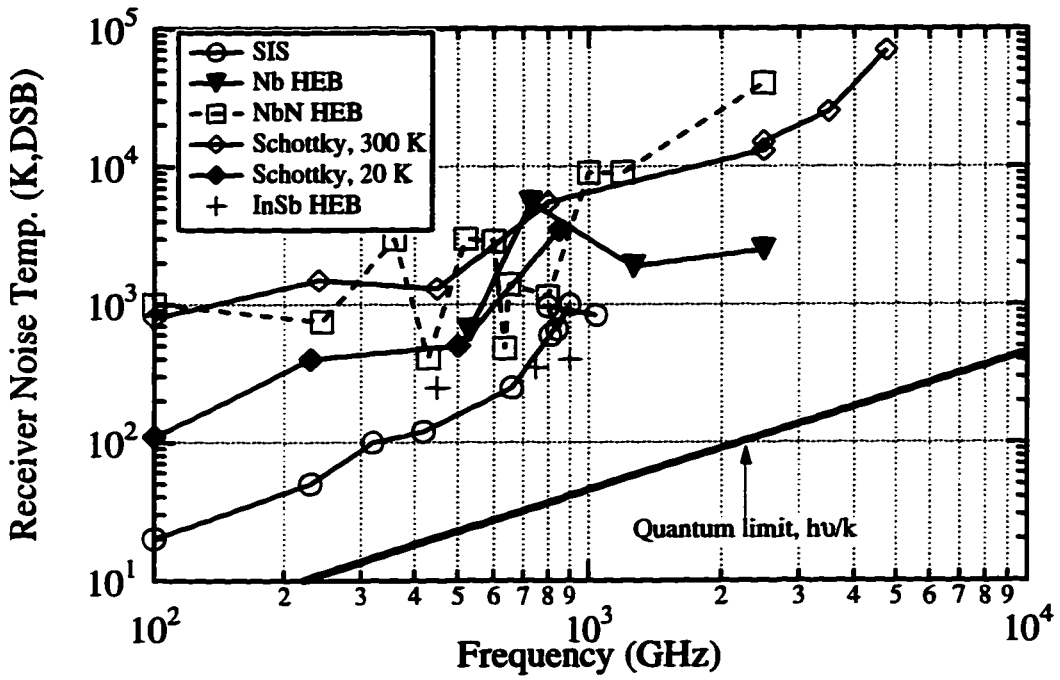

Figure 6.1: Receiver noise temperature vs. rf frequency for various technologies. (Adopted from Schoelkopf et al. (1997) and Karasik et al. (1997).)

Chapter 7

Conclusions

7.1 Summary of results presented in this thesis

In this thesis, the physical processes that govern the performance of diffusion-cooled hot-electron bolometers have been systematically investigated in a series of experiments measuring the conversion efficiency, output noise, and device differential impedance under a variety of experimental conditions for devices of several different lengths.

In chapter 2, a simple theoretical model was presented which treats the measured resistance vs. temperature curve phenomenologically and predicts the output noise, conversion efficiency, and device differential impedance as a function of the dc and ac power, the thermal conductance of the electrons to the bath, the electron temperature, and the normal state resistance.

An experimental setup was designed and constructed to allow the measurements of the conversion efficiency and output noise of a suite of devices with LO and rf frequencies from 8 to 40 GHz. A broadband coupling scheme to convert from coax to microstrip and then to the device through a "flip-chip" method was designed and constructed, allowing resonant free coupling to the devices from dc to 40 GHz. A cryogenically cooled amplifier with input noise of 25 K from 0.1-8 GHz was used to measure coherent signals generated by the device at the intermediate frequency as well as incoherent noise generated by the device. Two calibration schemes were devised and shown to agree. The *in-situ* calibration scheme used the Johnson noise from the device when it was biased above T_c

as a source of known absolute power to calibrate the amplifier gain and noise. In this way, the noise generated by the device could be measured by subtracting off the amplifier noise contribution.

The conversion efficiency and output noise were measured with a bath temperature of 2 K as a function of dc bias voltage for a variety of devices in two cases: when enough LO power was applied to completely suppress the critical current (the overpumped case), and when the LO power was adjusted to maximize the (coupled) conversion efficiency. The *mixer noise* in the two cases was very similar, but the output noise and conversion efficiency were higher by a factor of 2-3 in the optimum gain case than the overpumped case. The conversion efficiencies measured ranged from -6 dB to -11 dB in the optimum gain case, and the output noise ranged from 50 K to 230 K. In the overpumped case, the conversion efficiencies ranged from -10 dB to -13.5 dB, while the output noise ranged from 13-70 K. These results did not depend sensitively on the LO frequency used as long as it was larger than $(2\pi\tau_{th})^{-1}$. A dramatic enhancement of the noise was found for device A1 in the overpumped case when the applied LO frequency was below $(2\pi\tau_{th})^{-1}$.

The measured output noise and conversion efficiency were compared with the theoretical predictions of chapter 2 in two ways: first, the value of dR/dT_e was estimated from the measured R vs. T curve, and the output noise and conversion efficiency was overpredicted in all cases using this method. A second method used the measured dc I-V curve to estimate dR/dT_e, and this method overpredicted the output noise in some cases and underpredicted it in others. However, the qualitative dependence on bias voltage was well predicted, and this is in accord with the general principles of the device operation. The mixer noise was calculated by dividing the measured output noise by the measured conversion efficiency, and found to be between 120 K and 530 K. This low noise suggests that the diffusion-cooled hot-electron bolometers are the best candidates for ultra-sensitive THz receivers.

The dependence of the gain and output noise on intermediate frequency was also measured for the suite of devices. The conversion efficiency and output noise decrease when the intermediate frequency is larger than the inverse of the thermal time constant. The mechanism which determines the thermal time-constant depends on the device length. For devices longer than the electron-phonon length L_{e-ph}, the thermal time-constant is given by the electron-phonon interaction rate. This time constant allows for a gain bandwidth of approximately 100 MHz in Nb, which is too slow for practical

applications. If the device length is less than πL_{e-ph}, then out-diffusion of heat into the highly conducting normal metal leads can dominate the cooling process. In this case, the thermal time constant is given by the diffusion time, and scales as the device length squared. The time constants were determined for devices of different lengths by fitting the conversion efficiency as a function of intermediate frequency. The scaling with device length obeyed the theoretical predictions, and the crossover from phonon dominated to diffusion dominated behavior was observed as the length of the device varied. A factor of 50 improvement in the gain bandwidth was achieved by using diffusion instead of phonon cooling. The shortest device had a gain bandwidth of at least 6 GHz, which is the largest bandwidth achieved in a low-T_c hot-electron mixer as of the writing of this thesis. Since the component of the output noise due to thermal fluctuations was found to decrease with intermediate frequency, the *mixer noise* did not begin to increase until the thermal fluctuation noise component was smaller than the Johnson noise component. This implies that the noise bandwidth was larger than the gain bandwidth by a factor of 1.4-9.4, which may be useful in actual receivers. Thus, while the absolute conversion efficiency and output noise are not well-predicted by the theory, the dependence on intermediate frequency is.

The crossover from phonon to diffusion dominated behavior was also observed by using noise thermometry in the normal state to measure the increase in electron temperature as a function of applied dc power. The crossover was observed in a single device by varying the device temperature, which changes L_{e-ph} and hence the ratio L/L_{e-ph}. The ratio L/L_{e-ph} determines whether diffusion or phonon cooling dominates. The crossover was also observed by measuring the response to dc power of devices of varying lengths at approximately the same temperature of 6 K.

Additionally, the device differential impedance was measured, using a scalar measurement technique. The rf coupling to the devices was measured to be better than approximately 90% for all devices both above and below $(2\pi\tau_{th})^{-1}$, with the exception of device E, where the coupling was only approximately 50% at frequencies below $(2\pi\tau_{th})^{-1}$. These measurements are in agreement with the theoretical prediction that the impedance above $(2\pi\tau_{th})^{-1}$ is V_{dc}/I_{dc}, and that the impedance below $(2\pi\tau_{th})^{-1}$ is simply dV/dI.

Since the ultimate goal for diffusion-cooled hot-electron bolometers is operation in ultra-sensitive THz receivers, the data presented in this thesis was compared to the data measured on similar

devices at JPL with rf frequencies of 500 GHz, 1.2 THz, and 2.5 THz. The JPL measurements find device conversion efficiencies between -13 and -18 dB, which is approximately 8 dB lower than the measurements for this thesis work. The output noise measured at JPL was also lower, varying from 12 K to 37 K. One possible reason for the discrepancy could be a lower value of dR/dT_e. The *mixer noise* was similar to that found here, ranging from 210 K to 560 K (DSB). Additionally, the measured gain bandwidth of 1.9 GHz for a 0.27 μm device is in good agreement with the devices measured at Yale of similar length, even though the diffusion constant of the JPL devices is estimated to be different by a factor of approximately 3. The device performance measured at JPL at 1.2 THz and 2.5 THz already indicates that the devices are the best available mixers above 1 THz.

7.2 Suggestions for future experiments

In this thesis, we have investigated the dependence of the gain bandwidth and noise bandwidth on device length, for a fixed diffusion constant and with negligible electro-thermal feedback. The dependence of the thermal time constant on the diffusion constant for devices of fixed length with different diffusion constants would be a complimentary set of experiments to those presented in this thesis. Additionally, by adjusting the width and keeping the length fixed, the device resistance and hence electro-thermal feedback factor could be changed, without changing the "bare" time constant. It may be possible to engineer electro-thermal feedback effects to improve the conversion efficiency, but the output noise is also predicted to increase in this case. However, this would reduce the contribution of the IF amplifier noise to the system, and so may be worth investigating. The coupling of the device at the rf, LO, and IF frequencies to a 50 Ω system also would change with device resistance, and this effect (which is comparable in magnitude to the electro-thermal feedback effect) would need to be corrected for, making the experiments somewhat challenging.

The noise performance of the devices measured for this thesis and at JPL is already excellent for THz receivers. However, it is still at least an order of magnitude above the quantum limit. According to equation 2.31, the mixer noise should scale as GT_e^2/P_{LO}. For diffusion-cooled devices, G scales with T_e, and P_{LO} scales approximately inversely with T_e, so that lower T_c devices should have lower mixer noise. Therefore, the noise performance should improve by using lower T_c materials.

Finally, the temperature profile is a difficult quantity to measure experimentally, but an impor-

tant issue in diffusion-cooled bolometers. If lower T_c devices are used where the relevant length scales are longer than those for Nb, such as the electron-electron and electron-phonon interaction lengths, it might be possible to probe the electron energy distribution function along the length of the bridge with a series of normal and/or superconducting tunnel junctions. This would allow the non-equilibrium processes to be investigated as they develop along the length of the bridge.

Appendix A

Calculated values of α and α_0 from I-V curve.

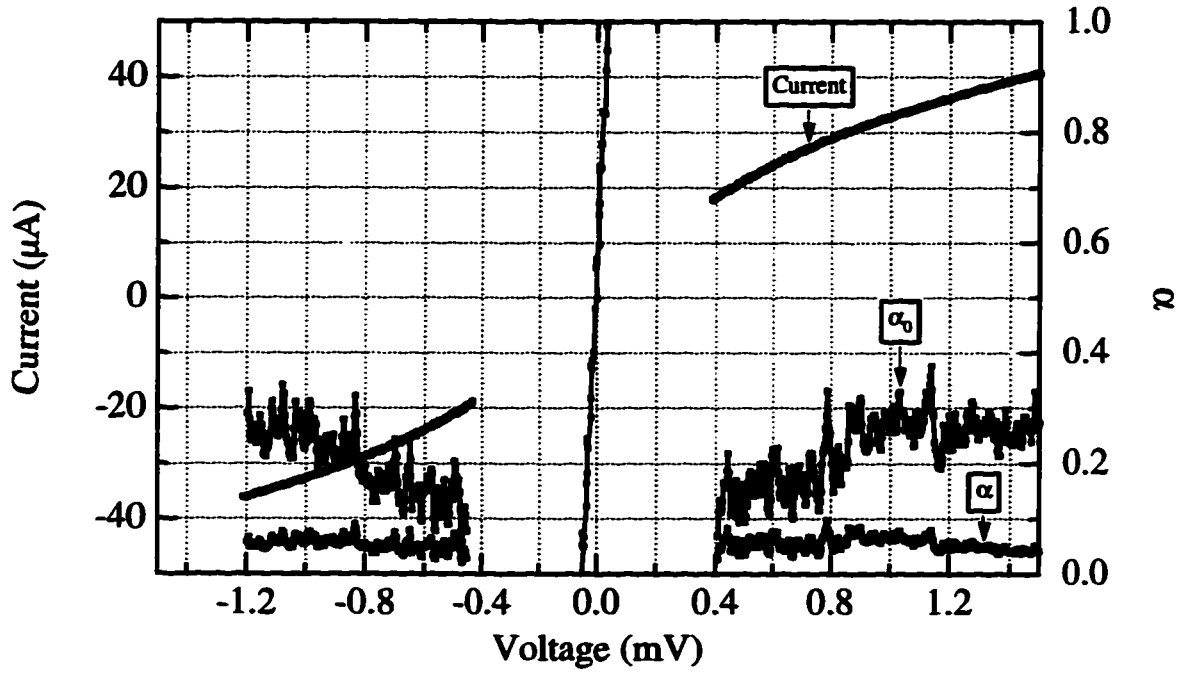

Figure A.1: α for device A1 in optimum gain case.

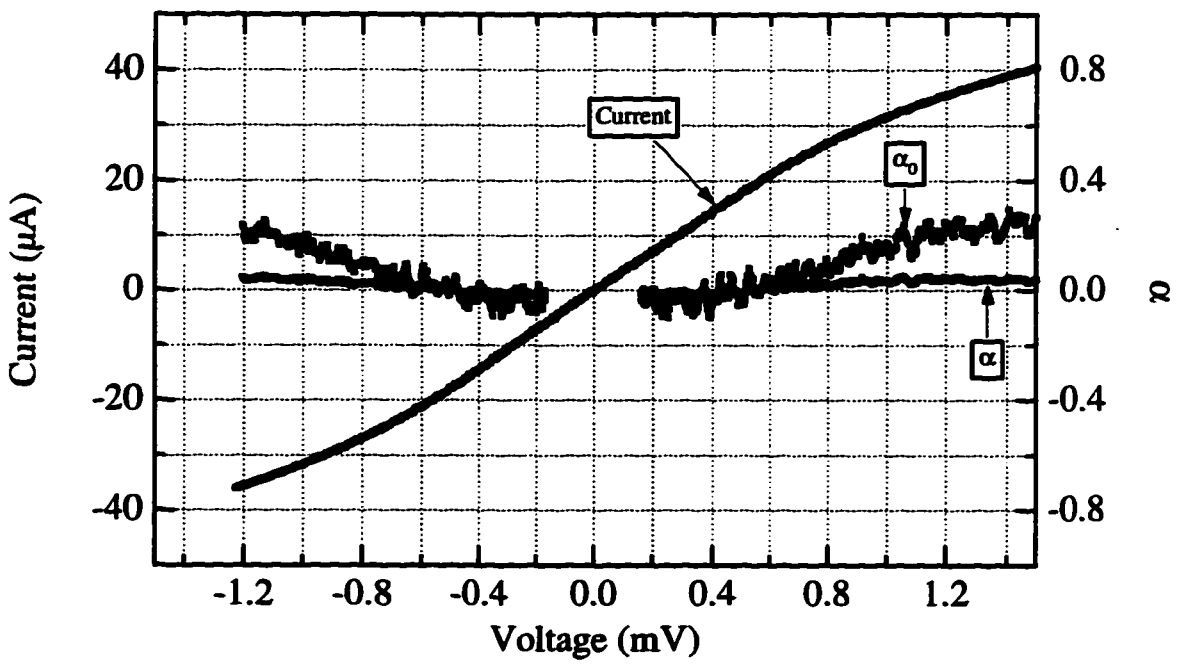

Figure A.2: α for device A1 in overpumped case.

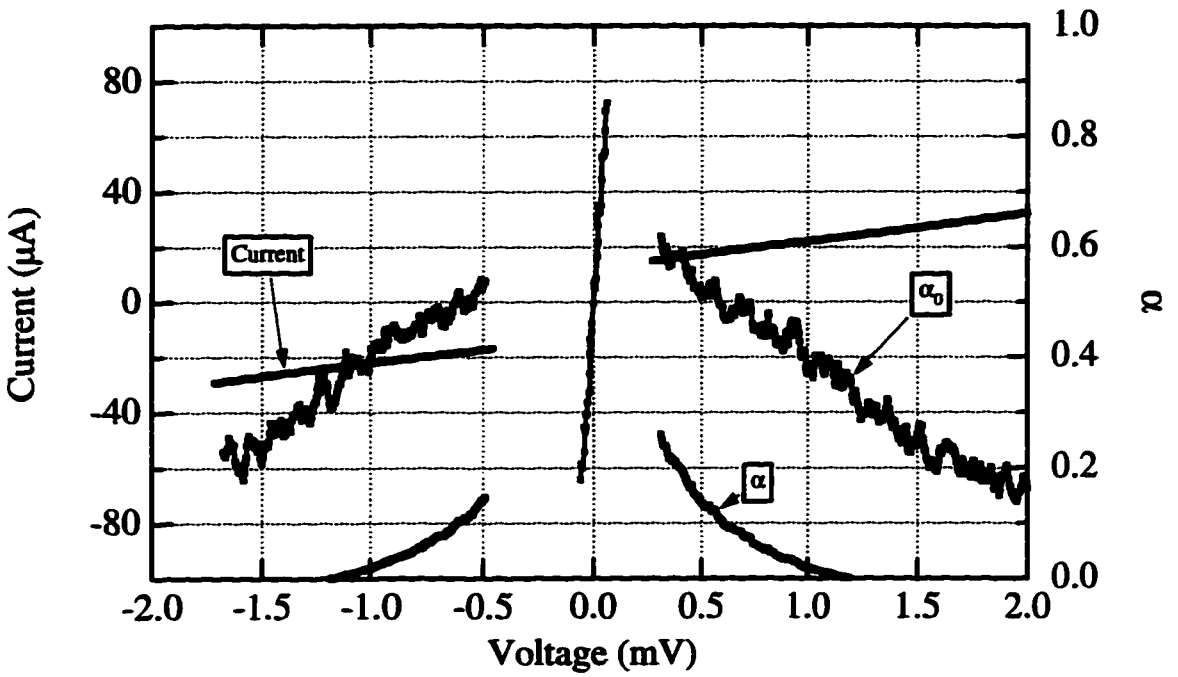

Figure A.3: α for device B in optimum gain case.

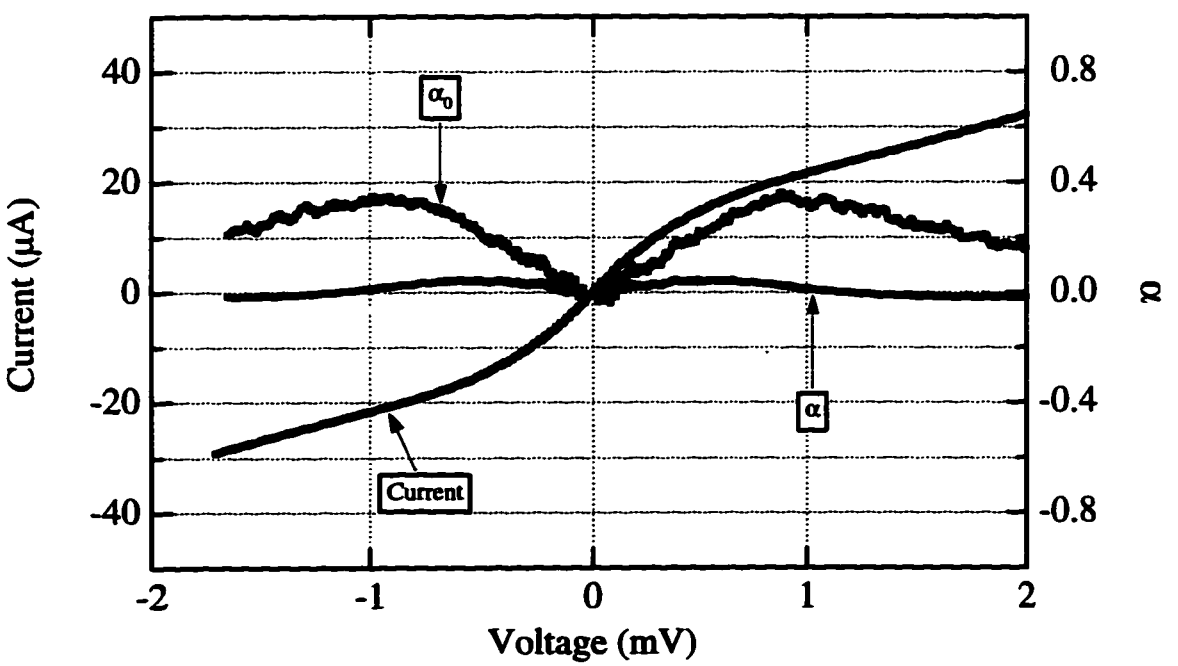

Figure A.4: α for device B in overpumped case.

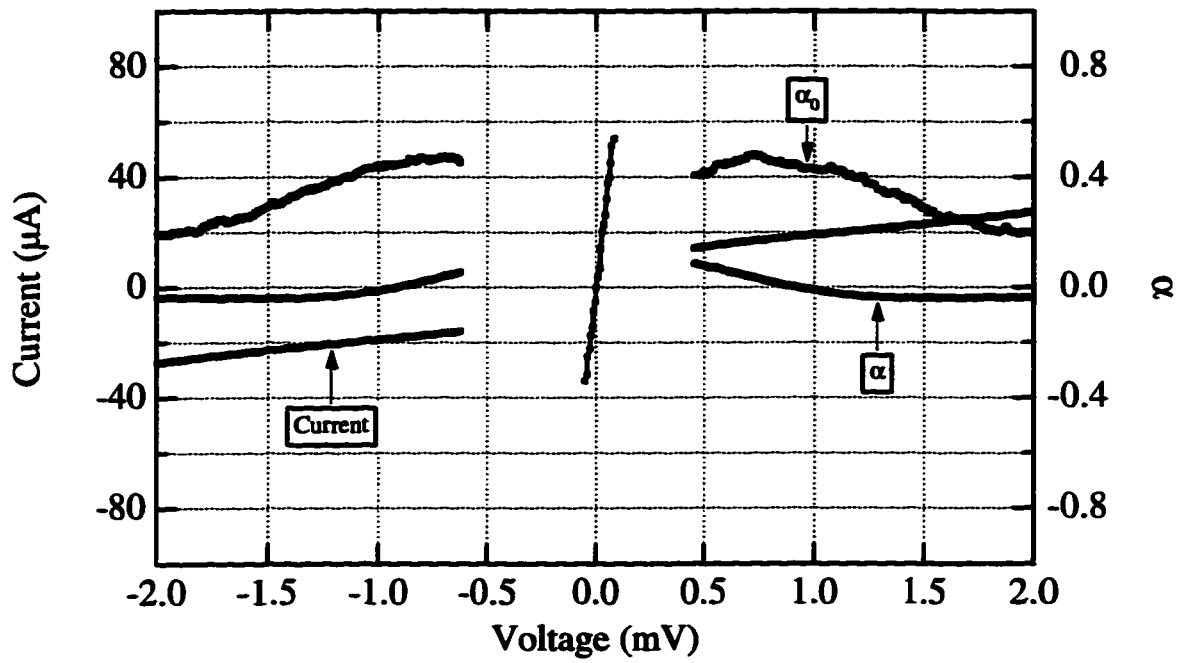

Figure A.5: α for device C in optimum gain case.

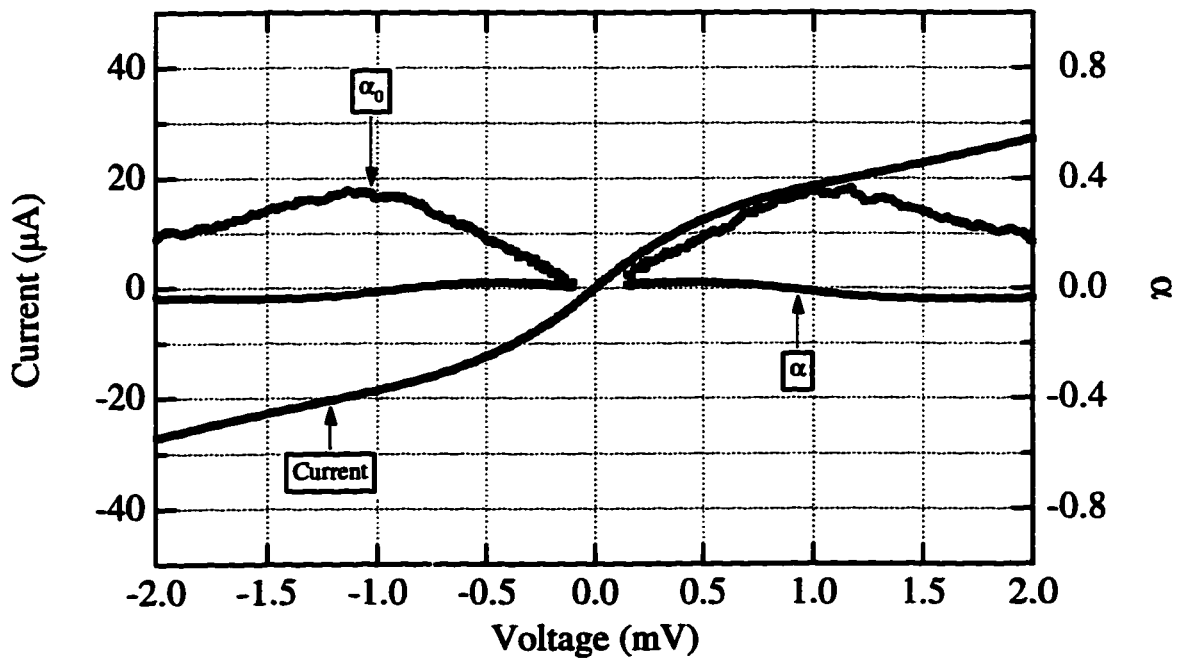

Figure A.6: α for device C in overpumped case.

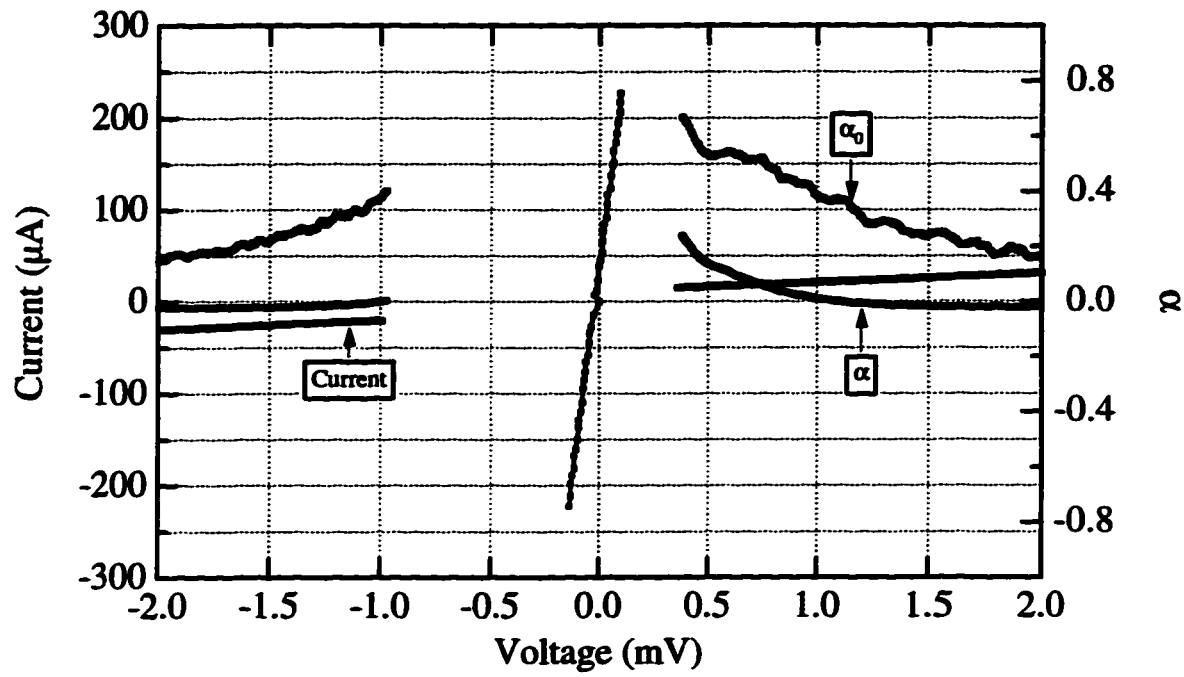

Figure A.7: α for device D in optimum gain case.

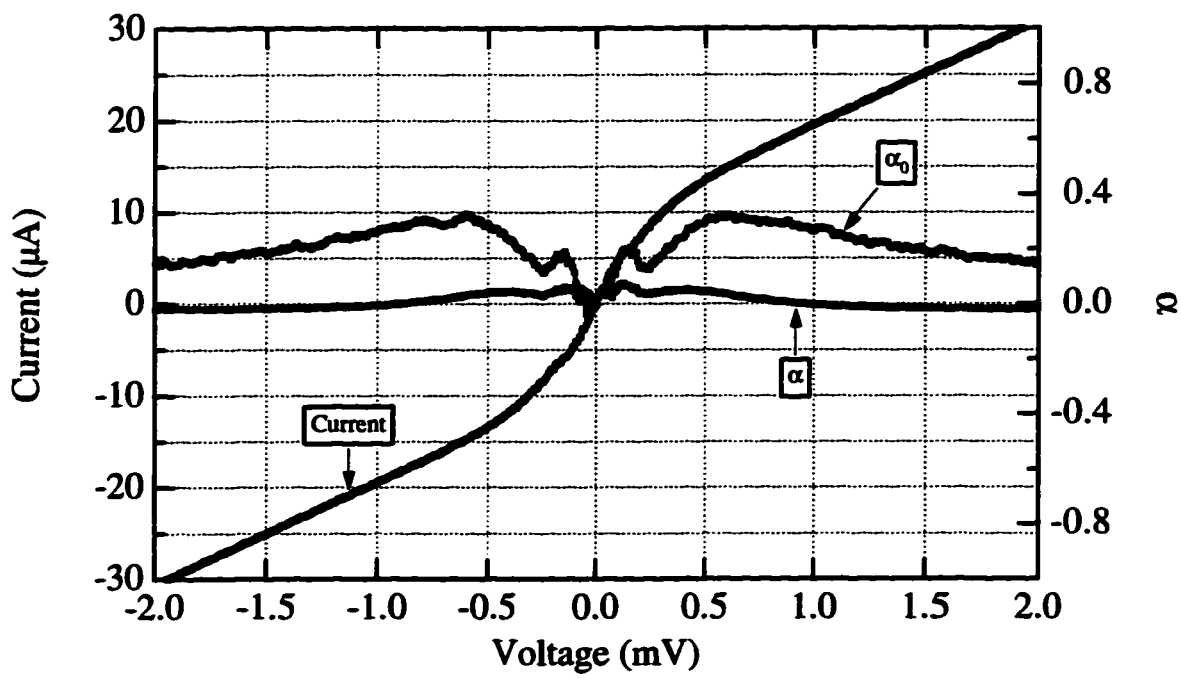

Figure A.8: α for device D in overpumped case.

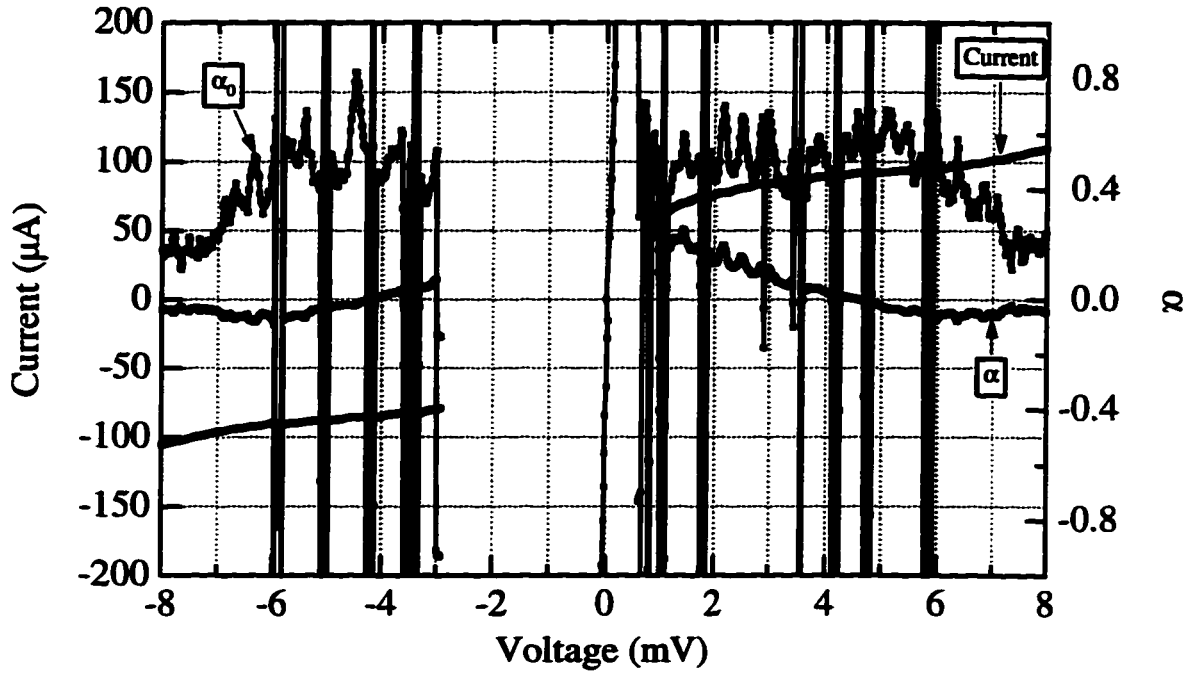

Figure A.9: α for device E in optimum gain case.

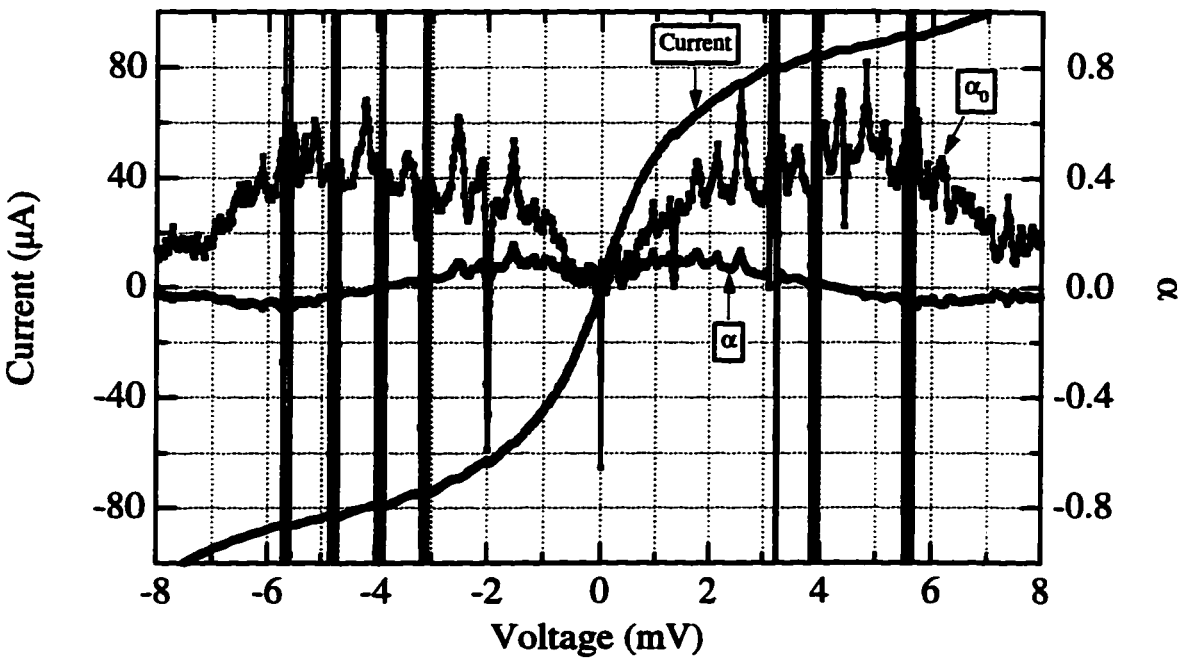

Figure A.10: α for device E in overpumped case.

Bibliography

Altshuler, B. and A. Aronov (1985). *Electron-Electron Interactions in Disordered Systems*, Chapter Electron-Electron Interaction in Disordered Conductors. Amsterdam: North Holland.

Arams, F., C. Allen, B. Peyton, and E. Sard (1966). Millimeter mixing and detection in bulk InSb. *Proceedings of the IEEE 54*(4), 612–622.

Brown, E. R., J. Keene, and T. G. Phillips (1985). A heterodyne receiver for the submillimeter wavelength region based on cyclotron resonance in InSb at low temperatures. *International Journal of Infrared and Millimeter Waves. 6*(11), 1121–1138.

Bumble, B. and H. G. LeDuc (1997). Fabrication of a diffusion cooled superconducting hot electron bolometer for THz mixing applications. *IEEE Transactions on Applied Superconductivity 7*(2), 3560–3563.

Callen, H. and T. Welton (1951). Irreversibility and generalized noise. *Physical Review 83*(1), 34–40.

Carslaw, H. and J. Jaeger (1959). *Conduction of Heat in Solids.* London: Oxford University Press.

Caves, C. (1981). Quantum limits on noise in linear amplifiers. *Physical Review D 26*(8), 1817–1839.

Chalsani, P. (1997). Simulations of the temperature profile in a hot electron bolometer. Senior Thesis, Yale University.

Crowe, T. W., R. J. Mattauch, H. P. Roser, W. L. Bishop, W. C. B. Peatman, and X. Liu (1992, November). GaAs schottky diodes for THz mixing applications. *Proceedings of the IEEE 80*(11), 1827–1841.

de Jong, M. J. M. (1995). *Shot Noise and Electrical Conduction in Mesoscopic Systems.* Ph. D. thesis, Leiden University.

Dzardanov, A., H. Ekström, G. Gol'tsman, S. Jacobsson, B. Karasik, E. Kollberg, O. Okunev, and S. Yngvesson (1994). Hot-electron superconducting mixers for 20-500 GHz operation. In M. N. Afsar (Ed.), *Proceedings of the International Conference on Millimeter and Submillimeter Waves and Applications*, San Diego, pp. 276–278. sponsored by the SPIE.

Ekström, H., B. Karasik, E. Kollberg, G. Gol'tsman, and E. Gershenzon (1995). 350 GHz NbN hot electron bolometer mixer. See Zmuidzinas and Rebiez (1995), pp. 269–283.

Ekström, H., B. Karasik, E. Kollberg, and K. Yngvesson (1995). Conversion gain and noise of niobium superconducting hot electron mixers. *IEEE Transactions on Microwave Theory and Techniques 43*(4).

Elant'ev, A. and B. Karasik (1989). Effect of high frequency current on Nb superconducting film in the resistive state. *Soviet Journal of Low Temperature Physics 15*(7), 379–383.

Elliott, R. S. (1981). *Antenna Theory and Design.* Englewood Cliffs, NJ: Prentice Hall.

Face, D., D. Prober, W. McGrath, and P. Richards (1986). High quality tantalum superconducting tunnel junctions for microwave mixing in the quantum limit. *Applied Physics Letters 16*(21), 1098–1100.

Gardiner, C. (1983). *Handbook of Stochastic Methods for Physics, Chemistry, and the Natural Sciences.* Berlin: Springer-Verlag.

Gardiner, C. (1991). *Quantum Noise.* Berlin: Springer-Verlag.

Gershenzon, E., M. Gershenzon, G. Gol'tsman, Lyul'kin, A. Semenov, and A. Sergeev (1990). Electron-phonon interaction in ultrathin Nb films. *Journal of Experimental and Theoretical Physics 70*(3), 505–511.

Gershenzon, E., M. Gershenzon, G. Gol'tsman, A. M. Lyul'kin, A. Semenov, and A. Sergeev (1989). On the limiting characteristics of high-speed superconducting bolometers. *Soviet Physics: Technical Physics 34*(2), 195–201.

Gershenzon, E., M. Gershenzon, G. Gol'tsman, A. Semenov, and A. Sergeev (1982). Nonselective

effect of electromagnetic radiation on superconducting film in the resistive state. *Journal of Experimental and Theoretical Physics Letters 36*(7), 296–299.

Gershenzon, E., G. Gol'tsman, I. G. Gogidze, Y. P. Gusev, A. I. Elant'ev, B. S. Karasik, and A. Semenov (1990). Millimeter and submillimeter range mixer based on electronic heating of superconducting films in the resistive state. *Superconductivity 3*(10), 1582–1597.

Gershenzon, E., G. N. Gol'tsman, A. Elant'ev, B. Karasik, and S. E. Potoskuev (1988). Intense electromagnetic radiation heating of electrons of a superconductor in the resistive state. *Soviet Journal of Low Temperature Physics 14*(7), 414–420.

Gershenzon, M., V. N. Gubandov, and Y. E. Zhuravlev (1983). Quantum effects in two-dimensional superconducting films at $T > T_c$. *Journal of Experimental and Theoretical Physics Letters 36*(7), 296–299.

Gol'tsman, G., A. Semenov, Y. P. Gousev, M. A. Zorin, I. G. Gogidze, E. Gershenzon, P. T. Lang, W. J. Knott, and K. F. Renk (1991). Sensitive picosecond NbN detector for radiation from millimetre wavelengths to visible light. *Superconducting Science and Technology 4*, 453–456.

Gol'tsman, G. N., B. S. Karasik, O. V. Okunev, A. L. Dzardanov, E. M. Gershenzon, H. Ekström, S. Jacobsson, and E. Kollberg (1995). NbN hot electron superconducting mixers for 100 GHz operation. *IEEE Transactions on Applied Superconductivity 5*(2), 3065–3068.

Gousev, Y. P., G. Gol'tsman, A. Semenov, E. Gershenzon, R. Nebosis, M. Heusinger, and K. Renk (1994). Broadband ultrafast superconducting NbN detector for electromagnetic radiation. *Journal of Applied Physics 75*(7), 3695–3697.

Harris, A. I. (1990). Coherent and incoherent detection. In *Proceedings of the 29th Liege International Astrophysics Coloquim on Ground-Based to Space-Borne Sub-mm Astronomy*, pp. 165–169.

Kanskar, M. and M. Wybourne (1994). Crossover between dissipative and nondissipative electron transport in metal wires. *Physical Review Letters 73*(15), 2123–2126.

Karasik, B. (1997). personal communication.

Karasik, B. and A. Elantev (1995). Analysis of the noise performance of a hot-electron superconducting bolometer mixer. See Zmuidzinas and Rebiez (1995), pp. 229–246.

Karasik, B., M. Gaidis, W. McGrath, B. Bumble, and H. G. LeDuc (1997). A low-noise 2.5 THz superconductive Nb hot-electron mixer. *IEEE Transactions on Applied Superconductivity 7*(2), 3580–3583.

Karasik, B., K. Il'in, E. Pechen, and S. Krasnosvobodtsev (1996). Diffusion cooling mechanism in a hot-electron NbC microbolometer mixer. *Applied Physics Letters 68*(16), 2285–2287.

Karasik, B. S. and A. I. Elantiev (1996). Noise temperature limit of a superconducting hot-electron bolometer mixer. *Applied Physics Letters 68*(6), 853–855.

Karasik, B. S., G. N. Gol'tsman, B. M. Voronov, S. I. Svechnikov, E. M. Gershenzon, H. Ekström, S. Jacobsson, E. Kollberg, and K. S. Yngvesson (1995). Hot electron quasioptical NbN superconducting mixer. *IEEE Transactions on Applied Superconductivity 5*(2), 2232–2235.

Kawamura, J., R. Blundell, C. Y. Tong, G. Gol'tsman, E. Gershenzon, and B. Voronov (1996). Performance of NbN lattice-cooled hot-electron bolometric mixers. *Journal of Applied Physics 80*(7), 4232–4234.

Kawamura, J., R. Blundell, C. Y. Tong, G. Gol'tsman, E. Gershenzon, and B. Voronov (1997). Low noise NbN lattice-cooled superconducting hot-electron bolometric mixers at submillimeter wavelengths. *Applied Physics Letters 70*(12), 1619–1621.

Keizer, J. (1987). *Statistical Thermodynamics of Nonequilibrium Processes.* New York: Springer-Verlag.

Kittel, C. (1980). *Thermal Physics, 2nd Edition.* New York: W H Freeman.

Kogan, S. M. (1991). Equations for the correlation functions using a generalized Keldysh technique. *Physical Review A 44*(12), 8072–8082.

Kogan, S. M. (1996). *Electronic Noise and Fluctuatoins in Solids.* Cambridge: Cambridge University Press.

Landau, L. D. and E. M. Lifshitz (1980). *Statistical Physics Part 2.* Oxford: Pergamon.

Maas, S. A. (1993). *Microwave Mixers.* Boston: Artech House.

Mandel, L. and E. Wolf (1995). *Optical Coherence and Quantum Optics.* Cambridge: Cambridge University Press.

Manney, G. L., L. Froidevaus, J. W. Waters, M. L. Santee, W. G. Read, D. A. Flower, R. F. Jarnot, and R. W. Zurek (1996). Arctic ozone depletion observed by UARS MLS during the 1994-95 winter. *Geophysical Research Letters 2*(1), 85–88.

Mather, J. C. (1982). Bolometer noise: Nonequilibrium theory. *Applied Optics 21*(6), 1125–1129.

Mather, J. C. (1984). Electrical self-calibration of nonideal bolometers. *Applied Optics 23*(18), 3181–3183.

McGrath, W., P. Richards, A. Smith, H. van Kempen, R. Batchelor, D. Prober, and P. Santhanam (1981). Large gain, negative resistance, and oscillations in superconducting quasiparticle heterodyne mixers. *Applied Physics Letters 39*(8), 655–658.

Mears, C. A., Q. Hu, P. L. Richards, A. H. Worsham, D. E. Prober, and A. V. Raisanen (1990). Quantum-limited heterodyne detection of millimeter waves using superconducting tantalum tunnel junctions. *Applied Physics Letters 57*(23), 2487–2489.

Mittal, A. (1995). personal communication.

Mittal, A. (1996). *Quantum Transport in Semiconductor Submicron Structures*, Chapter Electron-Phonon Scattering Rates in 2D Systems. Dordrecht, the Netherlands: Kluwer Academic Publishers.

Padman, R., G. J. White, R. Barker, D. Bly, N. Johnson, H. Gibson, M. Griffin, J. A. Murphy, R. Prestage, J. Rogers, and A. Scivetti (1992). A dual-polarization InSb receiver for 461/492 GHz range. *International Journal of Infrared and Millimeter Waves. 13*(10), 1487–1513.

Phillips, T. G. and K. B. Jefferts (1973). A low temperature bolometer heterodyne receiver for millimeter wave astronomy. *Reviews of Scientific Instruments 44*(8), 1009–1014.

Pothier, H., S. Gueron, N. O. Birge, and D. Esteve (1997). Energy distribution of electrons in an out-of-equilibrium metallic wire. *Zeitschrift für Physik B (Condensed Matter) 103*(2), 313–318.

Prober, D., M. Wybourne, and M. Kanskar (1995). Comment on "crossover between dissipative and nondissipative electron transport in metal wires" (and reply). *Physical Review Letters 75*(21), 3964–3965.

Prober, D. E. (1993). Superconducting Terahertz mixer using a transition-edge microbolometer. *Applied Physics Letters 62*(17), 2119–2121.

Rebeiz, G. M. (1992, November). Millimeter-wave and Terahertz integrated circuit antennas. *Proceedings of the IEEE 80*(11), 1–90.

Rutledge, D., D. Neikirk, and D. Kasilingam (1983). Integrated-circuit antennas. *Infrared and Millimeter Waves 10*, 1–90.

Santhanam, P., S. Wind, and D. Prober (1987). Localization, superconducting fluctuations, and superconductivity in thin films and narrow wires of aluminum. *Physical Review B 35*, 3188–3206.

Schoelkopf, R. J., P. Burke, D. Prober, B. Karasik, A. Skalare, W. McGrath, M. Gaidis, B. Bumble, and H. LeDuc (1997). Duffusion-cooled superconducting hot-electron bolometers. In *Proceedings of the 6th Internation Supercondutive Electronics Conference*, Braunschweig. Physikalisch-Technische Bundesanstalt.

Skalare, A. (1994). personal communication.

Skalare, A. (1997). personal communication.

Skalare, A., W. McGrath, B. Bumble, and H. G. LeDuc (1997). Measurement at 1267 GHz using a diffusion-cooled superconducting transition-edge bolometer. *IEEE Transactions on Applied Superconductivity 7*(2), 3568–3571.

Skalare, A., W. R. McGrath, B. Bumble, H. G. LeDuc, P. J. Burke, A. A. Verheijen, R. J. Schoelkopf, and D. E. Prober (1996). Length scaling of bandwidth and noise in hot-electron superconducting mixers. *Applied Physics Letters 68*, 1558.

Skocpol, W. (1974). *Electrical Behavior of Superconducting Microbridges*. Ph. D. thesis, Harvard University.

Skocpol, W., M. Beasley, and M. Tinkham (1974). *Journal of Applied Physics 45*, 4045.

Steinbach, A. H., J. M. Martinis, and M. H. Devoret (1996). Observation of hot-electron shot noise in a metallic resistor. *Physical Review Letters 76*(20), 3806–3809.

Tucker, J. and M. Feldman (1985). Quantum detection at millimeter wavelengths. *Reviews of Modern Physics 57*(4), 1055–1113.

Van der Ziel, A. (1976). *Noise in Measurements*. New York: John Wiley and Sons.

van Vliet, K. M. and J. R. Fassett (1965). *Fluctuation Phenomena in Solids*, Chapter Flucuations Due to Electronic Transitions and Transport in Solids. Academic Press.

Voss, R. F. and J. Clarke (1976). Flicker (1/f) noise: Equilibrium temperature and resistance fluctuations. *Physical Review B 13*(2), 556–573.

Weikle, R. M., G. M. Rebeiz, and T. W. Crowe (Eds.) (1996). *Proceedings of the 7th International Symposium on Space Terahertz Technology*, University of Virginia.

Yagoubov, P., G. Gol'tsman, B. Voronov, L. Seidman, V. Siomash, S. Cherednichenko, and E. Gershenzon (1996). The bandwidth of HEB mixers employing ultrathin NbN films on sapphire substrate. See Weikle, Rebeiz, and Crowe (1996), pp. 290–302.

Yagoubov, P., G. Gol'tsman, B. Voronov, S. Svechnikov, S. Cherednichenko, E. Gershenzon, V. Belitsky, H. Ekström, E. Kollberg, A. Semenov, Y. Gousev, and K. Renk (1996). Quasioptical bolometer mixer at THz frequencies. See Weikle, Rebeiz, and Crowe (1996), pp. 303–317.

Yang, J. X., J. Li, C. F. Musante, and K. S. Yngvesson (1995). Microwave mixing and noise in the two-dimensional electron gas medium at low temperatures. *Applied Physics Letters 66*(15), 1983–1985.

Yang, Y., F. Agahi, D. Dai, C. Musante, W. Grammer, K. Lau, and K. Yngvession (1993). *IEEE Transactions on Microwave Theory and Techniques MTT-41*, 581.

Zmuidzinas, J. and G. Rebiez (Eds.) (1995). *Proceedings of the 6th Internation Symposium on Space Terahertz Technology*, CalTech, Pasadena.